



**This electronic thesis or dissertation has been  
downloaded from Explore Bristol Research,  
<http://research-information.bristol.ac.uk>**

*Author:*

**Cheesman, Noah**

*Title:*

**Applications of geometric singular perturbation theory to mechanics**

*the Painlevé paradox in 3D and related problems*

**General rights**

Access to the thesis is subject to the Creative Commons Attribution - NonCommercial-No Derivatives 4.0 International Public License. A copy of this may be found at <https://creativecommons.org/licenses/by-nc-nd/4.0/legalcode>. This license sets out your rights and the restrictions that apply to your access to the thesis so it is important you read this before proceeding.

**Take down policy**

Some pages of this thesis may have been removed for copyright restrictions prior to having it been deposited in Explore Bristol Research. However, if you have discovered material within the thesis that you consider to be unlawful e.g. breaches of copyright (either yours or that of a third party) or any other law, including but not limited to those relating to patent, trademark, confidentiality, data protection, obscenity, defamation, libel, then please contact [collections-metadata@bristol.ac.uk](mailto:collections-metadata@bristol.ac.uk) and include the following information in your message:

- Your contact details
- Bibliographic details for the item, including a URL
- An outline nature of the complaint

Your claim will be investigated and, where appropriate, the item in question will be removed from public view as soon as possible.

---

---

# Applications of geometric singular perturbation theory to mechanics

The Painlevé paradox in 3D and related problems

---

---

By

NOAH CHEESMAN



Department of Engineering Mathematics  
UNIVERSITY OF BRISTOL

A dissertation submitted to the University of Bristol in accordance with the requirements of the degree of DOCTOR OF PHILOSOPHY in the Faculty of Engineering.

MARCH 2022

Word count: twenty-five thousand nine hundred and ninety-eight



# Abstract

We study the dynamics of a slender rigid rod slipping with unilateral constraint on a rough surface, able to move and rotate in 3D, an extension of the classical (planar) Painlevé problem. We demonstrate that the potential nonexistence and nonuniqueness of forward-time solutions, due to the conflict between the rigid-body assumptions and the the resulting dynamics, seen in the 2D problem, persist in this 3D problem. We are the first to identify crucial aspects of the geometry of the problem and the importance of the azimuthal angular velocity to the dynamics. We show that the planar problem is a singular subset of the full 3D problem, and that crucial results that apply to the 2D problem lose significance in the 3D extension. Like Champneys and Várkonyi, we also study a particular type of orbit, not present in the planar problem, that reaches inconsistency from slipping, and we give a geometric justification for their results. We prove that, unlike in the planar problem, these orbits are typical.

We then proceed to resolve the “paradox”, generalising results obtained by Hogan and Kristiansen through regularising the 2D problem with compliance to the 3D problem. This compliance introduces a small parameter and we use geometric singular perturbation theory (GSPT) to study the resulting singularly perturbed problem. With the incorporation of this compliance, we recover impact without collision (IWC). We follow certain significant orbits from the rigid-body problem and find that they also undergo IWC. To facilitate studying this system, instead of viewing spatial Coulomb friction as a piecewise-smooth (PWS) system, we take it to be the limit of a smooth system, using blowup in the analysis.

The de-facto approach to PWS dynamical systems, with codimension–1 discontinuity sets, relies on the Filippov framework. But this framework does not generalise to systems with higher codimension discontinuities, such as those with spatial Coulomb friction. We study a general system with an isolated codimension–2 discontinuity set, regularising the nonsmooth system and viewing it as the limit of a smooth one, using blowup to study the dynamics. We present a framework for studying these problems, giving the local dynamics, and generalising Filippov sliding, crossing, and sliding vector fields. Whilst motivated by Coulomb friction, the approach is sufficiently general as to apply to any nonsmooth dynamical system with finite-time approach to a codimension-2 discontinuity. We also present a particular class of codimension-2 discontinuity problem, for which we give a more complete classification. This work, with a mathematically rigorous foundation, expands upon the formal work of Antali and Stépán.

Generally, we present a framework for the study of mechanical systems with Painlevé paradoxes, nonsmoothness, or other causes of nonexistence or nonuniqueness of solutions. This approach is to regularise the problem (through smoothing or an incorporation of compliance or other physics) and to use the framework of smooth dynamical systems to study the resulting problem (particularly GSPT and geometric blowup).

---

# Acknowledgements and dedications

## Acknowledgements

The work in this thesis was done in collaboration with my supervisors Professor John Hogan (University of Bristol) and Associate Professor Kristian Uldall Kristiansen (Technical University of Denmark). The initial concept for the work covered in Chapters 2 and 3 was first proposed by Prof. Hogan as part of the PhD proposal, and the concept for Chapter 4 was suggested by Assoc. Prof. Kristiansen in conversations with the author. Much of the work in Chapter 3 generalises results obtained by both Prof. John Hogan and Assoc. Prof. Kristiansen in their work [42].

As allowed by Annex 5 of the Regulations and Code of Practice for Research Degree Programmes, some chapters have been adapted from work that has been published or is currently under review. Chapter 2 is adapted from an article accepted for publication [17]. Chapter 3 is adapted from a paper in preparation [18]. Chapter 4 is adapted from an article published in the SIAM Journal on Applied Dynamical Systems [19]. Much of Chapters 2 and 4 is copied verbatim from the respective papers.

Throughout the document, all figures and tables, unless otherwise specified, were created by the author.

Other than the mathematics for the asymptotics in subsections 2.10.1 to 2.10.3, which was carried out by Prof. Hogan with assistance from the author, all work in Chapter 2 was carried out by the author under the supervision of Prof. Hogan and Assoc. Prof. Kristiansen.

The work within Chapter 3 was carried out by the author. Some of the mathematics, particularly the finding of the correct weights in the blowup in (3.21), was done collaboratively with Prof. John Hogan and Assoc. Prof. Kristiansen. Special thanks are given to Professor John King (University of Nottingham), who kindly assisted by recognising (3.35) to be equivalent to the type I Painlevé equation, a satisfying mathematical coincidence.

Other than Proposition 4.1, which was completed by Assoc. Prof. Kristiansen, the work covered in Chapter 4 was carried out by the author under the supervision and guidance of Assoc. Prof. Kristiansen. Particular details, such as the exact form of the regularisation function in Definition 4.1, were proposed by Assoc. Prof. Kristiansen.

---

## Dedications

Firstly, I would like to thank my supervisors John and Kristian for their help over the course of my PhD, and without whom this work would not have been possible. John's kindness and encouragement during my undergraduate project and summer research internship were a large part of my decision to undertake my PhD. During my research, his wisdom and intuition were important in guiding me around obstacles and our meetings were always as enjoyable as they were useful. I am indebted to Kristian for all his kindness, help, and support. My visits to him in DTU were not only incredibly productive, but also tremendously enjoyable. I am grateful not only for him teaching me about GSPT, but also his beloved Brøndbyernes Idrætsforening, and I will always cherish my trips to him in Denmark.

I have also benefited from discussions with many other academics at conferences and other meetings, including, but not limited to, Máté Antali, Gábor Stépán, Péter Várkonyi, Christian Kuehn, Sam Jelbart, Nikola Popovic, Peter Szmolyan, and particularly Panagiotis Kaklamanos. These people were important in welcoming me into mechanics and GSPT communities.

I would like to thank numerous members of staff at the University of Bristol who helped make me feel at home in the Department of Engineering Mathematics since 2013, especially Alan Champneys, Cameron Hall, Mike Jeffrey, Robert Szalai, and Eddie Wilson. I would like give particular thanks to Oscar Benjamin who has been a good friend and mentor — in not only academic matters but also bike maintenance.

Thanks to all members of the Buncaer, past and present, proper and honorary: Aaron, Ana, Ben(s), Chanelle, Charlotte, Ed, Fahad, Frank, Fanqi, Harry, Ioana, John, Liam, Mark, Nam, Natasha, Nico, Oscar, Robert, Seeralan, Simon(s), Stanisław, Sophie, Tom, Will, Yani, Zohar, and possibly countless others I have unfairly forgotten. Many of them deserve much more lengthy thanks for their friendship than they have been given here. I would particularly like to thank my academic brother Ben Collins; our small research group of two made my PhD much more fun.

I would also like to thank my family for all their support. My parents and sister were a source of encouragement during ebbs, and congratulations during flows. I am truly appreciative of everything they have done for me.

Finally, I would like to thank Rhiannon. Without her love and reassurance, the last few years would have been far more difficult.

# Author's declaration

I declare that the work in this dissertation was carried out in accordance with the requirements of the University's Regulations and Code of Practice for Research Degree Programmes and that it has not been submitted for any other academic award. Except where indicated by specific reference in the text, the work is the candidate's own work. Work done in collaboration with, or with the assistance of, others, is indicated as such. Any views expressed in the dissertation are those of the author.

SIGNED: N. CHEESMAN

DATE: JULY 10, 2022



---

# Table of Contents

	Page
<b>List of Tables</b>	<b>xi</b>
<b>List of Figures</b>	<b>xiii</b>
<b>List of Abbreviations</b>	<b>xvii</b>
<b>1 Introductions</b>	<b>1</b>
1.1 Introduction to the Painlevé paradox . . . . .	1
1.1.1 3D Painlevé Problem . . . . .	4
1.2 Introduction to slow-fast theory, geometric singular perturbation theory, blowup and regularisation . . . . .	14
1.2.1 Blowup of the planar fold . . . . .	18
1.3 Outline . . . . .	30
<b>2 Constraint-based approach</b>	<b>33</b>
2.1 Breakdown of rigid body equations . . . . .	33
2.2 Comparison with 2D problem . . . . .	36
2.3 Projections of the surfaces $b = 0$ and $p = 0$ . . . . .	38
2.4 Physics of the paradox . . . . .	41
2.5 Physical implications of parameter values . . . . .	42
2.6 The role of $\Psi$ . . . . .	43
2.7 Generic behaviour . . . . .	49
2.8 GB manifolds . . . . .	52
2.9 Phase portraits . . . . .	54
2.10 Slipping dynamics near the GB manifold . . . . .	56
2.10.1 Zero eigenvalue . . . . .	66
2.10.2 The case $\Psi = 0$ . . . . .	67
2.10.3 Behaviour near $\mu = \mu_P$ . . . . .	68
2.11 Putting it all together . . . . .	69

2.12	Conclusion . . . . .	73
<b>3</b>	<b>Compliance</b>	<b>75</b>
3.1	Slow-fast setting . . . . .	77
3.2	Slipping to inconsistent transition . . . . .	79
3.2.1	Entry chart: $\bar{p} = 1$ . . . . .	82
3.2.2	Scaling chart: $\bar{\varepsilon} = 1$ . . . . .	84
3.2.3	Exit chart: $\bar{\zeta} = 1$ . . . . .	89
3.3	Impact without collision . . . . .	91
3.3.1	Slipping compression . . . . .	92
3.3.2	Slipping-to-sticking and sticking compression . . . . .	95
3.3.3	Lift-off . . . . .	99
3.3.4	Piecing together full IWC orbit . . . . .	101
3.4	Conclusions . . . . .	102
<b>4</b>	<b>Regularisation of isolated codimension-2 discontinuity sets</b>	<b>103</b>
4.1	Introduction . . . . .	103
4.1.1	Deficiencies of the existing framework . . . . .	105
4.1.2	Outline . . . . .	107
4.2	Preliminaries . . . . .	107
4.2.1	Dynamics near the discontinuity set . . . . .	109
4.2.2	Regularisation . . . . .	111
4.2.3	Summary . . . . .	114
4.3	Blowup for the general regularised system . . . . .	114
4.3.1	Entry chart $\kappa_1$ : dynamics near the discontinuity set . . . . .	116
4.3.2	Scaling chart $\kappa_2$ : dynamics on the discontinuity set . . . . .	120
4.3.3	Summary . . . . .	123
4.4	Classification of the “e-linear” system . . . . .	126
4.4.1	Entry chart $\kappa_1$ : dynamics near the discontinuity set . . . . .	128
4.4.2	Scaling chart $\kappa_2$ : dynamics on the discontinuity set . . . . .	129
4.4.3	Cases . . . . .	132
4.4.4	Bifurcations . . . . .	139
4.4.5	Tables of classification . . . . .	142
4.4.6	Beyond the e-linear normal form . . . . .	147
4.4.7	Codimension- $n$ . . . . .	148
4.5	Examples . . . . .	148
4.5.1	Ball at bottom of a pool [2] . . . . .	148
4.5.2	System with attracting and repelling directions . . . . .	151
4.5.3	System with nonunique sliding vector field . . . . .	153

4.6 Discussion and conclusions . . . . .	154
<b>5 Discussion and Conclusions</b>	<b>157</b>
<b>Appendices</b>	<b>161</b>
<b>A Bifurcations of the geometry of <math>p = 0</math> and <math>b = 0</math></b>	<b>163</b>
<b>B Phase portraits of the constrained 3D Painlevé problem</b>	<b>165</b>
<b>C Initial conditions and parameter values for the numerics in Section 3.2</b>	<b>173</b>
C.1 Initial conditions and parameter values for the numerics in Figure 3.6 . . . . .	173
C.2 Initial conditions and parameter values for the numerics in Figures 3.7 and 3.8	174
<b>D Proof of the regularisation function lemma</b>	<b>175</b>
<b>E Lemma on the e-linear normal form</b>	<b>177</b>
<b>F Lemma on an alternative e-linear normal form with radial dependence</b>	<b>179</b>
<b>G Lemma on the suitability of the e-linear normal form</b>	<b>181</b>
<b>Bibliography</b>	<b>183</b>

TABLE OF CONTENTS

---

# List of Tables

<b>TABLE</b>	<b>Page</b>
4.1 The three cases of the <b>e</b> -linear normal form. . . . .	132
4.2 Generic multiplicity of radially attracting and repelling equilibria along the equator for the <b>e</b> -linear normal form. . . . .	142
4.3 Index for 0 equilibria along the equator. . . . .	142
4.4 Indices for 2 equilibria along the equator. . . . .	143
4.5 Indices for 4 equilibria along the equator. . . . .	143
C.1 Parameter values and initial conditions used in the numerics in Figure 3.6. . . . .	173
C.2 Parameter values and initial conditions used in the numerics in Figures 3.7 and 3.8. . . . .	174

## LIST OF TABLES

---

# List of Figures

FIGURE	Page
1.1 Chalk applied to blackboard. . . . .	2
1.2 Classical (planar) Painlevé problem. . . . .	2
1.3 Diagram of the Painlevé problem in 3D. . . . .	5
1.4 Hausdorff distance. . . . .	17
1.5 Slow-fast fold. . . . .	19
1.6 Blowup of the slow-fast fold. . . . .	20
1.7 Diagrams of the region covered by each directional chart in the blowup of the fold.	21
1.8 Compactification. . . . .	23
1.9 Qualitative behaviour of solutions to the Ricatti equations in (1.55). . . . .	25
1.10 Diagram demonstrating the geometry and the dynamics of 3 key entry/exit charts of the blowup in (1.47). . . . .	27
1.11 Representative solutions on the surface of the sphere in the blowup of the fold. . .	30
2.1 Geometry of $p(\theta, -\pi/2; \mu, \alpha)$ for different values of the coefficient of friction. . . . .	35
2.2 Paradoxical configurations. . . . .	35
2.3 Figure showing equivalence of definitions of the region $p < 0$ . . . . .	36
2.4 Modes of the Painlevé paradox in 2D and 3D. . . . .	37
2.5 Projections of $b$ and $p$ into $(\varphi, \Psi, \Theta)$ space. . . . .	39
2.6 Projections of $b$ and $p$ into $(\theta, \Psi, \Theta)$ space. . . . .	40
2.7 Physics of the Painlevé paradox. . . . .	41
2.8 Interpretation of the critical value of the coefficient $\mu_P(\alpha)$ . . . . .	42
2.9 Modes of the Painlevé paradox in 3D with varying $\Psi$ . . . . .	44
2.10 Modes of the Painlevé paradox for $\Psi = \Psi_L$ . . . . .	45
2.11 Modes of the Painlevé paradox for $\Psi = \Psi_1$ . . . . .	46
2.12 Modes of the Painlevé paradox for $\Psi = \Psi_2$ . . . . .	47
2.13 Modes of the Painlevé paradox for $\Psi = 0, \mu > \mu_L$ . . . . .	47
2.14 Modes of the Painlevé paradox for $\Psi = \Psi_L, \mu > \mu_L$ . . . . .	48
2.15 Modes of the Painlevé paradox for $\Psi = \Psi_1, \mu > \mu_L$ . . . . .	48
2.16 Modes of the Painlevé paradox for $\Psi = \Psi_2, \mu > \mu_L$ . . . . .	49



LIST OF FIGURES

---

2.17	Mechanisms I–III for the 3D Painlevé problem, for increasing $\Psi$ . . . . .	50
2.18	Parameter regions of Cases 1-7 and Mechanisms I-III. . . . .	51
2.19	Critical values $\theta_L$ , $\theta_1$ and $\theta_2$ as functions of $\mu$ . . . . .	51
2.20	Projection of the GB manifold into $(\varphi, \Psi, \Theta)$ space. . . . .	53
2.21	GB manifolds for mechanisms II and III. . . . .	53
2.22	Phase portraits in $(\varphi, \Theta)$ for fixed $\Psi = 0$ and sections of $\theta$ . $\alpha = 3$ and $\mu = 1.4$ . . . . .	55
2.23	Dynamics in the $(p, b)$ -plane for $\mu < \mu_L$ . . . . .	62
2.24	Dynamics in the $(p, b)$ -plane for $\mu > \mu_L$ . . . . .	63
2.25	Possible dynamics in $(p, b)$ space local to the GB manifold for $\Theta > 0$ . . . . .	64
2.26	Possible dynamics in $(p, b)$ space local to the GB manifold for $\Theta < 0$ . . . . .	64
2.27	Comparison of (2.53) and (2.63) for $\varepsilon^2 \hat{\mu} = 0.02$ , $\eta = 1$ , and $\alpha = 3$ . . . . .	69
2.28	Topology and stability of the GB manifold(s) for varying $\Psi$ . . . . .	70
2.29	Topology and stability of the GB manifold in $(\varphi, \Psi, \Theta)$ space. . . . .	70
2.30	Positions of the zeros of $\det \mathbf{K}$ on the GB manifold. . . . .	71
2.31	Eigenvectors along the GB manifold for $\Psi \neq 0$ . . . . .	72
2.32	Numerical integration near the separatrix between orbits that reach inconsistency and those that lift off. . . . .	73
3.1	Incorporation of compliance. . . . .	76
3.2	Diagram of the compliant 3D Painlevé problem. . . . .	76
3.3	Orbits tracked by the blowup of the transition from slipping to inconsistency. . . . .	81
3.4	Geometry of the blowup of the transition from slipping to inconsistency. . . . .	81
3.5	Sketch of the blowup chart $k_1$ with the first order approximation to the invariant manifold (3.29) labelled. . . . .	83
3.6	Numerical integration of the equations in the chart $k_1$ . . . . .	84
3.7	Special solution in the chart $k_2$ . . . . .	85
3.8	Orbits near by the special solution in the chart $k_2$ . . . . .	86
3.9	Qualitative behaviour of solutions to type I Painlevé equation in (3.38). . . . .	88
3.10	Sketch of the blowup of the vertical equilibrium. . . . .	92
3.11	Phase portraits of the layer problem in the chart $k_1$ for both the inconsistent and indeterminate regions. . . . .	93
3.12	Phase portraits of the layer problem in the chart $k_2$ , for both the inconsistent and indeterminate regions. . . . .	95

3.13	Sketch of the geometry of the blowup of $\eta, \xi = 0$ . In <b>(a)</b> , we show (3.71) as a toroidal blowup, with scaling chart found by setting $\bar{\xi} = 1$ and entry chart found by setting $\bar{\eta} = 1$ in the blowup. In <b>(b)</b> and <b>(c)</b> , we show an alternative representation of the blowup: as a polar blowup of the set $\eta = \xi = 0$ , made cylindrical by extending with $\varphi$ in <b>(c)</b> . <b>(c)</b> can be considered as the “unwrapping” of <b>(a)</b> . <b>(d)</b> shows the alternative to the blowup used in (3.71): a spherical blowup of $u = v = \xi = 0$ . Due to the convenience of the trigonometric terms and a single entry chart, this spherical blowup is not used. . . . .	96
3.14	Phase portraits of the limit $\varepsilon \rightarrow 0$ of (3.70) in the blowup (3.71) projected down onto the plane $\xi = 0$ . . . . .	99
3.15	Phase portraits of the sticking system before lift off. . . . .	101
3.16	Full IWC orbit. . . . .	101
4.1	Linear and spatial Coulomb friction. . . . .	104
4.2	The difference between the intersection of two codimension-1 discontinuity sets and an isolated codimension-2 discontinuity set. . . . .	105
4.3	Generic nonuniqueness of the Filippov sliding vector field for codimension-2 discontinuity sets. . . . .	106
4.4	Straightening of $\Sigma$ and the geometric interpretation of $\mathbf{e}$ . . . . .	108
4.5	Smoothing of $\mathbf{e}$ to $\mathbf{e}_\Psi$ . . . . .	112
4.6	Sketches of the blowup geometry. . . . .	116
4.7	Sketch demonstrating how orbits travel up the side of the sphere. . . . .	118
4.8	Sketches of the dynamics in the chart $\kappa_1$ for $\varepsilon_1 = 0$ . . . . .	119
4.9	Sketches of possible limiting dynamics in the scaling chart $\kappa_2$ , corresponding to $\bar{\varepsilon} = 1$ in (4.36). . . . .	123
4.10	Sketches of examples of the dynamics of (4.34) after the blowup in (4.35) projected into the $(\bar{x}, \bar{y})$ plane. . . . .	124
4.11	Sketches of the dynamics projected onto $(\bar{x}, \bar{y}, \mathbf{z})$ space. . . . .	125
4.12	Sliding and crossing in the $\mathbf{e}$ -linear system. . . . .	127
4.13	Intersections of conics. . . . .	129
4.14	Geometric interpretation of the condition for the existence of a critical set in the scaling chart. . . . .	131
4.15	Sketches of the five possible cases of dynamics for Case I when $a, d < 0$ . . . . .	134
4.16	Numerical examples of the five possible cases of dynamics of Case I when $a, d < 0$ . . . . .	135
4.17	Sketches of the three possible qualitative phase portraits of Case II. . . . .	136
4.18	Demonstration of the effect the choice of regularisation function can have on the dynamics for Case III. . . . .	138
4.19	Phase portraits for Case III of the “ $\mathbf{e}$ -linear” system. . . . .	139
4.20	Bifurcation between the existence and absence of a critical set in the scaling chart. . . . .	140

LIST OF FIGURES

---

4.21	Saddle-node bifurcation of equilibria on the equator. . . . .	140
4.22	Possible phase portraits for 0 equilibria. . . . .	144
4.23	Possible phase portraits for 2 equilibria, both attracting. . . . .	144
4.24	Possible phase portraits for 2 equilibria, one radially attracting, one radially repelling. . . . .	144
4.25	Possible phase portraits for 4 equilibria, all radially attracting. . . . .	145
4.26	Possible phase portraits for 4 equilibria, all but one radially attracting. . . . .	145
4.27	Possible phase portraits for 4 equilibria, two adjacent equilibria radially attracting. . . . .	146
4.28	Possible phase portraits for 4 equilibria, two opposite equilibria radially attracting. . . . .	146
4.29	Ball at the bottom of a pool. . . . .	148
4.30	Dynamics of the ball at the bottom of the pool. . . . .	151
4.31	System with attracting and repelling limit directions. . . . .	152
A.1	All possible codimension-1 and codimension-2 bifurcations between geometric cases in $(\mu, \Psi)$ space. . . . .	164
B.1	Phase portraits in $(\varphi, \Theta)$ for fixed $\Psi = 0$ and sections of $\theta$ . $\alpha = 3$ and $\mu = 1.7$ . . . . .	166
B.2	Phase portraits in $(\varphi, \Theta)$ for fixed $\Psi = 1$ and sections of $\theta$ . $\alpha = 3$ and $\mu = 1.4$ . . . . .	167
B.3	Phase portraits in $(\varphi, \Theta)$ for fixed $\Psi = 1$ and sections of $\theta$ . $\alpha = 3$ and $\mu = 1.7$ . . . . .	168
B.4	Phase portraits in $(\theta, \Theta)$ for fixed $\Psi = 0$ and sections of $\varphi$ . $\alpha = 3$ and $\mu = 1.4$ . . . . .	169
B.5	Phase portraits in $(\theta, \Theta)$ for fixed $\Psi = 0$ and sections of $\varphi$ . $\alpha = 3$ and $\mu = 1.7$ . . . . .	170
B.6	Phase portraits in $(\theta, \Theta)$ for fixed $\Psi = 1$ and sections of $\varphi$ . $\alpha = 3$ and $\mu = 1.4$ . . . . .	171
B.7	Phase portraits in $(\theta, \Theta)$ for fixed $\Psi = 1$ and sections of $\varphi$ . $\alpha = 3$ and $\mu = 1.7$ . . . . .	172

# List of Abbreviations

<b>GSPT</b>	geometric singular perurbation theory
<b>IWC</b>	impact without collision
<b>LCP</b>	linear complementarity problem
<b>ODE</b>	ordinary differential equation
<b>PWS</b>	piecewise-smooth

LIST OF ABBREVIATIONS

---

# Chapter 1

## Introductions

In the following sections we introduce the problems and methods that shall be covered within the thesis. First, in section 1.1<sup>1</sup>, we introduce the key example studied within this thesis, the Painlevé paradox. This simple mechanical problem is one of the simplest to demonstrate a lack of existence or uniqueness of solutions under rigid body assumptions. Whilst a great deal of progress has been made in the study of the *planar* Painlevé problem, the full problem, the 3D Painlevé problem, is not as well-understood. In section 1.1, we introduce this full 3D problem and link it to the 2D one.

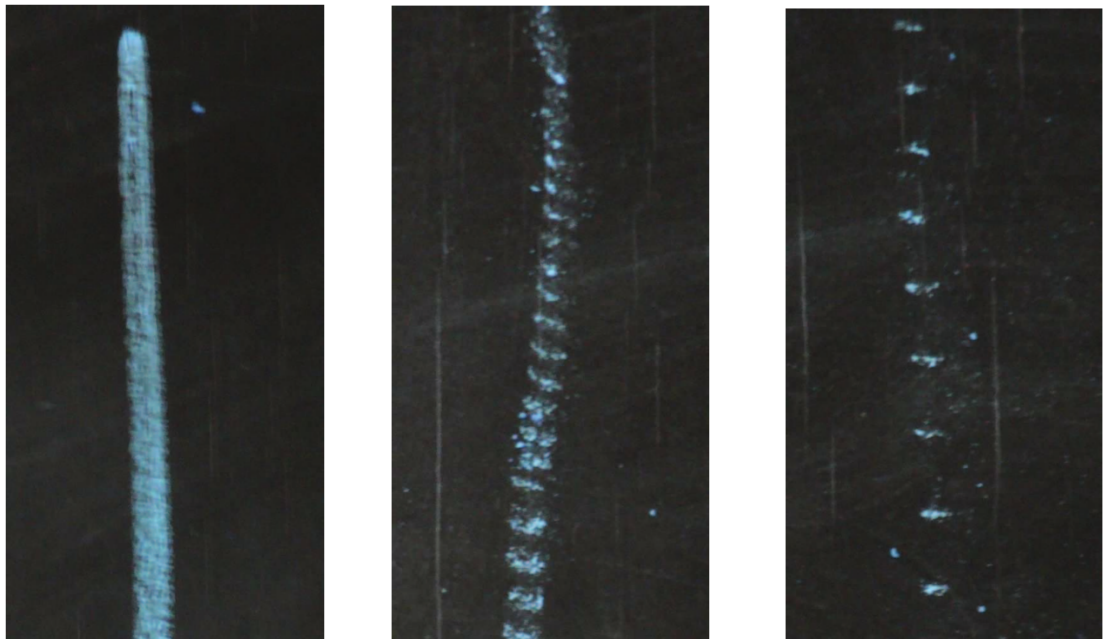
Secondly, in section 1.2, we will introduce the theory and techniques used within the thesis. These methods from the field of nonlinear dynamics are primarily fundamentals, such as phase plane analysis taught in differential equations or dynamical systems courses [100, 101]. However, whilst some of these methods, drawn from slow-fast theory and geometric singular perturbation theory, have proven useful, they are perhaps not as widely adopted as alternatives (matched asymptotic expansions etc.). Hence, a particular attention is given to these lesser-known theories and techniques.

### 1.1 Introduction to the Painlevé paradox

The Painlevé paradox is perhaps the simplest and most-well known example from a class of problems in mechanics where rigid-body assumptions can result in the lack of a unique forward solution in time. Instead, there are inconsistencies (a lack of existence of solutions) and indeterminacies (a lack of uniqueness of solutions). The standard case of this “paradox” consists of a rod slipping along a rough surface, where the forces and motions lie within a plane (shown in Figure 1.2) . As in [16], we will refer to this problem as the classical Painlevé problem. Related problems in statics had already been found in 1872 by Jellet [51], but the discovery by Painlevé led to celebrated discussion about the limits of rigid body theory [4, 5, 22–24, 41, 58, 71, 72, 79, 93]. The inconsistent mode in the classical Painlevé problem corresponds

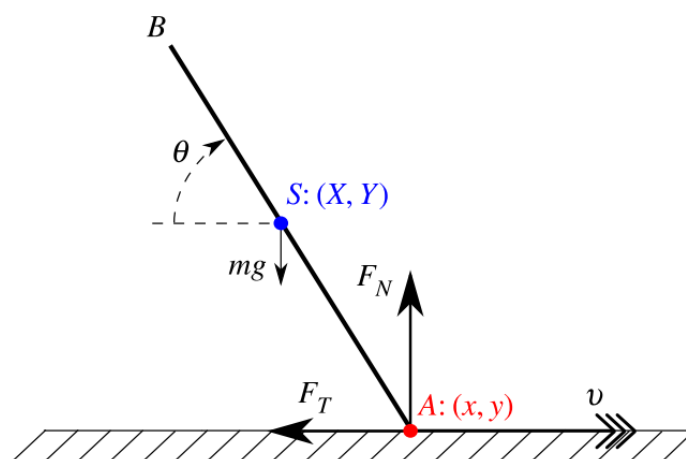
---

<sup>1</sup>Some of this section appears in [17]. See Acknowledgements for contributions.



(a) Applied pulling force      (b) Small applied pushing force      (c) Large applied pushing force

**Figure 1.1:** Figure reproduced. First published in [16] from an unpublished work [40]. “Three traces left by chalk moved by hand across a blackboard. In all figures the direction of motion is downwards. In (a), there is an acute angle between the chalk’s axis and the velocity vector, whereas in (b) and (c) the angle is obtuse. The difference between (b) and (c) is that an increased normal force is applied in (c).”[16]



**Figure 1.2:** Figure reproduced from [42]. This shows the configuration of the classical Painlevé problem

to conditions where both the free body acceleration and the acceleration from contact forces (friction and the normal reaction force) act to drive the rod tip into the surface, violating rigid body assumptions. The indeterminate mode in this system corresponds to the free body acceleration acting to lift up the rod tip away from the surface, whilst the contact forces “pull” it downwards. This results in ambiguity in whether the rod lifts off or remains slipping. Where these inconsistencies and indeterminacies are present in the rigid body model, in reality we see behaviour like jumps and juddering. Physically, the phenomenon can be seen in the behaviour of a piece of chalk when pushed along a chalkboard, where the juddering or squeal is related to this paradox (Figure 1.1). Whilst these paradoxes were viewed as curiosities of physics, they were initially not a cause for concern, as it was thought that the required coefficient of friction was unrealistically high. Nonetheless, interest in Painlevé paradoxes has been revived more recently, where they have been shown to occur in many important engineering systems, where the requisite coefficient of friction, which is a function of system parameters, can be considerably lower [1, 44, 77, 80, 98, 107, 108].

The theoretical study of Painlevé paradoxes in 2D received a great boost with the work by Génot and Brogliato [38]. They proved that the rod cannot reach an inconsistent state when slipping, unless the free acceleration at the rod tip vanishes at the same *critical point* in phase space. This work led to further research [15, 34, 45, 73, 76, 82–84, 95, 104, 105]. Experimental evidence of a Painlevé paradox has been found in a robotic system [112].

There have been many different approaches to “resolve” the paradox, that is to provide a mechanism whereby one can regain uniqueness of solutions. Not long after the problem was posed [85–87], Lecornu proposed that a jump in the vertical velocity could take the system out of the inconsistent state [71, 72]. This corresponds to the judder seen in the pushed chalk. This jump has come to be known as *impact without collision* (IWC) [38], although there have been other synonymous terms: *tangential impact* [44] and *dynamic jamming* [84]. Darboux [21] and Keller [57] both used the concept of this vertical velocity jump to resolve the paradox, considering the equations of motion with respect to a vertical impulse rather than time. However, this method can result in energy gains.

Another approach to resolving the paradox is to regularise the physical rigidity of the system [78], relaxing the rigid-body assumption. The method here is usually based on adding compliance at the interaction between the rod tip and the surface. This can be thought of as modelling the surface as being supported with a very stiff spring and sometimes a damper, allowing small compressions of the surface. It was not until recently that significant analytical developments have been made into the regularised planar Painlevé problem. Nordmark, Dankowicz and Champneys provided insight into the Painlevé paradox, regularised with stiffness *and* damping, identifying key phenomena such as *reverse chatter*[81]. Hogan and Kristiansen [42] gave the first rigorous proofs in the analysis of the 2D system with stiffness and damping, finding that IWC is found in the inconsistent and indeterminate cases. This IWC is shown to have three



distinct phases [42]:

1. slipping compression — the rod begins to compress the surface whilst the tip remains slipping
2. sticking compression — the rod tip sticks, and whilst the surface initially continues to compress, the surface then starts to force rod tip upwards
3. lift-off — at some time the rod tip is moving upwards more quickly than the compressed surface can and the rod lifts off.

The study of Painlevé paradoxes in 3D, where a rigid body moves and rotates whilst in contact with a rough surface (Figure 1.3), has received far less attention. The first paper to explicitly consider such a case appears to be that of Zhao *et al.* [110]. These authors derived the governing equations using energy methods and confirmed that Painlevé paradoxes could occur. Shen [94] considered a 3D elastic rod in rectilinear motion. This version of the problem allows for elastic waves in the rod, whilst still keeping the surface rigid. Champneys and Várkonyi [16] carried out numerical computations of the equations derived by [110] and showed that it was possible to enter the inconsistent region from slipping, unlike the 2D case [38]. However, the compliant system with spring and damping has not been previously covered for the 3D problem. This thesis aims to extend the analysis from [42] to investigate the 3D problem.

### 1.1.1 3D Painlevé Problem

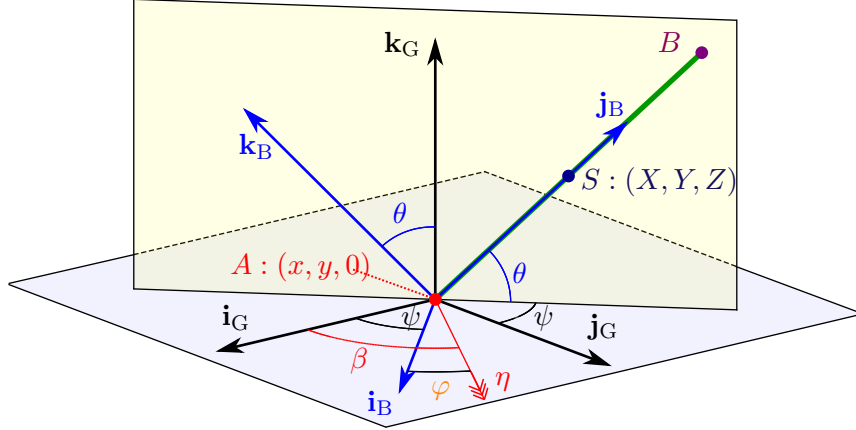
We consider a slender, rigid rod  $AB$  of mass  $m$  slipping on a planar rough horizontal surface, as shown in Figure 1.3.

A global inertial frame fixed to the surface has Cartesian axes  $(\mathbf{i}_G, \mathbf{j}_G, \mathbf{k}_G)$ , whilst a body frame fixed to the rod has axes  $(\mathbf{i}_B, \mathbf{j}_B, \mathbf{k}_B)$ . Note that  $\mathbf{i}_B \cdot \mathbf{k}_G = 0$ , that is  $\mathbf{i}_B$  is tangent to the plane spanned by  $\mathbf{i}_G$  and  $\mathbf{j}_G$ , and the  $\mathbf{j}_B$  axis coincides with the slender rod. The centre of mass of the rod  $S$ , which is at a distance  $l$  from the tip  $A$  in contact with the surface, has coordinates  $X\mathbf{i}_G + Y\mathbf{j}_G + Z\mathbf{k}_G$  in the inertial frame. Point  $A$  has coordinates  $x\mathbf{i}_G + y\mathbf{j}_G$  in the inertial frame.

The rod is inclined at an angle  $\theta$  to the horizontal, the *polar angle* between the  $\mathbf{k}_B$  axis and the  $\mathbf{k}_G$  axis. The *azimuthal angle* between the vertical plane containing the rod and the  $\mathbf{j}_G$  axis is denoted by  $\psi$ . Note that we only need two angles to describe fully this rotation because of the assumption that the rod is slender.

The rod moves on the rough surface with a variable speed  $\eta$  and at an angle  $\beta$  to the  $\mathbf{i}_G$  axis - an angle  $\varphi = \beta - \psi$  to the  $\mathbf{i}_B$  axis. We refer to  $\beta$  as the *slip angle* (or *heading*) and  $\varphi$  as the *relative slip angle* (or *relative heading*). We exclude the cases of the vertical rod and horizontal rod. So we take  $\theta \in (0, \pi/2)$ ,  $\psi \in [-\pi, \pi)$ ,  $\beta \in [-\pi, \pi)$  and  $\varphi \in (-\pi, 0]$ .

We derive the equations of motion of the slender rod as it moves in contact with the rough surface, using force and torque balances, in contrast to the energy method used in [110].



**Figure 1.3:** Diagram of the Painlevé problem in 3D. A slender rod  $AB$  (shown in green) of mass  $m$  moving on a planar rough surface with speed  $\eta \geq 0$ . The global frame of reference  $(\mathbf{i}_G, \mathbf{j}_G, \mathbf{k}_G)$  is fixed to the surface and  $(\mathbf{i}_B, \mathbf{j}_B, \mathbf{k}_B)$  is fixed to the body. The distance between the point of contact  $A$  and the centre of mass  $S$  is given by  $l$ . [110]. When  $\varphi = \pm\pi/2$  the velocity of the rod tip lies in the plane spanned by  $\mathbf{j}_B$  and  $\mathbf{k}_B$ .

The moment of inertia tensor  $\mathbf{I}$  of the rod about its centre with respect to its principal axes is given by

$$(1.1) \quad \mathbf{I} = \begin{pmatrix} I_0 & 0 & 0 \\ 0 & 0 & 0 \\ 0 & 0 & I_0 \end{pmatrix},$$

where  $I_0 = \frac{1}{3}ml^2$  for a uniform rod. The matrix  $\mathbf{I}$  is singular due to the assumed slenderness of the rod.

The angular velocity  $\boldsymbol{\Omega}$  of the rod is given by

$$(1.2) \quad \boldsymbol{\Omega} = \dot{\theta} \mathbf{i}_B + \dot{\psi} \mathbf{k}_G,$$

or in the body frame

$$(1.3) \quad \boldsymbol{\Omega} = \dot{\theta} \mathbf{i}_B + \dot{\psi} \sin \theta \mathbf{j}_B + \dot{\psi} \cos \theta \mathbf{k}_B.$$

The angular momentum in the rod frame is given by  $\mathbf{H} = \mathbf{I}\boldsymbol{\Omega}$ , and the rate of change is given by  $\dot{\mathbf{H}} = \mathbf{I}\dot{\boldsymbol{\Omega}} + \boldsymbol{\Omega} \times (\mathbf{I}\boldsymbol{\Omega})$ . Using (1.1) and (1.3), we find

$$(1.4) \quad \dot{\mathbf{H}} = I_0(\ddot{\theta} + \dot{\psi}^2 \sin \theta \cos \theta) \mathbf{i}_B + I_0(\ddot{\psi} \cos \theta - 2\dot{\theta}\dot{\psi} \sin \theta) \mathbf{k}_B,$$

which has no component in the  $\mathbf{j}_B$  direction due to the assumed slenderness.

Euler's rotation equations state that this rate of change of angular momentum  $\dot{\mathbf{H}}$  is equal to the applied torque  $\mathbf{G}$  of the forces acting on the rod. The force on the rod in the inertial frame

is denoted by  $\mathbf{F} = F_x \mathbf{i}_G + F_y \mathbf{j}_G + F_z \mathbf{k}_G$ . Then  $\mathbf{G} = \mathbf{r} \times (\underline{\mathbf{T}} \mathbf{F})$ , where  $\mathbf{r} = -l \mathbf{j}_B$  is the position vector of the contact point  $A$  relative to  $S$  in the body frame, and  $\underline{\mathbf{T}}$  is the rotation matrix from the inertial frame to the body frame given by

$$(1.5) \quad \underline{\mathbf{T}} = \left( \begin{pmatrix} \cos \psi & -\sin \psi & 0 \\ \sin \psi & \cos \psi & 0 \\ 0 & 0 & 1 \end{pmatrix} \begin{pmatrix} 1 & 0 & 0 \\ 0 & \cos \theta & -\sin \theta \\ 0 & \sin \theta & \cos \theta \end{pmatrix} \right)^\top,$$

$$(1.6) \quad \underline{\mathbf{T}} = \begin{pmatrix} \cos \psi & \sin \psi & 0 \\ -\sin \psi \cos \theta & \cos \psi \cos \theta & \sin \theta \\ \sin \psi \sin \theta & -\cos \psi \sin \theta & \cos \theta \end{pmatrix}.$$

So we find

$$(1.7) \quad \mathbf{G} = \mathbf{r} \times (\underline{\mathbf{T}} \mathbf{F}) = -l(\sin \psi \sin \theta F_x - \cos \psi \sin \theta F_y + \cos \theta F_z) \mathbf{i}_B + l(\cos \psi F_x + \sin \psi F_y) \mathbf{k}_B,$$

which again is zero in the  $\mathbf{j}_B$  component due to the slenderness of the rod.

Equating (1.4) and (1.7), we find

$$(1.8) \quad \begin{aligned} \ddot{\theta} &= -\frac{l}{I_0} (\sin \psi \sin \theta F_x - \cos \psi \sin \theta F_y + \cos \theta F_z) - \dot{\psi}^2 \sin \theta \cos \theta, \\ \ddot{\psi} &= \frac{l}{I_0 \cos \theta} (\cos \psi F_x + \sin \psi F_y) + 2\dot{\psi} \dot{\theta} \tan \theta. \end{aligned}$$

For the case of a uniform rod, (1.8) are identical to [110, eq. (12)], which were derived directly from the energy equations.

The translational dynamics are determined as follows. Using Newton's second law in the inertial frame, we have for the centre of mass  $S$  of the rod

$$(1.9) \quad m\ddot{X} = F_x, \quad m\ddot{Y} = F_y, \quad m\ddot{Z} = F_z - mg.$$

We are, however, more interested in the dynamics of the rod tip and change coordinates accordingly (from point  $S$  to point  $A$  in Figure 1.3). The position of the rod tip relative to the centre is given by  $\underline{\mathbf{T}}^{-1} \mathbf{r}$  and so the three equations that give the position of the rod tip can be given as

$$(1.10) \quad \begin{aligned} x &= X + l \cos \theta \sin \psi, \\ y &= Y - l \cos \theta \cos \psi, \\ z &= Z - l \sin \theta. \end{aligned}$$

Differentiating (1.10) twice with respect to time and substituting the results from (1.8) and

(1.9) gives the following ODEs

$$\begin{aligned}
 \ddot{x} &= \frac{ml^2}{I_0} \left[ \left( -\sin^2 \psi \cos^2 \theta + \frac{I_0}{ml^2} + 1 \right) \frac{F_x}{m} + (\cos^2 \theta \sin \psi \cos \psi) \frac{F_y}{m} \right. \\
 &\quad \left. + (\sin \theta \cos \theta \sin \psi) \frac{F_z}{m} + \frac{I_0}{ml} \left( -\dot{\psi}^2 \cos^3 \theta \sin \psi - \dot{\theta}^2 \cos \theta \sin \psi \right) \right], \\
 \ddot{y} &= \frac{ml^2}{I_0} \left[ (\sin \psi \cos \psi \cos^2 \theta) \frac{F_x}{m} + \left( -\cos^2 \psi \cos^2 \theta + \frac{I_0}{ml^2} + 1 \right) \frac{F_y}{m} \right. \\
 &\quad \left. - (\sin \theta \cos \theta \cos \psi) \frac{F_z}{m} + \frac{I_0}{ml} \left( \dot{\psi}^2 \cos^3 \theta \cos \psi + \dot{\theta}^2 \cos \theta \cos \psi \right) \right], \\
 \ddot{z} &= \frac{ml^2}{I_0} \left[ (\sin \psi \sin \theta \cos \theta) \frac{F_x}{m} - (\cos \theta \cos \psi \sin \theta) \frac{F_y}{m} \right. \\
 &\quad \left. + \left( \cos^2 \theta + \frac{I_0}{ml^2} \right) \frac{F_z}{m} + \frac{I_0}{ml} \left( \dot{\psi}^2 \cos^2 \theta \sin \theta + \dot{\theta}^2 \sin \theta - \frac{I_0}{ml^2} g \right) \right].
 \end{aligned}
 \tag{1.11}$$

We now adopt the scalings  $(x, y, z) = l(\tilde{x}, \tilde{y}, \tilde{z})$ ,  $(F_x, F_y, F_z) = mg(\tilde{F}_x, \tilde{F}_y, \tilde{F}_z)$ ,  $\alpha = ml^2/I_0$  and  $t = \tilde{t}/\omega$ , where  $\omega^2 = g/l$ . Then, by dropping the tildes for the sake of legibility, we are left with the set of nondimensionalised second order ODEs

$$\begin{aligned}
 \ddot{x} &= (-\alpha \sin^2 \psi \cos^2 \theta + \alpha + 1) F_x + (\alpha \cos^2 \theta \sin \psi \cos \psi) F_y + (\alpha \sin \theta \cos \theta \sin \psi) F_z \\
 &\quad + \left( -\dot{\psi}^2 \cos^3 \theta \sin \psi - \dot{\theta}^2 \cos \theta \sin \psi \right), \\
 \ddot{y} &= (\alpha \sin \psi \cos \psi \cos^2 \theta) F_x + (-\alpha \cos^2 \psi \cos^2 \theta + \alpha + 1) F_y - (\alpha \sin \theta \cos \theta \cos \psi) F_z \\
 &\quad + \left( \dot{\psi}^2 \cos^3 \theta \cos \psi + \dot{\theta}^2 \cos \theta \cos \psi \right), \\
 \ddot{z} &= (\alpha \sin \psi \sin \theta \cos \theta) F_x - (\alpha \cos \theta \cos \psi \sin \theta) F_y + (\alpha \cos^2 \theta + 1) F_z \\
 &\quad + \left( \dot{\psi}^2 \cos^2 \theta \sin \theta + \dot{\theta}^2 \sin \theta - 1 \right), \\
 \ddot{\psi} &= \left( \frac{\alpha \cos \psi}{\cos \theta} \right) F_x + \left( \frac{\alpha \sin \psi}{\cos \theta} \right) F_y + \left( 2\dot{\psi}\dot{\theta} \frac{\sin \theta}{\cos \theta} \right), \\
 \ddot{\theta} &= -(\alpha \sin \psi \sin \theta) F_x + (\alpha \cos \psi \sin \theta) F_y - (\alpha \cos \theta) F_z - \left( \dot{\psi}^2 \sin \theta \cos \theta \right),
 \end{aligned}
 \tag{1.12}$$

or equivalently a set of 10 first-order ODEs

$$\begin{aligned}
 \dot{x} = u, \quad \dot{u} &= (-\alpha \sin^2 \psi \cos^2 \theta + \alpha + 1)F_x + (\alpha \cos^2 \theta \sin \psi \cos \psi)F_y \\
 &\quad + (\alpha \sin \theta \cos \theta \sin \psi)F_z + (-(\Psi^2 \cos^2 \theta + \Theta^2) \cos \theta \sin \psi), \\
 \dot{y} = v, \quad \dot{v} &= (\alpha \sin \psi \cos \psi \cos^2 \theta)F_x + (-\alpha \cos^2 \psi \cos^2 \theta + \alpha + 1)F_y \\
 &\quad - (\alpha \sin \theta \cos \theta \cos \psi)F_z + ((\Psi^2 \cos^2 \theta + \Theta^2) \cos \theta \cos \psi), \\
 (1.13) \quad \dot{z} = w, \quad \dot{w} &= (\alpha \sin \psi \sin \theta \cos \theta)F_x - (\alpha \cos \theta \cos \psi \sin \theta)F_y \\
 &\quad + (\alpha \cos^2 \theta + 1)F_z + ((\Psi^2 \cos^2 \theta + \Theta^2) \sin \theta - 1), \\
 \dot{\psi} = \Psi, \quad \dot{\Psi} &= \left(\frac{\alpha \cos \psi}{\cos \theta}\right)F_x + \left(\frac{\alpha \sin \psi}{\cos \theta}\right)F_y + (2\Psi\Theta \frac{\sin \theta}{\cos \theta}), \\
 \dot{\theta} = \Theta, \quad \dot{\Theta} &= (-\alpha \sin \psi \sin \theta)F_x + (\alpha \cos \psi \sin \theta)F_y + (-\alpha \cos \theta)F_z \\
 &\quad + (-\Psi^2 \sin \theta \cos \theta).
 \end{aligned}$$

Note that there are only 5 second-order ODEs. A generic 3D rigid body moving in 3D would require 6 second-order ODEs. However, from the assumption that the rod is slender, we need not consider rotations about the axis coincident with the rod.

In order to proceed, we must specify  $F_x$ ,  $F_y$  and  $F_z$ . Let us, for now, assume Coulomb friction, and hence when slipping

$$(1.14) \quad F_x = -\mu \cos \beta F_z, \quad F_y = -\mu \sin \beta F_z,$$

where  $\mu$  is the coefficient of friction between the rod and the surface, and the angle of slip,  $\beta$ , is defined by

$$(1.15) \quad \cos \beta = \frac{u}{\sqrt{u^2 + v^2}}, \quad \sin \beta = \frac{v}{\sqrt{u^2 + v^2}}.$$

This slip angle can be considered conceptually as the "heading" of the rod tip relative to the surface when slipping.

In this work, we will consider two forms of the vertical component of the contact force  $F_z$ . In Chapter 2, we assume that when the tip is in contact with the surface, the (nondimensionalised) force  $F_z$  acts to keep the rod tip on the surface, and  $F_z$  can be found by solving  $\ddot{z} = 0$ . In Chapter 3, we assume that there is compliance, and the force  $F_z$  has stiffness and damping terms.

First, let us substitute (1.14) into our set of nondimensionalised equations (1.12) and write as a set of ten first order differential equations

$$\begin{aligned}
 \dot{x} &= u, & \dot{u} &= q_1(\psi, \theta, u, v)F_z + a_1(\Psi, \Theta, \psi, \theta) = f_u, \\
 \dot{y} &= v, & \dot{v} &= q_2(\psi, \theta, u, v)F_z + a_2(\Psi, \Theta, \psi, \theta) = f_v, \\
 \dot{z} &= w, & \dot{w} &= p(\psi, \theta, u, v)F_z + b(\Psi, \Theta, \psi, \theta) = f_w, \\
 \dot{\psi} &= \Psi, & \dot{\Psi} &= d_1(\psi, \theta, u, v)F_z + c_1(\Psi, \Theta, \psi, \theta) = f_\Psi, \\
 \dot{\theta} &= \Theta, & \dot{\Theta} &= d_2(\psi, \theta, u, v)F_z + c_2(\Psi, \psi, \theta) = f_\Theta,
 \end{aligned}
 \tag{1.16}$$

where

$$\begin{aligned}
 q_1(\psi, \theta, u, v; \mu, \alpha) &:= -\alpha \sin \psi \cos \theta (\mu \cos \theta \sin (\beta(u, v) - \psi) - \sin \theta) - \mu(1 + \alpha) \cos \beta(u, v), \\
 q_2(\psi, \theta, u, v; \mu, \alpha) &:= +\alpha \cos \psi \cos \theta (\mu \cos \theta \sin (\beta(u, v) - \psi) - \sin \theta) - \mu(1 + \alpha) \sin \beta(u, v), \\
 p(\psi, \theta, u, v; \mu, \alpha) &:= +\alpha \sin \theta (\mu \cos \theta \sin (\beta(u, v) - \psi) - \sin \theta) + \alpha + 1, \\
 a_1(\Psi, \Theta, \psi, \theta) &:= -(\Psi^2 \cos^2 \theta + \Theta^2) \cos \theta \sin \psi, \\
 a_2(\Psi, \Theta, \psi, \theta) &:= +(\Psi^2 \cos^2 \theta + \Theta^2) \cos \theta \cos \psi, \\
 b(\Psi, \Theta, \theta) &:= +(\Psi^2 \cos^2 \theta + \Theta^2) \sin \theta - 1, \\
 d_1(\psi, \theta, u, v; \mu) &:= -\alpha \mu \cos \psi \sec \theta \cos \beta(u, v) - \alpha \mu \sin \psi \cos \theta \sin \beta(u, v), \\
 d_2(\psi, \theta, u, v; \mu, \alpha) &:= +\alpha \mu \sin \psi \sin \theta \cos \beta(u, v) - \alpha \mu \cos \psi \sin \theta \sin \beta(u, v) - \alpha \cos \theta, \\
 c_1(\Psi, \Theta, \theta) &:= 2\dot{\psi}\dot{\theta} \sin \theta \sec \theta, \\
 c_2(\Psi, \theta) &:= -\dot{\psi}^2 \sin \theta \cos \theta, \\
 \beta(u, v) &:= \arctan(v/u).
 \end{aligned}
 \tag{1.17}$$

Instead of considering global velocities  $u, v$ , it may be more useful to consider a speed  $\eta$  and a global bearing  $\beta$ , the slip direction. These are related to  $u$  and  $v$  by

$$\eta = \sqrt{u^2 + v^2}
 \tag{1.18}$$

and

$$\beta = \arctan(v/u)
 \tag{1.19}$$

(or equivalently  $u = \eta \cos \beta$  and  $v = \eta \sin \beta$ ).

Taking the time derivative of  $(\eta, \beta)^\top$

$$\begin{aligned}
 \begin{pmatrix} \dot{\eta} \\ \dot{\beta} \end{pmatrix} &= \begin{pmatrix} \frac{\partial \eta}{\partial u} & \frac{\partial \eta}{\partial v} \\ \frac{\partial \beta}{\partial u} & \frac{\partial \beta}{\partial v} \end{pmatrix} \begin{pmatrix} \dot{u} \\ \dot{v} \end{pmatrix}, \\
 &= \begin{pmatrix} \cos \beta & \sin \beta \\ -\frac{1}{\eta} \sin \beta & \frac{1}{\eta} \cos \beta \end{pmatrix} \left( \begin{pmatrix} q_1 \\ q_2 \end{pmatrix} F_z + \begin{pmatrix} a_1 \\ a_2 \end{pmatrix} \right), \\
 (1.20) \quad &= \begin{pmatrix} Q_1 \\ \frac{1}{\eta} Q_2 \end{pmatrix} F_z + \begin{pmatrix} A_1 \\ \frac{1}{\eta} A_2 \end{pmatrix},
 \end{aligned}$$

where

$$(1.21) \quad \begin{pmatrix} Q_1 & A_1 \\ Q_2 & A_2 \end{pmatrix} := \begin{pmatrix} \cos \beta & \sin \beta \\ -\sin \beta & \cos \beta \end{pmatrix} \begin{pmatrix} q_1 \\ q_2 \end{pmatrix}.$$

Thus, our equations of motion become

$$\begin{aligned}
 \dot{x} &= \eta \cos \beta, & \dot{\eta} &= Q_1(\psi, \theta, \beta) F_z + A_1, \\
 \dot{y} &= \eta \sin \beta, & \eta \dot{\beta} &= Q_2(\psi, \theta, \beta) F_z + A_2, \\
 (1.22) \quad \dot{z} &= w, & \dot{w} &= p(\psi, \theta, \beta) F_z + b(\Psi, \Theta, \psi, \theta), \\
 \dot{\psi} &= \Psi, & \dot{\Psi} &= d_1(\psi, \theta, \beta) F_z + c_1(\Psi, \Theta, \psi, \theta), \\
 \dot{\theta} &= \Theta, & \dot{\Theta} &= d_2(\psi, \theta, \beta) F_z + c_2(\Psi, \psi, \theta).
 \end{aligned}$$

As in [110], we introduce the variable  $\varphi = \beta - \psi$ . This is the relative slip angle: the relative angle between the orientation of the rod and the direction of slipping (see Figure 1.3). Re-writing (1.22) in terms of  $\varphi$ ,

$$\begin{aligned}
 \dot{x} &= \eta \cos(\psi + \varphi), & \dot{\eta} &= Q_1 F_z + A_1, \\
 \dot{y} &= \eta \sin(\psi + \varphi), & \eta \dot{\varphi} &= Q_2 F_z + A_2 - \eta \Psi, \\
 (1.23) \quad \dot{z} &= w, & \dot{w} &= p F_z + b, \\
 \dot{\psi} &= \Psi, & \dot{\Psi} &= d_1 F_z + c_1, \\
 \dot{\theta} &= \Theta, & \dot{\Theta} &= d_2 F_z + c_2,
 \end{aligned}$$

where

$$\begin{aligned}
 Q_1 &= Q_1(\theta, \varphi; \mu, \alpha) := \alpha \cos \theta \sin \varphi (\mu \cos \theta \sin \varphi - \sin \theta) - (1 + \alpha)\mu, \\
 Q_2 &= Q_2(\theta, \varphi; \mu, \alpha) := \alpha \cos \theta \cos \varphi (\mu \cos \theta \sin \varphi - \sin \theta), \\
 p &= p(\theta, \varphi; \mu, \alpha) := 1 + \alpha + \alpha \sin \theta (\mu \cos \theta \sin \varphi - \sin \theta), \\
 A_1 &= A_1(\Psi, \Theta, \theta, \varphi) := (\Psi^2 \cos^2 \theta + \Theta^2) \cos \theta \sin \varphi, \\
 A_2 &= A_2(\Psi, \Theta, \psi, \theta) := (\Psi^2 \cos^2 \theta + \Theta^2) \cos \theta \cos \varphi, \\
 b &= b(\Psi, \Theta, \theta) := (\Psi^2 \cos^2 \theta + \Theta^2) \sin \theta - 1, \\
 d_1 &= d_1(\theta, \varphi; \mu, \alpha) := -\alpha \mu \frac{\cos \varphi}{\cos \theta}, \\
 d_2 &= d_2(\theta, \varphi; \mu, \alpha) := -\alpha \mu \sin \theta \sin \varphi - \alpha \cos \theta, \\
 c_1 &= c_1(\Psi, \Theta, \theta) := 2\Psi\Theta \frac{\sin \theta}{\cos \theta}. \\
 c_2 &= c_2(\Psi, \theta) := -\Psi^2 \sin \theta \cos \theta.
 \end{aligned}
 \tag{1.24}$$

Of particular importance in the sequel are

$$b(\Psi, \Theta, \theta) := (\Psi^2 \cos^2 \theta + \Theta^2) \sin \theta - 1
 \tag{1.25}$$

and

$$p(\theta, \varphi; \mu, \alpha) := 1 + \alpha + \alpha \sin \theta (\mu \cos \theta \sin \varphi - \sin \theta).
 \tag{1.26}$$

**Proposition 1.1.** *From (1.23) and (1.24),  $\{\Psi = 0\} \cap \{\varphi = \pm\pi/2\}$  (the planar Painlevé problem) is an invariant manifold.*

**Proof.** Substituting  $\Psi = 0$  and  $\varphi = \pm\pi/2$  into (1.23), we find

$$\begin{aligned}
 \dot{x} &= \eta \mp \cos \psi, & \dot{\eta} &= Q_1(\theta, \pm\pi/2; \mu, \alpha)F_z + A_1(0, \Theta, \theta, \pm\pi/2), \\
 \dot{y} &= \eta \pm \sin \psi, & \dot{\eta}\dot{\varphi} &= 0, \\
 \dot{z} &= w, & \dot{w} &= p(\theta, \pm\pi/2; \mu, \alpha)F_z + b(0, \Theta, \theta), \\
 \dot{\psi} &= 0, & \dot{\Psi} &= 0, \\
 \dot{\theta} &= \Theta, & \dot{\Theta} &= d_2(\theta, \pm\pi/2; \mu, \alpha)F_z,
 \end{aligned}$$



where

$$Q_1(\theta, \pm\pi/2; \mu, \alpha) = \alpha \cos \theta \pm (\pm\mu \cos \theta - \sin \theta) - (1 + \alpha)\mu$$

$$p(\theta, \pm\pi/2; \mu, \alpha) = 1 + \alpha + \alpha \sin \theta (\pm\mu \cos \theta - \sin \theta)$$

$$A_1(0, \Theta, \theta, \pm\pi/2) = \pm\Theta^2 \cos \theta$$

$$b(0, \Theta, \theta) = \Theta^2 \sin \theta - 1$$

$$d_2(\theta, \pm\pi/2; \mu, \alpha) = \mp\alpha\mu \sin \theta - \alpha \cos \theta.$$

Since  $\dot{\varphi} = \dot{\Psi} = 0$  in  $\{\Psi = 0\} \cap \{\varphi = \pm\pi/2\}$  is an invariant manifold of (1.23). ■

These slipping equations are not well-defined when the rod sticks,  $u = v = 0$  ( $\eta = 0$ ). It will be convenient for discussion later to regularise these equations, viewing them as the limit of a smoother system. This regularisation takes the form of smoothing the step function involved in Coulomb friction. In this work we will only consider the nonsmooth limit of this smooth function, as our small smoothing parameter tends to zero.

Practically speaking, whilst we had previously modelled friction as taking the form

$$F_x = -\mu \frac{u}{\sqrt{u^2 + v^2}} F_z, \quad F_y = -\mu \frac{v}{\sqrt{u^2 + v^2}} F_z,$$

or in polar form

$$F_x = -\mu \frac{\eta \cos \beta}{|\eta|} F_z, \quad F_y = -\mu \frac{\eta \sin \beta}{|\eta|} F_z,$$

we will at times consider instead the non smooth limit ( $\xi \rightarrow 0$ ) of

$$F_x = -\mu \frac{u}{\sqrt{u^2 + v^2 + \xi^2}} F_z, \quad F_y = -\mu \frac{v}{\sqrt{u^2 + v^2 + \xi^2}} F_z,$$

or

$$F_x = -\mu \frac{\eta \cos \beta}{\sqrt{\eta^2 + \xi^2}} F_z, \quad F_y = -\mu \frac{\eta \sin \beta}{\sqrt{\eta^2 + \xi^2}} F_z$$

in polar form, where  $\xi$  is the small smoothing parameter  $0 < \xi \ll 1$ . Using these models the

equations of motion are then given as is (1.23) except that now

$$\begin{aligned}
 Q_1 &= Q_1^\xi(\theta, \varphi, R(\eta, \xi); \mu, \alpha) := Q_1\theta, \varphi; \mu R(\eta, \xi), \alpha), \\
 &= \alpha \cos \theta \sin \varphi (\mu R(\eta, \xi) \cos \theta \sin \varphi - \sin \theta) - (1 + \alpha)\mu R(\eta, \xi), \\
 Q_2 &= Q_2^\xi(\theta, \varphi, R(\eta, \xi); \mu, \alpha) := Q_2\theta, \varphi; \mu R(\eta, \xi), \alpha), \\
 &= \alpha \cos \theta \cos \varphi (\mu R(\eta, \xi) \cos \theta \sin \varphi - \sin \theta), \\
 p &= p^\xi(\theta, \varphi, R(\eta, \xi); \mu, \alpha) := p\theta, \varphi; \mu R(\eta, \xi), \alpha), \\
 (1.27) \quad &= 1 + \alpha + \alpha \sin \theta (\mu R(\eta, \xi) \cos \theta \sin \varphi - \sin \theta), \\
 d_1 &= d_1^\xi(\theta, \varphi, R(\eta, \xi); \mu, \alpha) := d_1\theta, \varphi; \mu R(\eta, \xi), \alpha), \\
 &= -\alpha \mu R(\eta, \xi) \frac{\cos \varphi}{\cos \theta}, \\
 d_2 &= d_2^\xi(\theta, \varphi, R(\eta, \xi); \mu, \alpha) := d_2\theta, \varphi; \mu R(\eta, \xi), \alpha), \\
 &= -\alpha \mu R(\eta, \xi) \sin \theta \sin \varphi - \alpha \cos \theta, \\
 R(\eta, \xi) &:= \frac{\eta}{\sqrt{\eta^2 + \xi^2}}.
 \end{aligned}$$

<sup>2</sup> This method of smoothing Coulomb friction will be used to obtain results in Chapter 3. However, the discussion of the theory behind this approach is left until Chapter 4.

In section 2.1, we will show that under rigid-body assumptions, the equations (1.23) exhibit nonuniqueness and nonexistence of solutions. In Chapter 3, our approach to resolving this problem is through the incorporation of compliance. This compliance (the inverse of stiffness) is very small, however, and so we introduce a small parameter  $\varepsilon$ . We have also mentioned the introduction of a separate small smoothing parameter  $\xi$  to aid with the study of friction.

Implicitly, in the following chapters we shall take that  $1 \gg \varepsilon \gg \xi > 0$ ; effectively assuming that the surface is more compliant than the friction law is smoothed. This may be physically realistic as for certain surfaces their compliances may be noticeable, whilst the friction law will be effectively nonsmooth. In Chapter 3 we focus more on the dynamics corresponding to the compliance  $\varepsilon$  (compression and lift-off), whilst in subsection 3.3.2 and Chapter 4, we study the dynamics corresponding to  $\xi$  (slipping and sticking).

Whilst these small parameters result in dynamics that occur at drastically different scales, introducing complex behaviours into the system, they also provide an opportunity. In the

---

<sup>2</sup>Note that, as with  $Q_i^\xi$  and  $d_i^\xi$ ,  $p^\xi(\theta, \varphi, R(\eta, 0)) \equiv p(\theta, \varphi; \mu R(\eta, 0), \alpha) \equiv p(\theta, \varphi; \mu, \alpha)$  for  $\eta > 0$ , since  $R(\eta, 0) \equiv 1$  for  $\eta > 0$ .

following section, we introduce the methods used within this thesis which exploit these small parameters to gain understanding of the dynamics.

## 1.2 Introduction to slow-fast theory, geometric singular perturbation theory, blowup and regularisation

In many dynamical systems it is common to find that variables evolve on different time scales. Differences in the orders of magnitude of parameters or variables can lead to systems where different aspects of the dynamics occur on different time scales. Slow-fast theory essentially uses this separation of time scales to reduce a potentially difficult multi-dimensional problem into simpler lower-dimensional problems for each of the time scales.

**Remark 1.1.** *Slow-fast systems can also be called fast-slow systems; this is perhaps more logical as it corresponds to the standard chronology of the dynamics (the fast behaviour happens first) and the way in which one studies these systems (tending to analyse the fast dynamics first). Moreover, both of these terms have their limitations as they do not generalise well to systems where there are more than two time scales (multiple time scale dynamical systems)[70]. Nevertheless we will use the term slow-fast herein.*

Geometric singular perturbation theory (GSPT), perhaps unsurprisingly given its name, gives a more geometric approach to singular perturbation problems, like those that arise in the study of slow-fast systems. GSPT is an alternative to singular perturbation methods such as matched asymptotic expansions. One of the key components of GSPT is Fenichel’s Theorem which effectively states that, under certain conditions, the dynamics of a slow-fast system are close to the solution made by piecing together the limiting cases of simpler lower-dimensional problems (fast and slow). Nevertheless, it is where these conditions are not met that we require another mathematical tool, the blowup method. The blowup method helps to resolve some of the problems with the limitations of Fenichel’s Theorem by extending and manipulating the geometry of the original slow-fast problem.

There are some good texts discussing slow-fast theory, GSPT and blowup. Christian Kuehn’s “Multiple Time Scale Dynamics” [70] gives an invaluable introduction to all three of those topics. Christopher Jones’ lecture series “Geometric Singular Perturbation Theory” [54] provides a great “exposition” of the area, collecting (and making more accessible) some of the crucial building blocks of GSPT (including Fenichel’s Theorem [35] and The Exchange Lemma [53]) as well as giving examples. The initial developments in blowup were made by Dumortier and Roussarie in [30, 31] and then continued by Krupa and Szymolyan in [67–69]. We shall give a short and informal introduction into useful methods and terminology from this theory for the sake of completeness. We shall tend to follow [67, 70] especially closely, including sufficient information such that the reader should only need to be familiar with the more standard parts of the study

of nonlinear dynamics and ODEs [100, 101] in order to follow the methods used in following chapters. In this work, we tend to use blowup in a slightly different way to some other authors. Whilst the rigour of the blowup method is powerful when constructing proofs, we shall instead use the method as a way to gain geometric insights about difficult dynamical problems, and also as a means of matching across local regimes in which the dynamics are more tractable.

### 1.2.0.1 Slow-fast theory and GSPT

Let us start by introducing slow-fast theory. A slow-fast system of ordinary differential equations (ODEs) in *standard* form can be written as

$$(1.28) \quad \begin{aligned} \frac{d\mathbf{x}}{dt} &= \mathbf{f}(\mathbf{x}, \mathbf{y}; \varepsilon), \\ \frac{d\mathbf{y}}{dt} &= \varepsilon \mathbf{g}(\mathbf{x}, \mathbf{y}; \varepsilon). \end{aligned}$$

where  $\mathbf{x} \in \mathbb{R}^m$  and  $\mathbf{y} \in \mathbb{R}^n$ , the functions  $\mathbf{f} : \mathbb{R}^m \times \mathbb{R}^n \rightarrow \mathbb{R}^m$  and  $\mathbf{g} : \mathbb{R}^m \times \mathbb{R}^n \rightarrow \mathbb{R}^n$ , and the parameter  $\varepsilon$  is small ( $0 < \varepsilon \ll 1$ ).

Simply from inspecting the form of these equations, we can see that the  $\mathbf{x}$  variables will typically evolve faster than the  $\mathbf{y}$  variables. If  $\mathbf{f}, \mathbf{g} \approx \mathcal{O}(1)$  then  $d\mathbf{x}/dt \approx \mathcal{O}(1)$  whilst  $d\mathbf{y}/dt \approx \mathcal{O}(\varepsilon)$ . Hence, we will call  $\mathbf{x}$  the *fast variables* and  $\mathbf{y}$  the *slow variables*.

Writing (1.28) in a rescaled time  $\tau = t/\varepsilon$  gives equations in the form

$$(1.29) \quad \begin{aligned} \varepsilon \frac{d\mathbf{x}}{d\tau} &= \mathbf{f}(\mathbf{x}, \mathbf{y}, \varepsilon), \\ \frac{d\mathbf{y}}{d\tau} &= \mathbf{g}(\mathbf{x}, \mathbf{y}, \varepsilon). \end{aligned}$$

In this timescale, we can still see that  $\mathbf{x}$  will evolve more quickly than  $\mathbf{y}$ , but now both variables are faster moving:  $d\mathbf{x}/d\tau \approx \mathcal{O}(\varepsilon^{-1})$  and  $d\mathbf{y}/d\tau \approx \mathcal{O}(1)$ . Hence, the equation (1.28) is said to be in fast time (with respect to the fast time scale  $t$ ) whilst (1.29) is said to be in slow time (with respect to the slow time scale  $\tau$ ).

So far, we have not yet simplified our problem at all; we have only written our equations in two time scales, and trajectories of (1.28) and (1.29) are equivalent. The simplification comes when we look at the limiting case  $\varepsilon \rightarrow 0$  of both (1.28) and (1.29), given by

$$(1.30) \quad \begin{aligned} \frac{d\mathbf{x}}{dt} &= \mathbf{f}(\mathbf{x}, \mathbf{y}, 0), \\ \frac{d\mathbf{y}}{dt} &= 0, \end{aligned}$$

and

$$(1.31) \quad \begin{aligned} 0 &= \mathbf{f}(\mathbf{x}, \mathbf{y}, 0), \\ \frac{d\mathbf{y}}{d\tau} &= \mathbf{g}(\mathbf{x}, \mathbf{y}, 0). \end{aligned}$$

Now, (1.31) and (1.30) are not equivalent; for example in (1.30),  $\mathbf{y}$  is stationary, whilst in (1.31),  $\mathbf{y}$  can evolve. We refer to (1.31) as the *reduced problem*, whilst we refer to (1.30) as the *layer problem*. These are also known as the slow (1.31) and fast (1.30) subsystems.

The layer problem gives an  $m$ -dimensional differential equation

$$(1.32) \quad \frac{d\mathbf{x}}{dt} = \mathbf{f}(\mathbf{x}, \mathbf{y}^*, 0),$$

effectively parameterised by

$$(1.33) \quad \frac{d\mathbf{y}}{dt} = 0 \implies \mathbf{y} = \mathbf{y}^*,$$

where  $\mathbf{y}^*$  is a  $n$ -dimensional vector of constants.

The reduced problem gives an differential-algebraic equation: an  $n$ -dimensional *differential equation*

$$(1.34) \quad \frac{d\mathbf{y}}{d\tau} = \mathbf{g}(\mathbf{x}, \mathbf{y}, 0),$$

subject to the *algebraic constraint*

$$(1.35) \quad 0 = \mathbf{f}(\mathbf{x}, \mathbf{y}, 0).$$

The dynamics prescribed by (1.34) occur on this  $n$ -dimensional (codimension- $m$ ) set (1.35).

Here we see that the algebraic constraint of the reduced problem (1.35) gives the set of equilibria of the layer problem (1.32) (for a given  $\mathbf{y} = \mathbf{y}^*$ ). This set  $C_0 = \{(\mathbf{x}, \mathbf{y}) | \mathbf{x} \in \mathbb{R}^m, \mathbf{y} \in \mathbb{R}^n, \mathbf{f}(\mathbf{x}, \mathbf{y}, 0) = 0\}$  is called the *critical set*. If  $C_0$  is also a submanifold of  $\mathbb{R}^{m+n}$ , then  $C_0$  is called the *critical manifold*.

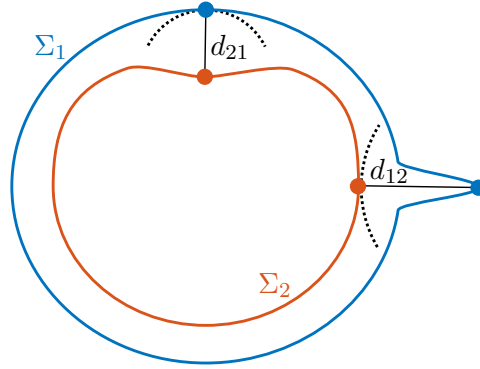
Suppose  $S_0$  is a compact submanifold of the critical manifold  $C_0$  and that is normally hyperbolic with respect to (1.32) (the real parts of eigenvalues of the Jacobian of (1.32) evaluated at all points on  $S_0$  are non-zero). Fenichel's theorem states that, for sufficiently small  $\varepsilon > 0$ ,  $S_0$  perturbs to a slow manifold  $S_\varepsilon$ . This slow manifold  $S_\varepsilon$  is

1. locally invariant
2. diffeomorphic to  $S_0$ ,
3. Hausdorff distance  $\mathcal{O}(\varepsilon)$  close to  $S_0$ <sup>3,4</sup>,
4. has the same stability as the critical manifold with respect the fast variables,
5. and the flow along  $S_\varepsilon$  converges to the slow flow (1.34), as  $\varepsilon \rightarrow 0$ .

---

<sup>3</sup>For a definition of the Hausdorff distance see Figure 1.4.

<sup>4</sup>The slow manifold is not, in fact, unique, and is actually a "band" of slow manifolds. However, slow manifolds in this band are "beyond all orders" ( $\mathcal{O}(e^{-K/\varepsilon})$ ) close, so for all purposes covered in the following chapters, this band shall be treated as being a unique slow manifold.



**Figure 1.4:** The Hausdorff distance gives a measure of how far two subsets of a metric space are from each other. If one of these sets is  $\Sigma_1$  and the other  $\Sigma_2$ , then the Hausdorff distance between the two is given by

$$d_H(\Sigma_1, \Sigma_2) = \max \left\{ \sup_{\sigma_1 \in \Sigma_1} \left( \inf_{\sigma_2 \in \Sigma_2} d(\sigma_1, \sigma_2) \right), \sup_{\sigma_2 \in \Sigma_2} \left( \inf_{\sigma_1 \in \Sigma_1} d(\sigma_1, \sigma_2) \right) \right\}.$$

Informally, it is the maximum of  $d_{12}$  (the maximum of all the minimum distances from  $\Sigma_1$  to  $\Sigma_2$ ) and  $d_{21}$  (the maximum of all the minimum distances from  $\Sigma_2$  to  $\Sigma_1$ ).

Speaking very informally, Fenichel’s Theorem effectively states that under certain conditions, the “error” in approximating the overall slow-fast flow by combining the layer and reduced problems is  $\varepsilon$  small. One of the conditions is that the submanifold in question of the critical set is compact: essentially it contains its boundary and points in the set are all finite distances from each other. The other is that points along the submanifold are all normally hyperbolic with respect to the layer problem. A point on critical set is said to be normally hyperbolic with respect to the layer problem when the real parts of the eigenvalues of the Jacobian of the linearisation at point are strictly nonzero. However, Fenichel’s Theorem no longer applies when the critical set is not normally hyperbolic with respect to the layer problem (at least one eigenvalue of the Jacobian evaluated at a point on the set lies on the imaginary axis). In this case, we can gain the normal hyperbolicity required in order to use Fenichel’s Theorem through the use of geometric blowup. Informally, this method regains hyperbolicity at the expense of increasing the dimension of the problematic set where the hyperbolicity breaks-down. Through this method, once again, we separate a difficult problem into multiple (simpler) problems where existing theorems and methods can be applied. Furthermore, this blowup method can also be applied to problems where there is no lack of normal hyperbolicity, as a means to match across regimes.

In order to explain the essence of the method, we will use the example of a planar fold (as in [70] but here more informally) first solved with blowup in [67].

### 1.2.1 Blowup of the planar fold

We will consider the following system,

$$(1.36) \quad \begin{aligned} \frac{dx}{dt} &= -y + x^2, \\ \frac{dy}{dt} &= -\varepsilon. \end{aligned}$$

We see that this is a slow-fast system in standard form written in the fast time scale, with one fast variable  $x$  and one slow variable  $y$ . As such, we can find the layer problem through taking the limit  $\varepsilon \rightarrow 0$  of (1.36),

$$(1.37) \quad \begin{aligned} \frac{dx}{dt} &= -y + x^2, \\ \frac{dy}{dt} &= 0 \implies y = y^*. \end{aligned}$$

This is a one dimensional ODE

$$(1.38) \quad \frac{dx}{dt} = -y^* + x^2$$

parameterised by  $y^*$ . The critical set here is  $y = x^2$ . This ODE (1.38) gives a prototypical saddle node (or fold) bifurcation as  $y^*$  passes through 0 creating a stable branch  $x = x_- := -\sqrt{y^*}$ ,  $y^* > 0$  and an unstable branch  $x = x_+ := \sqrt{y^*}$ ,  $y^* > 0$ . The stability of each branch can be found by linearising (1.38) about each

$$(1.39) \quad \tilde{x} = x - x_-, \quad \frac{d\tilde{x}}{dt} = -2\sqrt{y^*}\tilde{x} + \mathcal{O}(\tilde{x}^2),$$

and

$$(1.40) \quad \hat{x} = x - x_+, \quad \frac{d\hat{x}}{dt} = +2\sqrt{y^*}\hat{x} + \mathcal{O}(\hat{x}^2).$$

When  $y^* \equiv 0$  there is a single nonhyperbolic equilibrium at the origin

$$(1.41) \quad \check{x} = x, \quad \frac{d\check{x}}{dt} = \check{x}^2,$$

evident from the lack of a linear term.

As previously discussed, the layer problem (or fast subsystem) does not do a good job of approximating the dynamics of the overall system (1.36), as in (1.37)  $y$  never evolves. When we took the limit  $\varepsilon \rightarrow 0$  of (1.36) we lost information about the slow dynamics. Rescaling time by  $\varepsilon$  in (1.36), we find

$$(1.42) \quad \begin{aligned} \varepsilon \frac{dx}{d\tau} &= -y + x^2, \\ \frac{dy}{d\tau} &= -1, \end{aligned}$$

in slow time  $\tau$  where  $d\tau/dt = \varepsilon$ . Taking the singular limit  $\varepsilon \rightarrow 0$  of (1.42), we obtain the reduced problem

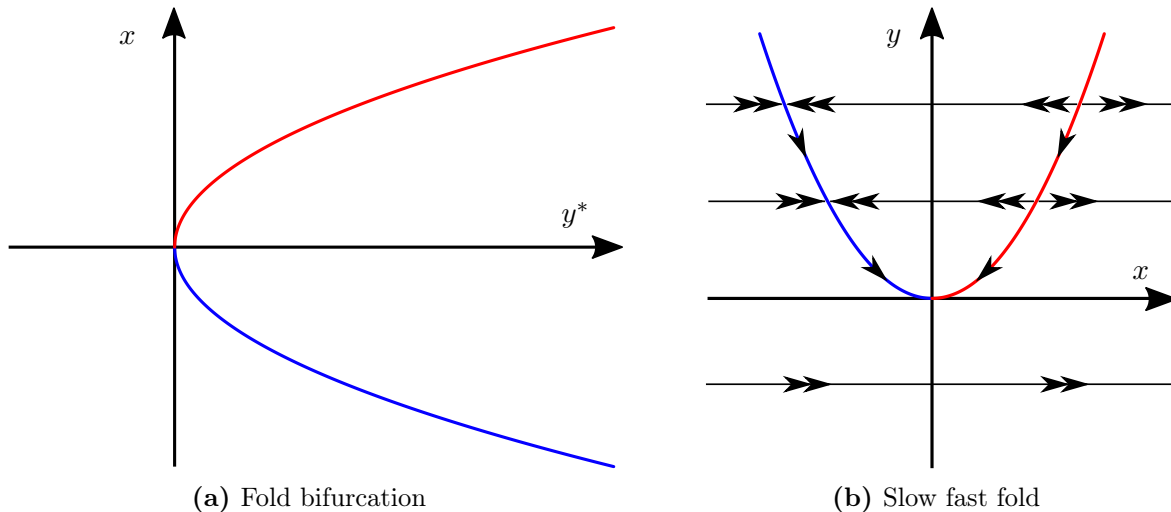
$$(1.43) \quad \begin{aligned} 0 &= -y + x^2, \\ \frac{dy}{d\tau} &= -1, \end{aligned}$$

a differential-algebraic system of equations with a one dimensional ODE

$$(1.44) \quad \frac{dy}{d\tau} = -1,$$

subject to the algebraic constraint  $y = x^2$ .

From both the layer problem (1.37) and the reduced problem (1.43) we can begin to piece together an approximation to the overall system (1.36) in Figure 1.5b. However, we see that we encounter a problem. The reduced problem (1.43) drives the bifurcation parameter of the layer problem  $y$  to the bifurcation; the critical set is hyperbolic for  $y > 0$  and so a slow manifolds exist for  $y > \delta > 0$ , along which the slow flow leads to the origin. At the origin the critical set is not normally-hyperbolic and so Fenichel's theorem does not apply here. Since trajectories that reach the stable part of the critical set generically pass to the nonhyperbolic origin in the singular limit, we cannot describe their behaviour with Fenichel's theorems. It is here that we use the method of geometric blowup to “inject” normal hyperbolicity at this troublesome point.



**Figure 1.5:** Slow fast fold. **(a)** A prototypical fold bifurcation, parameterised by  $y^*$ . **(b)** Slow-fast fold, with fast flow onto the parabola and slow flow towards the origin. The attracting branch is shown in blue and the repelling branch in red. Note the switch of axes;  $y^*$  is the bifurcation parameter of the fold bifurcation and is shown as the horizontal axis in **(a)** (so to agree with standard depictions of the fold bifurcation), but  $y$  is shown on the vertical axis in full system in **(b)**.



As we have discussed, the penalty of the use of blowup is the extension of the dimension of where it is needed. Firstly, we consider the extended system

$$(1.45a) \quad \frac{dx}{dt} = -y + x^2,$$

$$(1.45b) \quad \frac{dy}{dt} = -\varepsilon,$$

$$(1.45c) \quad \frac{d\varepsilon}{dt} = 0,$$

treating the small parameter  $\varepsilon$  as a variable. In this extended system, each plane of constant  $\varepsilon$  is an invariant manifold, and the family of solutions to (1.36) for each  $\varepsilon$  exist on these planes. In (1.45), the origin is a nonhyperbolic point with all eigenvalues of the linearisation equalling zero. To tackle this lack of hyperbolicity, we then proceed to blow up the point  $x = y = \varepsilon = 0$  to a (hemi)sphere. In particular, the blowup used is given by the transformation

$$(1.46) \quad \Phi : (r, (\bar{x}, \bar{y}, \bar{\varepsilon})) \mapsto (x, y, \varepsilon),$$

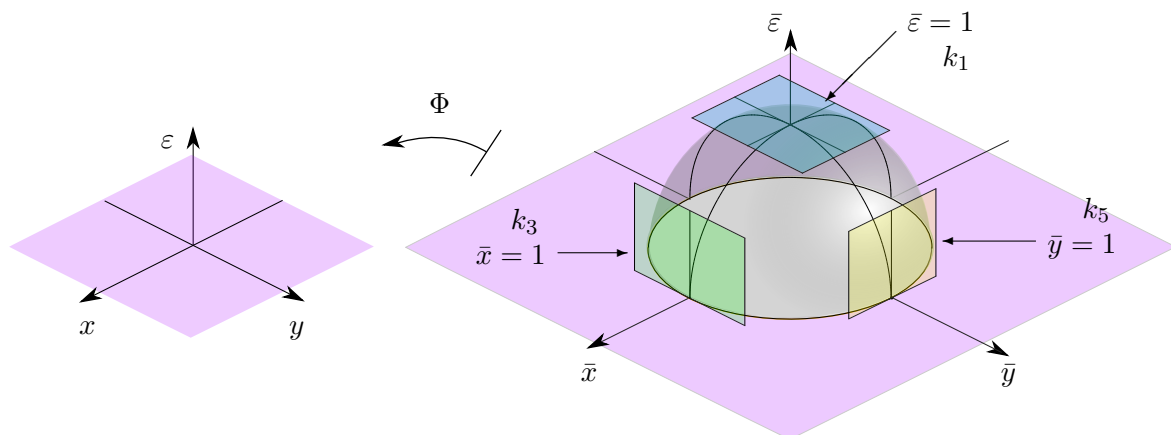
defined by

$$(1.47) \quad x = r\bar{x}, \quad y = r^2\bar{y}, \quad \varepsilon = r^3\bar{\varepsilon}, \quad (r, (\bar{x}, \bar{y}, \bar{\varepsilon})) \in [0, \infty) \times S_+^2,$$

where  $S_+^2$  is the hemisphere

$$(1.48) \quad S_+^2 = \{(\bar{x}, \bar{y}, \bar{\varepsilon}) \mid \bar{x}^2 + \bar{y}^2 + \bar{\varepsilon}^2 = 1, \bar{\varepsilon} \geq 0\}.$$

This blowup is shown in Figure 1.6. The weights, the exponents of  $r$  in (1.47), are chosen carefully to “desingularise” the fold point; after re-writing in local coordinates, we will be able to gain normal hyperbolicity through “dividing-out” a shared factor on the right hand side of the equations. The specific choice of the weights will be explained later.

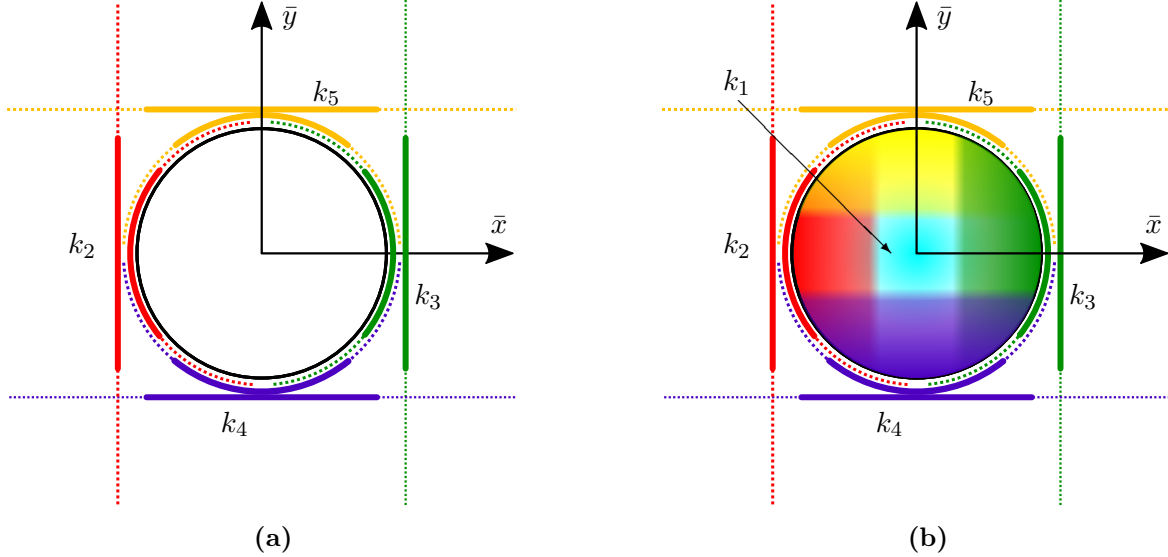


**Figure 1.6:** Blowup of the point at the origin  $x = y = \varepsilon = 0$  to the (hemi)sphere  $S_+^2$  in (1.48). Geometric interpretations of the charts found by setting  $r = 0$  and  $\bar{x} = 1$ ,  $\bar{y} = 1$  and  $\bar{\varepsilon} = 1$  are also given.

Whilst the blowup can be used to desingularise the point, it is usually impractical to study the whole system at once as the equations can become intractable. Instead, it is advantageous to study multiple local problems and piece them together. The local coordinate systems, called *directional charts*, are found by fixing specific variables in the blowup (1.47), see Figure 1.6. Here, these directional charts, which we shall denote  $k_i$ , are found by setting  $\bar{\varepsilon} = 1$ ,  $\bar{x} = \mp 1$ , and  $\bar{y} = \mp 1$  respectively in the blowup transformation (1.47)

$$\begin{aligned}
 (1.49a) \quad k_1 : \quad & x = r_1 x_1, & y = r_1^2 y_1, & \varepsilon = r_1^3, \\
 (1.49b) \quad k_2 : \quad & x = -r_2, & y = r_2^2 y_2, & \varepsilon = r_2^3 \varepsilon_2, \\
 (1.49c) \quad k_3 : \quad & x = r_3, & y = r_3^2 y_3, & \varepsilon = r_3^3 \varepsilon_3, \\
 (1.49d) \quad k_4 : \quad & x = r_4 x_4, & y = -r_4^2, & \varepsilon = r_4^3 \varepsilon_4, \\
 (1.49e) \quad k_5 : \quad & x = r_5 x_5, & y = r_5^2, & \varepsilon = r_5^3 \varepsilon_5.
 \end{aligned}$$

Each of these charts covers a different part of the phase space, and  $r_i = 0$  for each  $i \in \{1, 2, 3, 4, 5\}$  covers a different hemisphere of the sphere in the blowup. The scaling chart  $k_1$  covers the neighbourhood of northern hemisphere,  $k_2$  and  $k_3$  cover the eastern and western hemispheres,  $k_3$  and  $k_5$  the “back” and “front” (see Figures 1.7 and 1.10).



**Figure 1.7:** Diagram of the region covered by each directional in the blowup of the fold:  $k_i$ ,  $i \in \{2, 3, 4, 5\}$ . In (a), we show the directional charts covering the “equator” of the blowup for  $\bar{\varepsilon} = 0$ : charts  $k_i$ ,  $i \in \{2, 3, 4, 5\}$ . In (b), we show a schematic diagram of all charts covering the northern hemisphere projected onto  $\bar{\varepsilon} = 0$ : charts  $k_i$ ,  $i \in \{1, 2, 3, 4, 5\}$ . For example, the chart  $k_2$  covers the left half of the equator. The diagram also depicts the regions of overlap between each charts. For example, charts  $k_3$  and  $k_5$  overlap, but the positive  $\bar{x}$ -axis is only visible in the  $k_3$  chart, and the positive  $\bar{y}$ -axis is only visible in the  $k_5$  chart. Charts  $k_2$  and  $k_3$ , however, do not overlap.

To map between these charts, we use coordinate transforms  $k_{ij}$ , which transform coordinates from chart  $k_i$  to chart  $k_j$ . Some transforms that will be of use are

$$(1.50a) \quad k_{12} : \quad x_1 = -\varepsilon_2^{-\frac{1}{3}}, \quad y_1 = \varepsilon_2^{-\frac{2}{3}} y_2, \quad r_1 = \varepsilon_2^{\frac{1}{3}} r_2,$$

$$(1.50b) \quad k_{13} : \quad x_1 = \varepsilon_3^{-\frac{1}{3}}, \quad y_1 = \varepsilon_3^{-\frac{2}{3}} y_3, \quad r_1 = \varepsilon_3^{\frac{1}{3}} r_3,$$

$$(1.50c) \quad k_{15} : \quad x_1 = \varepsilon_5^{-\frac{1}{3}} x_5, \quad y_1 = \varepsilon_5^{-\frac{2}{3}}, \quad r_1 = \varepsilon_5^{\frac{1}{3}} r_5,$$

$$(1.50d) \quad k_{25} : \quad r_2 = -r_5 x_5, \quad y_2 = x_5^{-2}, \quad \varepsilon_2 = -\varepsilon_5 x_5^{-3},$$

$$(1.50e) \quad k_{53} : \quad x_5 = y_3^{-\frac{1}{2}}, \quad y_5 = r_3 y_3^{-\frac{1}{2}}, \quad \varepsilon_5 = \varepsilon_3 y_3^{-\frac{3}{2}}.$$

Note that these changes of coordinates only exist for charts that overlap (see Figures 1.6 and 1.7).

### 1.2.1.1 Scaling chart

The crucial directional chart is found by setting  $\bar{\varepsilon} = 1$  in (1.47), the chart  $k_1$  (1.49a). Re-writing (1.45) in terms of the local coordinates  $(x_1, y_1, r_1)$ , we find

$$(1.51) \quad \begin{aligned} \frac{dx_1}{dt} &= r_1 (-y_1 + x_1^2), \\ \frac{dy_1}{dt} &= -r_1, \\ \frac{dr_1}{dt} &= 0, \end{aligned}$$

or equivalently

$$(1.52) \quad \begin{aligned} \frac{dx_1}{dt} &= \varepsilon^{\frac{1}{3}} (-y_1 + x_1^2), \\ \frac{dy_1}{dt} &= -\varepsilon^{\frac{1}{3}}. \end{aligned}$$

In this chart, the variables have been scaled to balance certain terms, here the right hand sides of (1.52) are now both of equal order ( $\mathcal{O}(\varepsilon^{\frac{1}{3}})$ ), and accordingly this particular directional chart is called the *scaling chart*;  $x$  and  $y$  are rescaled by  $\varepsilon^{\frac{1}{3}}$  and  $\varepsilon^{\frac{2}{3}}$ , respectively.

However, how did we find weightings of the powers of  $\varepsilon$  in (1.49a)? If we take some arbitrary scalings  $x = \varepsilon^a x_1$ ,  $y = \varepsilon^b y_1$ , and substitute into (1.36) we find

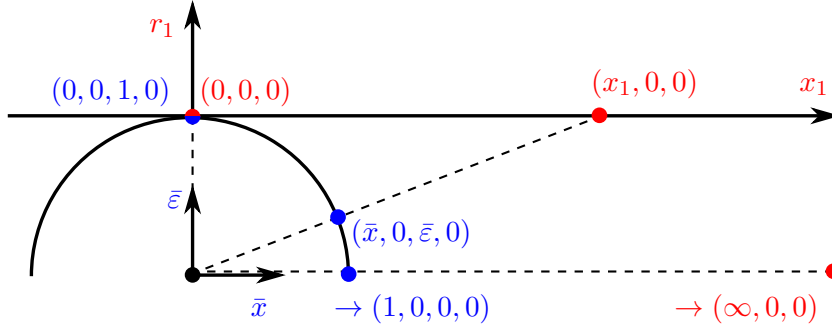
$$(1.53) \quad \begin{aligned} \frac{dx_1}{dt} &= -\varepsilon^{b-a} y_1 + \varepsilon^a x_1^2, \\ \frac{dy_1}{dt} &= -\varepsilon^{1-b}. \end{aligned}$$

To bring each of these terms on “equal footing”, we desire that the powers of  $\varepsilon$  are all equal, that is

$$(1.54) \quad b - a \equiv a \equiv 1 - b.$$

Solving, we find that  $a = \frac{1}{3}$  and  $b = \frac{2}{3}$ , as in (1.49a).

In most applications it is not this simple; it may not be possible to, or we may not want to, balance *all* the terms on the right-hand side of the ODEs. Choosing which terms to balance is an important task, and an understanding of which terms are most significant is necessary.



**Figure 1.8:** Compactification: demonstration of how the surface of the hemisphere is a compactification of the surface  $r_1 = 0$  in the scaling chart, shown for  $\bar{y} = 0$ . The points  $(x_1, y_1, r_1) = (\infty, 0, 0)$ ,  $(x_1, 0, 0)$  and  $(0, 0, 0)$  project onto the sphere  $r = 0$  at  $(\bar{x}, \bar{y}, \bar{\varepsilon}, r) = (1, 0, 0, 0)$ ,  $(\bar{x}, 0, \bar{\varepsilon}, 0)$  and  $(0, 0, 1, 0)$  respectively. To study the dynamics at occurring infinity in the scaling chart  $k_1$ , the other charts must be used.

**Remark 1.2.** *The surface of the hemisphere of the sphere in the blowup is a Poincaré compactification of the infinite plane of  $(x_1, y_1)$ . The equator of the hemisphere appears at infinity in the scaling chart [37, Figure 1]. This compactification is shown in Figure 1.8.*

Rescaling time in (1.52) to  $\tilde{\tau} = r_1 t$ , where  $r_1 = \varepsilon^{\frac{1}{3}}$  is a constant, we find

$$(1.55a) \quad \frac{dx_1}{d\tilde{\tau}} = -y_1 + x_1^2,$$

$$(1.55b) \quad \frac{dy_1}{d\tilde{\tau}} = -1.$$

Integrating (1.55b) directly and substituting into (1.55a) we are left with a Riccati equation

$$(1.56) \quad \frac{dx_1}{d\tilde{\tau}} = -(y_1(0) - \tilde{\tau}) + x_1^2.$$

This particular Riccati equation, can be transformed into the Airy equation

$$(1.57) \quad \frac{d^2 X(\hat{t})}{d\hat{t}^2} = \hat{t} X(\hat{t}),$$

using the transformation

$$(1.58) \quad \hat{t} = -\tilde{\tau} + y_1(0), \quad x_1 = \frac{1}{X} \frac{dX}{d\hat{t}}.$$

The Airy equation does not have solutions in terms of elementary functions, instead its solutions can be expressed in terms of special functions (i.e. Airy functions or Bessel functions).

The qualitative behaviour of solutions to (1.55) can be summarised as follows [67]:

1. Every orbit has its own horizontal asymptote  $y_1 = y_{1,+}$ , such that  $y_1 \rightarrow y_{1,+}$  from above as  $x_1 \rightarrow \infty$ .
2. There exists an  $\Omega_0 > 0$ , such that there is a unique orbit  $\gamma_1$  (which can be parameterised as  $(x_1, s(x_1))$  for  $x_1 \in \mathbb{R}$ ) that is asymptotic to the left hand branch of the parabola  $y_1 = x_1^2$  for  $x_1 \rightarrow -\infty$  and asymptotic  $y_1 \rightarrow -\Omega_0$  from above as  $x_1 \rightarrow \infty$ .
3. The function  $s(x)$  is asymptotic to

$$(1.59) \quad s(x) = x^2 + \frac{1}{2x} + \mathcal{O}\left(\frac{1}{x^4}\right), \quad \text{as } x \rightarrow -\infty,$$

and

$$(1.60) \quad s(x) = -\Omega_0 + \frac{1}{x} + \mathcal{O}\left(\frac{1}{x^3}\right), \quad \text{as } x \rightarrow \infty.$$

4. All orbits above  $\gamma_1$  are asymptotic to the right branch of the parabola in backwards time.
5. Every orbit below  $\gamma_1$  has its own horizontal asymptote  $y_1 = y_{1,-} > y_{1,+}$ , such that  $y \rightarrow y_{1,-}$  from below as  $x_1 \rightarrow -\infty$ .

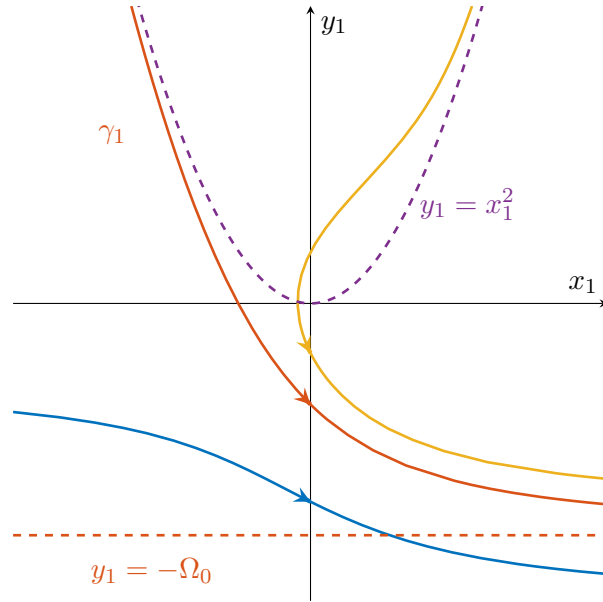
This qualitative behaviour is shown in Figure 1.9.

These dynamics in the scaling chart for  $r_1 = 0$  capture the essential dynamics.

**Remark 1.3.** *The appearance of special equations in the scaling chart of a blowup is common and expected. The exercise of geometric blowup involves balancing a few of the lower-order nonlinear terms in an ODE. This often leads to systems that are sufficiently nonlinear as not to have solutions in terms of elementary functions, but also sufficiently common as to have been previously studied.*

**Remark 1.4.** *Special unique solutions (like  $\gamma_1$ ) are also to be expected in scaling charts of blowups. We anticipate these special orbits as they often correspond to unique connections between equilibria along the equator of the blowup.*

Regular perturbation theory only works on compact domains in  $k_1$ , and we must compactify using the other charts. Whilst we have described the dynamics in the scaling chart  $k_1$ , we have yet to describe how orbits reach or leave the scaling chart. To do this, we study the dynamics in the so-called entry/exit charts:  $k_i$ ,  $i \in \{2, 3, 4, 5\}$ .



**Figure 1.9:** Qualitative behaviour of solutions to the Riccati equations in (1.55). The special solution  $\gamma_1$  is backwards asymptotic to the left branch of the parabola  $y_1 = x_1^2$  and forwards asymptotic to  $y_1 = -\Omega_0$ .

### 1.2.1.2 Entry chart $k_2$

Let us first study the dynamics in the entry chart  $k_2$  given in (1.49b) and depicted in Figures 1.10a and 1.10c. Substituting (1.49b) into (1.45) and re-arranging, we find

$$(1.61a) \quad \frac{dr_2}{dt} = r_2^2(y_2 - 1),$$

$$(1.61b) \quad \frac{dy_2}{dt} = r_2(-2y_2^2 + 2y_2 + \varepsilon_2),$$

$$(1.61c) \quad \frac{d\varepsilon_2}{dt} = -3\varepsilon_2 r_2(y_2 - 1).$$

We notice that  $r_2 = 0$  (the surface of the hemisphere) is a set of equilibria of (1.61). Linearising around this set we find

$$(1.62) \quad \frac{d}{dt} \begin{pmatrix} r_2 \\ y_2 \\ \varepsilon_2 \end{pmatrix} = \begin{pmatrix} 0 & 0 & 0 \\ -2y_2^2 + 2y_2 + \varepsilon_2 & 0 & 0 \\ -3\varepsilon_2(y_2 - 1) & 0 & 0 \end{pmatrix} \begin{pmatrix} r_2 \\ y_2 \\ \varepsilon_2 \end{pmatrix},$$

and the corresponding Jacobian has 3 eigenvalues, all of which are zero. This set therefore lacks any normally hyperbolicity in the time scale in (1.61). Nonetheless, we can gain some normal hyperbolicity by considering (1.61) with respect to a new timescale  $t_2$ , where  $dt_2 = r_2 dt$ . This transformation, which effectively acts to divide the right hand side of (1.61) by  $r_2$ , preserves orbits, but acts to change the speed along them; the transformation speeds up orbits nearby

$r_2 = 0$ , and slows down orbits far from  $r_2 = 0$ . Re-writing (1.61) in this new time  $t_2$  we find

$$(1.63a) \quad \frac{dr_2}{dt_2} = r_2(y_2 - 1),$$

$$(1.63b) \quad \frac{dy_2}{dt_2} = -2y_2^2 + 2y_2 + \varepsilon_2,$$

$$(1.63c) \quad \frac{d\varepsilon_2}{dt_2} = -3\varepsilon_2(y_2 - 1).$$

The planes  $r_2 = 0$  and  $\varepsilon_2 = 0$  are invariant manifolds of (1.63), and the dynamics along their intersection is given by  $dy_2/dt_2 = 2y_2(1 - y_2)$ . Hence, this system has two equilibria, one at

$$(1.64) \quad C_{2,1} = \{(r_2, y_2, \varepsilon_2) | (r_2, y_2, \varepsilon_2) = (0, 0, 0)\},$$

and the other at

$$(1.65) \quad C_{2,2} = \{(r_2, y_2, \varepsilon_2) | (r_2, y_2, \varepsilon_2) = (0, 1, 0)\}.$$

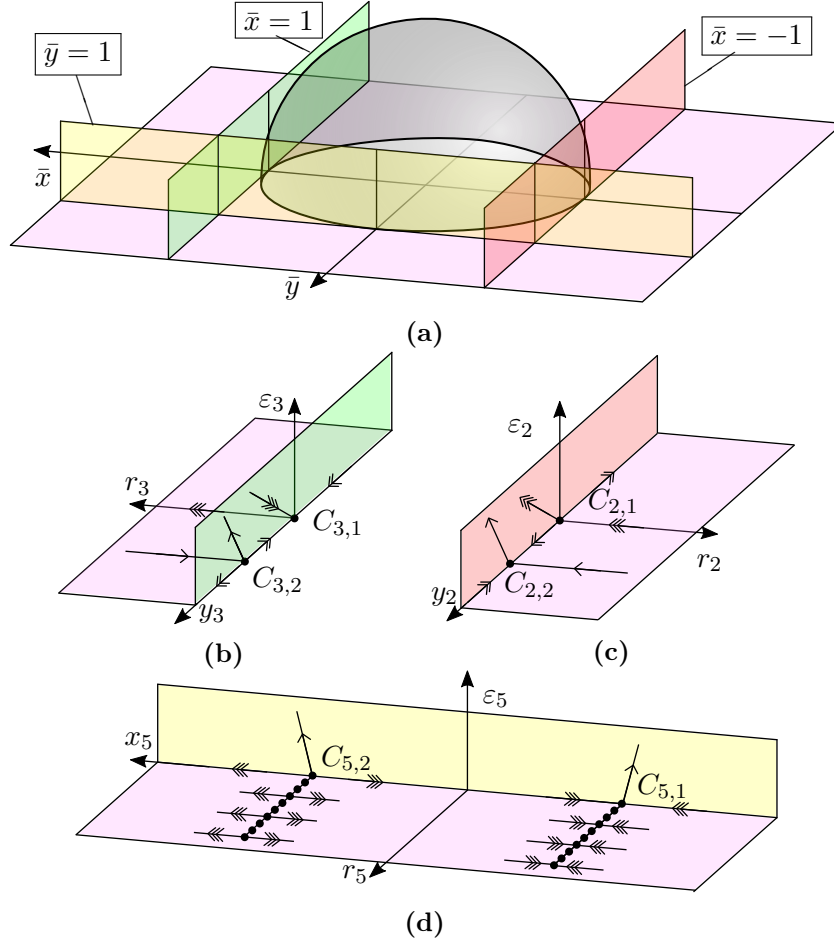
Linearising around  $C_{2,1}$ , we find

$$(1.66) \quad \frac{d}{dt_2} \begin{pmatrix} r_2 \\ y_2 \\ \varepsilon_2 \end{pmatrix} = \begin{pmatrix} -1 & 0 & 0 \\ 0 & 2 & 1 \\ 0 & 0 & 3 \end{pmatrix} \begin{pmatrix} r_2 \\ y_2 \\ \varepsilon_2 \end{pmatrix},$$

and the corresponding Jacobian has three nonzero eigenvalues -1, 2, and 3. From the stable manifold theorem [89], there is a unstable manifold of  $C_{2,1}$  tangent to the eigenvectors associated with the positive eigenvalues, and a stable manifold of  $C_{2,1}$  tangent to the eigenvector associated with the negative eigenvalues. With the other equilibrium,  $C_{2,2}$ , we find

$$(1.67) \quad \frac{d}{dt_2} \begin{pmatrix} r_2 \\ y_2 \\ \varepsilon_2 \end{pmatrix} = \begin{pmatrix} 0 & 0 & 0 \\ 0 & -2 & 1 \\ 0 & 0 & 0 \end{pmatrix} \begin{pmatrix} r_2 \\ y_2 - 1 \\ \varepsilon_2 \end{pmatrix},$$

and the corresponding eigenvalues are 0 (with multiplicity 2) and -2 (with multiplicity 1). From the centre manifold theorem [89], we find that there is a centre manifold of  $C_{2,2}$ , tangent to the eigenvectors associated with the zero eigenvalues. Hence we can see that we have increased our understanding of the structure and gained (some) normal hyperbolicity. This structure can be seen in Figure 1.10c.



**Figure 1.10:** Diagram demonstrating the geometry and the dynamics of 3 key entry/exit charts of the blowup in (1.47). (a) Geometry of charts  $k_2$ ,  $k_3$  and  $k_5$ . (b)-(d) Dynamics in charts  $k_2$ ,  $k_3$  and  $k_5$  respectively, showing the equilibria and their eigenvectors. Hyperbolic directions are shown using double and triple arrowheads (triple arrowheads denote the stronger direction), single arrowheads denote nonhyperbolic directions (and the directions are deduced using higher order terms).

### 1.2.1.3 Entry chart $k_3$

Similarly, we can study the entry/exit chart  $k_3$  (1.49c), found by setting  $\bar{x} = -1$  in (1.47). Writing (1.45), in coordinates  $(r_3, y_3, \varepsilon_3)$ , we find

$$(1.68a) \quad \frac{dr_3}{dt} = r_3^2(1 - y_3),$$

$$(1.68b) \quad \frac{dy_3}{dt} = r_3(2y_3^2 - 2y_3 + \varepsilon_3),$$

$$(1.68c) \quad \frac{d\varepsilon_3}{dt} = -3\varepsilon_3 r_3(1 - y_3).$$



Transforming time as to divide the right hand side of (1.68) by  $r_3$ , we find

$$(1.69a) \quad \frac{dr_3}{dt_3} = r_3(1 - y_3),$$

$$(1.69b) \quad \frac{dy_3}{dt_3} = 2y_3^2 - 2y_3 + \varepsilon_3,$$

$$(1.69c) \quad \frac{d\varepsilon_3}{dt_3} = -3\varepsilon_3(1 - y_3),$$

where  $dt_3 = r_3 dt$ . There are two equilibria of (1.69),

$$(1.70) \quad C_{3,1} = \{(r_3, y_3, \varepsilon_3) | (r_3, y_3, \varepsilon_3) = (0, 1, 0)\},$$

and the other at

$$(1.71) \quad C_{3,2} = \{(r_3, y_3, \varepsilon_3) | (r_3, y_3, \varepsilon_3) = (0, 0, 0)\}.$$

Linearising around (1.69) around  $C_{3,1}$ ,

$$(1.72) \quad \frac{d}{dt_3} \begin{pmatrix} r_3 \\ y_3 \\ \varepsilon_3 \end{pmatrix} = \begin{pmatrix} 1 & 0 & 0 \\ 0 & -2 & 1 \\ 0 & 0 & -3 \end{pmatrix} \begin{pmatrix} r_3 \\ y_3 \\ \varepsilon_3 \end{pmatrix},$$

We find that the corresponding Jacobian has three nonzero eigenvalues 1, -2, and -3. Linearising around  $C_{3,2}$ , we find

$$(1.73) \quad \frac{d}{dt_2} \begin{pmatrix} r_3 \\ y_3 \\ \varepsilon_3 \end{pmatrix} = \begin{pmatrix} 0 & 0 & 0 \\ 0 & 2 & 1 \\ 0 & 0 & 0 \end{pmatrix} \begin{pmatrix} r_3 \\ y_3 - 1 \\ \varepsilon_3 \end{pmatrix},$$

and the corresponding eigenvalues are 0 (twice) and 2 (once). Hence, the dynamics in chart  $k_3$  are described by Figure 1.10b.

#### 1.2.1.4 Entry chart $k_5$

Furthermore, we can study the dynamics of the side of the sphere where  $y > 0$  using the chart  $k_5$  (1.49e). Writing (1.45) in  $k_5$ ,

$$(1.74a) \quad \frac{dx_5}{dt} = \frac{1}{2}r_5(2x_5^2 - \varepsilon_5x_5 - 2),$$

$$(1.74b) \quad \frac{dr_5}{dt} = -\frac{1}{2}r_5^2\varepsilon_5,$$

$$(1.74c) \quad \frac{d\varepsilon_5}{dt} = -\frac{3}{2}r_5\varepsilon_5^2.$$

Transforming time, attempting to desingularise  $r_5 = 0$ ,

$$(1.75a) \quad \frac{dx_5}{dt_5} = \frac{1}{2} (2x_5^2 - \varepsilon_5 x_5 - 2),$$

$$(1.75b) \quad \frac{dr_5}{dt_5} = -\frac{1}{2} r_5 \varepsilon_5,$$

$$(1.75c) \quad \frac{d\varepsilon_5}{dt_5} = -\frac{3}{2} \varepsilon_5^2.$$

There are two sets of equilibria

$$(1.76) \quad C_{5,1} = \{(x_5, r_5, \varepsilon_5) | (x_5, \varepsilon_5) = (1, 0), r_5 > 0\},$$

and

$$(1.77) \quad C_{5,2} = \{(x_5, r_5, \varepsilon_5) | (x_5, \varepsilon_5) = (-1, 0), r_5 > 0\}.$$

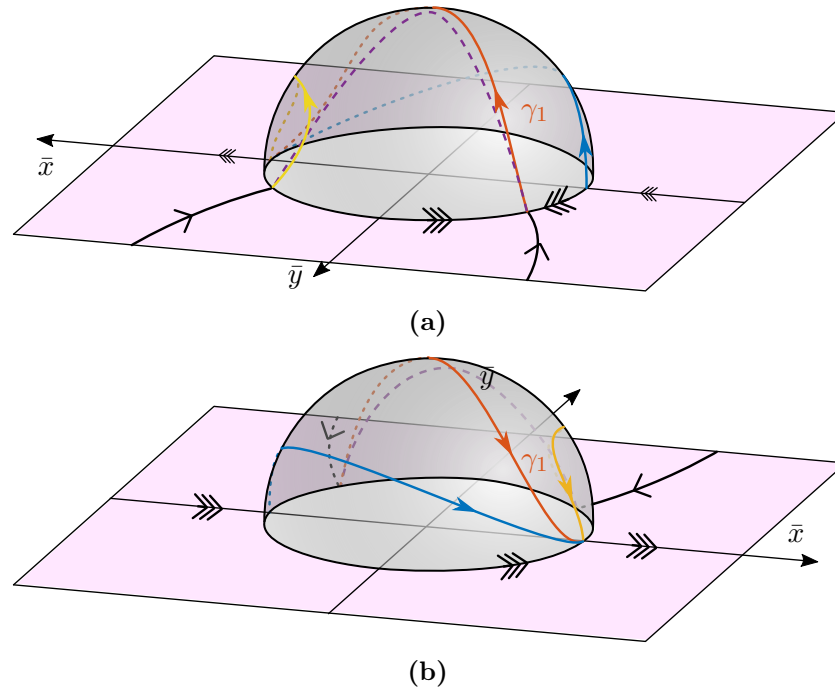
The only nonzero eigenvalues of the Jacobian of the linearisation of (1.75) around  $C_{5,1}$  and  $C_{5,2}$  are 2 and  $-2$  respectively. However, since  $y$  is always decreasing (1.45b), we can determine the direction of dynamics along the centre manifolds extending from  $C_{5,1}$  and  $C_{5,2}$  (see Figure 1.10d).

### 1.2.1.5 Matching across charts

Since we have now analysed the dynamics in each of the coordinate charts, we now hope to match across them, to piece together complete orbits.

Firstly, we find that  $C_{5,2} \mapsto C_{3,2}$  using  $k_{53}$  (1.50e), and  $C_{2,2} \mapsto C_{5,1}$  using  $k_{25}$  (1.50d). This occurs due to the overlaps of the charts  $k_2$  and  $k_5$ , and  $k_5$  and  $k_3$ . Secondly we find that the two branches the parabola  $y_1 = x_1^2$  reach the equator of the blowup at  $\{C_{5,1} | r_5 = 0\}$  and  $\{C_{5,2} | r_5 = 0\}$  in the chart  $k_5$  using the transformation  $k_{13}$  (1.50b). Hence the orbit  $\gamma_1$  in the scaling chart is backwards asymptotic to  $C_{5,2}$ . Finally, we find that the orbit  $\gamma_1$  is forwards asymptotic to the equilibrium  $C_{3,1}$  in the chart  $k_3$  using the transformation  $k_{1,3}$ .

In conclusion, we can piece together the dynamics of (1.45) in the limit  $\varepsilon \rightarrow 0$  from the dynamics in the separate charts (see Figure 1.11). Whilst studying the perturbed problem (for  $0 < \varepsilon \ll 1$  involves more detail, here, like in the sequel, we use this blowup simply as a way to gain better insight about the possible dynamics for the perturbed problem. Nonetheless, standard tools of dynamical systems are applicable to study dynamics away from  $r = 0$  and  $\bar{\varepsilon} = 0$ .



**Figure 1.11:** Representative solutions on the surface of the sphere  $r = 0$  and in the plane  $\bar{\varepsilon} = 0$  in the blowup of the fold. Orbits on the sphere correspond to the significant orbits in the scaling chart shown in Figure 1.9. Perturbed solutions for  $1 \gg \varepsilon > 0$  are perturbations away from these solutions.

### 1.3 Outline

We have now introduced most of the necessary background, methods and theory for the following chapters. Over the course of the sequel we shall study both the Painlevé paradox in 3D and other mechanical problems that arise (those relating to the study of spatial Coulomb friction..

In Chapter 2, we shall study the Painlevé problem using a constraint-based approach. We make rigid body assumptions about the interaction between the rod and the surface. With this unilateral constraint, we assume the normal reaction force compensates for other forces and keeps the rod in contact with the rigid surface when slipping. We show that the resulting ODEs demonstrate a lack of unique forward-time solutions. We then describe the geometry of the problem and describe key features of the slipping dynamics. We also describe the importance of the angular velocity  $\Psi$  in the 3D problem. Furthermore, we give a geometric justification for the existence of physically significant orbits, ones which reach inconsistency from slipping, a phenomenon that does not exist in the planar Painlevé problem.

In Chapter 3, we aim to “resolve the paradox” through the incorporation of compliance. In this regularised system, we recover IWC where previously there had been a lack of unique solutions. We use blowup to study important regimes and then match across them. We also discover that the significant orbits in the rigid problem also undergo IWC in the compliant

problem. In order to study the transition from slipping to sticking that occurs as part of IWC, we regularise Coulomb friction by treating it as a nonsmooth limit of a smooth system.

In Chapter 4, we investigate this regularisation of Coulomb friction and generalise to a broader class of systems of ODEs with isolated codimension-2 discontinuities. We present a general framework for these codimension-2 problems, and give specific results for the local dynamics in a class of problems, finding analogues for Filippov crossing, sliding and the Filippov convention for the sliding vector field.

Finally, in Chapter 5, we discuss the broader implications of the thesis. In particular, we propose that the approaches demonstrated in the thesis can be applied to other related mechanical problems.



## Chapter 2

# Constraint-based approach

In this chapter<sup>5</sup>, we analyse the rigid body equations (1.23). In particular, we highlight where they break down, compare them with the 2D problem, and demonstrate the role of the azimuthal angular velocity  $\Psi$ . Our focus is on the vertical acceleration  $\dot{w} = pF_z + b$ .

### 2.1 Breakdown of rigid body equations

The Painlevé problem can be thought of [38, 77] as the linear complementarity problem (LCP)

$$(2.1) \quad 0 \leq F_z \perp z \geq 0.$$

that is,

$$(2.2) \quad z \geq 0, \quad F_z \geq 0, \quad z \cdot F_z = 0.$$

When the rod slips along the surface  $z = 0$ , its tip must be in vertical equilibrium, that is,  $w = \dot{w} = 0$ . In this case, solving  $\dot{w} = 0$  in (1.23), we have <sup>6</sup>

$$(2.3) \quad \begin{aligned} F_z &= -\frac{b(\Psi, \Theta, \theta)}{p(\theta, \varphi; \mu, \alpha)} \\ &= -\frac{(\Psi^2 \cos^2 \theta + \Theta^2) \sin \theta - 1}{1 + \alpha + \alpha \sin \theta (\mu \cos \theta \sin \varphi - \sin \theta)}. \end{aligned}$$

So the LCP (2.1) with (2.3) has four modes, dependent on the signs of  $b$  and  $p$  <sup>7</sup>.

$b < 0, p > 0$ : From (2.3), we have  $F_z > 0$  and the rod is *slipping* along the rough surface.

---

<sup>5</sup>This chapter is adapted from [17]. See Acknowledgements for contributions.

<sup>6</sup>During the review process for [17], a reviewer pointed out that that (2.3) stems from the contact problem which is constructed from (2.1) assuming  $z = \dot{z} = 0$  (see for instance chapter 5 in the third edition of the book [14]), to get  $0 \leq F_z \perp \dot{z} \geq 0$ .

<sup>7</sup>During the review process for [17], a reviewer pointed out that the fundamental theorem of complementarity theory [33, 74] could be invoked when  $p > 0$ .

$b > 0, p > 0$ : Both components of the vertical acceleration  $\dot{w}$  acting on the rod tip are directed away from the surface and *lift-off* occurs.

$b < 0, p < 0$ : Both the free acceleration  $b$  and the vertical acceleration from contact forces  $pF_z$  act vertically downwards. This is *inconsistent* with our assumption of a rigid surface and we have *nonexistence* of solutions to (1.23).

$b > 0, p < 0$ : From (2.3), we have  $F_z > 0$ . But because the free acceleration  $b$  is upwards, lift-off is still possible. So the motion of the rod is *indeterminate* and we have *nonuniqueness* of solutions to (1.23).

Hence we need  $p < 0$  to have a paradox. From (1.26), it is straightforward to show that  $p < 0$  when

$$(2.4) \quad \mu > \mu_{\text{P}}^*(\varphi; \alpha) := \frac{2\sqrt{1+\alpha}}{\alpha|\sin\varphi|}$$

for  $\theta \in (\theta_-, \theta_+)$  where

$$(2.5) \quad \theta_{\pm}(\varphi; \mu, \alpha) = \arctan\left(-\frac{1}{2}\mu\alpha\sin\varphi \pm \frac{1}{2}\sqrt{\mu^2\alpha^2\sin^2\varphi - 4(\alpha+1)}\right).$$

Similarly, solving  $p = 0$  for  $\varphi$ , we find  $\varphi = \varphi_{\pm}$  where

$$(2.6) \quad \varphi_{\mp}(\theta; \mu, \alpha) := -\frac{\pi}{2} \mp \arccos\left(\frac{1+\alpha\cos^2\theta}{\alpha\mu\sin\theta\cos\theta}\right).$$

**Remark 2.1.** When  $\varphi = -\pi/2$ , (2.4) and (2.5) reduce to

$$(2.7) \quad \mu_{\text{P}}(\alpha) := \mu_{\text{P}}^*(-\pi/2; \alpha) = \frac{2}{\alpha}\sqrt{\alpha+1}$$

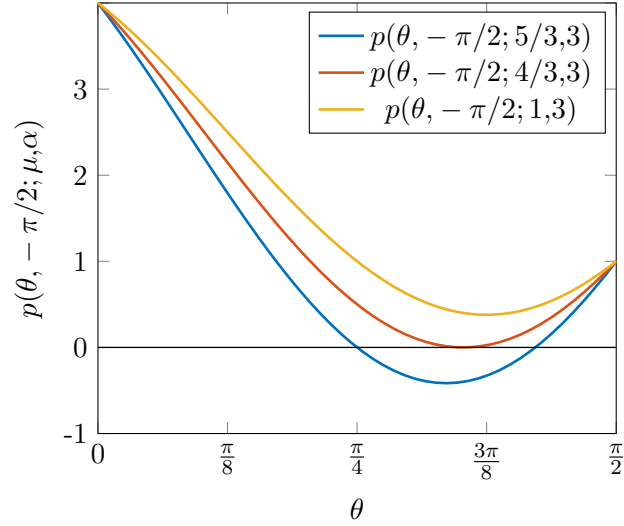
and

$$(2.8) \quad \begin{aligned} \theta_1(\mu, \alpha) &:= \theta_- \left(-\frac{\pi}{2}; \mu, \alpha\right) = \arctan\left(\frac{1}{2}\mu\alpha - \frac{1}{2}\sqrt{\mu^2\alpha^2 - 4(\alpha+1)}\right), \\ \theta_2(\mu, \alpha) &:= \theta_+ \left(-\frac{\pi}{2}; \mu, \alpha\right) = \arctan\left(\frac{1}{2}\mu\alpha + \frac{1}{2}\sqrt{\mu^2\alpha^2 - 4(\alpha+1)}\right). \end{aligned}$$

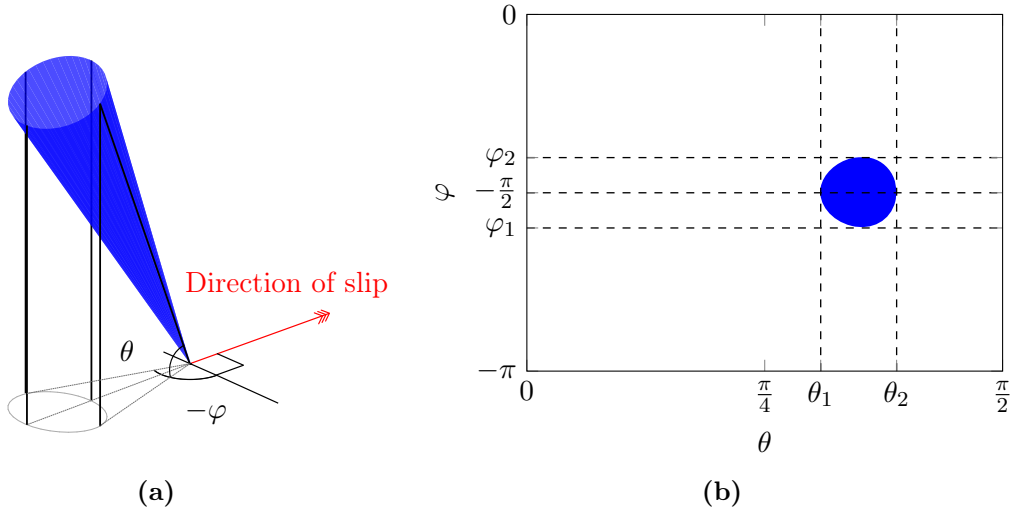
corresponding to [42, eq. (2.13), (2.14)] respectively for the 2D Painlevé problem (Proposition 1.1). The geometry of  $p(\theta, -\pi/2; \mu, \alpha)$  is depicted in Figure 2.1.

Figure 2.2 shows an example of regions in which  $p < 0$  for the 3D Painlevé problem. In Figure 2.2a,  $p < 0$  inside the blue cone where the state of the rod is either inconsistent or indeterminate. In Figure 2.2b, we show where  $p < 0$  in the  $(\theta, \varphi)$ -plane. The bounds of the blue region in the  $(\theta, \varphi)$ -plane are important in the sequel. They can be determined as follows. From (1.26), it can be shown by differentiation that when  $p = 0$ ,

$$(2.9) \quad \frac{d\varphi}{d\theta} = \frac{2(\mu\cos 2\theta\sin\varphi - \sin 2\theta)}{\mu\sin 2\theta\cos\varphi}$$



**Figure 2.1:** Geometry of  $p(\theta, -\pi/2; \mu, \alpha)$  for different values of the coefficient of friction:  $\mu > \mu_P(\alpha)$ ,  $\mu = \mu_P(\alpha)$ , and  $\mu < \mu_P(\alpha)$ .



**Figure 2.2:** Region, shown in blue, inside which  $p < 0$  for  $\alpha = 3, \mu = 1.4$  where we have either inconsistency or indeterminacy. Here  $\theta_1 = 0.9702$ ,  $\theta_2 = 1.2209$  from (2.8) and  $\varphi_1 = -1.8807$ ,  $\varphi_2 = -1.2610$  when  $\theta = \theta_P = 1.1071$  from (2.11) and (2.10) respectively: **(a)** in physical space, **(b)** in  $(\theta, \varphi)$  space.



The blue region in Figure 2.2b is bounded in  $\theta$  when  $\frac{d\varphi}{d\theta}$  is infinite, that is, when  $\cos \varphi = 0$ ,  $\varphi = -\frac{\pi}{2}$  where  $\theta = \theta_{1,2}(\mu, \alpha)$  are given in (2.8). It is bounded in  $\varphi$  when  $\frac{d\varphi}{d\theta} = 0$ . This happens when  $\sin \varphi = \frac{1}{\mu} \tan 2\theta$ , that is, when  $\theta = \theta_P(\alpha)$  where

$$(2.10) \quad \theta_P := \sqrt{1 + \alpha}.$$

Hence  $\varphi \in (\varphi_1, \varphi_2)$  in Figure 2.2b where

$$(2.11) \quad \varphi_{1,2}(\mu, \alpha) := \varphi_{\mp}(\theta_P(\alpha); \mu, \alpha) = -\frac{\pi}{2} \mp \arccos\left(\frac{2\sqrt{1+\alpha}}{\alpha\mu}\right)$$

and  $p(\theta_P, \varphi_{1,2}) = 0$ .

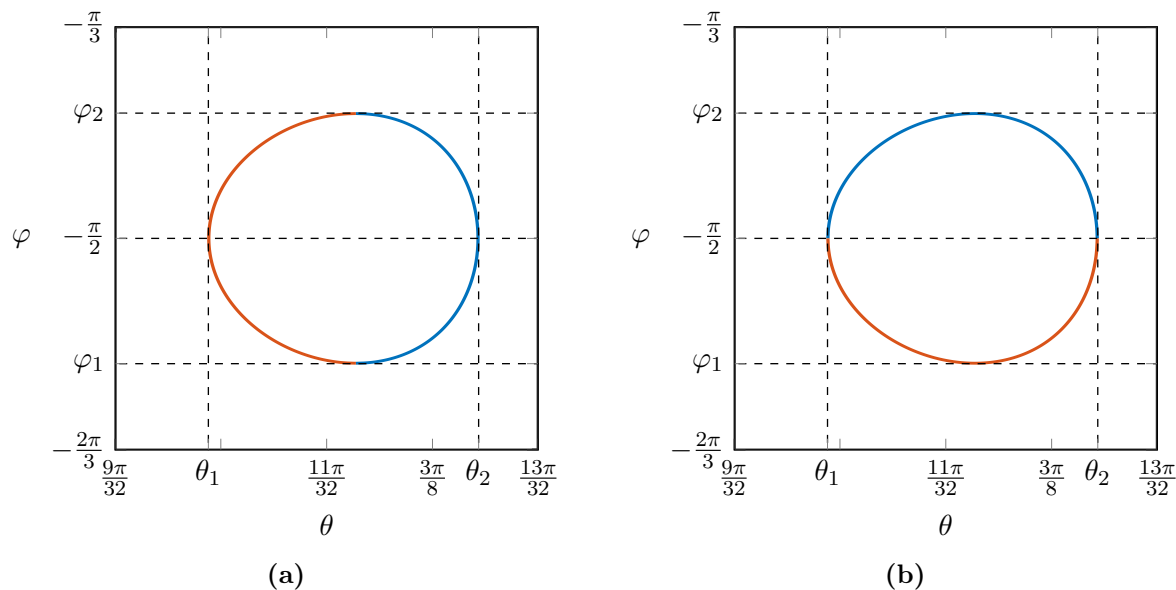
Therefore, the region where  $p < 0$  can be written as

$$(2.12) \quad \{(\theta, \varphi) | \varphi \in (\varphi_-(\theta), \varphi_+(\theta)), \theta \in (\theta_1, \theta_2)\},$$

or equivalently

$$(2.13) \quad \{(\theta, \varphi) | \theta \in (\theta_-(\varphi), \theta_+(\varphi)), \varphi \in (\varphi_1, \varphi_2)\},$$

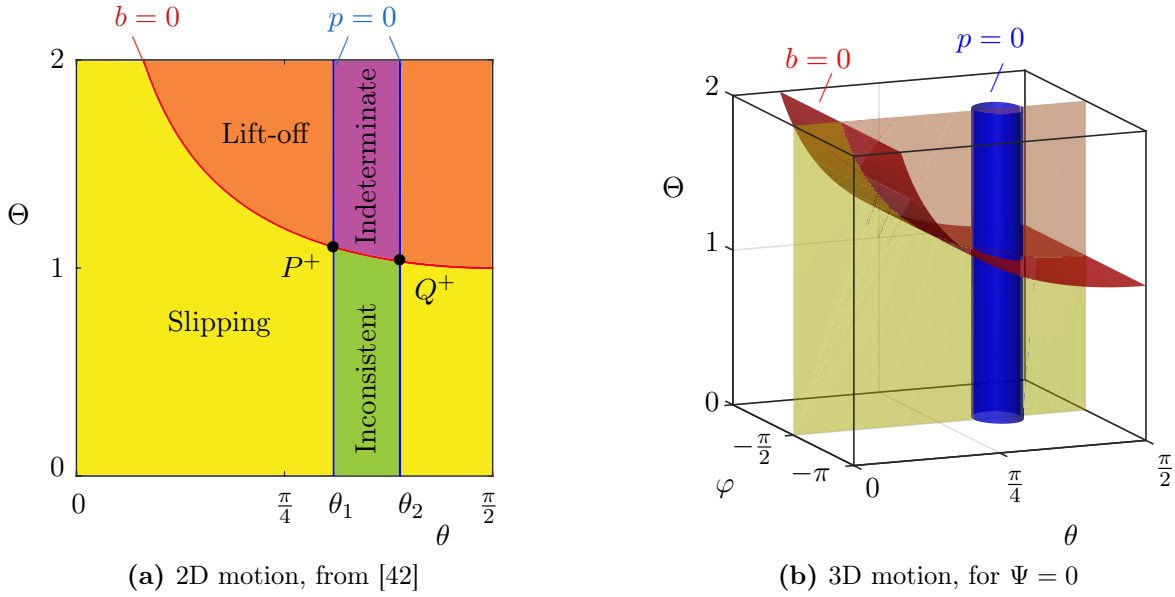
for  $\mu > \mu_P(\alpha)$  (see Figure 2.3).



**Figure 2.3:** Figure showing (a)  $\theta_{\pm}(\varphi; \alpha, \mu)$  given in (2.5) and (b)  $\varphi_{\pm}(\theta; \alpha, \mu)$  (2.6) for  $\alpha = 3$  and  $\mu = 1.4$ . Figures demonstrate the equivalence of (2.12) and (2.13).

## 2.2 Comparison with 2D problem

We compare the 2D and 3D problems, taking [38]  $\alpha = 3$ , corresponding to a uniform slender rod and  $\mu = 1.4 > \mu_P(3) = \frac{4}{3}$  from (2.7). Figure 2.4 shows, for  $\Theta \equiv \dot{\theta} > 0$ , the codimension-1



**Figure 2.4:** Kinematics for  $\Theta \equiv \dot{\theta} > 0$ : **(a)** 2D motion, reproduced from [42]: the curves  $b = 0$  and  $p = 0$  intersect at  $P^+$  and  $Q^+$ . They separate phase space into four regions, with different rigid body dynamics: *slipping* ( $b < 0$ ,  $p > 0$ , in yellow), *lift-off* ( $b > 0$ ,  $p > 0$ , in orange), *inconsistent* ( $b < 0$ ,  $p < 0$ , in lime) and *indeterminate* ( $b > 0$ ,  $p < 0$ , in purple). **(b)** 3D motion with  $\Psi \equiv \dot{\psi} = 0$ : the sets  $b = 0$  and  $p = 0$  intersect in the Génot-Brogliato (or GB) manifold [106]. A paradox occurs inside the blue cylinder: indeterminate above the surface  $b = 0$  (in red), inconsistent below. Outside the blue cylinder, we have lift-off above the surface  $b = 0$  (in red), slipping below. The cross section at  $\varphi = -\pi/2$  gives **(a)**. In both figures, we set  $\alpha = 3$ ,  $\mu = 1.4$ .

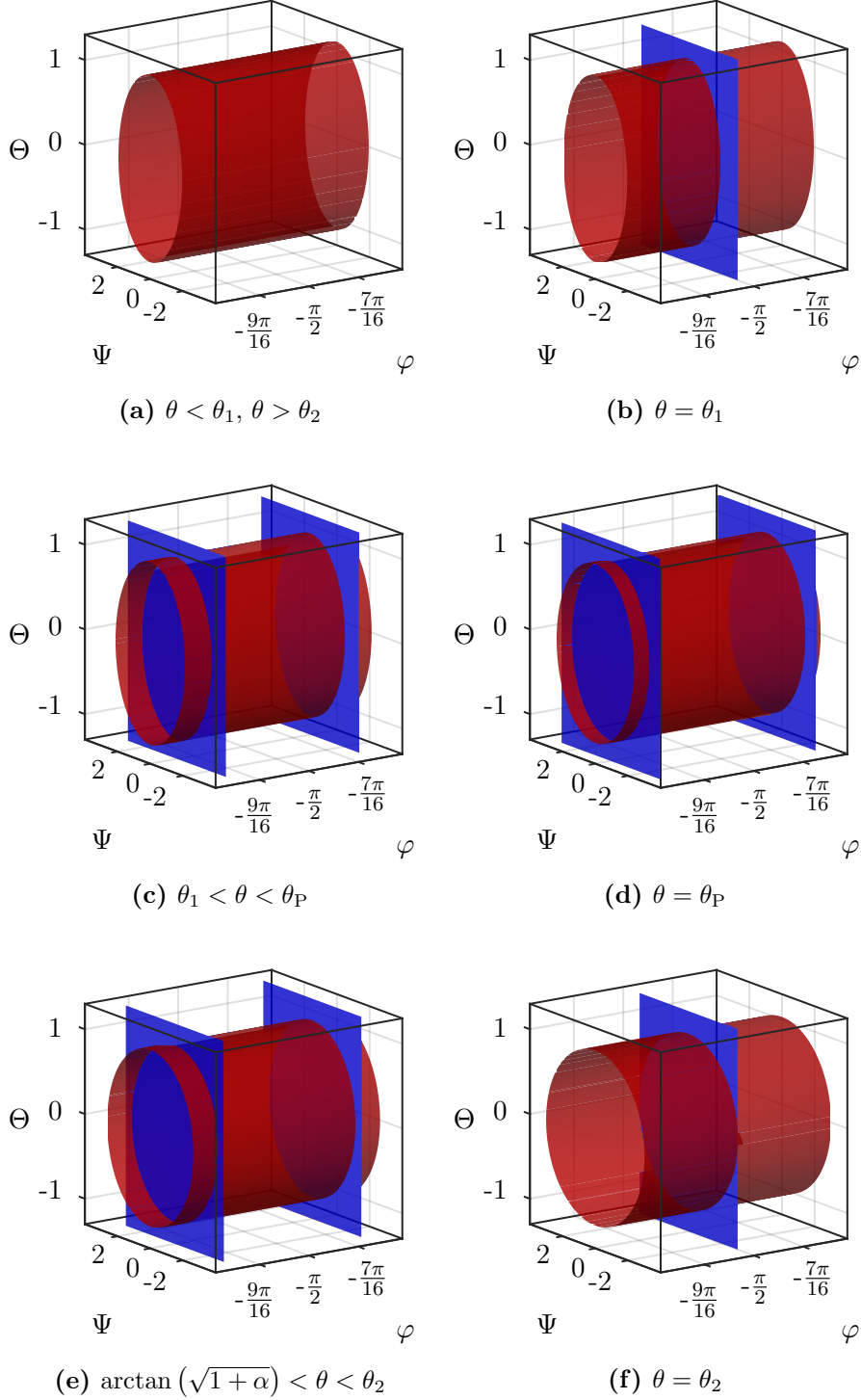
surfaces where  $b = 0$  (in red) and  $p = 0$  (in blue). For the 2D problem (Figure 2.4a), these surfaces are projected into  $(\theta, \Theta)$ -space, where they intersect at points  $P^+$  and  $Q^+$  (labelled  $P_{c1}^+$ ,  $P_{c2}^+$  respectively in [38, fig. 2]). For the 3D problem, these surfaces are shown for fixed  $\Psi = 0$  and projected into  $(\theta, \varphi, \Theta)$ -space (Figure 2.4b), where they intersect at a closed curve. This is the  $\Psi = 0$  section of the *Génot-Brogliato manifold* (or *GB manifold*) [106]. In Figure 2.21, we will see how this section varies for  $\Psi \neq 0$ . The 2D section at  $\varphi = -\pi/2$  in Figure 2.4b gives Figure 2.4a.

The surfaces  $b = 0$  and  $p = 0$ , symmetric about  $\Theta = 0$  and  $\varphi = -\pi/2$ , segment phase space into four different regions corresponding to the four modes (slipping, lift-off, inconsistent and indeterminate) of the LCP (2.1). In Figure 2.4a, these regions are labelled and a paradox ( $p < 0$ ) occurs between the blue lines  $p = 0$ . It is not possible to avoid a paradox whilst increasing  $\theta$ . In Figure 2.4b, a paradox occurs inside the blue cylinder  $p = 0$ : *indeterminate* above the surface  $b = 0$  and *inconsistent* below. Outside the blue cylinder  $p = 0$ , we have *lift-off* above the surface  $b = 0$  and *slipping* below. From (1.26), the shape of  $p = 0$  is independent of  $\Psi$  and hence in 3D it is always possible to avoid a paradox, if it occurs, by choosing the relative slip angle  $\varphi$  such that either  $\varphi \in (-\pi, \varphi_1)$  or  $\varphi \in (\varphi_2, 0)$ , see also Figure 2.2b.

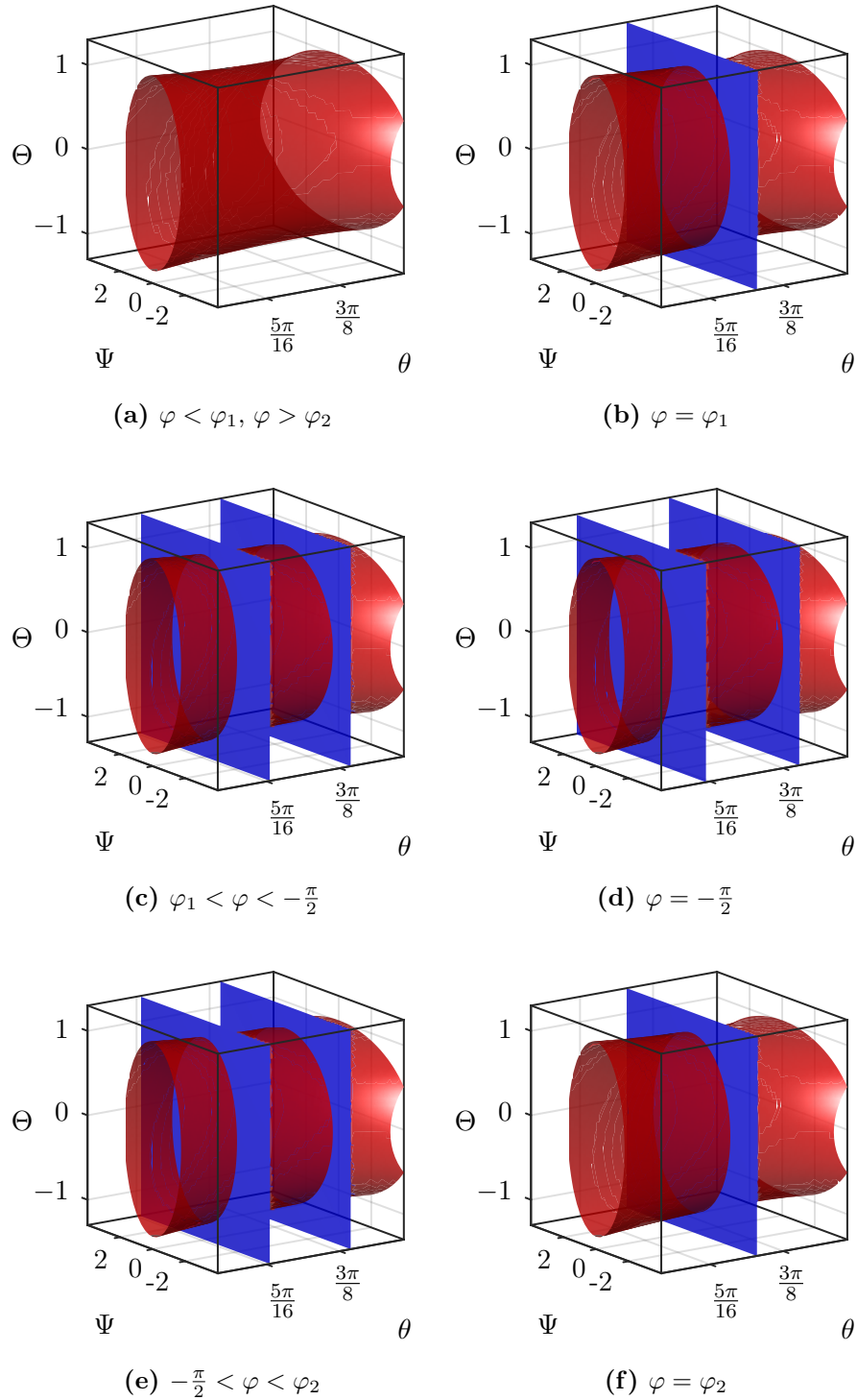
A figure similar to Figure 2.4 can be drawn for  $\Theta < 0$  where, for the 2D problem, the lines  $p = 0$  and  $b = 0$  intersect at  $P^-$  and  $Q^-$  (labelled  $P_{c1}^-, P_{c2}^-$  respectively in [38]). But since there is no effect on the kinematics, it is not shown here. However as we shall see in section 2.10, the geometry of the dynamics in  $\Theta > 0$  is very different from that in  $\Theta < 0$ .

### 2.3 Projections of the surfaces $b = 0$ and $p = 0$

In order to further understand the geometry of the Painlevé paradox in 3D we project the surfaces  $b(\theta, \Psi, \Theta) = 0$  and  $p(\theta, \varphi) = 0$  into  $(\varphi, \Psi, \Theta)$  space for fixed  $\theta$  (Figure 2.5), and into  $(\theta, \Psi, \Theta)$  space for fixed  $\varphi$  (Figure 2.6).



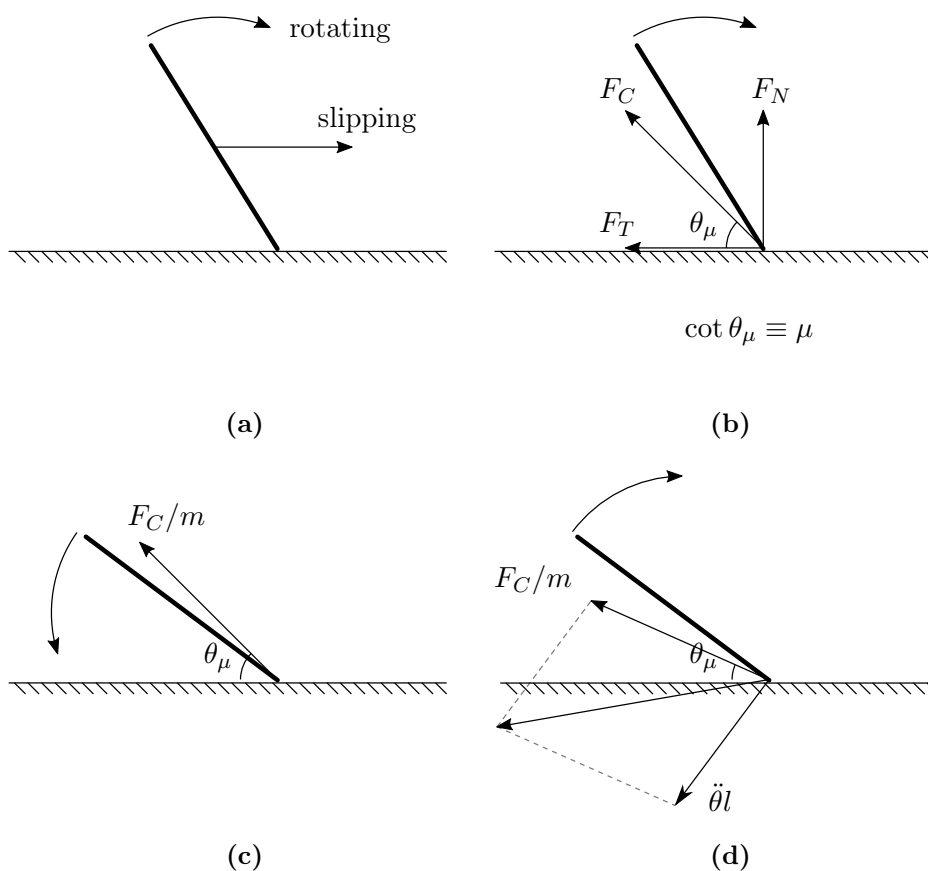
**Figure 2.5:** Figures (a)-(f) show the surfaces  $b(\theta, \Psi, \Theta) = 0$  (in red) and  $p(\theta, \varphi) = 0$  (in blue) for significant values of fixed  $\theta$ , projected into  $(\varphi, \Psi, \Theta)$  space. All figures use  $\mu = 1.4, \alpha = 3$ .



**Figure 2.6:** Figures (a)-(f) show the surfaces  $b(\theta, \Psi, \Theta) = 0$  (in red) and  $p(\theta, \varphi) = 0$  (in blue) for significant values of fixed  $\varphi$ , projected into  $(\theta, \Psi, \Theta)$  space. All figures use  $\mu = 1.4$ ,  $\alpha = 3$ .

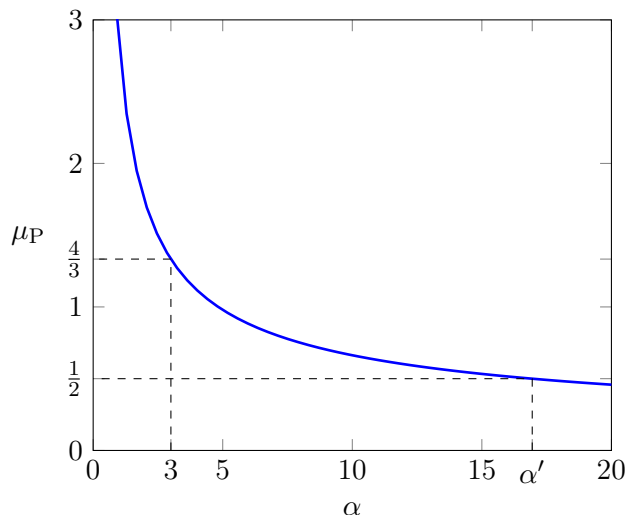
## 2.4 Physics of the paradox

Physically, this paradox occurs due to the moment induced by the friction at the contact. If the rod is slipping along the rough surface and able to rotate, the force at the contact point can cause the rod to accelerate angularly. If this angular acceleration is great enough, the resultant vertical acceleration of the contact tip downwards can be greater than the acceleration of the rod tip upwards due to the contact forces. This results in acceleration downwards into the surface, contradicting the rigid body assumptions (see Figure 2.7).



**Figure 2.7:** These figures demonstrate the physics of the “paradox”. We begin with the rod slipping on a rough surface and able to rotate (a). While this is happening, the surface is exerting both normal and tangential forces, denoted  $F_N$  and  $F_T$  respectively (b). We can view these two forces as a single force contact force  $F_C$  which will make an angle  $\theta_\mu \equiv \arctan(1/\mu)$  with the surface. If this angle  $\theta_\mu$  is greater than  $\theta$ , and the line of action of the force is above the rod, then this will cause an anticlockwise moment which could make the rod fall (c). However, if  $\theta_\mu < \theta$  then this will cause a clockwise moment on the rod (d). If this angular acceleration is great enough, then the component of the acceleration of the rod tip downwards from this moment may be greater than the component of the contact force upwards. This would result in an acceleration downwards which violates our assumption of the rigidity of the surface: the “paradox”.

## 2.5 Physical implications of parameter values



**Figure 2.8:** Interpretation of the critical value of the coefficient  $\mu_P(\alpha)$ .

We can draw conclusions about the implications of the condition (2.4). For example, in the case of a uniform rod, the inertial ratio is given by  $\alpha = 3$  [16, 38, 42, 64]. The coefficient of friction required for the paradox is therefore

$$(2.14) \quad \mu > \mu_P(3) = \frac{4}{3}.$$

Whilst potentially achievable (perhaps for copper-copper, silver-silver or aluminium-aluminium contact), the overwhelming majority of estimates for the coefficients of friction between materials is below 1 [13, 25]. Therefore, for almost all combinations of materials for the rod and the surface, the Painlevé paradox would not be achievable for a *uniform* rod.

Nevertheless, we see that the coefficient of friction required for the paradox is dependent on the value of our initial ratio  $\alpha$ . In the limit as  $\alpha \rightarrow \infty$ , the necessary coefficient of friction for  $p < 0$  tends to 0. In this way, rods with very high values of  $\alpha$  will not require such large values for the coefficient of friction before the rigid body equations of motion exhibit the lack of existence or uniqueness of solutions. But this raises further questions. How large does the value of  $\alpha$  have to be before the coefficient of friction becomes more physically realistic? How physically realistic is that value of  $\alpha$ ?

Let us perform some “back of the envelope” calculations to answer some of these questions. Let us suppose that the body is made up of a uniform rod  $b_R$  of mass  $m$  and half-length  $l$ , and a point mass  $b_M$  of mass  $M$  fixed to the centre of the rod. Using this body, we can find

$$(2.15) \quad \alpha_B = \frac{(m+M)l^2}{ml^2/3} = \frac{3(m+M)}{m} = 3 \left( 1 + \frac{M}{m} \right).$$

Furthermore, instead of making our condition on  $\mu$  in terms of  $\alpha$ , we can find the necessary value of  $\alpha$  given  $\mu$ ,

$$(2.16) \quad \alpha \geq \alpha_P(\mu) := \frac{2(1 + \sqrt{1 + \mu^2})}{\mu^2}.$$

Suppose we consider a more physically common value of the coefficient of friction, say  $\mu = \mu' := 0.5$ . This would mean that the minimum required inertial ratio  $\alpha = \alpha_P(1/2) \approx 17$ , which in turn means that the necessary ratio of the masses  $M/m \approx 14/3$ . The point mass would have to have more than four times the mass of the rod  $b_R$ . This seems like a very unusual composite body, should engineers be at all worried about Painlevé paradoxes?

Whilst in the case of this classical Painlevé problem the paradox may seem nonphysical, it may well be that for other bodies, or when external forcing is added, that the parameter values necessary for the paradox to occur may be more attainable. Furthermore, experimental evidence exists that demonstrates that physical systems, such as double pendula interacting with moving rail [112], do exhibit the "tangential impact" that are associated with these Painlevé paradoxes.

## 2.6 The role of $\Psi$

Now we investigate the role of the azimuthal angular velocity  $\Psi \equiv \dot{\psi}$ . We shall see that when  $|\Psi|$  is large enough, lift-off can occur, independently of a paradox (for  $p > 0$ ), even when  $\Theta = \dot{\theta} = 0$ . At even larger values of  $\Psi$ , indeterminacy can occur when  $\Theta = 0$  and the inconsistent region can even disappear.

In numerical plots for  $\alpha = 3$  and  $\mu = 1.4$ , between  $\Psi = \pm 1.56$  (Figure 2.9a) and  $\Psi = \pm 1.7$  (Figure 2.9b), we see that the area of lift-off (above  $b = 0$ , outside the cylinder  $p = 0$ ) has deformed so much that it is possible for the rod to lift off the rough surface even when  $\Theta = 0$ . The rotation about the vertical  $\mathbf{K}$  axis in the inertial frame (see Figure 1.3) is sufficient to generate an overall upwards acceleration of the rod tip. This can be thought of as resulting from "centrifugal forces"; the rod tip accelerates upwards in similar way to the weights on a centrifugal governor. A further increase to  $\Psi = \pm 2.2$  (Figure 2.9c) sees the possibility of indeterminacy (above  $b = 0$ , inside the cylinder  $p = 0$ ) when  $\Theta = 0$ . Then between Figure 2.9c and Figure 2.9d, the inconsistent region (below  $b = 0$ , inside the cylinder  $p = 0$ ) ceases to exist.

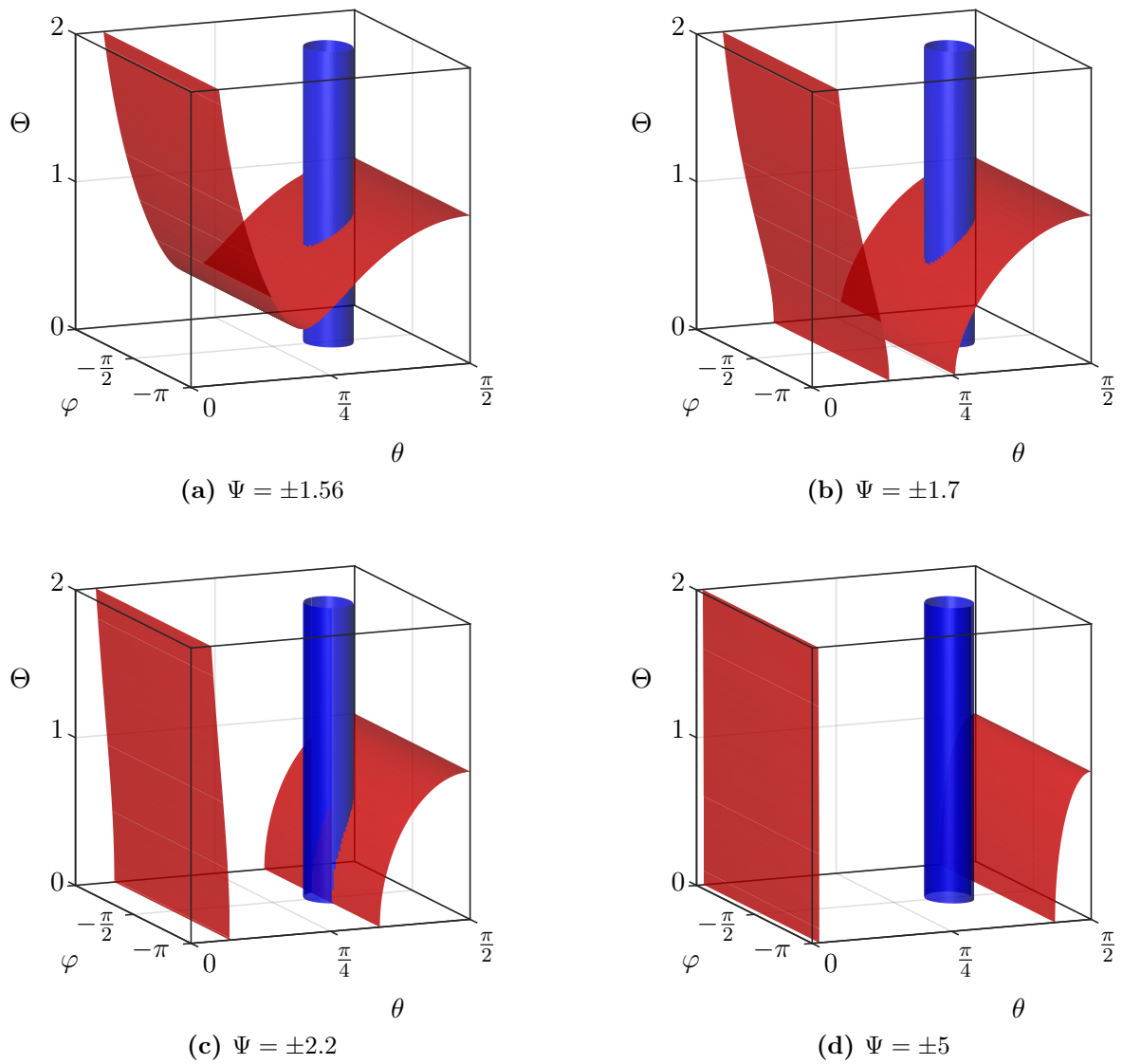
We now find expressions for these critical values of  $\Psi$ . The smallest value of  $\Psi$  where lift-off can be obtained when  $\Theta = \dot{\theta} = 0$  occurs when  $\frac{\partial b}{\partial \theta} = \frac{\partial b}{\partial \Theta} = 0$  on  $b = 0$ . From (1.25), it can be shown that this occurs when  $(\theta, \Psi) = (\theta_L, \pm \Psi_L)$ , where

$$(2.17) \quad \sin \theta_L := \frac{1}{\sqrt{3}},$$

so that

$$(2.18) \quad \theta_L := \arcsin\left(\frac{1}{\sqrt{3}}\right) \approx 0.6155 \approx 35.3^\circ,$$



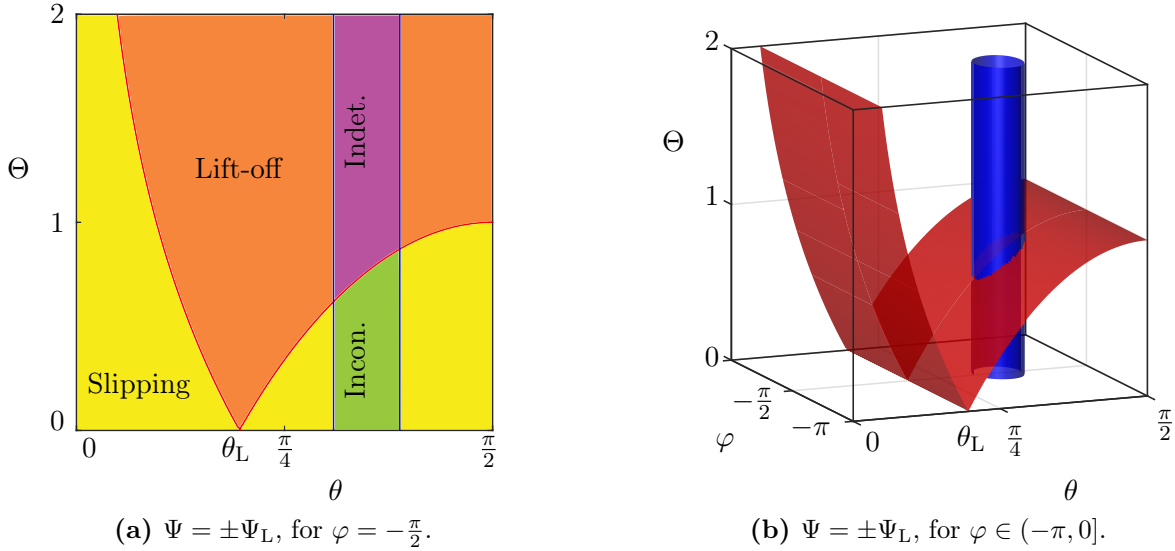


**Figure 2.9:** Surfaces  $b = 0$  (in red) and  $p = 0$  (in blue) as  $\Psi$  varies. In all figures we set  $\alpha = 3$ ,  $\mu = 1.4$ .

and

$$(2.19) \quad \Psi_L := \left( \frac{3\sqrt{3}}{2} \right)^{\frac{1}{2}} \approx 1.6119.$$

We show this case as a 2D section with  $\varphi = -\frac{\pi}{2}$  in Figure 2.10a and in 3D for  $\varphi \in (-\pi, 0]$  in Figure 2.10b. Note that this potential for lift-off when  $\Theta = \dot{\theta} = 0$  for  $\Psi > \Psi_L$  can occur even when there is no paradox.



**Figure 2.10:** Areas of different dynamics for 3D motion when  $\Psi = \pm\Psi_L$ , from (2.19). Lift-off can occur for  $|\Psi| \geq \Psi_L$  even when  $\Theta = \dot{\theta} = 0$ : (a)  $\varphi = -\frac{\pi}{2}$ , (b)  $\varphi \in (-\pi, 0]$ . In both figures we set  $\alpha = 3$ ,  $\mu = 1.4$ .

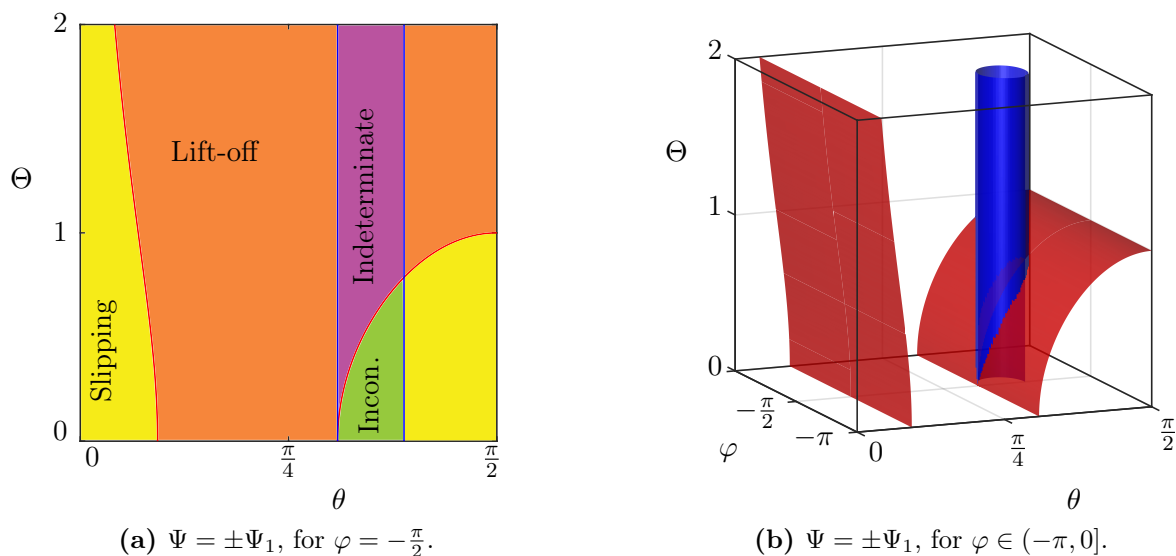
The next critical value of  $\Psi$  occurs when the surface  $b = 0$  is tangential to the cylinder  $p = 0$  at  $\theta = \theta_1$ , where  $\theta_1$  is given in (2.8). A straightforward calculation shows that this happens when  $\Psi = \pm\Psi_1$ , where

$$(2.20) \quad \Psi_1(\mu, \alpha) := \frac{(1 + \tan^2 \theta_1)^{\frac{3}{4}}}{(\tan \theta_1)^{\frac{1}{2}}}.$$

When  $\alpha = 3$ ,  $\mu = 1.4$ , this corresponds to  $\Psi_1 = 1.9480$  with  $\theta_1 = 0.9702$ . We show this case in Figure 2.11; as a 2D section with  $\varphi = -\frac{\pi}{2}$  in Figure 2.11a and for  $\varphi \in (-\pi, 0]$  in Figure 2.11b. When  $\theta_L < \theta_1$ , this is the smallest value of  $\Psi$  for which indeterminacy can occur for  $\Theta = 0$ . It will be important to note that  $\Psi_1 \geq \Psi_L$ , with equality occurring when  $\theta_1 = \theta_L \approx 0.6155$  from (2.18), when

$$(2.21) \quad \mu = \mu_L(\alpha) := \frac{2\alpha + 3}{\alpha\sqrt{2}}.$$

For a uniform slender rod with  $\alpha = 3$ ,  $\mu_L(3) = \frac{3}{\sqrt{2}} \approx 2.1213$ .

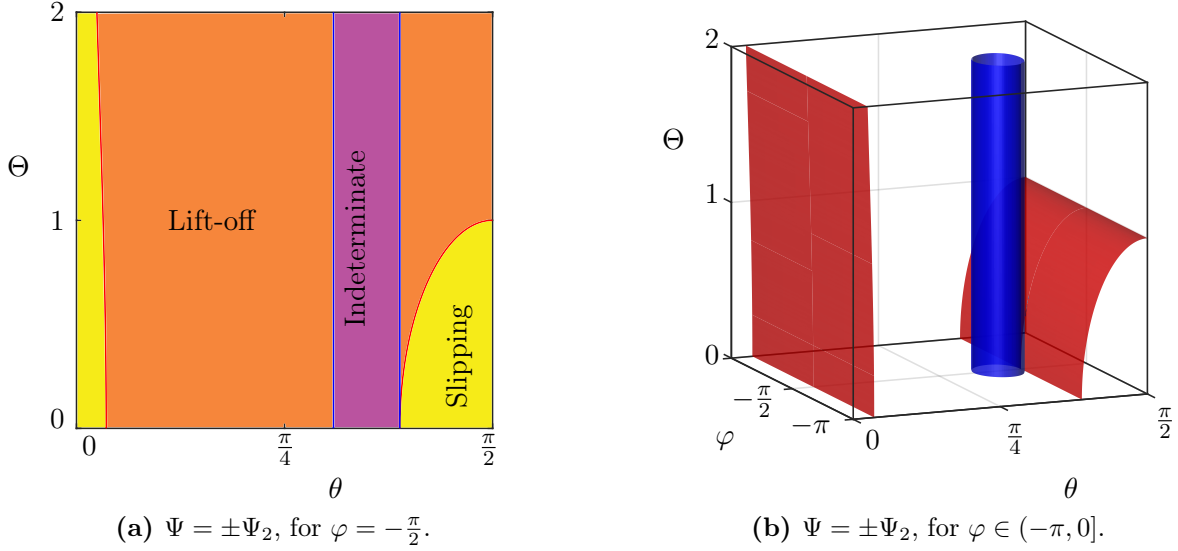


**Figure 2.11:** Areas of different dynamics for 3D motion when  $\Psi = \pm\Psi_1$ , from (2.20). The surface  $b = 0$  is tangential to the cylinder  $p = 0$  at  $\theta = \theta_1$ : (a)  $\varphi = -\frac{\pi}{2}$ , (b)  $\varphi \in (-\pi, 0]$ . Both figures use  $\alpha = 3$ ,  $\mu = 1.4$ .

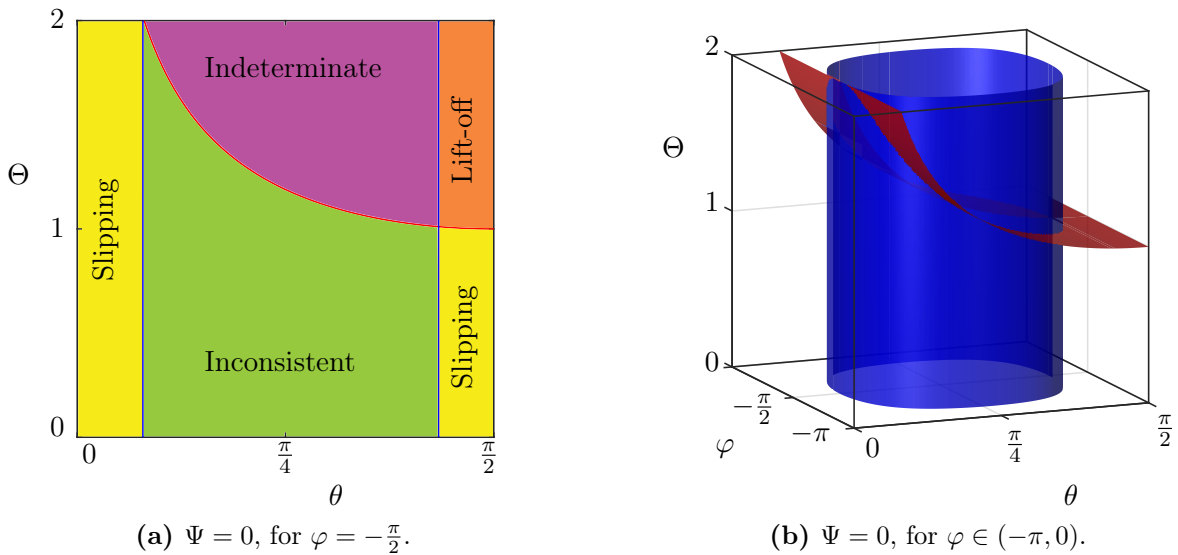
The final critical value of  $\Psi$  occurs when the surface  $b = 0$  is tangential to the cylinder  $p = 0$  at  $\theta = \theta_2$ , where  $\theta_2$  is given in (2.8). This happens when  $\Psi = \pm\Psi_2$ , where

$$(2.22) \quad \Psi_2(\mu, \alpha) := \frac{(1 + \tan^2 \theta_2)^{\frac{3}{4}}}{(\tan \theta_2)^{\frac{1}{2}}}.$$

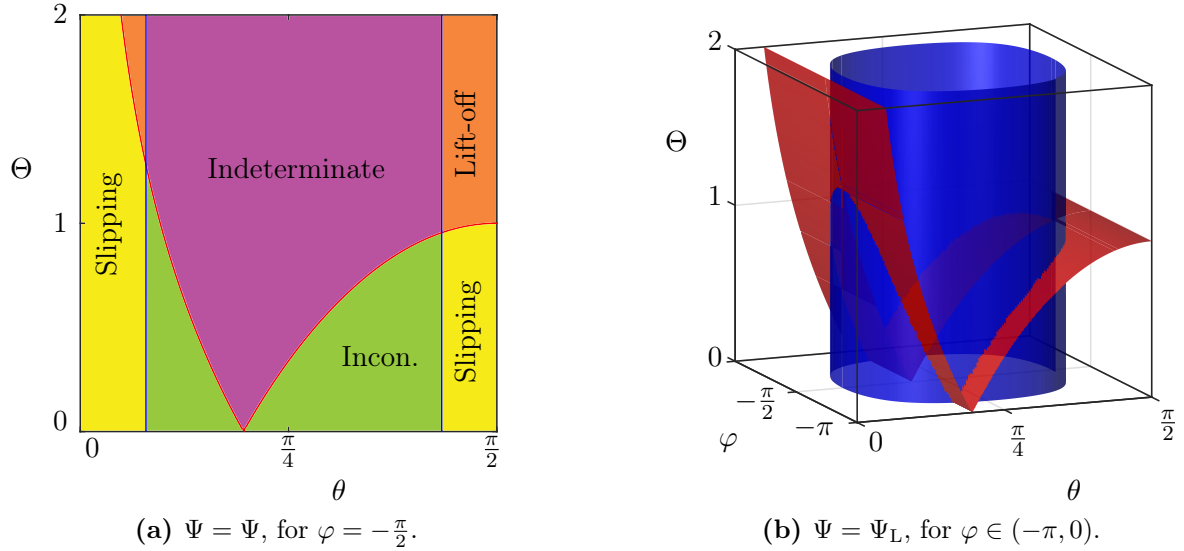
When  $\alpha = 3$ ,  $\mu = 1.4$ , this corresponds to  $\Psi_2 = 3.0097$  with  $\theta_2 = 1.2209$ . We show this case in Figure 2.12; as a 2D section with  $\varphi = -\frac{\pi}{2}$  in Figure 2.12a and for  $\varphi \in (-\pi, 0]$  in Figure 2.12b. When  $|\Psi| \geq \Psi_2$ , there is no inconsistent paradox.



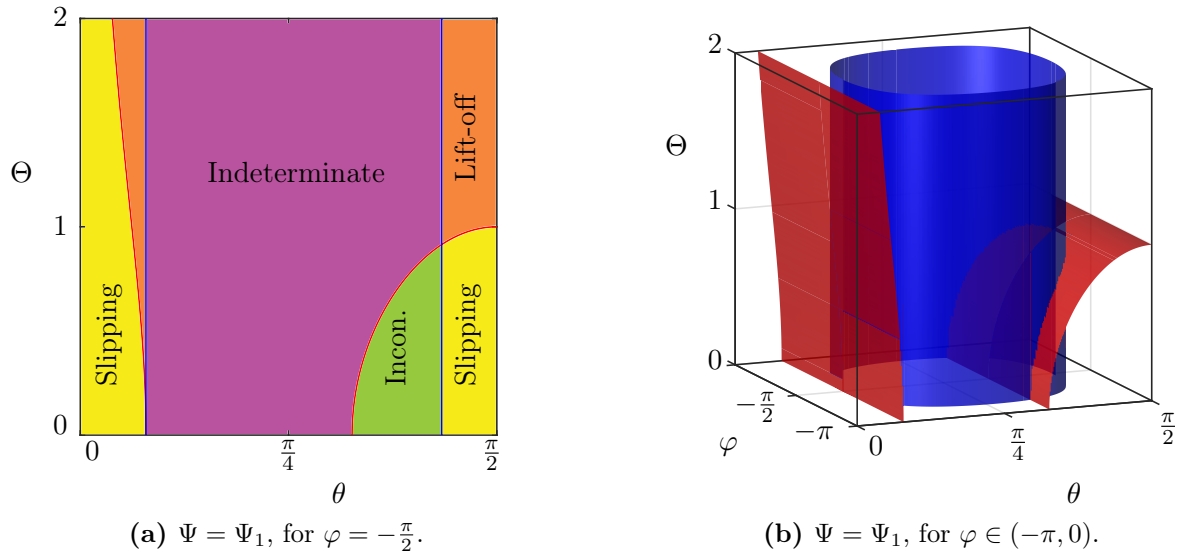
**Figure 2.12:** Areas of different dynamics for 3D motion when  $\Psi = \pm\Psi_2$ , from (2.22). The inconsistent paradox disappears for  $|\Psi| \geq \Psi_2$ : (a)  $\varphi = -\frac{\pi}{2}$ , (b)  $\varphi \in (-\pi, 0]$ . Both figures use  $\alpha = 3$ ,  $\mu = 1.4$ .



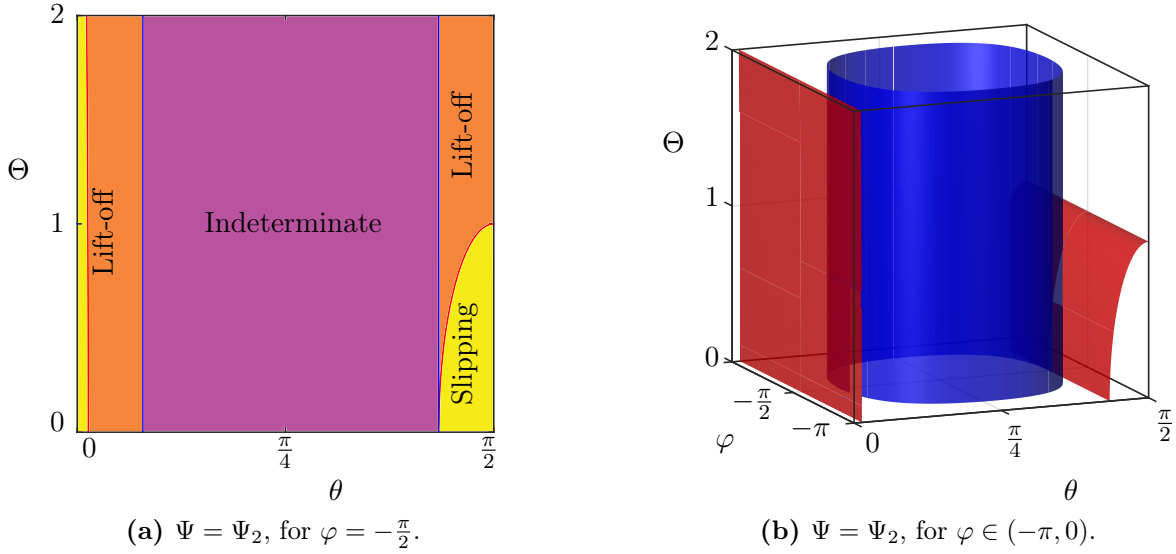
**Figure 2.13:** As Figure 2.4 but for  $\alpha = 0.2$  and  $\mu = 25$ ; areas of different dynamics for 3D motion when  $\Psi = 0$ .



**Figure 2.14:** As Figure 2.10 but for  $\alpha = 0.2$  and  $\mu = 25$ : areas of different dynamics for 3D motion when  $\Psi = \Psi_L$ . However, here lift-off is not possible along  $\Theta = 0$ .



**Figure 2.15:** As Figure 2.11 but for  $\alpha = 0.2$  and  $\mu = 25$ : areas of different dynamics for 3D motion when  $\Psi = \Psi_1$ , from (2.20). The surface  $b = 0$  is tangential to the cylinder  $p = 0$  at  $\theta = \theta_1$ : (a)  $\varphi = -\frac{\pi}{2}$ , (b)  $\varphi \in (-\pi, 0)$ .



**Figure 2.16:** As Figure 2.12 but for  $\alpha = 0.2$  and  $\mu = 25$ : areas of different dynamics for 3D motion when  $\Psi = \Psi_2$ , from (2.22). The surface  $b = 0$  is tangential to the cylinder  $p = 0$  at  $\theta = \theta_2$ : (a)  $\varphi = -\frac{\pi}{2}$ , (b)  $\varphi \in (-\pi, 0)$ .

## 2.7 Generic behaviour

As we have seen, variation in  $\Psi$  causes changes to the shape of the surface  $b = 0$  projected into  $(\theta, \varphi, \theta)$  and hence to the topology of the GB manifold  $b = p = 0$  in this view. In fact there are three different *mechanisms* I-III by which the GB manifold deforms, for fixed  $\alpha$  and  $\mu$ , as  $\Psi$  increases. They are illustrated in Figure 2.17, as follows:

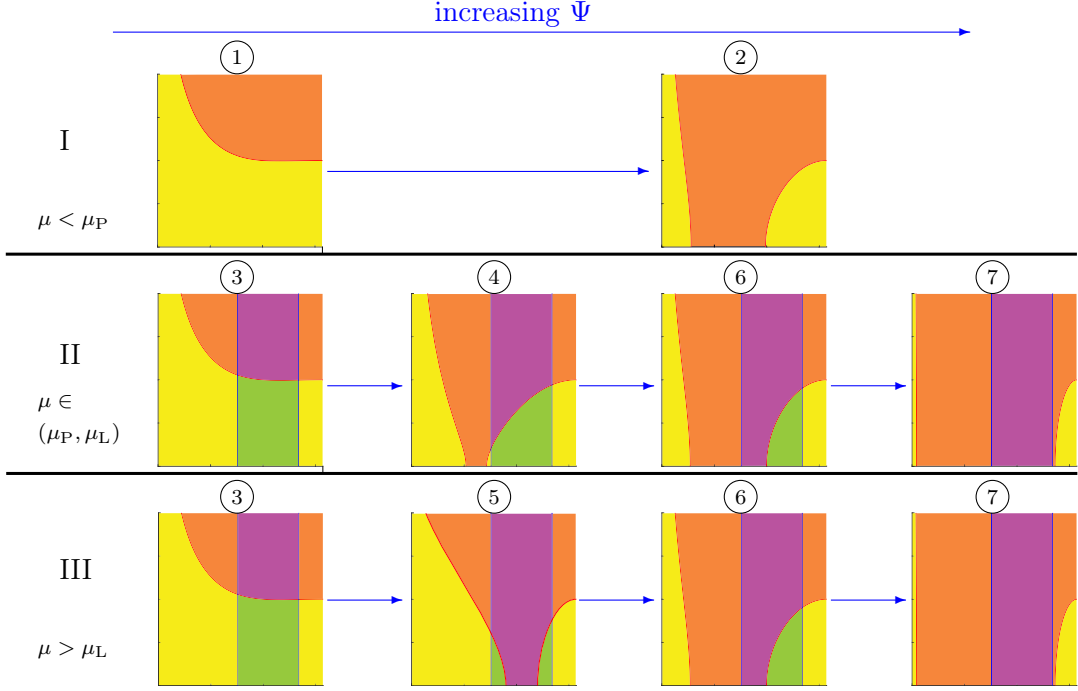
I ( $\mu < \mu_P$ ): there is no paradox and the rod can either slip or lift-off.

- For  $|\Psi| < \Psi_L$ , we have case (1).
- For  $|\Psi| > \Psi_L$ , we have case (2).

II ( $\mu_P < \mu < \mu_L$ ):  $p < 0$  for  $\theta \in (\theta_-, \theta_+)$  and so a Painlevé paradox can occur.

- For  $\Psi < |\Psi_L|$ , we have case (3) and all four modes (slipping, lift-off, inconsistent and indeterminate) are possible.
- For  $\Psi_L < |\Psi| < \Psi_1$ , lift-off is possible for  $\Theta = 0$ ; case (4).
- For  $\Psi_1 < |\Psi| < \Psi_2$ , both lift-off and indeterminate modes as possible for  $\Theta = 0$ ; case (6).
- For  $|\Psi| > \Psi_2$ , the inconsistent mode ceases to exist; case (7).

III ( $\mu > \mu_L$ ):  $p < 0$  for  $\theta \in (\theta_-, \theta_+)$  and so a Painlevé paradox can occur. Mechanism III is the same as mechanism II except when  $\Psi_L < |\Psi| < \Psi_1$ , where the indeterminate mode (rather than lift-off) is possible for  $\Theta = 0$ ; case ⑤.



**Figure 2.17:** Mechanisms I–III for the 3D Painlevé problem, for increasing  $\Psi$ . Prototypical cases are adapted from numerical examples for the sake of clarity.

The different types of behaviour labelled ①–⑦ occur for different values of  $\Psi$  as a function of  $\mu$ , as shown in Figure 2.18a. Mechanisms I–III occur at different values of  $\mu$  as a function of  $\alpha$ , as shown in Figure 2.18b.

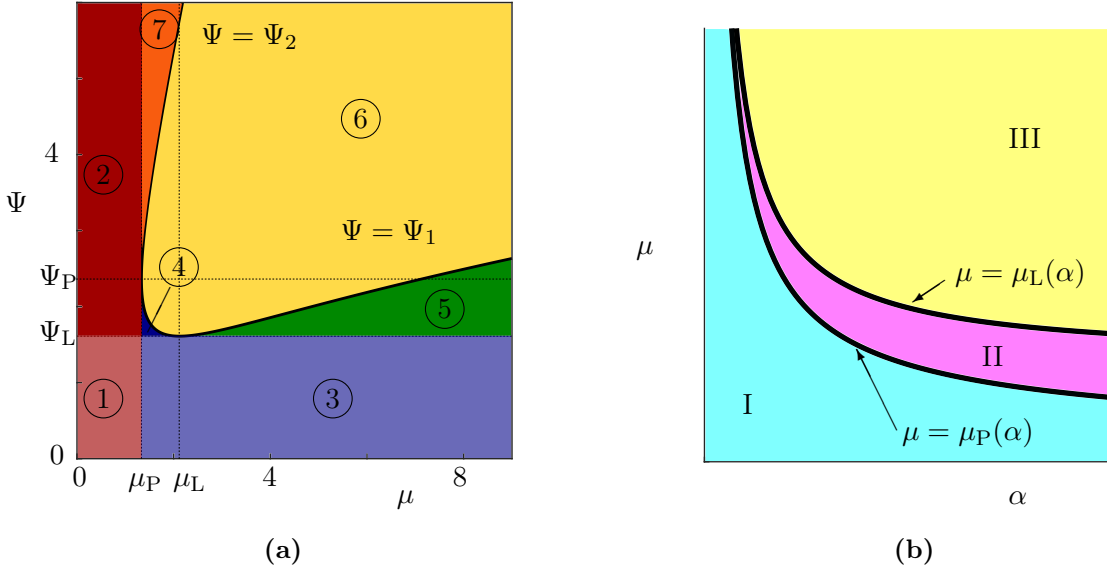
In Figure 2.18a, we show  $\Psi_L$ ,  $\Psi_1$  and  $\Psi_2$  as functions of  $\mu$  for  $\alpha = 3$  when  $\Psi > 0$ . At  $\mu = \mu_P(\alpha)$ , we have

$$(2.23) \quad \Psi_1(\mu_P(\alpha), \alpha) \equiv \Psi_2(\mu_P(\alpha), \alpha) = \Psi_P(\alpha) := \left( \frac{(2 + \alpha)^3}{(1 + \alpha)} \right)^{\frac{1}{4}}.$$

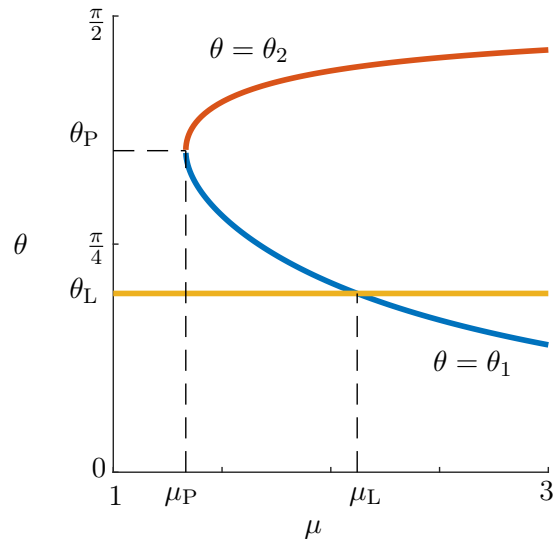
So  $\Psi_P \approx 2.3644$  when  $\alpha = 3$ . Recall that  $\Psi_1 \geq \Psi_L$ , with equality occurring when  $\theta_1 = \theta_L \approx 0.6155$  from (2.18), when  $\mu = \mu_L(\alpha)$  (2.21).

In Figure 2.18b, we show  $\mu_P(\alpha)$  from (2.7) and  $\mu_L(\alpha)$  from (2.21). In Figure 2.19, we show the critical polar angles  $\theta_L$ ,  $\theta_1$ ,  $\theta_2$  as functions of  $\mu$  for  $\alpha = 3$ . At  $\mu = \mu_P(\alpha)$ ,  $\theta_1 = \theta_2 = \theta_P(\alpha)$ , see (2.10). It is straightforward to show that  $\theta_2 > \theta_L \forall \alpha, \mu$ .

In Figure 2.17, we show only the generic cases of the geometry of the surfaces  $p = 0$  and  $b = 0$  for fixed  $\Psi$ . In Figure A.1 in Appendix A, we show all the bifurcations between these cases with changes in the variable  $\Psi$  and the parameter  $\mu$ .



**Figure 2.18:** (a) Regions where the seven types of kinematic behaviour occur in the 3D Painlevé problem for  $\alpha = 3$ . (b) Regions where mechanisms I–III occur in the 3D Painlevé problem. Note that  $\mu_P(\alpha)$  is given in (2.7),  $\mu_L(\alpha)$  in (2.21),  $\Psi_L$  in (2.19),  $\Psi_P$  in (2.23),  $\Psi_1$  in (2.20),  $\Psi_2$  in (2.22).



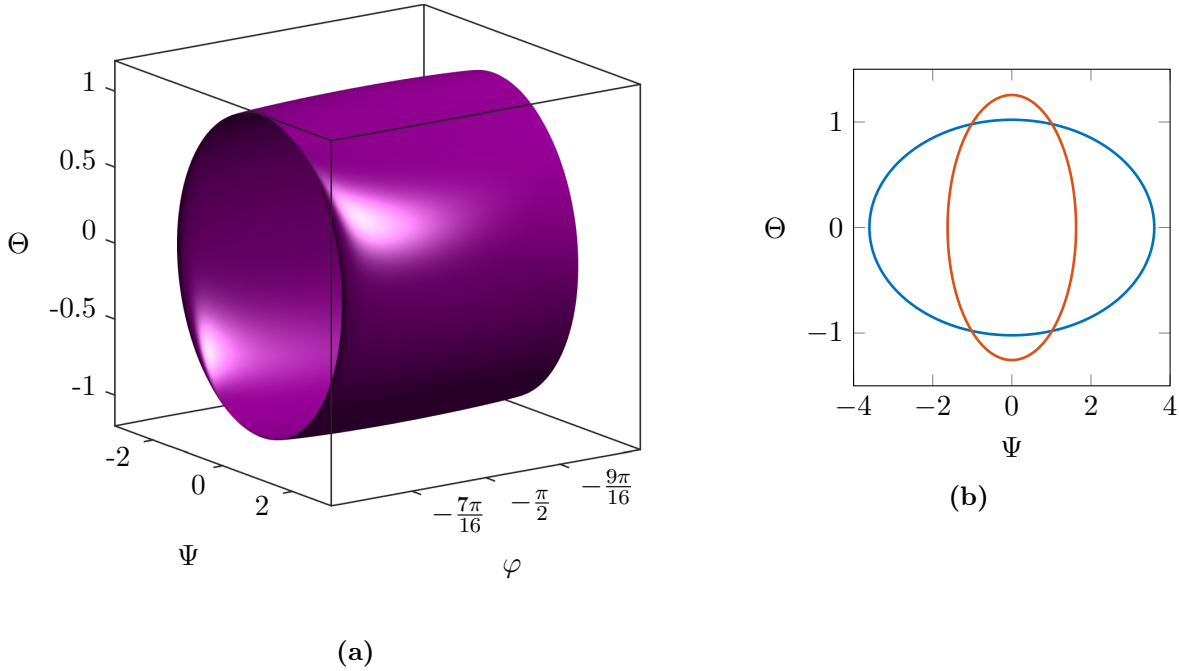
**Figure 2.19:** Critical values  $\theta_L$ ,  $\theta_1$  and  $\theta_2$  as functions of  $\mu$  for  $\alpha = 3$ . Here  $\theta_L = \arcsin \frac{1}{\sqrt{3}} \approx 0.6155$  from (2.17) and  $\theta_P \approx 1.1071$  from (2.10).  $\theta_1, \theta_2$  are given in (2.8) and  $\mu_P = \frac{4}{3}$ ,  $\mu_L = \frac{3}{\sqrt{2}}$ .



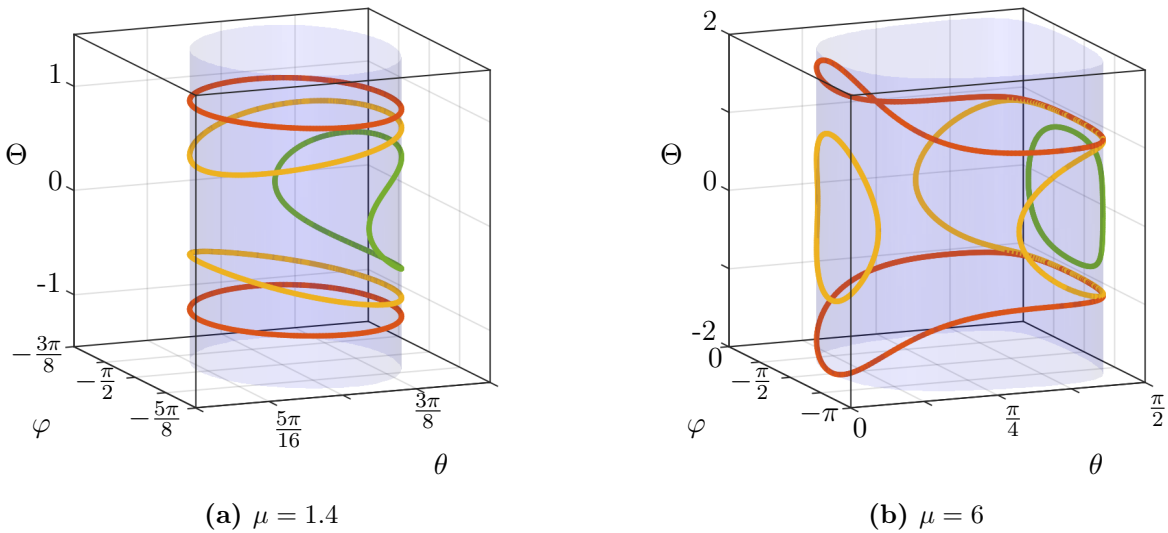
## 2.8 GB manifolds

The GB manifold is the intersection of the codimension-1 sets  $b = 0$  and  $p = 0$ , and hence is codimension-2. For the 2D problem ( $\varphi = \pm\pi/2$ ,  $\Psi = 0$ ) this intersection corresponds to 4 points ( $P^\pm$ ,  $Q^\pm$ ) when projected into the plane ( $\theta$ ,  $\Theta$ ) if  $\mu > \mu_P$ , see Figure 2.4 and [38, fig. 2]. In 3D, this set is a more complicated and higher dimensional object. In Figure 2.20, we show the sets  $b(\theta_1(\varphi), \Psi, \Theta) = 0$  and  $b(\theta_2(\varphi), \Psi, \Theta) = 0$ , a projection of the GB manifold into  $(\varphi, \Psi, \Theta)$  space.

In 3D, for fixed  $\Psi$ , this set can take on a number of different forms, or it may not exist. In Figure 2.21, we show the GB manifold in  $\Theta \geq 0$  for representative values of  $\Psi$  when  $\alpha = 3$  with  $\mu = 1.4$  and  $\mu = 6$ . There is no GB manifold in the 3D problem when  $|\Psi| > \Psi_2$ . In Figure 2.21a  $\mu = 1.4 \in (\mu_P, \mu_L)$  corresponds to mechanism II. Since  $\Psi_L = 1.6118$ ,  $\Psi_1 = 1.9480$  and  $\Psi_2 = 3.0097$  then  $\Psi = 0$  (■) corresponds to type (3) behaviour,  $\Psi = 1.7800$  (■) to type (4) and  $\Psi = 2.4789$  (■) to type (6). In Figure 2.21b  $\mu = 6 > \mu_L$  corresponds to mechanism III. Since  $\Psi_L = 1.6118$ ,  $\Psi_1 = 2.1876$  and  $\Psi_2 = 17.8171$  then  $\Psi = 0$  (■) corresponds to type (3) behaviour,  $\Psi = 1.8997$  (■) to type (5) and  $\Psi = 10.0024$  (■) to type (6).



**Figure 2.20:** (a): projections of the GB manifold  $(b(\Psi, \Theta, \theta_+(\varphi; \alpha, \mu)) = 0$  and  $b(\Psi, \Theta, \theta_-(\varphi; \alpha, \mu)) = 0$ ) into  $(\varphi, \Psi, \Theta)$  space. (b): a slice of (a) for  $\varphi = -\pi/2$ , giving  $(b(\Psi, \Theta, \theta_2(\alpha, \mu)) = 0$  and  $b(\Psi, \Theta, \theta_1(\alpha, \mu), \Psi) = 0)$ . Figure uses  $\alpha = 3$   $\mu = 1.4$ .

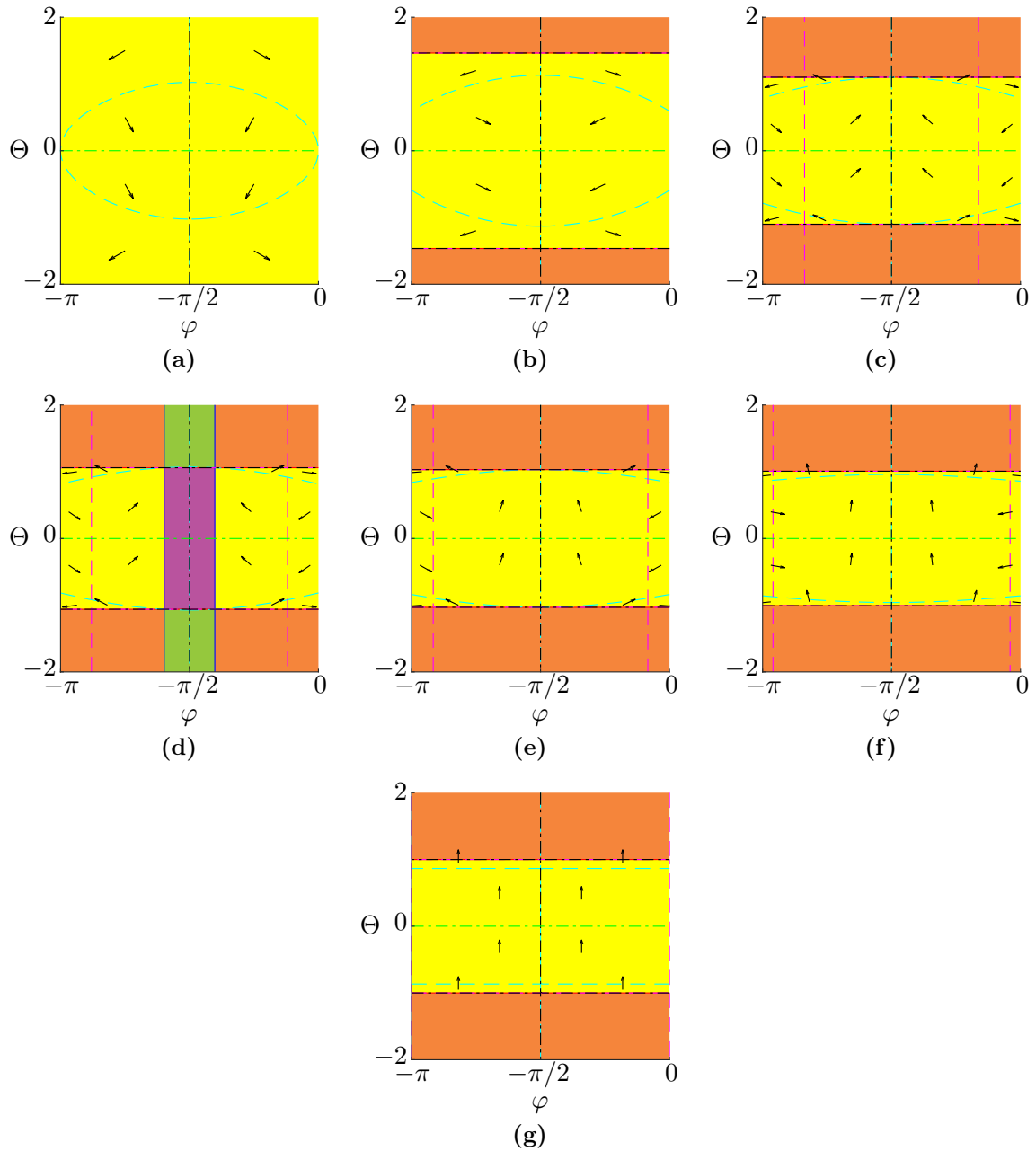


**Figure 2.21:** GB manifolds for  $\alpha = 3$ . (a) mechanism II:  $\mu = 1.4$  and  $\Psi = 0$  (■), 1.7800 (■), 2.4789 (■). (b) mechanism III:  $\mu = 6$  and  $\Psi = 0$  (■), 1.8997 (■), 10.0024 (■).

## 2.9 Phase portraits

In [38], phase portraits in  $(\theta, \Theta)$ -space were a powerful tool in describing the qualitative behaviour of the system. Now with the introduction of further dimensions in the 3D Painlevé problem, phase portraits in state variables are far less intelligible, due to the need to take planar sections of higher-dimensional space.

In Figure 2.22, we present phase portraits in  $(\varphi, \Theta)$  space at varying sections of  $\theta$  for fixed values of the other variables and parameters. Clearly, this approach is limited; we may need to find a useful projection in order to describe the dynamics (see section 2.10). Nonetheless, we include further phase portraits for varying values of parameters and variables in Appendix B



**Figure 2.22:** Phase portraits in  $(\varphi, \Theta)$  for fixed  $\Psi = 0$  and sections of  $\theta$ . (a)  $\theta = 0$ , (b)  $\theta = 0.48508$ , (c)  $\theta = 0.97016$ , (d)  $\theta = 1.0955$ , (e)  $\theta = 1.2209$ , (f)  $\theta = 1.3958$ , (g)  $\theta = 1.5708$ .  $\dot{\varphi} = 0$  ■,  $\dot{\theta} = 0$  ■,  $\dot{\Psi} = 0$  ■,  $\dot{\Theta} = 0$  ■. The parameters  $\alpha = 3$  and  $\mu = 1.4$ .

## 2.10 Slipping dynamics near the GB manifold

In the previous section, we have seen how the surfaces  $b = 0$  and  $p = 0$  divide phase space. But this kinematic analysis does not tell us how the rod, when slipping, can move into another region (or mode). In this section, we consider the rod dynamics close to  $b = p = 0$ , in order to see which transitions from slipping<sup>8</sup> are allowed.

In the classical 2D Painlevé problem, for  $\mu > \mu_P$ , Génot and Brogliato [38] showed that slipping trajectories starting with  $\theta \in (0, \theta_1)$  cannot pass through the boundary  $p = 0$  of the Painlevé region without also passing through the lift-off boundary  $b = 0$ . In that case, the rod must pass through the point  $P^+$  of Figure 2.4a (the rod can also stick, of course)<sup>9</sup>.

Génot and Brogliato [38] also found a new critical value  $\mu_C(\alpha)$  of the coefficient of friction given, for general  $\alpha$  [84], by

$$(2.24) \quad \mu_C(\alpha) := \frac{2}{\sqrt{3}}\mu_P(\alpha) = \frac{4}{\alpha} \sqrt{\frac{\alpha+1}{3}}.$$

The importance of  $\mu > \mu_C$  in the 2D problem is summarised in [84, Theorem 1]. For  $\mu \in (\mu_P, \mu_C]$ , all slipping solutions undergo lift-off before reaching inconsistency; the point  $P^+$  cannot be reached. For  $\mu > \mu_C$ , there is a region of initial conditions where  $P^+$  is reached, where the normal reaction force becomes unbounded.

In this section, we investigate the slipping dynamics close to the GB manifold  $b = p = 0$  in the 3D problem. In [16, section 7.2], it was shown that system trajectories can cross  $p = 0$  transversely away from the GB manifold because  $p(\theta, \varphi)$  tends to zero faster than  $b(\Psi, \Theta, \theta)$  (see also numerical evidence in [16, Fig. 17]).

In fact we can show that crossing of  $p = 0$  away from  $b = 0$  is the norm in 3D and that the 2D problem is highly singular. From (1.23) and (1.26), we have that

$$(2.25) \quad \begin{aligned} \dot{p}|_{p=0} &= \left( \frac{\partial p}{\partial \theta} \dot{\theta} + \frac{\partial p}{\partial \varphi} \dot{\varphi} \right)_{p=0} \\ &= \frac{1}{\eta} (1 + \alpha) \alpha \mu \cos^2 \theta \cos^2 \varphi b. \end{aligned}$$

So, away from  $\theta = \pi/2$  and  $\varphi = -\pi/2$ , we find that  $\text{sign}(\dot{p})|_{p=0} = \text{sign}(b)$ . When slipping, we have  $b < 0$ , so in this mode we have  $\text{sign}(\dot{p})|_{p=0} = \text{sign}(b) < 0$ . Hence we move from  $p = 0$  into  $p < 0$ . But since  $b < 0$ , the rod moves into the inconsistent region.

There are two cases where  $\text{sign}(\dot{p})|_{p=0} = 0 \forall \Psi$ . When  $\theta = \pi/2$ , the rod is vertical and we have excluded this case. The other exception is when  $\varphi = -\pi/2$ . When  $\Psi = 0$ , this is the classical 2D Painlevé problem. In other words, the 2D problem is the *exception* in requiring that  $p = 0$  can be crossed only when  $b = 0$ .

<sup>8</sup>We do not consider movements from the other modes for obvious reasons.

<sup>9</sup>Trajectories starting with  $\theta \in (\theta_2, \frac{\pi}{2})$  are all directed away from the point  $Q^+$  in Figure 2.4a, so the line  $p = 0$  can not be crossed there at all. The line  $p = 0$  can not be crossed from slipping anywhere in  $\Theta < 0$  [38].

But the result in (2.25) implicitly assumes the existence of an inconsistent region for fixed values of the parameters, which is not the case if  $|\Psi| > \Psi_2$ . So we need to understand in more detail the dynamics of the 3D problem (1.23) near  $b = p = 0$ .

To proceed, we disregard equations for  $x$  and  $y$  in (1.23), as they are cyclic. We shall not consider them again.

Now when the rod is slipping,  $z = w = 0$ , and so  $F_z = -b/p$  from (1.23). If we substitute this result into the remaining six equations in (1.23), we are left with a system with singularities at  $\eta = 0$  and  $p = 0$  due to the appearance of  $b$  and  $p$  on the denominators. To facilitate studying this system, we multiply the right-hand sides of the equations by  $\eta p$  using the so-called multiplication trick [20]; this is equivalent to a transformation of time  $t \rightarrow s$  given by  $\eta p ds = dt$ <sup>10</sup>. Whilst this step preserves orbits, it reverses time for  $\eta p < 0$ . Nonetheless, this does not concern us since we are studying the rod when slipping where  $\eta, p > 0$ .

After this multiplication step, we find

$$(2.26) \quad \mathbf{x}' = \mathbf{f}(\mathbf{x})$$

where

$$(2.27) \quad \mathbf{x} = (\eta, \varphi, \psi, \Psi, \theta, \Theta)^\top,$$

differentiation with respect to the new time is denoted by a dash and

$$(2.28) \quad \mathbf{f}(\mathbf{x}) = (f_\eta, f_\varphi, f_\psi, f_\Psi, f_\theta, f_\Theta)^\top$$

$$(2.29) \quad = \begin{pmatrix} \eta(-Q_1 b + A_1 p) \\ -Q_2 b + (A_2 - \eta \Psi)p \\ \eta p \Psi \\ \eta(-d_1 b + c_1 p) \\ \eta p \Theta \\ \eta(-d_2 b + c_2 p) \end{pmatrix}$$

The GB manifold ( $\{p(\theta, \varphi) = 0\} \cap \{b(\Psi, \Theta, \theta) = 0\}$ ) is a set of equilibria of the rescaled problem in (2.28). Let us then consider a point on the GB manifold, where  $\theta = \theta_{\text{GB}}$ ,  $\varphi = \varphi_{\text{GB}}$ ,  $\Psi = \Psi_{\text{GB}}$ ,  $\Theta = \Theta_{\text{GB}}$  (such that  $b(\Psi_{\text{GB}}, \Theta_{\text{GB}}, \theta_{\text{GB}}) = 0$  and  $p(\theta_{\text{GB}}, \varphi_{\text{GB}}) = 0$ ). We linearise (2.26) about this point to find

$$(2.30) \quad \begin{pmatrix} \delta \eta \\ \delta \varphi \\ \delta \psi \\ \delta \Psi \\ \delta \theta \\ \delta \Theta \end{pmatrix}' = \begin{pmatrix} 0 & \eta A_1 p_{,\varphi} & 0 & -\eta Q_1 b_{,\Psi} & \eta(A_1 p_{,\theta} - Q_1 b_{,\theta}) & -\eta Q_1 b_{,\Theta} \\ 0 & (A_2 - \eta \Psi) p_{,\varphi} & 0 & -Q_2 b_{,\Psi} & (A_2 - \eta \Psi) p_{,\theta} - Q_2 b_{,\theta} & -Q_2 b_{,\Theta} \\ 0 & \eta \Psi p_{,\varphi} & 0 & 0 & \eta \Psi p_{,\theta} & 0 \\ 0 & \eta c_1 p_{,\varphi} & 0 & -\eta d_1 b_{,\Psi} & \eta(c_1 p_{,\theta} - d_1 b_{,\theta}) & -\eta d_1 b_{,\Theta} \\ 0 & \eta \Theta p_{,\varphi} & 0 & 0 & \eta \Theta p_{,\theta} & 0 \\ 0 & \eta c_2 p_{,\varphi} & 0 & -\eta d_2 b_{,\Psi} & \eta(c_2 p_{,\theta} - d_2 b_{,\theta}) & -\eta d_2 b_{,\Theta} \end{pmatrix} \begin{pmatrix} \delta \eta \\ \delta \varphi \\ \delta \psi \\ \delta \Psi \\ \delta \theta \\ \delta \Theta \end{pmatrix}$$

<sup>10</sup>This multiplication trick shall be used frequently in what follows.

where  $(p, q, b, a) = \left( \frac{\partial p}{\partial q}, \frac{\partial b}{\partial q} \right)$ , the square matrix is evaluated on  $b = p = 0$ , (that is, at  $\theta = \theta_{\text{GB}}$ ,  $\varphi = \varphi_{\text{GB}}$ ,  $\Psi = \Psi_{\text{GB}}$ ,  $\Theta = \Theta_{\text{GB}}$ ) and  $\delta\eta$ ,  $\delta\varphi$ ,  $\delta\psi$ ,  $\delta\Psi$ ,  $\delta\theta$ , and  $\delta\Theta$  denote perturbations from a point on the GB manifold.

Then (2.30) can be written in the form

$$(2.31) \quad \delta\mathbf{x}' = \mathbf{J}\mathbf{x} = \underline{\mathbf{A}}\underline{\mathbf{B}}\delta\mathbf{x} = \left( \frac{\partial}{\partial(p, b)} \mathbf{f} \right) \left( \frac{\partial}{\partial\mathbf{x}^\top} (p, b)^\top \right) \delta\mathbf{x}$$

where  $\mathbf{J}$  is the Jacobian of  $\mathbf{f}(\mathbf{x})$  about  $\delta\mathbf{x} = \mathbf{0}$  and the matrices  $\underline{\mathbf{A}}$  and  $\underline{\mathbf{B}}$  are given by

$$(2.32) \quad \underline{\mathbf{A}} := \begin{pmatrix} f_{\eta, p} & f_{\eta, b} \\ f_{\varphi, p} & f_{\varphi, b} \\ f_{\psi, p} & f_{\psi, b} \\ f_{\Psi, p} & f_{\Psi, b} \\ f_{\theta, p} & f_{\theta, b} \\ f_{\Theta, p} & f_{\Theta, b} \end{pmatrix} = \begin{pmatrix} \eta A_1 & -\eta Q_1 \\ A_2 - \eta\Psi & -Q_2 \\ \eta\Psi & 0 \\ \eta c_1 & -\eta d_1 \\ \eta\Theta & 0 \\ \eta c_2 & -\eta d_2 \end{pmatrix}$$

and

$$(2.33) \quad \underline{\mathbf{B}} := \begin{pmatrix} p, \eta & p, \varphi & p, \psi & p, \Psi & p, \theta & p, \Theta \\ b, \eta & b, \varphi & b, \psi & b, \Psi & b, \theta & b, \Theta \end{pmatrix}$$

$$(2.34) \quad = \begin{pmatrix} 0 & p, \varphi & 0 & 0 & p, \theta & 0 \\ 0 & 0 & 0 & b, \Psi & b, \theta & b, \Theta \end{pmatrix}.$$

In order to understand the dynamics near  $b = p = 0$ , we must calculate the eigenvalues and eigenvectors of the Jacobian  $\mathbf{J} = \underline{\mathbf{A}}\underline{\mathbf{B}}$ . To do this we use the following result [9, Proposition 4.4.10].

**Lemma 2.1.** *If an  $m \times m$  matrix  $\mathbf{J}$  can be expressed as the matrix product of  $\mathbf{J} = \underline{\mathbf{A}}\underline{\mathbf{B}}$  (where  $\underline{\mathbf{A}}$  is an  $m \times n$  matrix,  $\underline{\mathbf{B}}$  is an  $n \times m$  matrix and  $m \geq n$ ), then the eigenvalues of  $\mathbf{J}$  are the  $n$  eigenvalues of  $\underline{\mathbf{K}} = \underline{\mathbf{B}}\underline{\mathbf{A}}$  and  $m - n$  zero eigenvalues. If  $\lambda$  is an eigenvalue of  $\underline{\mathbf{K}}$ , then it is also an eigenvalue of the  $\mathbf{J}$ .*

So in (2.31), since  $m = 6$ , the eigenvalues of  $\mathbf{J} = \underline{\mathbf{A}}\underline{\mathbf{B}}$  are given by  $n = 2$  eigenvalues of  $\underline{\mathbf{K}} = \underline{\mathbf{B}}\underline{\mathbf{A}}$ , plus  $m - n = 4$  zero eigenvalues. A straightforward calculation shows that  $\underline{\mathbf{K}}$  is given by

$$(2.35) \quad \underline{\mathbf{K}} = \begin{pmatrix} \eta\Theta p, \theta + (A_2 - \eta\Psi)p, \varphi & -Q_2 p, \varphi \\ \eta(\Theta b, \theta + c_1 b, \Psi + c_2 b, \Theta) & -\eta(d_1 b, \Psi + d_2 b, \Theta) \end{pmatrix}$$

evaluated on  $b = p = 0$ . This is important as it shows that the local dynamics are dominated by the dynamics corresponding to this Jacobian<sup>11</sup>.

<sup>11</sup>This useful structure results from the form of the dependence of (2.28) on terms  $b$  and  $p$ .

We shall now show that  $\underline{\mathbf{K}}$  governs the rod dynamics in the  $(p, b)$ -plane near  $b = p = 0$ , the GB manifold, since for  $\mathbf{y} = (p, b)^\top$ ,

$$(2.36) \quad \mathbf{y}' = \underline{\mathbf{K}} \mathbf{y}$$

to leading order.

Let  $\mathbf{y} = (p, b)^\top$  be the variations in  $(p, b)^\top$ . Since  $\underline{\mathbf{B}} = \frac{\partial}{\partial \mathbf{x}}(p, b)|_{\delta \mathbf{x}=\mathbf{0}}$ , we have  $\mathbf{y} = \underline{\mathbf{B}} \delta \mathbf{x}$  to leading order. Therefore

$$(2.37) \quad \mathbf{y}' = \underline{\mathbf{B}} \delta \mathbf{x}' = \underline{\mathbf{B}} \underline{\mathbf{A}} \underline{\mathbf{B}} \delta \mathbf{x} = \underline{\mathbf{K}} \mathbf{y}.$$

Hence  $\underline{\mathbf{K}}$  is the Jacobian of the rod dynamics in the  $(p, b)$ -plane about a point on the GB manifold.

**Remark 2.2.** *This finding that the matrix  $\underline{\mathbf{B}} \underline{\mathbf{A}} = \underline{\mathbf{K}}$  is equivalent to the Jacobian of  $(p, b)$ , and the ability to decompose (2.30) into matrices  $\underline{\mathbf{A}}$  and  $\underline{\mathbf{B}}$ , is not a coincidence. This results from the form of the dependence of (1.23) on the contact forces, and hence the form of the dependence of the desingularised equations (2.28), on  $p$  and  $b$ .*

Using expressions in (1.24) for the coefficients  $Q_i, A_i, d_i, c_i$ , for  $(i = 1, 2)$ , we find that

$$(2.38) \quad \underline{\mathbf{K}} \equiv \begin{pmatrix} K_{11} & K_{12} \\ K_{21} & K_{22} \end{pmatrix} = \begin{pmatrix} \alpha \mu \cos^2 \theta \cos^2 \varphi + \eta [\Theta (\tan \theta - (1 + \alpha) \cot \theta) & (1 + \alpha) \alpha \mu \cos^2 \theta \cos^2 \varphi \\ -\Psi \alpha \mu \sin \theta \cos \theta \cos \varphi & \\ \eta \Theta \cot \theta & \eta (2 \Psi \alpha \mu \sin \theta \cos \theta \cos \varphi - 2 \Theta \tan \theta) \end{pmatrix}$$

and hence

$$(2.39) \quad \det \underline{\mathbf{K}} = \eta \alpha \cos^2 \theta \cos^2 \varphi \left[ \Theta (-2 \tan \theta - (1 + \alpha) \cot \theta) + 2 \Psi \alpha \mu \sin \theta \cos \theta \cos \varphi \right] \\ + \eta^2 \left[ \Theta^2 (2(1 + \alpha) - 2 \tan^2 \theta) + \Theta \Psi \alpha \mu \sin \theta \cos \theta \cos \varphi (4 \tan \theta - 2(1 + \alpha) \cot \theta) \right. \\ \left. - 2 \Psi^2 (\alpha \mu \sin \theta \cos \theta \cos \varphi)^2 \right].$$

We note the following group symmetry:

$$(2.40) \quad \underline{\mathbf{K}}|_{\varphi=\bar{\varphi}, \Psi=\bar{\Psi}} \equiv \underline{\mathbf{K}}|_{\varphi=-\pi-\bar{\varphi}, \Psi=-\bar{\Psi}}$$

and the absence of any symmetry in  $\Theta$  when  $\theta \in [0, \pi/2]$ .

Locally to the GB manifold,  $\mathbf{y} = (p, b)^\top = \mathbf{0}$ , the dynamics of the rod are approximately governed by (2.36) and hence described by the eigenvalues  $\lambda_\pm$  and eigenvectors  $\mathbf{e}_\pm$  of  $\underline{\mathbf{K}}$ .



Let us briefly recap the properties of  $\underline{\mathbf{K}}$  for the planar (2D) problem, where the GB manifold reduces to the four points  $P^\pm, Q^\pm$ , see Figure 2.4 and [38, fig.2]. From (2.38) with  $\varphi = -\frac{\pi}{2}$  we have

$$(2.41) \quad \underline{\mathbf{K}}_{\varphi=-\frac{\pi}{2}} \equiv \underline{\mathbf{K}}_{2D} = \eta\Theta \begin{pmatrix} \tan \theta - (1 + \alpha) \cot \theta & 0 \\ \cot \theta & -2 \tan \theta \end{pmatrix},$$

evaluated at  $\theta = \theta_{1,2}$  from (2.8). The eigenvalues  $\lambda_{1,2} = \lambda_\pm|_{\varphi=-\frac{\pi}{2}}$  and associated eigenvectors  $\mathbf{e}_{1,2} = \mathbf{e}_\pm|_{\varphi=-\frac{\pi}{2}}$  of  $\underline{\mathbf{K}}_{2D}$  are

$$(2.42) \quad \{\lambda_1, \lambda_2\} = \{\eta\Theta(\tan \theta - (1 + \alpha) \cot \theta), -2\eta\Theta \tan \theta\}$$

and

$$(2.43) \quad \{\mathbf{e}_1, \mathbf{e}_2\} = \left\{ \begin{pmatrix} 3 \tan^2 \theta - (1 + \alpha) \\ 1 \end{pmatrix}, \begin{pmatrix} 0 \\ 1 \end{pmatrix} \right\}.$$

It can be shown that  $\lambda_1 = \eta\Theta(\tan \theta - (1 + \alpha) \cot \theta) = 0$  when  $\mu = \mu_P$  and that  $e_{1,1} = 3 \tan^2 \theta - (1 + \alpha) = 0$  when  $\mu = \mu_C$ . In summary, for the 2D problem, with respect to the new time introduced in (2.26),

- For  $\mu \in [0, \mu_P)$ , there is no paradox.
- For  $\mu \in (\mu_P, \mu_C)$ :
  - $P^+$  is a stable node and  $P^-$  is an unstable node;  $\mathbf{e}_1$  lies in the first and third quadrants of the  $(p, b)$  plane and  $\mathbf{e}_2$  lies on the  $b$ -axis.
  - $Q^\pm$  are both saddles.
- For  $\mu > \mu_C$ :
  - $P^+$  is a stable node and  $P^-$  is an unstable node;  $\mathbf{e}_1$  in the second and fourth quadrants of the  $(p, b)$  plane and  $\mathbf{e}_2$  lies on the  $b$ -axis.
  - $Q^\pm$  are both saddles.

Mathematically we see that  $\mu = \mu_C$  corresponds to a change in the orientation of  $\mathbf{e}_1$  relative to  $\mathbf{e}_2$ .

The 2D problem is the  $\varphi = -\frac{\pi}{2}$  section of the 3D problem with  $\Psi = 0$  (Figure 2.4), so as we move around the GB manifold, as in Figure 2.21, nodes at  $P^\pm$  must undergo a bifurcation to become saddles at  $Q^\pm$ , for any value of  $\mu > \mu_P$ .

To fully understand the dynamics of the 3D problem, we will need a combination of analysis and numerical methods. We show one numerical example in Figure 2.23, where we set  $\eta = 1$ ,  $\Psi = 0$ ,  $\alpha = 3$  and  $\mu = 1.4$ . Each figure shows the eigenvectors<sup>12</sup> in the  $(p, b)$ -plane at selected

---

<sup>12</sup>The eigenvectors are shown in the new time introduced in (2.26). Orbits in the first, second and third quadrants of Figures 2.23 to 2.26 are artefacts.

points around the GB manifold with  $\Theta > 0$  (shown in Figure 2.4b). The shading corresponds to that of Figure 2.4a. Figure 2.23b shows a stable node (the point  $P^+$  in Figure 2.4a). The strong direction (in blue) is aligned with the  $b$ -axis and the weak direction (in red) lies in the first and third quadrants. Figure 2.23f shows a saddle (the point  $Q^+$  in Figure 2.4a).

As we move through Figure 2.23, we move around the GB manifold from  $\theta = \theta_1$  to  $\theta = \theta_2$ . At a certain point, shown in Figure 2.23d, the eigenvalue  $\lambda_+$  passes through zero, as the stable node becomes a saddle. At this point, the system is nonhyperbolic.

In each of Figures 2.23c to 2.23e, the orbit that approaches the GB manifold along the (strong) stable manifold at that point acts as a separatrix<sup>13</sup> between orbits that reach the inconsistent region and those that lift off.

We can now see how the 2D picture (Figure 2.4a) fits into these results. Moving around the GB manifold from Figure 2.23b, the eigenvector frame distorts away from the  $b$ -axis, allowing movement from the slipping region (in yellow) to the inconsistent region (in lime). After the bifurcation (Figure 2.23d), the eigenvector frame distorts back towards the  $b$ -axis, eventually giving Figure 2.23f, the point  $Q^+$  in Figure 2.4a, where crossing  $p = 0$  is no longer possible.

We show another numerical example in Figure 2.24, where  $\eta = 1$ ,  $\Psi = 0$ ,  $\alpha = 3$  and now  $\mu = 1.7 > \mu_C = \frac{8}{3\sqrt{3}} \approx 1.5396$ . Figures 2.24b and 2.24f correspond to the 2D problem. In Figure 2.24b, the strong direction (in blue) now lies in the first and third quadrants, with the weak direction (in red) aligned with the  $b$ -axis. Moving around the GB manifold from Figure 2.24b, the eigenvector frame distorts, with the weak (red) eigenvector moving off the  $b$ -axis, into the first and third quadrants, allowing movement from the slipping region (in yellow) to the inconsistent region (in lime). After the bifurcation (Figure 2.24d), the eigenvector frame distorts even more, with the strong (blue) eigenvector eventually aligning itself with the  $b$ -axis, where crossing the line  $p = 0$  is no longer possible. The weak (red) eigenvector remains in the first and third quadrants. In each of Figures 2.24c to 2.24e, the orbits that approach along the (strong) stable manifold of points along the GB manifold act as a separatrix between orbits that reach the inconsistent region and those that lift off.

Note that Figures 2.23b and 2.24b are the one qualitatively different pair between Figures 2.23 and 2.24, which suggests that the critical value  $\mu_C$  maybe be less significant in the 3D problem.

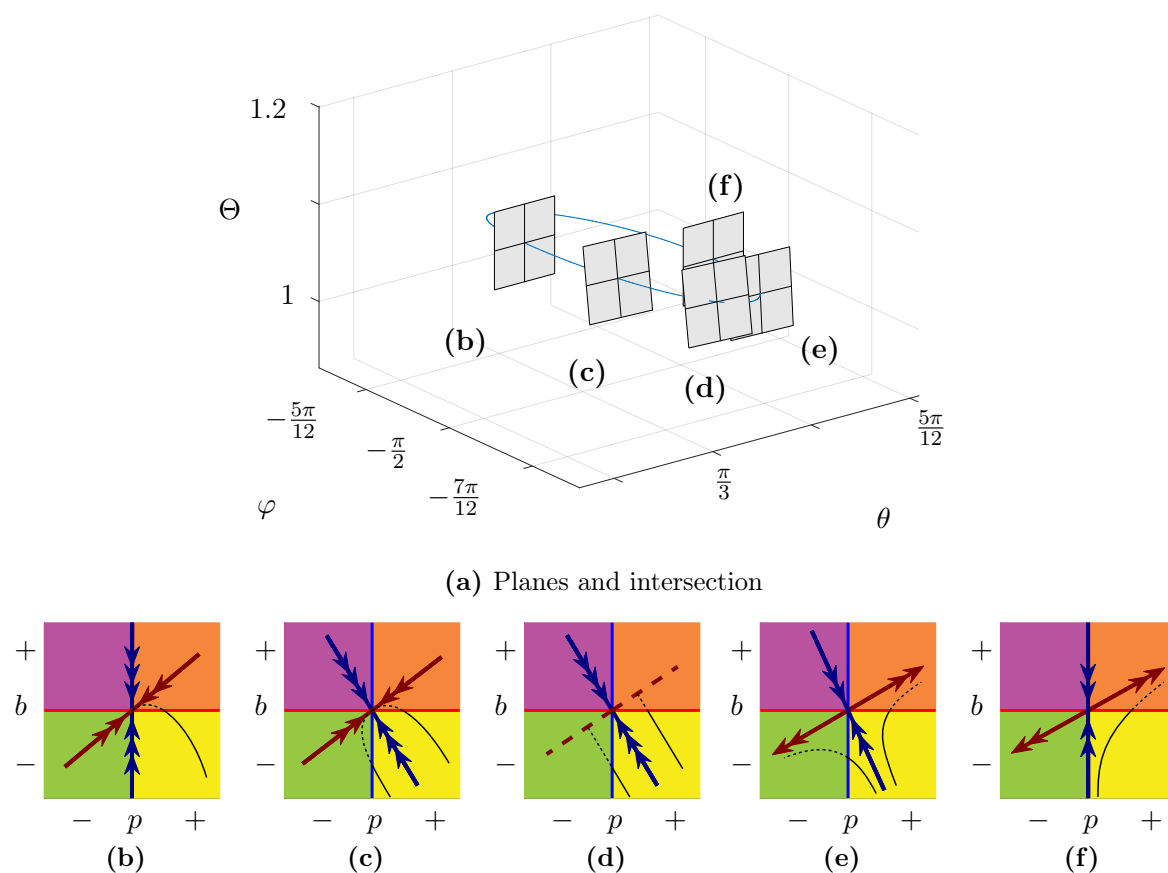
Figures 2.23d and 2.24d show bifurcations on the GB manifold. In the following section we embark on a general study of such bifurcations. However, we shall first give some general statements about the generic dynamics local to the GB manifold.

**Theorem 2.1.** *Local to the GB manifold but for  $\varphi \neq -\frac{\pi}{2}$ :*

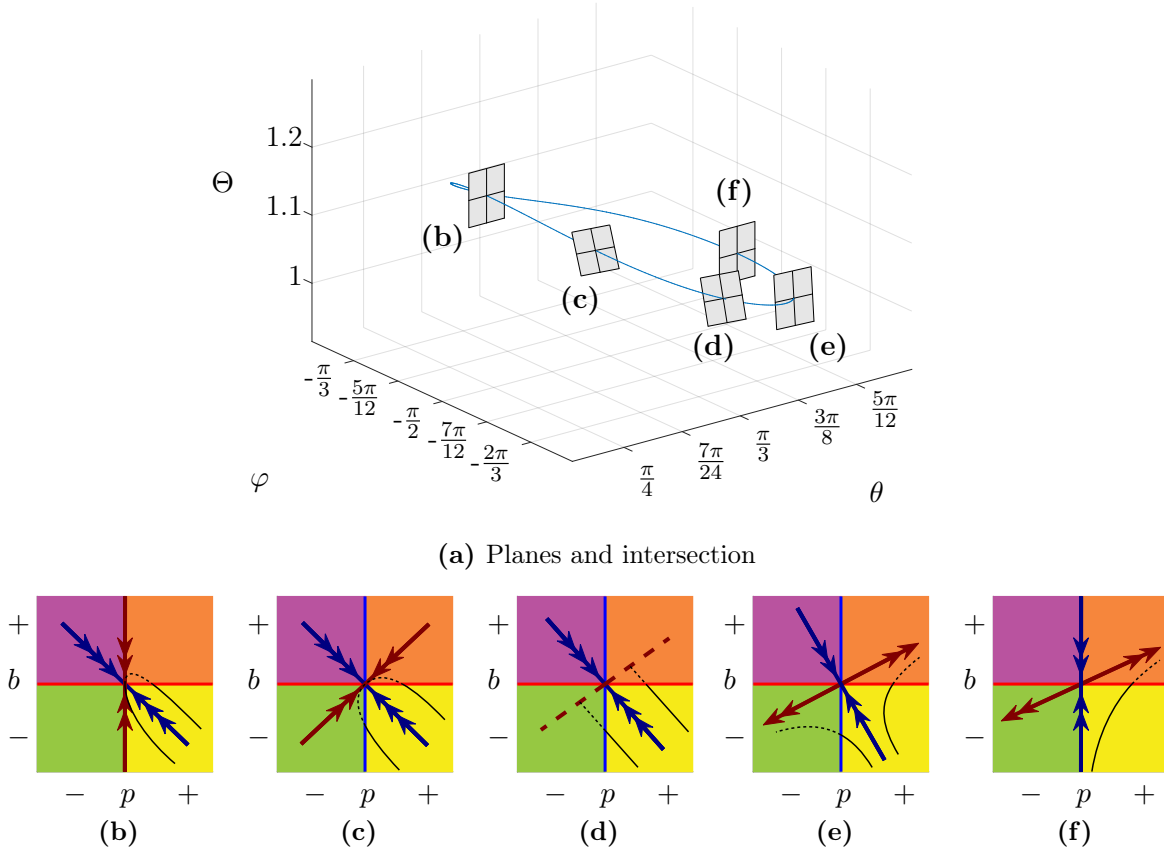
1. *For  $\Theta > 0$ , there is a separatrix between orbits that reach the inconsistent paradox and those that lift off, and there are three generic phase portraits in  $(p, b)$  space (shown in Figure 2.26).*

---

<sup>13</sup>We use the term separatrix to mean an orbit, or set thereof, which locally separates orbits that result in different behaviours.



**Figure 2.23:** Dynamics in the  $(p, b)$ -plane for the 3D Painlevé paradox for  $\eta = 1$ ,  $\Psi = 0$ ,  $\alpha = 3$  and  $\mu = 1.4$  close to the GB manifold  $b = p = 0$  when  $\Psi = 0$ . The shading of each region corresponds to that of Figure 2.4a: slipping (yellow), lift-off (orange), indeterminate (purple), inconsistent (lime). Each subfigure shows eigenvectors at selected points around the GB manifold (see Figure 2.4b), with coordinates  $(\theta, \varphi, \Psi, \Theta) = (\theta_{\text{GB}}, \varphi_{\text{GB}}, 0, \Theta_{\text{GB}})$ , where  $\Theta_{\text{GB}} = \sqrt{\csc \theta_{\text{GB}}}$  from (1.25):  $(\theta_{\text{GB}}, \varphi_{\text{GB}})$  are given by **(b)**  $(\theta_1, -\frac{\pi}{2}) = (0.9702, -1.5708)$  corresponding to  $P^+$  in Figure 2.4a, **(c)**  $(1.0094, -1.7832)$ , **(d)**  $(1.0953, -1.8793)$ , **(e)**  $(1.1872, -1.7978)$  and **(f)**  $(\theta_2, -\frac{\pi}{2}) = (1.2209, -1.5708)$ , corresponding to  $Q^+$  in Figure 2.4a. The eigenvectors are shown in the new time introduced in (2.26) which reverses  $t$  in  $p < 0$ . They are not drawn to scale.

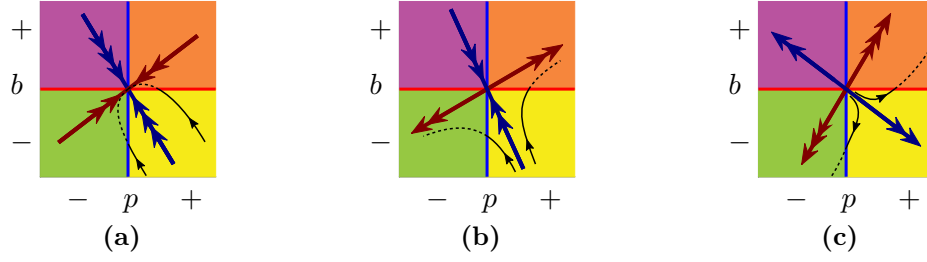


**Figure 2.24:** As Figure 2.23, for  $\mu = 1.7$ . Here  $(\theta_{\text{GB}}, \varphi_{\text{GB}})$  are given by (b)  $(\theta_1, -\frac{\pi}{2}) = (0.7692, -1.5708)$ , (c)  $(0.8517, -1.9969)$ , (d)  $(1.0227, -2.2143)$ , (e)  $(1.2562, 2.1107)$  and (f)  $(\theta_2, -\frac{\pi}{2}) = (1.3333, -1.5708)$ .

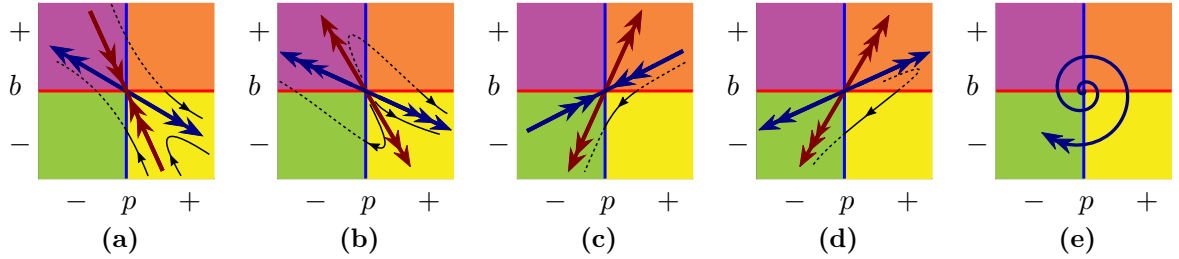
2. For  $\Theta < 0$ , there are 5 generic phase portraits in  $(p, b)$  space (shown in Figure 2.26), and depending on the local phase portrait either the rod remains slipping or reaches inconsistency locally. Lift-off is not possible and the GB manifold is unstable.

**Proof.** Consider the Jacobian  $\mathbf{K}$  from (2.38), with eigenvectors  $\lambda_{\pm}$  and eigenvectors  $\mathbf{e}_{\pm}$  given by

$$(2.44) \quad \mathbf{e}_{\pm} := \left( \frac{K_{12}}{\lambda_{\pm} - K_{11}}, 1 \right)^{\top}.$$



**Figure 2.25:** Possible dynamics in  $(p, b)$  space local to the GB manifold for  $\Theta > 0$ . In (a), the point on the GB manifold is a stable node where the strong eigenvector is in the fourth quadrant and the corresponding strong stable manifold acts as a separatrix between orbits that reach the inconsistent region and those that lift off. In (b), the point on the GB manifold is a saddle where stable eigenvector is in the fourth quadrant and the corresponding stable manifold acts as a separatrix between orbits that reach the inconsistent region and those that lift off. In (c), the point on the GB manifold is an unstable node where the weakly unstable eigenvector is in the fourth quadrant and the corresponding weakly unstable manifold acts as a separatrix between orbits that reach the inconsistent region and those that lift off.



**Figure 2.26:** Possible dynamics in  $(p, b)$  space local to the GB manifold for  $\Theta < 0$ . In (a) and (b), orbits either remain slipping, following the (strongly) unstable manifold of the GB manifold in the fourth quadrant, or reach the inconsistent region, tending to the (strongly) unstable manifold of the GB manifold in the second quadrant. In (c)-(e) all local orbits tend to reach inconsistency.

The product of the first component of the eigenvectors is

$$\begin{aligned}
 \left( \frac{K_{12}}{\lambda_+ - K_{11}} \right) \left( \frac{K_{12}}{\lambda_- - K_{11}} \right) &= \frac{K_{12}^2}{\lambda_+ \lambda_- - K_{11}(\lambda_1 + \lambda_2) + K_{11}^2} \\
 &= \frac{K_{12}^2}{(K_{11}K_{22} - K_{12}K_{21}) - K_{11}(K_{11} + K_{22}) + K_{11}^2} \\
 (2.45) \qquad \qquad \qquad &\equiv -\frac{K_{12}}{K_{21}}.
 \end{aligned}$$

1. For  $\Theta > 0$ , the product (2.45) is negative, from (2.38) and hence the eigenvectors are in different quadrants. Furthermore, from the signs of the off-diagonal elements of  $\mathbf{K}$ , we can infer that a point on the GB manifold is either a stable node with the strong eigenvector in the fourth quadrant (see Figure 2.25a), a saddle with the stable eigenvector in the fourth

quadrant (see Figure 2.25b), or an unstable node with the weakly unstable eigenvector in the fourth quadrant (see Figure 2.25c). Each of the cases in Figures 2.25a to 2.25c can be realised.

2. For  $\Theta < 0$ , the product (2.45) is positive, and hence the eigenvectors (if real) are in the same quadrant. Furthermore, eliminating  $\Psi$  from  $\underline{\mathbf{K}}$ , we find

$$(2.46) \quad K_{11} = +2\alpha\mu \cos^2 \theta \cos^2 \varphi - 2(1 + \alpha)\eta\Theta \cot \theta - \text{tr}(\underline{\mathbf{K}}),$$

$$(2.47) \quad K_{22} = -2\alpha\mu \cos^2 \theta \cos^2 \varphi + 2(1 + \alpha)\eta\Theta \cot \theta + 2\text{tr}(\underline{\mathbf{K}}).$$

where  $\text{tr}(\underline{\mathbf{K}})$  is the trace of  $\underline{\mathbf{K}}$ . Hence, the determinant of  $\underline{\mathbf{K}}$  (2.39) can be written as the following polynomial in  $\text{tr}(\underline{\mathbf{K}})$ :

$$(2.48) \quad \begin{aligned} \det(\underline{\mathbf{K}}) &= K_{11}K_{22} - K_{12}K_{21} \\ &= C_2 \text{tr}(\underline{\mathbf{K}})^2 + C_1 \text{tr}(\underline{\mathbf{K}}) + C_0 \end{aligned}$$

where

$$C_2 := -2,$$

$$C_1 := 6(\alpha\mu \cos^2 \theta \cos^2 \varphi - (1 + \alpha)\eta\Theta \cot \theta),$$

$$C_0 := (-4\eta^2\Theta^2(1 + \alpha)^2 \cot^2 \theta + 7\eta\Theta(1 + \alpha)\alpha\mu \cot \theta \cos^2 \theta - 4\alpha^2\mu^2 \cos^4 \theta \cos^4 \varphi).$$

We can show that there are no negative roots of this polynomial in  $\text{tr}(\underline{\mathbf{K}})$  when  $\Theta < 0$ , using Descartes' rule of signs and so stable nodes and foci are not possible. From the signs of the off-diagonal entries of  $\underline{\mathbf{K}}$ , we can deduce that only the phase portraits in Figure 2.26 are possible. Hence lift-off is not possible locally. Each case in Figures 2.26a to 2.26e can be realised. ■

**Corollary 2.1.** *For  $\mu > \mu_P$ , there exists an open set of initial conditions that reach the inconsistent region from slipping in finite time.*

**Proof.** Follows from Theorem 2.1. ■

In Figures 2.26a and 2.26b, orbits either follow the (strongly) unstable manifold of the GB manifold in the fourth quadrant, and remain slipping, or tend to the (strongly) unstable manifold of the GB manifold in the second quadrant, reaching the inconsistent region. In Figures 2.26c to 2.26e, all orbits reach the inconsistent region, whether tending to a (strongly) unstable manifold in the third quadrant (Figures 2.26c and 2.26d) or rotating round the GB manifold (locally a set of unstable foci Figure 2.26e).

In Figures 2.25a, 2.25b and 2.26a, there exist unique orbits which reach the GB manifold. These types of orbit have been shown to be of interest [64].

### 2.10.1 Zero eigenvalue

Figures 2.23 and 2.24 show that the dynamics of the 3D problem is governed, not only by changes in the topology of the GB manifold  $b = p = 0$ , but also by changes in the sign of the eigenvalues.

At least one of the eigenvalues vanishes when  $\det \underline{\mathbf{K}} = \lambda_+ \lambda_- = K_{11}K_{22} - K_{12}K_{21} = 0$ . Hence, from (2.39),  $\det \underline{\mathbf{K}} = 0$  when

$$(2.49) \quad A\Psi^2 + B\Psi\Theta + \Gamma\Psi = \Delta\Theta^2 + E\Theta$$

where

$$(2.50) \quad \begin{aligned} A &:= -2\eta\alpha^2\mu^2 \tan^3 \theta \cos^2 \varphi, \\ B &:= 2\eta\alpha\mu \cos \varphi \tan \theta (1 + \tan^2 \theta) [2 \tan^2 \theta - (1 + \alpha)], \\ \Gamma &:= 2\alpha^2\mu^2 \cos^3 \varphi \tan^2 \theta, \\ \Delta &:= 2\eta \tan \theta (1 + \tan^2 \theta)^2 [\tan^2 \theta - (1 + \alpha)], \\ E &:= \alpha\mu \cos^2 \varphi (1 + \tan^2 \theta) [2 \tan^2 \theta + (1 + \alpha)]. \end{aligned}$$

Equations (2.49) and (2.50) must be evaluated on the GB manifold  $b = p = 0$ . The term  $p(\theta, \varphi)$  is independent of  $\Psi$  and  $\Theta$  (1.26), and  $b(\Psi, \Theta, \theta) = 0$  can be written as

$$(2.51) \quad M\Psi^2 + \Theta^2 = N$$

where

$$(2.52) \quad \begin{aligned} M &:= \frac{1}{1 + \tan^2 \theta}, \\ N &:= \frac{(1 + \tan^2 \theta)^{\frac{1}{2}}}{\tan \theta} \end{aligned}$$

(1.25). In  $(\Psi, \Theta)$ -space, (2.49) is a conic, depending on the sign of the discriminant  $B^2 + 4A\Delta$ , and (2.51) is an ellipse. So in general, we can expect 0, 2 or 4 solutions of these equations, corresponding to intersections of the two conics. Eliminating  $\Theta$  from (2.49) and (2.51) gives a quartic in  $\Psi$ :

$$(2.53) \quad \sum_{i=0}^4 C_i \Psi^i = 0,$$

where

$$(2.54) \quad \begin{aligned} C_4 &:= (A + M\Delta)^2 + MB^2, \\ C_3 &:= 2[A\Gamma + M(\Gamma\Delta - EB)], \\ C_2 &:= \Gamma^2 - 2\Delta N(A + M\Delta) - NB^2 + ME^2, \\ C_1 &:= 2N(EB - \Gamma\Delta), \\ C_0 &:= N(N\Delta^2 - E^2). \end{aligned}$$

Since the  $C_i$  are all real, we do indeed have either 0, 2 or 4 real roots for  $\Psi$ , which will depend on  $\eta$  in general.

A theoretical analysis of (2.53) becomes unwieldy very quickly. In order to progress, we focus on the case  $\Psi = 0$  and on the behaviour near  $\mu = \mu_P$  for  $\Psi \neq 0$ .

### 2.10.2 The case $\Psi = 0$

When  $\Psi = 0$ , we show that unstable foci can exist on the GB manifold, as well as nodes and saddles, but only in  $\Theta < 0$ . From (2.38), a focus occurs when  $(K_{11} - K_{22})^2 + 4K_{12}K_{21} < 0$ . Setting  $\Psi = 0$  in (2.38), we see that

$$(2.55) \quad (K_{11} - K_{22})^2 + 4K_{12}K_{21} = R_2\Theta^2 + R_1\Theta + R_0$$

where

$$(2.56) \quad \begin{aligned} R_2 &:= \eta^2 [3 \tan \theta - (1 + \alpha) \cot \theta]^2, \\ R_1 &:= 2\eta\alpha\mu \cos^2 \theta \cos^2 \varphi [3 \tan \theta + (1 + \alpha) \cot \theta], \\ R_0 &:= \alpha^2 \mu^2 \cos^4 \theta \cos^4 \varphi. \end{aligned}$$

The quadratic (2.55) is always positive when  $\Theta > 0$ , and so foci do not occur on the GB manifold in this case.

But it is possible for  $(K_{11} - K_{22})^2 + 4K_{12}K_{21} < 0$  for  $\mu > \mu_C$  when  $\Theta \in (\Theta_-, \Theta_+)$  where

$$(2.57) \quad \Theta_{\pm} := -\frac{\alpha\mu \cos^2 \theta \cos^2 \varphi}{\eta[\sqrt{3 \tan \theta} \pm \sqrt{(1 + \alpha) \cot \theta}]^2} < 0.$$

In this case the real part of the corresponding eigenvalue is given by  $\frac{1}{2}(K_{11} + K_{22})$  which is always positive from (2.38) for  $\Theta < 0$ . So any focus that exists for  $\Psi = 0$  is always unstable.

Numerical results show that unstable foci can also occur in  $\Theta < 0$  when  $\Psi \neq 0$ , see section 2.11.

When  $\Psi = 0$ , (2.53) reduces to

$$(2.58) \quad C_0 = 0 \iff N\Delta^2 - E^2 = 0,$$

since  $N \neq 0$  in general<sup>14</sup>. After a lengthy calculation, (2.58) reduces to

$$(2.59) \quad \alpha\mu \cos^2 \varphi = \pm 2\eta \tan^{\frac{1}{2}} \theta (1 + \tan^2 \theta)^{\frac{5}{4}} \frac{[(1 + \alpha) - \tan^2 \theta]}{[(1 + \alpha) + 2 \tan^2 \theta]}$$

where  $\pm$  corresponds to  $\Theta \gtrless 0$ . We use (2.59) as a check on our numerical results in section 2.11.

<sup>14</sup> $N = 0$  corresponds to  $\theta = \frac{\pi}{2}$ , the case of the vertical rod, which we have excluded from our analysis.



### 2.10.3 Behaviour near $\mu = \mu_P$

We consider (2.53) near  $\mu = \mu_P = \frac{2}{\alpha}\sqrt{1+\alpha}$ . From Figure 2.18a, we can see that any perturbation analysis will tell us about bifurcations in the dynamics on the GB manifold for  $\Psi \lesssim \Psi_P$ , where  $\Psi_P$  is given in (2.23).

At  $\mu = \mu_P$  we have  $\varphi = -\frac{\pi}{2}$  and  $\tan \theta_P = \sqrt{1+\alpha}$ . Let us take

$$(2.60) \quad \begin{aligned} \mu &= \mu_P(1 + \varepsilon^2 \hat{\mu}) = \frac{2}{\alpha}\sqrt{1+\alpha}(1 + \varepsilon^2 \hat{\mu}), \\ \varphi &= -\frac{\pi}{2} + \varepsilon \hat{\varphi}, \\ \theta_{\pm} &= \theta_P + \varepsilon \hat{\theta}_{\pm}, \end{aligned}$$

where  $\varepsilon \ll 1$  and  $\hat{\mu} \geq 0$  since there is no paradox for  $\mu < \mu_P$ . Then

$$(2.61) \quad \tan \theta_{\pm} \approx \tan \theta_P + \varepsilon \hat{\theta}_{\pm}(1 + \tan^2 \theta_P) = \sqrt{1+\alpha} + (2+\alpha)\varepsilon \hat{\theta}_{\pm}$$

and hence from (2.5) we have

$$(2.62) \quad \hat{\theta}_{\pm} = \pm \frac{\sqrt{1+\alpha}}{2+\alpha} \sqrt{2\hat{\mu} - \hat{\varphi}^2}.$$

In addition, we note that  $\cos \varphi = \cos(-\frac{\pi}{2} + \varepsilon \hat{\varphi}) \approx \varepsilon \hat{\varphi}$ .

So now we can obtain the leading order terms in the coefficients  $A, B, \Gamma, \Delta, E$  of (2.50) and hence in the coefficients  $C_i$  of (2.53). After a lengthy calculation we find, to leading order, that (2.53) becomes

$$(2.63) \quad \sum_{i=0}^4 C_i^{\varepsilon} \Psi^i = 0,$$

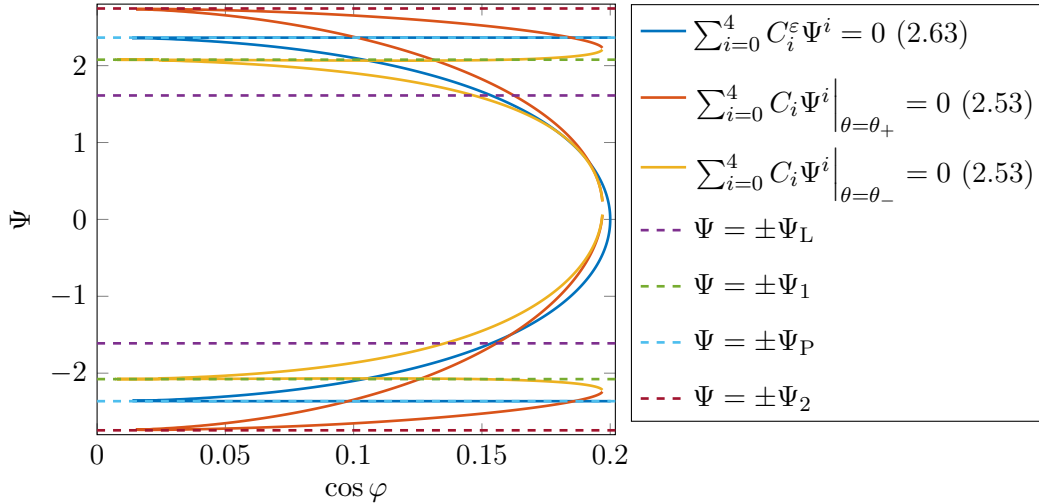
where

$$(2.64) \quad \begin{aligned} C_4^{\varepsilon} &:= (1+\alpha)^2[2(2+\alpha)\hat{\mu} - \hat{\varphi}^2], \\ C_3^{\varepsilon} &:= 0, \\ C_2^{\varepsilon} &:= -(1+\alpha)^{\frac{3}{2}}(2+\alpha)^{\frac{3}{2}}[4(2+\alpha)\hat{\mu} - (3+\alpha)\hat{\varphi}^2], \\ C_1^{\varepsilon} &:= 0, \\ C_0^{\varepsilon} &:= (1+\alpha)(2+\alpha)^4[2\hat{\mu} - \hat{\varphi}^2]. \end{aligned}$$

In Figure 2.27, we show agreement between (2.53) and (2.63) for  $\varepsilon^2 \hat{\mu} = 0.01$  when  $\alpha = 3$ , corresponding to mechanism II, Figure 2.17. There are several points to note. From the group symmetry property (2.40), we plot results for  $\cos \varphi > 0$  only. For  $|\Psi| < \Psi_L = 1.6119$ , the perturbation analysis (2.63) in blue is in good agreement with the exact results (2.53) in red and yellow, for this type (3) behaviour<sup>15</sup>.

<sup>15</sup>From (2.63), when  $\Psi = 0$ , we have simply  $C_0^{\varepsilon} = 0 \implies \hat{\mu} = \frac{1}{2}\hat{\varphi}^2$  and so  $\varepsilon \hat{\varphi} \approx \pm 0.1414 \approx \cos \varphi$ , giving symmetrically placed bifurcations around  $\varphi = -\frac{\pi}{2}$ .

Since here  $\mu = 1.01\mu_P \approx 1.3467$ , we have that  $\Psi_1 = 2.1526$ ,  $\Psi_2 = 2.6220$ . In Figure 2.27, for  $\Psi_L < |\Psi| < \Psi_1$ , we have type ④ behaviour. The positions of the bifurcations get closer to  $\varphi = -\frac{\pi}{2}$ , as the topology of the GB manifold is about to change. Here the agreement between (2.63) and (2.53) is not so good. For  $\Psi_1 < |\Psi| < \Psi_2$ , agreement is poor, as the topology of the GB manifold has completely changed.



**Figure 2.27:** Comparison of (2.53) and (2.63) for  $\varepsilon^2\hat{\mu} = 0.02$ ,  $\eta = 1$ , and  $\alpha = 3$ . This figure demonstrates that the approximation breaks down for larger  $\Psi$ , when the topology changes.

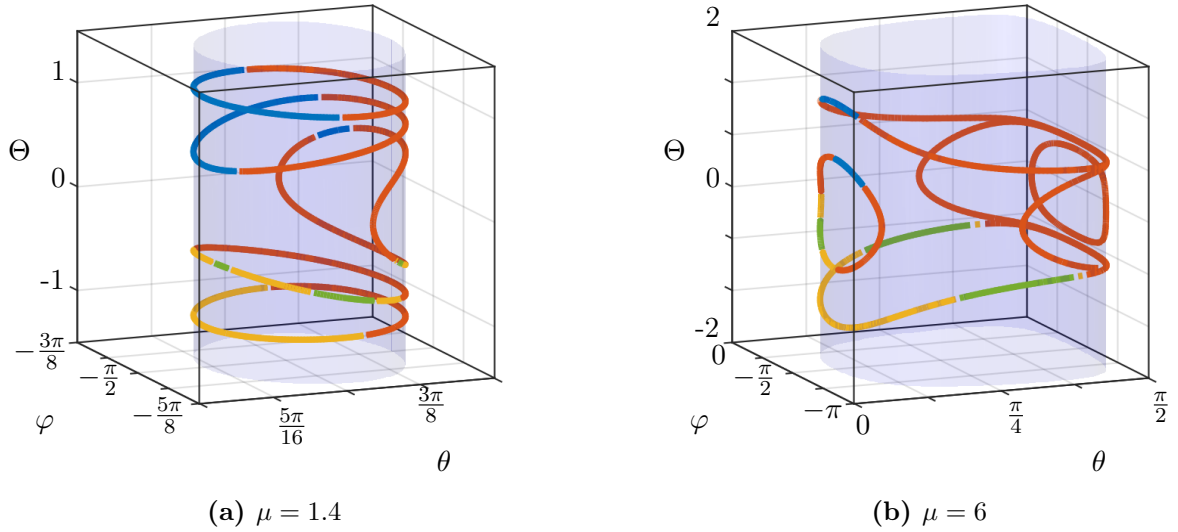
## 2.11 Putting it all together

In section 2.6, we saw the importance of  $\Psi$  in the topology of the GB manifold (to the extent that it does not exist for  $|\Psi| > \Psi_2$ ). In section 2.10 we saw how the dynamics can vary on the GB manifold. Here, we put both these effects together to provide a full picture of the geometry of the 3D Painlevé paradox.

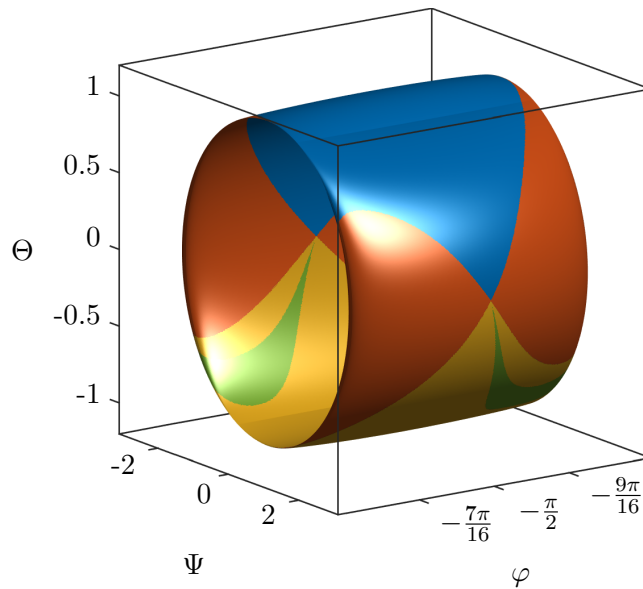
In Figure 2.28, we see the effect the increase in  $\Psi$  has on the dynamics when  $\alpha = 3$  for two values of  $\mu$ . The position of the zeros of  $\det \mathbf{K}$  around the GB manifold is a strong function of  $\Psi$ . We demonstrate this asymmetry in another way in Figure 2.30, for  $\alpha = 3$ ,  $\mu = 1.7$  and  $\eta = 10$ , where  $\Psi_P = 2.3644$  and  $\Psi_L = 1.6119$ .

In Figure 2.31 we show the eigenvectors around the GB manifold when  $\alpha = 3$ ,  $\mu = 1.7$  and  $\eta = 10$  for the case  $\Psi = 1.0620$  from Figure 2.30. There are four critical points, labelled **(d)**, **(h)**, **(j)** and **(l)**. Since  $\Psi \neq 0$ , there is no symmetry about  $\varphi = -\pi/2$  and hence we show eigenvectors for  $\varphi \geq -\pi/2$ . In every case, except **(b)** and **(f)** where  $\varphi = -\pi/2$ , trajectories in the slipping region (in yellow) can enter the inconsistent region (in lime).

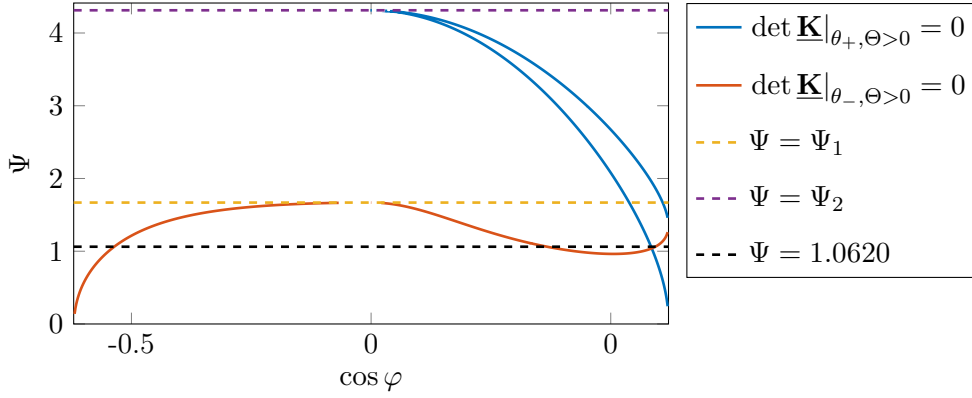
Using numerical methods, Champneys and Várkonyi [106] found that trajectories are able to reach  $p = 0$  away from  $b = 0$  in for the 3D problem. From their results [106, Figure 17], it is



**Figure 2.28:** Topology and stability of the GB manifold(s) for varying  $\Psi$  when  $\alpha = 3$ . Stable node ■, saddle ■, unstable node ■, and unstable focus ■. GB manifolds are shown for  $\Psi = 0$ ,  $\Psi = (\Psi_L + \Psi_1)/2$ , and  $\Psi = (\Psi_1 + \Psi_2)/2$ .



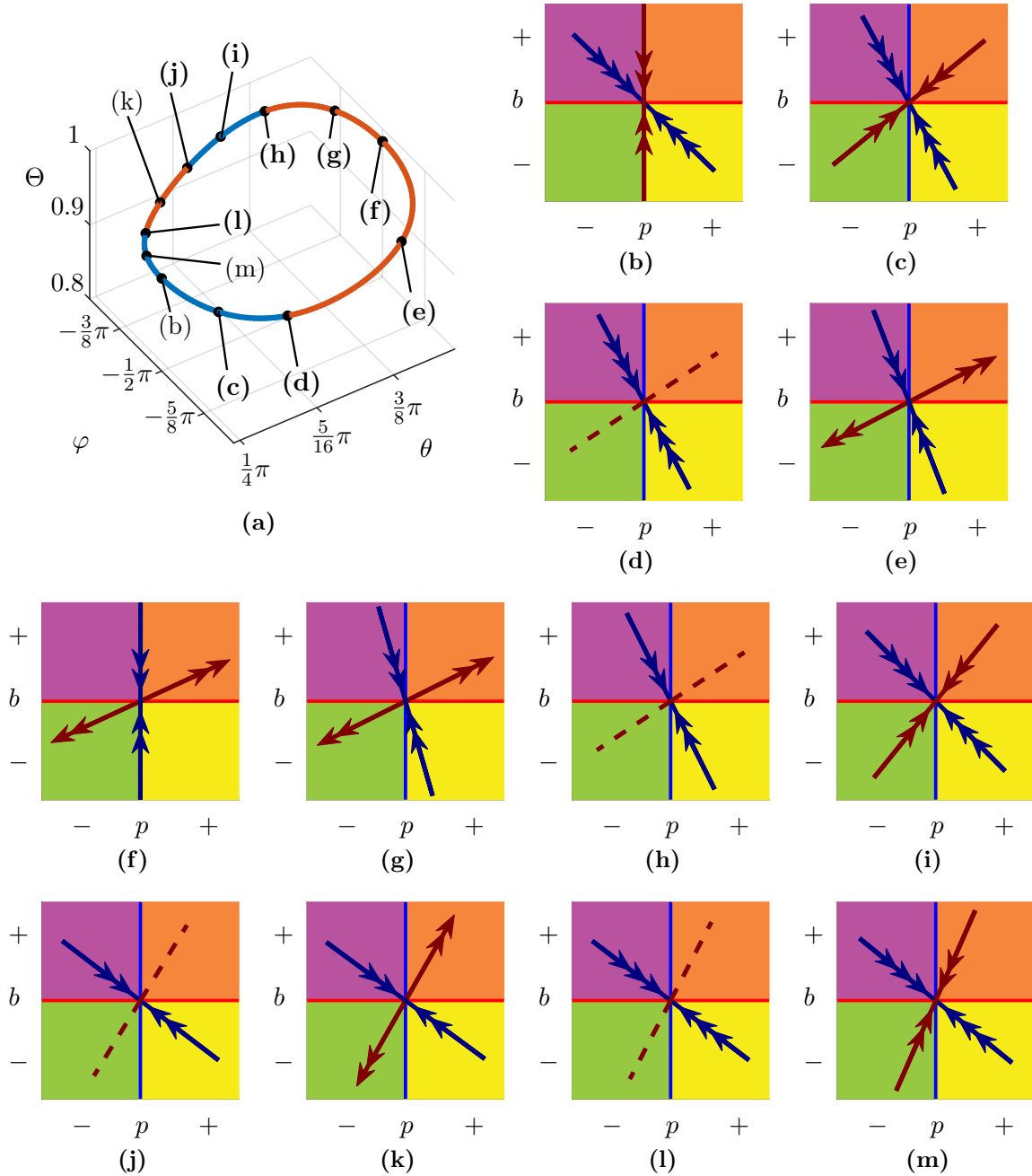
**Figure 2.29:** Projections of the GB manifold ( $b(\theta_1(\varphi; \alpha, \mu), \Psi) = 0$  and  $b(\theta_2(\varphi; \alpha, \mu), \Psi) = 0$ ) into  $(\varphi, \Psi, \Theta)$  space, as in Figure 2.20. Coloured by the stability, as in Figure 2.28. At the extrema of the surface with respect to  $\varphi$ , both eigenvalues of  $\underline{\mathbf{K}}$  reach zero. Figure uses  $\alpha = 3$   $\mu = 1.4$ .



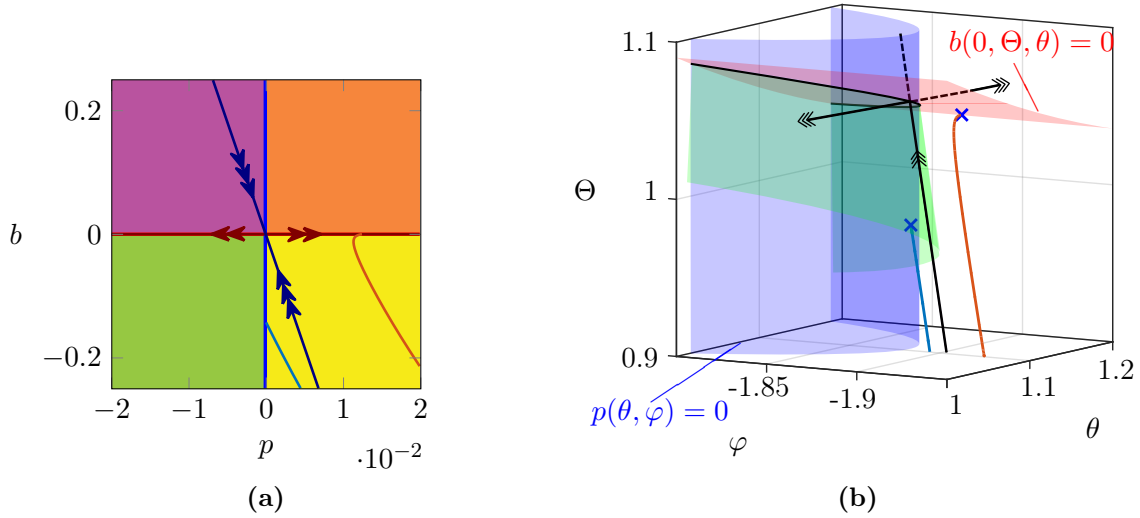
**Figure 2.30:** Positions of the zeros of  $\det \underline{\mathbf{K}}$  on the GB manifold, for  $\alpha = 3$ ,  $\mu = 1.7$  and  $\eta = 10$ . The section  $\Psi = 1.0620$  is shown in Figure 2.31. Here  $\Psi_1 = 1.6689$  and  $\Psi_2 = 4.3121$

evident that a separatrix exists between slipping trajectories that reach  $p = 0$  and those that do not. In Figure 2.32, we see that this separatrix corresponds to the eigenvector associated with the leading eigenvalue of the linearisation of the system about the GB manifold<sup>16</sup>.

<sup>16</sup>Várkonyi, P. 2021 *Personal Communication* has pointed out that it was difficult to obtain the numerical results in [106, Figure 17]. We can now see that this is because the small eigenframe rotation around the GB manifold makes it difficult to find initial conditions between the eigenvector and  $p = 0$ .



**Figure 2.31:** Eigenvectors along the GB manifold when  $\alpha = 3$ ,  $\mu = 1.7$  and  $\eta = 10$  for  $\Psi = 1.062$ , with four critical points: (d), (h), (j) and (l). Since  $\Psi \neq 0$ , there is no symmetry about  $\varphi = -\pi/2$  and hence we show eigenvectors for  $\varphi \gtrsim -\pi/2$ .



**Figure 2.32:** Numerical integration of the equations (2.26) demonstrates that the separatrix between orbits that reach inconsistency ( $p = 0$ ) and those that lift off ( $b = 0$ ) is tangent to the eigenvector corresponding to the leading eigenvalue of the linearisation of the dynamics about each point on the GB manifold. Both solutions are for  $\alpha = 3$  and  $\mu = 1.4$ . Initial conditions: ■  $\theta(0) = 1.1067$ ,  $\eta(0) = 2.1307$ ,  $\varphi(0) = -1.8913$ ,  $\Psi(0) = -0.1027$ ,  $\Theta(0) = 0.9000$ ; ■  $\theta(0) = 1.1031$ ,  $\eta(0) = 2$ ,  $\varphi(0) = -1.9233$ ,  $\Psi(0) = 0$ ,  $\Theta(0) = 0.9000$ . (a) Numerical integration shown in  $(p, b)$  space. (b) Numerical integration shown in  $(\theta, \varphi, \Theta)$  space. The surface in green is tangent to the eigenvector corresponding to the leading eigenvalue at each point along the GB manifold. Matlab's stiff solver `ode15s` was used with default tolerances.

## 2.12 Conclusion

We have studied the problem of a rigid body slipping along a rough horizontal plane with one point of contact, subject to Coulomb friction.

In 2D, this is the celebrated Painlevé problem [85–87], which gives rise to paradoxes when the coefficient of friction  $\mu$  exceeds a critical value  $\mu_P(\alpha)$ , which depends on the moment of inertia of the rigid body.

In 3D, the critical value  $\mu_P^*(\varphi; \alpha)$  is also dependent on the relative slip angle  $\varphi$ . We have shown that it is possible to avoid an existing paradox by a judicious choice of  $\varphi$  (see Figure 2.2).

The 3D problem involves motion in the azimuthal direction  $\psi$ . We have shown that, in the absence of motion in the polar direction  $\theta$ , it is possible for the body to lift off the surface, whether or not there is a paradox, when the azimuthal angular velocity  $\Psi = \dot{\psi}$  is such that  $|\Psi| > \Psi_L$ , where  $\Psi_L$  is given in (2.19), see Figure 2.10.

There are two other critical values of  $\Psi$ ;  $\Psi_1$  and  $\Psi_2$ . When

$$(2.65) \quad |\Psi| > \begin{cases} \Psi_1, & \mu \in (\mu_P, \mu_L] \\ \Psi_L, & \mu > \mu_L \end{cases},$$

the rigid body can undergo an indeterminate paradox even when the polar angular velocity  $\Theta = \dot{\theta} = 0$  (see Figure 2.11). When  $|\Psi| > \Psi_2 > \Psi_1$ , the inconsistent paradox vanishes (see Figure 2.12).

These observations lead to the conclusion that there are three different mechanisms in the 3D Painlevé problem as  $\Psi$  increases, dependent on  $\mu$  (see Figure 2.17).

When not sticking, the rigid body can exist in four modes: slipping, lift-off, inconsistent and indeterminate. Transitions from slipping are of greatest interest. In the absence of a paradox, the rigid body can either slip or lift off, depending on the sign of the free acceleration  $b$ , given in (1.25). A paradox occurs whenever the quantity  $p$ , given in (1.26), becomes negative.

The surfaces  $b = 0$  and  $p = 0$  intersect in the GB manifold [106]. We analyse the dynamics close to the GB manifold in section 2.10. In 2D, slipping trajectories cannot pass through  $p = 0$  without also passing through  $b = 0$  [38]. In 3D, slipping trajectories cross  $p = 0$  away from the GB manifold except when  $\varphi = -\frac{\pi}{2}$ , and an open set of initial conditions that reach inconsistency from slipping (Corollary 2.1). Hence the 2D problem is highly singular. For  $|\Psi| > \Psi_2$ , the GB manifold does not exist. In this case, slipping trajectories, which only exist in restricted parts of phase space, may lift off (unless they stick).

We have discovered bifurcations in the dynamics on the GB manifold, which explain behaviour in the 2D problem (see Figure 2.28), as well as changes in the topology of the GB manifold. Finally, we have shown that there is a separatrix between orbits that reach inconsistency ( $p = 0$ ) and those that undergo lift-off ( $b = 0$ ) tangent to the eigenvector corresponding to the smallest eigenvalue of the linearisation of the dynamics about the GB manifold for  $\Theta > 0$  (see Theorem 2.1 and Figures 2.25, 2.26 and 2.32).

The discovery of the Painlevé paradoxes caused controversy because it implied that rigid body theory and Coulomb friction could be incompatible. Lecornu [71] suggested that in order to escape an inconsistent Painlevé paradox, there should be a jump in velocity ("*l'arcboutement dynamique*"). Subsequently this became known as *impact without collision* or *tangential impact*, which was incorporated into rigid body theory [21, 57].

But real progress was made by taking some elasticity into account (*contact regularisation*) [11, 14, 16, 32, 42, 64, 78, 81, 82, 99, 111]. Here the rod is assumed to be rigid, but the rough surface is taken to be elastic. Now the friction-induced moment at the moving rod tip drives the *surface* down until the rod, still in contact with the surface, stops sliding. With the couple no longer acting, the surface rebounds and the rod lifts off. The analysis using this approach has previously been carried out for the 2D problem [42]; we carry out its extension to the 3D problem in the following chapter.

## Chapter 3

# Compliance

In this chapter<sup>17</sup>, we assume that there is compliance at the point where the rod tip meets the surface, when the two are in contact. We require the normal force to be nonnegative, as we do not want to consider phenomena such as adhesion. We also require that the normal force is PWS in  $(z, w)$ ; the surface cannot exert a force upon the rod when the two are not in contact, and when in contact the normal reaction force is a function of the vertical position and velocity of the rod tip. Hence, we take the normal reaction force to be given by

$$(3.1) \quad F_z(z, w) = [f_z(z, w)] := \begin{cases} 0 & \text{for } z > 0 \\ \max\{f_z(z, w), 0\} & \text{for } z \leq 0 \end{cases},$$

noting the piecewise definition of square brackets  $[\cdot]$ . Assuming linear stiffness and damping, a suitable function is given by

$$(3.2) \quad f_z(z, w) = \varepsilon^{-1} (-\varepsilon^{-1}z - \delta w),$$

where  $\varepsilon$  is a small coefficient related to the stiffness, and  $\delta$  is coefficient related to the damping. In this way, like in [42, 64], we model the surface as being supported by a stiff spring and damper system, which allows the surface to be compressed so that  $z < 0$  (see Figures 3.1 and 3.2). The particular scalings in this function (3.2) ensure that the critical damping coefficient is independent of the small parameter  $\varepsilon$  [78].

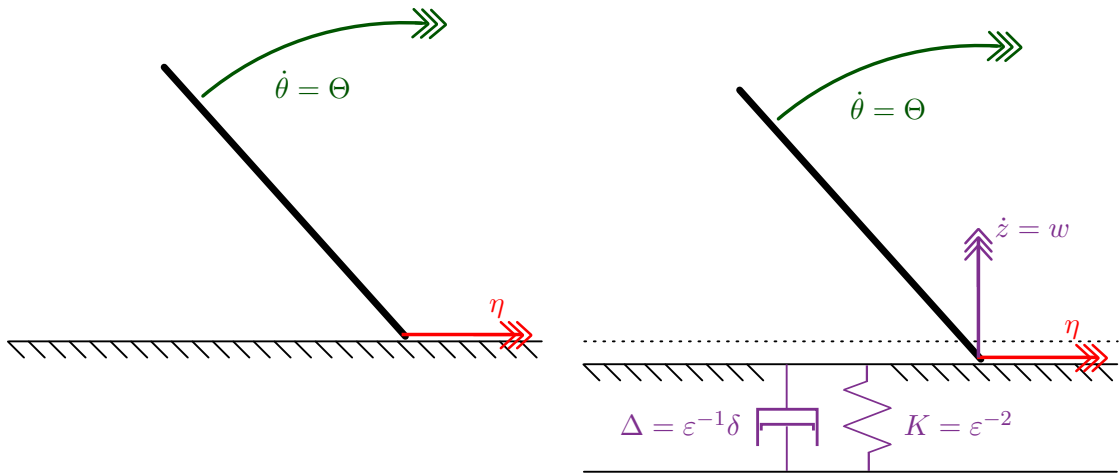
**Remark 3.1.** *It may be important to note that this force  $F_z(z, w)$  is nondimensionalised. The true (dimensional) force has stiffness  $K = \varepsilon^{-2} \frac{mg}{l}$  and damping  $\Delta = \varepsilon^{-1} \delta m \sqrt{\frac{g}{l}}$ .*

It will also be useful to study the nonsmooth limit of our regularised Coulomb friction as it facilitates the discussion of “stability” of sticking. We will show that the resulting dynamics when the rod tip is stuck are equivalent to using Newton’s laws when the lateral movement of

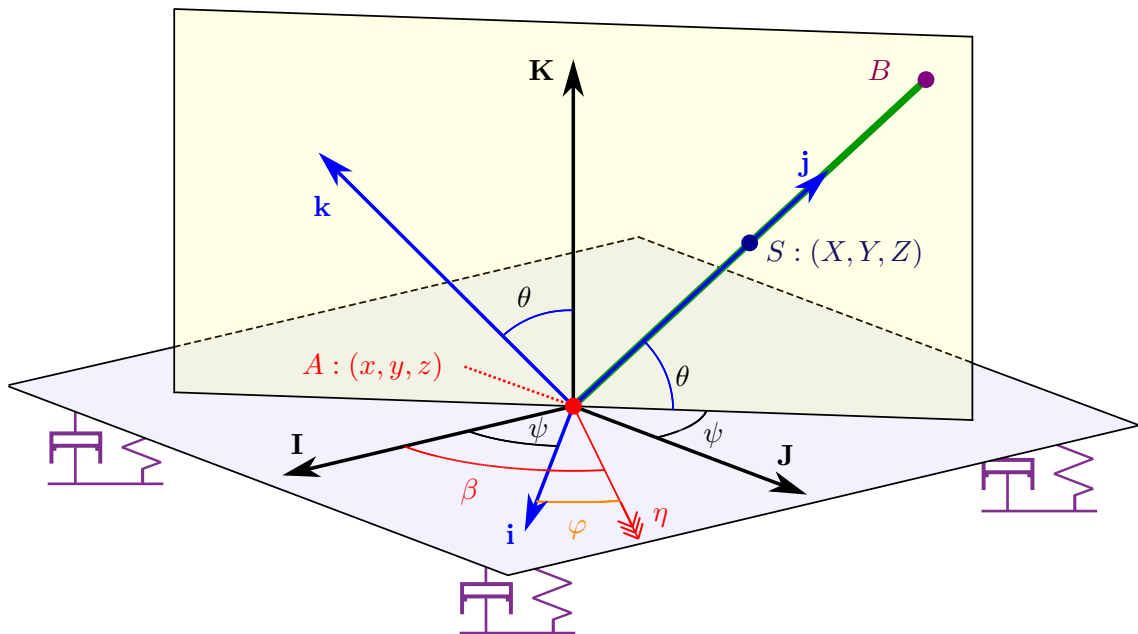
---

<sup>17</sup>This chapter is adapted from [18]. See Acknowledgements for contributions.





**Figure 3.1:** Diagram demonstrating the particular form of compliance. The surface is effectively modelled as being supported by a Hookean spring and linear damper (or system thereof). The effective (nondimensional) stiffness is given by  $K = \epsilon^{-2}$  and the damping is given by  $\Delta = \epsilon^{-1}\delta$ . The dimensional stiffness and damping are given in Remark 3.1.



**Figure 3.2:** As in Figure 1.3, but now with springs and dampers. Note the added degree of freedom at the rod tip  $A$ .

the rod tip is constrained. Therefore, substituting (3.1) into (1.23), we find

$$\begin{aligned}
 (3.3) \quad \dot{x} &= \eta \cos(\psi + \varphi), & \dot{\eta} &= Q_1^\xi(\theta, \varphi, R(\eta; \xi)) F_z(z, w; \varepsilon) + A_1(\Psi, \Theta, \theta, \varphi), \\
 \dot{y} &= \eta \sin(\psi + \varphi), & \eta \dot{\varphi} &= Q_2^\xi(\theta, \varphi, R(\eta; \xi)) F_z(z, w; \varepsilon) + A_2(\Psi, \Theta, \theta, \varphi) - \eta \Psi, \\
 \dot{z} &= w, & \dot{w} &= p^\xi(\theta, \varphi, R(\eta; \xi)) F_z(z, w; \varepsilon) + b(\Psi, \Theta, \theta), \\
 \dot{\psi} &= \Psi, & \dot{\Psi} &= d_1^\xi(\theta, \varphi, R(\eta; \xi)) F_z(z, w; \varepsilon) + c_1(\Psi, \Theta, \theta), \\
 \dot{\theta} &= \Theta, & \dot{\Theta} &= d_2^\xi(\theta, \varphi, R(\eta; \xi)) F_z(z, w; \varepsilon) + c_2(\Psi, \theta),
 \end{aligned}$$

where the coefficients are given in (1.24) and (1.27).

### 3.1 Slow-fast setting

The equations (3.3) are singularly perturbed with respect to the small parameter  $\varepsilon$ . Through an initial scaling (as in [42]) we can bring (3.3) into standard slow-fast form. Specifically, we apply the scaling

$$(3.4) \quad z = \varepsilon \zeta,$$

and define

$$(3.5) \quad \hat{f}_z(\zeta, w) := \varepsilon f_z(\varepsilon \zeta, w) = -\zeta - \delta w$$

and

$$(3.6) \quad \hat{F}_z(\zeta, w) := \left[ \hat{f}_z(\zeta, w) \right].$$

Writing (3.3) in terms of  $\zeta$  and rescaling time, we find

$$\begin{aligned}
 (3.7) \quad x' &= \varepsilon \eta \cos(\psi + \varphi), & \eta' &= \varepsilon A_1(\Psi, \Theta, \theta, \varphi) + Q_1^\xi(\theta, \varphi, R(\eta, \xi)) \hat{F}_z(\zeta, w), \\
 y' &= \varepsilon \eta \sin(\psi + \varphi), & \eta \varphi' &= \varepsilon (A_2(\Psi, \Theta, \theta, \varphi) - \eta \Psi) + Q_2^\xi(\theta, \varphi, R(\eta, \xi)) \hat{F}_z(\zeta, w), \\
 \zeta' &= w, & w' &= \varepsilon b(\Psi, \Theta, \theta) + p^\xi(\theta, \varphi, R(\eta, \xi)) \hat{F}_z(\zeta, w), \\
 \psi' &= \varepsilon \Psi, & \Psi' &= \varepsilon c_1(\Psi, \Theta, \theta) + d_1^\xi(\theta, \varphi, R(\eta, \xi)) \hat{F}_z(\zeta, w), \\
 \theta' &= \varepsilon \Theta, & \Theta' &= \varepsilon c_2(\Psi, \theta) + d_2^\xi(\theta, \varphi, R(\eta, \xi)) \hat{F}_z(\zeta, w),
 \end{aligned}$$

where  $(\cdot)' := \frac{d}{d\tau}(\cdot)$  and  $\frac{d\tau}{dt} = \varepsilon^{-1}$ . By inspection, this is a slow-fast system written in fast time, where  $x, y, \psi$ , and  $\theta$  are slow and the rest of the variables are fast.

Taking the limits  $\varepsilon \rightarrow 0$  (rigid surface) and  $\xi \rightarrow 0$  (nonsmooth friction) for  $\eta > 0$  (slipping), and now using the smooth extension of (3.7), found by replacing  $\hat{F}_z(\zeta, w)$  with  $\hat{f}_z(\zeta, w)$ , we

obtain the layer problem

$$\begin{aligned}
 (3.8) \quad x' &= 0, & \eta' &= Q_1(\theta, \varphi) \hat{f}_z(\zeta, w), \\
 y' &= 0, & \eta\varphi' &= Q_2(\theta, \varphi) \hat{f}_z(\zeta, w), \\
 \zeta' &= w, & w' &= p(\theta, \varphi) \hat{f}_z(\zeta, w), \\
 \psi' &= 0, & \Psi' &= d_1(\theta, \varphi) \hat{f}_z(\zeta, w), \\
 \theta' &= 0, & \Theta' &= d_2(\theta, \varphi) \hat{f}_z(\zeta, w).
 \end{aligned}$$

The set

$$(3.9) \quad C = \{(x, y, \zeta, \psi, \theta, \eta, \varphi, w, \Psi, \Theta) | \zeta = 0, w = 0\}$$

contains critical points of (3.8). This set corresponds to the vertical equilibrium of the rod tip.

The linearisation of (3.8) about a point in  $C$ ,

$$(3.10) \quad (x, y, \zeta, \psi, \theta, \eta, \varphi, w, \Psi, \Theta) = (x_0, y_0, 0, \psi_0, \theta_0, \eta_0, \varphi_0, 0, \Psi_0, \Theta_0),$$

gives a Jacobian with the characteristic polynomial

$$(3.11) \quad \lambda^8 (\lambda^2 + p(\theta_0, \varphi_0)(\delta\lambda + 1)) = 0$$

with only two nonzero eigenvalues

$$(3.12) \quad \lambda_{\pm}(\theta_0, \varphi_0) = -\frac{\delta p(\theta_0, \varphi_0)}{2} \pm \frac{1}{2} \sqrt{\delta^2 p(\theta_0, \varphi_0)^2 - 4p(\theta_0, \varphi_0)}.$$

The eigenvectors corresponding to  $\lambda_{\pm}$  are

$$(3.13) \quad \mathbf{v}_{\pm} = \left( 0, 0, \frac{p}{\lambda_{\pm}}, 0, 0, Q_1, \frac{1}{\eta} Q_2, p, d_1, d_2 \right)^{\top}.$$

When in the slipping region from the constrained problem,  $p > 0$  and hence the real parts of  $\lambda_{\pm}$  are both negative. Physically, this means that the rod is in stable vertical equilibrium at the surface. If  $p \geq 4\delta^{-2}$  both eigenvalues are real and negative (each point on  $C$  is a stable node under the flow of (3.8)). If  $0 < p < 4\delta^{-2}$ ,  $\lambda_{\pm}$  are a complex conjugate pair of eigenvalues with negative real part ( $C$  is stable but with local spiralling dynamics under the flow of (3.8)). For  $p = 0$ ,  $\lambda_{\pm} = 0$  and  $C$  is not normally hyperbolic.

Within the inconsistent and indeterminate regions where  $p < 0$ ,  $\lambda_- < 0 < \lambda_+$  and the point on  $C$  is a saddle with stable and unstable manifolds (tangent to  $\mathbf{v}_{\mp}$  respectively at the point on  $C$ ).

Hence, we have identified that whilst in  $p > 0$  the rod can remain in stable vertical equilibrium, within  $p < 0$  the rod cannot. In section 3.2, we proceed to study the orbits that travel through  $p = 0$ . In section 3.3, we study orbits within  $p < 0$

### 3.2 Slipping to inconsistent transition

It has previously been identified [16] that whilst in the classical (2D) Painlevé problem trajectories do not reach  $p = 0$  without also reaching  $b = 0$ . This is no longer the case in the 3D Painlevé problem. In fact, a considerable range of initial conditions result in trajectories like these (Figures 2.23, 2.24 and 2.32 and Theorem 2.1).

In the constrained system we cannot follow these solutions as they become inconsistent with the rigid body assumptions. Instead, let us study these trajectories in the regularised (compliant) system.

Starting from our equations of motion after our initial scaling (3.7) in the limit  $\xi \rightarrow 0$  for  $\eta > 0$

$$\begin{aligned}
 (3.14) \quad x' &= \varepsilon\eta \cos(\varphi + \psi), & \eta' &= \varepsilon A_1(\Psi, \Theta, \theta, \varphi) + Q_1(\theta, \varphi)\hat{F}_z(\zeta, w), \\
 y' &= \varepsilon\eta \sin(\varphi + \psi), & \eta\varphi' &= \varepsilon (A_2(\Psi, \Theta, \theta, \varphi) - \eta\Psi) + Q_2(\theta, \varphi)\hat{F}_z(\zeta, w), \\
 \zeta' &= w, & w' &= \varepsilon b(\Psi, \Theta, \theta) + p(\theta, \varphi)\hat{F}_z(\zeta, w), \\
 \psi' &= \varepsilon\Psi, & \Psi' &= \varepsilon c_1(\Psi, \Theta, \theta) + d_1(\theta, \varphi)\hat{F}_z(\zeta, w), \\
 \theta' &= \varepsilon\Theta, & \Theta' &= \varepsilon c_2(\Psi, \theta) + d_2(\theta, \varphi)\hat{F}_z(\zeta, w).
 \end{aligned}$$

From Theorem 2.1, we find that trajectories reach  $p = 0$  in finite time in the constrained problem. To find if such orbits in the regularised problem enter  $p < 0$  we shall look locally and derive an extended system with  $p$  as a variable. The derivative of  $p$  with respect to the same time as in (3.14) is

$$(3.15) \quad p' = \varepsilon\Pi(\Psi, \Theta, \theta, \varphi, \eta, p) + k(\eta, \theta, \varphi, p)\hat{F}_z(\zeta, w)$$

where

$$\begin{aligned}
 (3.16) \quad \Pi(\Psi, \Theta, \theta, \varphi, \eta) &:= \frac{\partial p(\theta, \varphi)}{\partial \theta}\Theta + \frac{1}{\eta} \frac{\partial p(\theta, \varphi)}{\partial \varphi} (A_2(\Psi, \Theta, \theta, \varphi) - \eta\Psi) \\
 &= \frac{1}{\eta} \alpha\mu \sin \theta \cos^2 \theta \cos^2 \varphi b(\Psi, \Theta, \theta) + p(\Theta(\cot \theta - \tan \theta)) \\
 &\quad + \Theta(\tan \theta - (1 + \alpha) \cot \theta) - \Psi\alpha\mu \sin \theta \cos \theta \cos \varphi
 \end{aligned}$$

and

$$\begin{aligned}
 (3.17) \quad k(\theta, \varphi, \eta, p) &:= \frac{1}{\eta} \frac{\partial p(\theta, \varphi)}{\partial \varphi} Q_2(\theta, \varphi), \\
 &:= -\frac{1}{\eta} ((1 + \alpha) - p)\alpha\mu \cos^2 \theta \cos^2 \varphi,
 \end{aligned}$$

We can then write an extension of (3.14) as

$$\begin{aligned}
 (3.18) \quad x' &= \varepsilon \eta \cos(\varphi + \psi), & \eta' &= \varepsilon A_1(\Psi, \Theta, \theta, \varphi) + Q_1(\theta, \varphi) \hat{F}_z(\zeta, w), \\
 y' &= \varepsilon \eta \sin(\varphi + \psi), & \eta \varphi' &= \varepsilon (A_2(\Psi, \Theta, \theta, \varphi) - \eta \Psi) + Q_2(\theta, \varphi) \hat{F}_z(\zeta, w), \\
 \zeta' &= w, & w' &= \varepsilon b(\Psi, \Theta, \theta) + p \hat{F}_z(\zeta, w), \\
 \psi' &= \varepsilon \Psi, & \Psi' &= \varepsilon c_1(\Psi, \Theta, \theta) + d_1(\theta, \varphi) \hat{F}_z(\zeta, w), \\
 \theta' &= \varepsilon \Theta, & \Theta' &= \varepsilon c_2(\Psi, \theta) + d_2(\theta, \varphi) \hat{F}_z(\zeta, w), \\
 & & p' &= \varepsilon \Pi(\Psi, \Theta, \theta, \varphi, \eta, p) + k(\eta, \theta, \varphi, p) \hat{F}_z(\zeta, w)
 \end{aligned}$$

**Remark 3.2.** Here, we are taking an extended system in (3.18), treating  $p$  as a variable. This will be useful in later calculations due to the fact that neither  $\theta$  nor  $\varphi$  can be written as a function of the other on  $p(\theta, \varphi) = 0$  (see (2.5) and (2.6)).

Taking the layer problem of (3.18), the set  $C$  (3.9) is still a critical set, about which the eigenvalues are

$$(3.19) \quad \lambda_{\pm} = -\frac{p\delta}{2} \pm \frac{\sqrt{p^2\delta^2 - 4p}}{2}.$$

Along the critical manifold  $C$ , we can see that the reduced problem is given by the set of ODEs

$$\begin{aligned}
 (3.20) \quad x' &= \eta \cos(\varphi + \psi), & \eta' &= A_1(\Psi, \Theta, \theta, \varphi), \\
 y' &= \eta \sin(\varphi + \psi), & \eta \varphi' &= A_2(\Psi, \Theta, \theta, \varphi) - \eta \Psi, \\
 \psi' &= \Psi, & \Psi' &= c_1(\Psi, \Theta, \theta), \\
 \theta' &= \Theta, & \Theta' &= c_2(\Psi, \theta), \\
 & & p' &= \Pi(\Psi, \Theta, \theta, \varphi, \eta, p).
 \end{aligned}$$

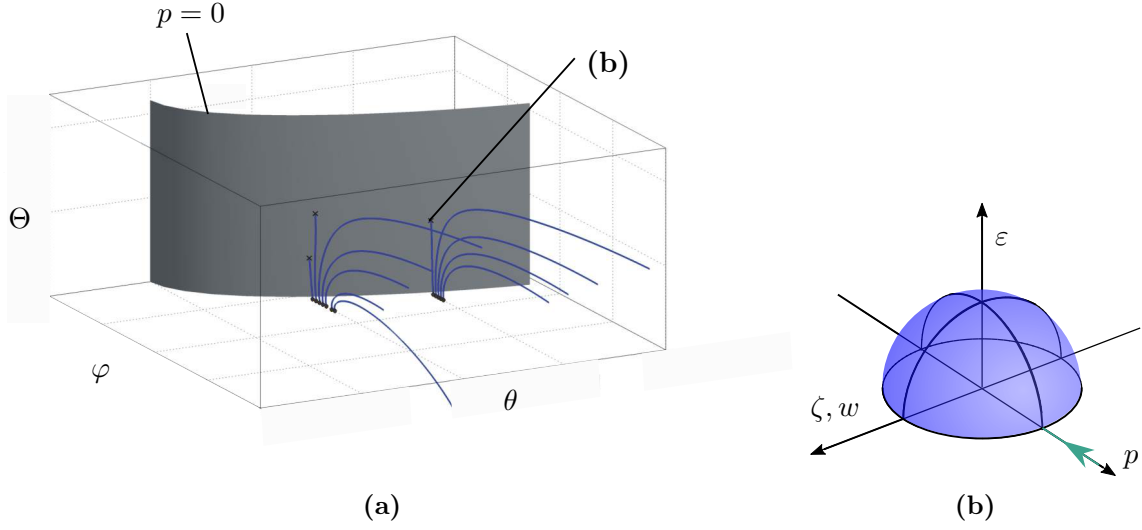
It is possible to show that  $\Pi(\Psi, \Theta, \theta, \varphi, \eta, p)$  can be negative near  $p = 0$ . Hence  $p$  can reach zero along this slow manifold, at which point the critical manifold loses normal hyperbolicity since  $\lambda_{\pm}|_{p=0} \equiv 0$ .

In order to investigate the dynamics near  $p = 0$  and discover what happens after the loss of normal hyperbolicity, we will use geometric blowup (shown in Figure 3.3). In particular, we blow up  $p = \zeta = w = \varepsilon = 0$  to a hyper-hemisphere, using the transformation

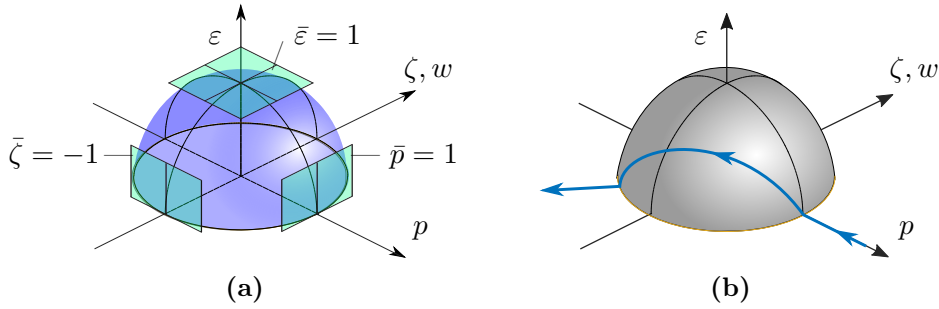
$$(3.21) \quad p = r^2 \bar{p}, \quad \zeta = r^3 \bar{\zeta}, \quad w = r^4 \bar{w}, \quad \varepsilon = r^5 \bar{\varepsilon}, \quad r \geq 0, \quad (\bar{p}, \bar{\zeta}, \bar{w}, \bar{\varepsilon}) \in S_+^3,$$

where

$$(3.22) \quad S_+^3 := \{(\bar{p}, \bar{\zeta}, \bar{w}, \bar{\varepsilon}) \mid \bar{p}^2 + \bar{\zeta}^2 + \bar{w}^2 + \bar{\varepsilon}^2 = 1, \bar{\varepsilon} > 0\}.$$



**Figure 3.3:** Adapted from [16], (a) depicts the orbits of the rigid body system studied in Chapter 2 that we aim to track using the blowup in (3.21). (b) gives a geometric interpretation of the blowup. The rod tip is in vertical equilibrium  $\zeta = w = 0$  whilst  $p(\theta, \varphi) \rightarrow 0$ . (b) sketches the blowup of  $\zeta = w = p = \varepsilon = 0$  in (3.21), which effectively replaces each point where  $\zeta = w = p = \varepsilon = 0$  with the 3-(hemi)sphere (3.22).



**Figure 3.4:** Blowup of the transition from slipping to inconsistency. (a) Relevant charts in the blowup (3.21). (b) The special solution along the surface of the hemisphere of the blowup.

In the blowup, we proceed to study three charts, the entry chart  $k_1$ , the scaling chart  $k_2$ , and the exit chart  $k_3$ . These are found by setting  $\bar{p} = 1$ ,  $\bar{\varepsilon} = 1$ , and  $\bar{\zeta} = -1$  respectively in (3.21),

$$(3.23) \quad \bar{p} = 1 \implies k_1 : \quad p = r_1^2, \quad \zeta = r_1^3 \zeta_1, \quad w = r_1^4 w_1, \quad \varepsilon = r_1^5 \varepsilon_1,$$

$$(3.24) \quad \bar{\varepsilon} = 1 \implies k_2 : \quad p = r_2^2 p_2, \quad \zeta = r_2^3 \zeta_2, \quad w = r_2^4 w_2, \quad \varepsilon = r_2^5,$$

$$(3.25) \quad \bar{\zeta} = -1 \implies k_3 : \quad p = r_3^2 p_3, \quad \zeta = -r_3^3, \quad w = r_3^4 w_3, \quad \varepsilon = r_3^5 \varepsilon_3.$$

These charts are demonstrated in Figure 3.4.

### 3.2.1 Entry chart: $\bar{p} = 1$

In order study orbits reaching  $p = 0$  from  $p > 0$  we use the  $\bar{p} = 1$  chart (3.23) where (3.18) becomes

$$(3.26) \quad \begin{aligned} x' &= r_1^5 \varepsilon_1 \eta \cos(\varphi + \psi), & \eta' &= r_1^5 \varepsilon_1 A_1(\Psi, \Theta, \theta, \varphi) + Q_1(\theta, \varphi)[-r_1^3 \zeta_1 - \delta r_1^4 w_2], \\ y' &= r_1^5 \varepsilon_1 \eta \sin(\varphi + \psi), & \eta\varphi' &= r_1^5 \varepsilon_1 (A_2(\Psi, \Theta, \theta, \varphi) - \eta\Psi) + Q_2(\theta, \varphi)[-r_1^3 \zeta_1 - \delta r_1^4 w_1], \\ \zeta_1' &= r_1 w_1 - 3 \frac{\zeta_1}{r_1} r_1', & w_1' &= r_1 \varepsilon_1 b(\Psi, \Theta, \theta) + [-r_1 \zeta_1 - \delta r_1^2 w_1] - 4 \frac{w_1}{r_1} r_1', \\ \psi' &= r_1^5 \varepsilon_1 \Psi, & \Psi' &= r_1^5 \varepsilon_1 c_1(\Psi, \Theta, \theta) + d_1(\theta, \varphi)[-r_1^3 \zeta_1 - \delta r_1^4 w_1], \\ \theta' &= r_1^5 \varepsilon_1 \Theta, & \Theta' &= r_1^5 \varepsilon_1 c_2(\Psi, \theta) + d_2(\theta, \varphi)[-r_1^3 \zeta_1 - \delta r_1^4 w_1], \\ \varepsilon_1' &= -5 \frac{\varepsilon_1}{r_1} r_1' & r_1' &= \frac{1}{2r_1} (r_1^5 \varepsilon_1 \Pi(\Psi, \Theta, \theta, \varphi, \eta, r_1^2) + k(\eta, \theta, \varphi, r_1^2)[-r_1^3 \zeta_1 - \delta r_1^4 w_1]). \end{aligned}$$

From now on, to be concise, we omit the dependence of functions, neglect cyclic variables  $x$ ,  $y$ , and  $\psi$ , and group similar equations. Transforming time in order to “divide out” a factor of  $r_1$  from the right-hand side, we find

$$(3.27) \quad \begin{aligned} \begin{pmatrix} \eta' \\ \eta\varphi' \\ \Psi' \\ \Theta' \\ \theta' \end{pmatrix} &= r_1^2 \begin{pmatrix} r_1^2 \varepsilon_1 \\ A_1 \\ A_2 \\ c_1 \\ c_2 \\ \Theta \end{pmatrix} + \begin{pmatrix} Q_1 \\ Q_2 \\ d_1 \\ d_2 \\ 0 \end{pmatrix} [-\zeta_1 - \delta r_1 w_2], \\ \begin{pmatrix} r_1' \\ \varepsilon_1' \\ \zeta_1' \\ w_1' \end{pmatrix} &= \begin{pmatrix} \frac{1}{2} r_1 \\ -\frac{5}{2} \varepsilon_1 \\ -\frac{3}{2} \zeta_1 \\ -2w_1 \end{pmatrix} (r_1^2 \varepsilon_1 \Pi + k[-\zeta_1 - \delta r_1 w_1]) + \begin{pmatrix} 0 \\ 0 \\ w_1 \\ \varepsilon_1 b + [-\zeta_1 - \delta r_1 w_1] \end{pmatrix} \end{aligned}$$

If we constrain the dynamics to the surface of the sphere  $r_1 = 0$  then  $(x, y, \psi, \theta, \eta, \varphi, \Psi, \Theta, r_1)' = \mathbf{0}$ , and

$$(3.28) \quad \begin{aligned} \varepsilon_1' &= -\frac{5}{2} \varepsilon_1 k[-\zeta_1], \\ \zeta_1' &= w_1 - \frac{3}{2} \zeta_1 k[-\zeta_1], \\ w_1' &= \varepsilon_1 b + (1 - 2w_1 k)[- \zeta_1], \end{aligned}$$

Considering the smooth extension of (3.28) and linearising around the equilibrium  $\zeta_1 = \varepsilon_1 = w_1 = 0$ , we find the Jacobian has a pair of imaginary eigenvalues  $\pm i$  and a zero eigenvalue. The eigenvector corresponding to the zero eigenvalue is  $(1, b, 0)^\top$ . Hence, we can suppose that, similar

to [64], there is an invariant manifold extending from  $\zeta_1 = \varepsilon_1 = w_1 = 0$

$$(3.29) \quad \begin{aligned} \zeta_1 &= b\varepsilon_1 - 3b^3k^2\varepsilon_1^3 + \mathcal{O}(\varepsilon_1^4), \\ w_1 &= b^2k\varepsilon_1^2 + \mathcal{O}(\varepsilon_1^4), \\ \varepsilon_1 &> 0 \end{aligned}$$

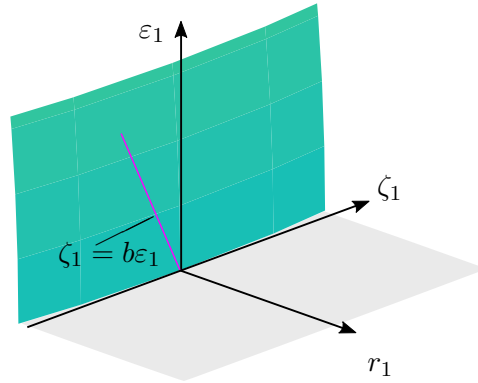
along which  $\varepsilon_1$  is locally increasing, since

$$(3.30) \quad \varepsilon_1' = \frac{5}{2}kb\varepsilon_1^2 + \mathcal{O}(\varepsilon_1^4) > 0,$$

for small  $\varepsilon_1$  along the invariant manifold (3.29). Due to the imaginary pair of eigenvalues  $\pm i$ , we expect that locally there is rotation about this invariant manifold (3.29).

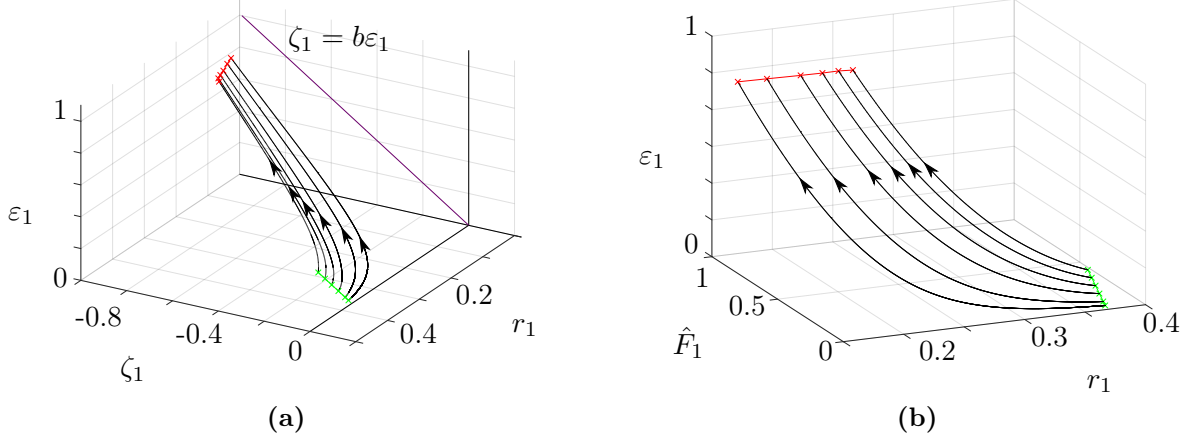
In Figure 3.5, we give a sketch of the first order approximation to the invariant manifold in (3.29).

In Figure 3.6, we show numerical integration of (3.27) for initial conditions near  $(\zeta_1, w_1) = (0, 0)$ . We see that orbits tend to follow the invariant manifold (3.29) up the sphere.



**Figure 3.5:** Sketch of the blowup chart  $k_1$  with the first order approximation to the invariant manifold (3.29) labelled.





**Figure 3.6:** Figures demonstrating numerical integration of the equations in the chart  $k_1$ . For  $\varepsilon_1 > 0$  orbits still tend to follow close to the invariant manifold (3.29). In **(a)**, orbits are shown in  $(\zeta_1, r_1, \varepsilon_1)$  space, whilst in **(b)** orbits are shown in  $(\hat{F}_1, r_1, \varepsilon_1)$  space, where  $\hat{F}_1 = -\zeta_1 - \delta r_1 w_1$ . Initial conditions are given and described in Appendix C.1 and Table C.1.

### 3.2.2 Scaling chart: $\bar{\varepsilon} = 1$

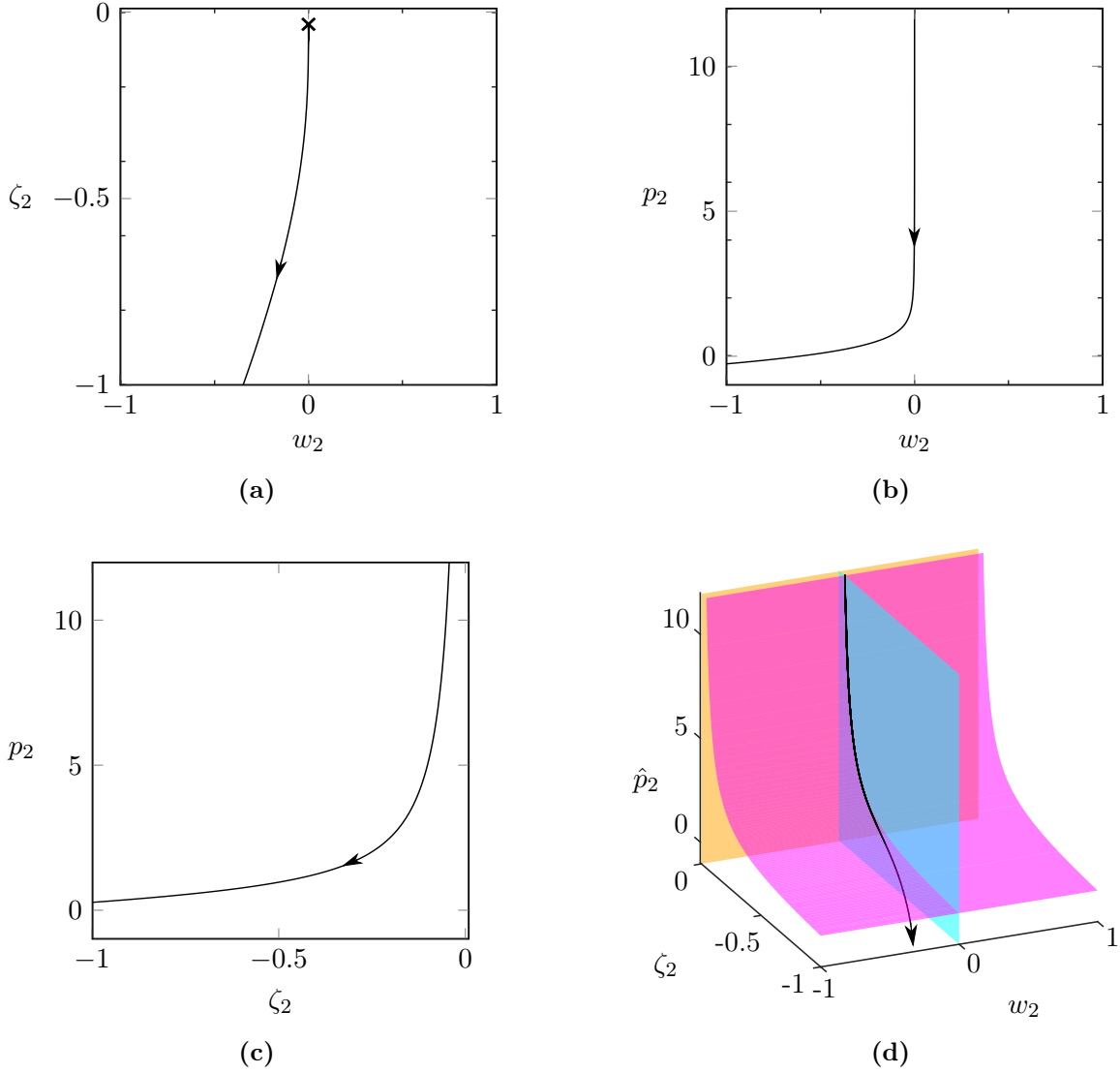
To study orbits as they pass through  $p = 0$ , we study the  $\bar{\varepsilon} = 1$  chart (3.24), where (3.18) becomes

$$\begin{aligned}
 (3.31) \quad x' &= r_2^5 \eta \cos(\varphi + \psi), & \eta' &= r_2^5 A_1(\Psi, \Theta, \theta, \varphi) + Q_1(\theta, \varphi)[-r_2^3 \zeta_2 - \delta r_2^4 w_2], \\
 y' &= r_2^5 \eta \sin(\varphi + \psi), & \eta\varphi' &= r_2^5 (A_2(\Psi, \Theta, \theta, \varphi) - \eta\Psi) + Q_2(\theta, \varphi)[-r_2^3 \zeta_2 - \delta r_2^4 w_2], \\
 \zeta_2' &= r_2 w_2, & w_2' &= r_2 b(\Psi, \Theta, \theta) + p_2[-r_2 \zeta_2 - \delta r_2^2 w_2], \\
 \psi' &= r_2^5 \Psi, & \Psi' &= r_2^5 c_1(\Psi, \Theta, \theta) + d_1(\theta, \varphi)[-r_2^3 \zeta_2 - \delta r_2^4 w_2], \\
 \theta' &= r_2^5 \Theta, & \Theta' &= r_2^5 c_2(\Psi, \theta) + d_2(\theta, \varphi)[-r_2^3 \zeta_2 - \delta r_2^4 w_2], \\
 & & p_2' &= r_2^3 \Pi(\Psi, \Theta, \theta, \varphi, \eta, r_2^2 p_2) + k(\theta, \varphi, \eta, r_2^2 p_2)[-r_2 \zeta_2 - \delta r_2^2 w_2].
 \end{aligned}$$

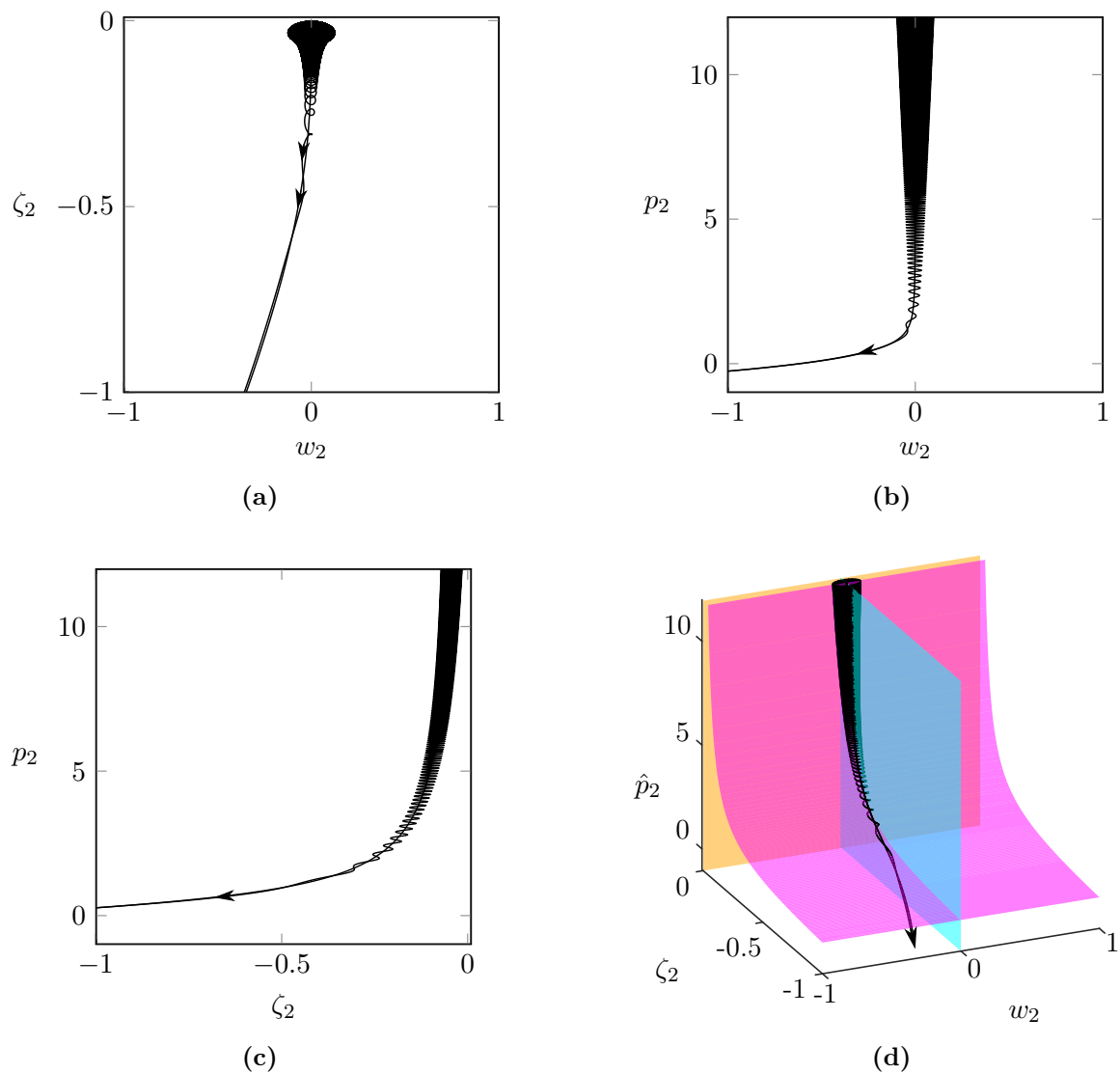
Rescaling time in order to divide out a factor of  $\varepsilon^{\frac{1}{5}}$ ,

$$\begin{aligned}
 (3.32) \quad x' &= r_2^4 \eta \cos(\varphi + \psi), & \eta' &= r_2^4 A_1(\Psi, \Theta, \theta, \varphi) + Q_1(\theta, \varphi)[-r_2^2 \zeta_2 - \delta r_2^3 w_2], \\
 y' &= r_2^3 \eta \sin(\varphi + \psi), & \eta\varphi' &= r_2^3 (A_2(\Psi, \Theta, \theta, \varphi) - \eta\Psi) + Q_2(\theta, \varphi)[-r_2^2 \zeta_2 - \delta r_2^3 w_2], \\
 \zeta_2' &= w_2, & w_2' &= b(\Psi, \Theta, \theta) + p_2[-\zeta_2 - \delta r_2 w_2], \\
 \psi' &= r_2^4 \Psi, & \Psi' &= r_2^4 c_1(\Psi, \Theta, \theta) + d_1(\theta, \varphi)[-r_2^2 \zeta_2 - \delta r_2^3 w_2], \\
 \theta' &= r_2^4 \Theta, & \Theta' &= r_2^4 c_2(\Psi, \theta) + d_2(\theta, \varphi)[-r_2^2 \zeta_2 - \delta r_2^3 w_2], \\
 & & p_2' &= r_2^2 \Pi(\Psi, \Theta, \theta, \varphi, \eta, r_2^2 p_2) + k(\theta, \varphi, \eta, r_2^2 p_2)[- \zeta_2 - \delta r_2 w_2].
 \end{aligned}$$

This is a sort of slow-fast system with respect to  $r_2$ , where only  $\zeta_2$  and  $w_2$  are fast.



**Figure 3.7:** Figures depicting the special solution in the chart  $k_2$  from the numerical integration of (3.33). Cyan  $\blacksquare$  indicates the nullcline  $\zeta_2' = 0$ , magenta  $\blacksquare$  indicates the nullcline  $w_2' = 0$  and yellow  $\blacksquare$  indicates the nullcline  $\hat{p}_2' = 0$  (which is also where the rod lifts off in this chart  $\zeta_2 = 0$ ). Initial conditions are given and described in Appendix C.2 and Table C.2.  $\zeta_2$ ,  $p_2$  and  $w_2$  all decrease.



**Figure 3.8:** Figures depicting an orbit close to the special solution in the chart  $k_2$  from the numerical integration of (3.33), as in Figure 3.7. This demonstrates that orbits nearby the special solution tend to oscillate around the intersection of the nullclines  $\zeta_2' = 0$  and  $w_2' = 0$ , with a sort of contraction. Initial conditions are given and described in Appendix C.2 and Table C.2.  $\zeta_2$ ,  $p_2$  and  $w_2$  all tend to decrease.

If we take the layer problem  $r_2 = 0$ ,  $x' = \dots = 0$  and

$$(3.33) \quad \begin{aligned} \zeta_2' &= w_2, \\ w_2' &= b(\Psi, \Theta, \theta) + p_2[-\zeta_2], \\ p_2' &= k(\theta, \varphi, \eta, 0)[- \zeta_2]. \end{aligned}$$

From (3.17), we find that the term

$$(3.34) \quad k(\theta, \varphi, \eta, 0) = -\frac{1}{\eta}(1 + \alpha) \cos^2 \varphi \cos^2 \theta \leq 0,$$

and so for clarity, we set  $K := -k > 0$ . Similarly, since we are studying the boundary between the slipping and inconsistent region, where  $b(\Psi, \Theta, \theta) < 0$ , we set  $B := -b > 0$ .

Using the smooth extension of (3.33), we can write a single nonlinear nonautonomous second order ODE in  $p_2$

$$(3.35) \quad p_2'' = -\frac{1}{2}p_2^2 - KBt + \kappa,$$

where  $\kappa$  is an arbitrary integration constant satisfying initial conditions.

Through a transformation of dependent and independent variables given by

$$(3.36) \quad t = \left(\frac{12}{KB}\right)^{\frac{1}{5}} \tau + \frac{\kappa}{KB}, \quad p_2 = -\left(\frac{12}{KB}\right)^{\frac{3}{5}} KBf,$$

or conversely

$$(3.37) \quad \tau = \left(\frac{KB}{12}\right)^{\frac{1}{5}} \left(t - \frac{\kappa}{KB}\right), \quad f = -\left(\frac{KB}{12}\right)^{\frac{3}{5}} \frac{1}{KB} p_2,$$

it is possible to show that (3.35) is equivalent to the type I Painlevé equation

$$(3.38) \quad \frac{d^2 f(\tau)}{d\tau^2} = 6f(\tau)^2 + \tau$$

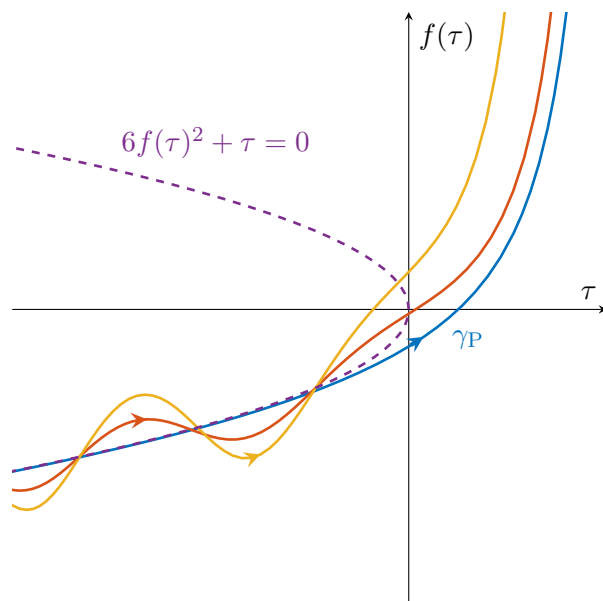
[29].

Whilst it is a satisfying mathematical coincidence that the governing equations of a scaled version of what is often called the ‘‘Painlevé parameter’’ in a particular chart in the blowup of the Painlevé paradox are equivalent to the type I Painlevé equation, this finding does somewhat limit our analysis; we know that we cannot write an analytic solution for  $p_2$  in terms of elementary functions (e.g. polynomial, rational, trigonometric, hyperbolic, and exponential functions and finite product sums, products and compositions thereof)<sup>18</sup>.

Nevertheless, like many other special functions, much is known about type I Painlevé equation[29].

In particular, it is known that [29, 56, 96]:

<sup>18</sup>This was the case in subsection 1.2.1.1, where the governing equation was the Airy equation, and is to be expected (see Remarks 1.3 and 1.4).



**Figure 3.9:** Qualitative behaviour of solutions to type I Painlevé equation in (3.38). The special solution  $\gamma_P$  is backwards asymptotic to the lower branch of the parabola  $6f(\tau)^2 + \tau$ .

- There is a special monotonically increasing solution of (3.38),  $\gamma_P$ , which is asymptotic to

$$(3.39) \quad f(\tau) \approx -\sqrt{-\frac{1}{6}\tau} \quad \text{as } \tau \rightarrow -\infty.$$

- There are also solutions such that

$$(3.40) \quad f(\tau) = -\sqrt{-\frac{1}{6}|\tau|} + \delta_O |\tau|^{-\frac{1}{8}} \sin(\phi(\tau) - \theta_O) + \iota(|\tau|^{-\frac{1}{8}}) \quad \text{as } \tau \rightarrow -\infty,$$

where

$$(3.41) \quad \phi(\tau) = 24^{\frac{1}{4}} \left( \frac{4}{5} |x|^{\frac{5}{4}} - \frac{5}{8} d_O \ln|x| \right),$$

and  $d_O$  and  $\theta_O$  are constants. These solutions oscillate around the special solution  $\gamma_P$ .

- Solutions  $f(\tau)$  tend to  $\infty$  as  $\tau$  increases reaching a pole.

This behaviour is shown in Figure 3.9.

In terms of our variables, this special solution  $\gamma_P$  corresponds to a monotonically decreasing solution for  $p_2$ , which is asymptotic to

$$(3.42) \quad p_2(t) = \sqrt{2} \sqrt{-BKt + \kappa} \quad \text{as } t \rightarrow -\infty.$$

This implies there are monotonically decreasing solutions for  $\zeta_2(t)$  and  $w_2(t)$  which are asymptotic to

$$(3.43) \quad \zeta_2(t) = -\frac{B}{\sqrt{2}} (-BKt + \kappa)^{-\frac{1}{2}} \quad \text{as } t \rightarrow -\infty$$

and

$$(3.44) \quad w_2(t) = -\frac{\sqrt{2}KB^2}{4} (-BKt + \kappa)^{-\frac{3}{2}} \quad \text{as } t \rightarrow -\infty.$$

As we did in subsection 1.2.1, we can write these special solutions (3.42)–(3.44) in the entry/exit chart  $k_1$ , using the change of coordinates

$$(3.45) \quad k_{1,2} : \quad \zeta_1 = p_2^{-\frac{3}{2}} \zeta_2, \quad w_1 = p_2^{-\frac{4}{2}} w_2, \quad \varepsilon_1 = p_2^{-\frac{5}{2}},$$

we find

$$(3.46) \quad \zeta_1 = -B\varepsilon_1,$$

$$(3.47) \quad w_1 = -KB^2\varepsilon_1^2.$$

This means that the invariant manifold (3.29) observed in the chart  $k_1$  connects with this special solution in chart  $k_2$ . The special solutions for  $p_2$ ,  $\zeta_2$ , and  $w_2$  are monotonic decreasing and tend to  $-\infty$ , hence the orbit passes into the inconsistent region  $p < 0$  and the rod begins to compress the surface. Furthermore, from (3.33), for  $b < 0$  and in the octant  $\{(p_2, \zeta_2, w_2) | p_2 < 0, \zeta_2 < 0, w_2 < 0\}$ ,  $p'_2, \zeta'_2, w'_2 < 0$ . Orbits in this octant shall be picked up in the following chart.

### 3.2.3 Exit chart: $\bar{\zeta} = 1$

To follow the orbit as it enters  $p < 0$  and  $\zeta$  is decreasing, we study the chart  $k_3$  (3.25), found by setting  $\bar{\zeta} = -1$  in (3.21)<sup>19</sup>. In this chart, (3.18) becomes

$$(3.48) \quad \begin{aligned} x' &= r_3^5 \varepsilon_3 \cos(\varphi + \psi), & \eta' &= r_3^3 (r_3^2 \varepsilon_3 A_1 + Q_1 [1 - \delta r_3 w_2]), \\ y' &= r_3^5 \varepsilon_3 \sin(\varphi + \psi), & \eta\varphi' &= r_3^3 (r_3^2 \varepsilon_3 (A_2 - \eta\Psi) + Q_2 [1 - \delta r_3 w_3]), \\ r_3' &= -\frac{1}{3} r_3^2 w_3, & w_3' &= r_3 \left( \varepsilon_3 b + p_3 [1 - \delta r_3 w_1] + \frac{4}{3} w_3^2 \right), \\ \psi' &= r_3^5 \varepsilon_3 \Psi, & \Psi' &= r_3^3 (r_3^2 \varepsilon_3 c_1 + d_1 [1 - \delta r_3 w_3]), \\ \theta' &= r_3^5 \varepsilon_3 \Theta, & \Theta' &= r_3^3 (r_3^2 \varepsilon_3 c_2 + d_2 [1 - \delta r_3 w_3]), \\ \varepsilon_3' &= \frac{5}{3} r_3 \varepsilon_3 w_3, & p_3' &= r_3 \left( r_3^2 \varepsilon_3 \Pi + k [1 - \delta r_3 w_3] + \frac{2}{3} p_3 w_3 \right), \end{aligned}$$

after temporarily omitting the dependence of functions.

We see that there is a common factor of  $r_3$  on the right-hand sides of (3.48). We can desingularise  $r_3 = 0$  by transforming time such that we divide the right-hand sides of (3.48) by

<sup>19</sup>Whilst we could also use the chart found by setting  $\bar{p} = -1$  as the exit chart, the resulting system of differential equations is more tractable in the chart  $\bar{\zeta} = 1$ .

$r_3$

$$\begin{aligned}
 (3.49) \quad x' &= r_3^4 \varepsilon_3 \cos(\varphi + \psi), & \eta' &= r_3^2 (r_3^2 \varepsilon_3 A_1 + Q_1[1 - \delta r_3 w_2]), \\
 y' &= r_3^4 \varepsilon_3 \sin(\varphi + \psi), & \eta\varphi' &= r_3^2 (r_3^2 \varepsilon_3 (A_2 - \eta\Psi) + Q_2[1 - \delta r_3 w_3]), \\
 r_3' &= -\frac{1}{3} r_3 w_3, & w_3' &= \varepsilon_3 b + p_3[1 - \delta r_3 w_1] + \frac{4}{3} w_3^2, \\
 \psi' &= r_3^4 \varepsilon_3 \Psi, & \Psi' &= r_3^2 (r_3^2 \varepsilon_3 c_1 + d_1[1 - \delta r_3 w_3]), \\
 \theta' &= r_3^4 \varepsilon_3 \Theta, & \Theta' &= r_3^2 (r_3^2 \varepsilon_3 c_2 + d_2[1 - \delta r_3 w_3]), \\
 \varepsilon_3' &= \frac{5}{3} \varepsilon_3 w_3 & p_3' &= r_3^2 \varepsilon_3 \Pi + k[1 - \delta r_3 w_3] + \frac{2}{3} p_3 w_3.
 \end{aligned}$$

If we constrain (3.49) to the surface of the sphere  $r_3 = 0$ , we find  $x' = y' = r_3' = \psi' = \theta' = \eta' = \varphi' = \Psi' = \Theta' = 0$  and are left with

$$\begin{aligned}
 (3.50) \quad w_3' &= \varepsilon_3 b(\Psi, \Theta, \theta) + \hat{p}_3 + \frac{4}{3} w_3^2, \\
 \varepsilon_3' &= \frac{5}{3} \varepsilon_3 w_3, \\
 \hat{p}_3' &= k(\theta, \varphi, \eta, 0) + \frac{2}{3} \hat{p}_3 w_3.
 \end{aligned}$$

If we further constrain (3.50) to the equator of the sphere, we find

$$\begin{aligned}
 (3.51) \quad w_3' &= \hat{p}_3 + \frac{4}{3} w_3^2, \\
 p_3' &= -K + \frac{2}{3} \hat{p}_3 w_3.
 \end{aligned}$$

where  $K := -k(\theta, \varphi, \eta, 0)$  as earlier. We find that there is a unique equilibrium of the system at the equator  $r_3 = \varepsilon_3 = 0$ , where  $w_3 = w_3^* := -\frac{1}{2} 3^{\frac{2}{3}} K^{\frac{1}{3}} < 0$  and  $p_3 = p_3^* := -3^{\frac{1}{3}} K^{\frac{2}{3}} < 0$ . The linearisation of the system in (3.49) around this equilibrium gives 4 nonzero eigenvalues: three negative eigenvalues

$$(3.52) \quad \lambda_{1,-} = \frac{4}{3} w_3^*, \quad \lambda_{2,-} = \frac{5}{3} w_3^*, \quad \text{and} \quad \lambda_{3,-} = 2w_3^*;$$

and one positive eigenvalue

$$(3.53) \quad \lambda_{1,+} = -\frac{1}{3} w_3^*.$$

Due to the equilibrium being both unique and attracting on the sphere, we can be sure that the special solution in subsection 3.2.2 is attracted to it.

The unstable manifold corresponding to  $\lambda_{1,+}$  is tangent to

$$(3.54) \quad \Gamma_{1,+} = \left\{ (x, y, r_3, \psi, \theta, \eta, \varphi, w_3, \Psi, \Theta, \varepsilon_3, p_3) \mid w_3 = w_3^* - \frac{4}{7} \delta w_3^{*2} r_3, p_3 = p_3^* - \frac{3}{7} K \delta r_3 \right\}.$$

Orbits (including the special solution) then tend to follow  $\Gamma_{1,+}$ . Writing (3.54) in terms of  $(\zeta, w, p)$ ,

$$(3.55) \quad p = p_3^*(-\zeta)^{\frac{2}{3}} + \frac{3}{7} K \delta \zeta, \quad w = w_3^*(-\zeta)^{\frac{4}{3}} - \frac{4}{7} \delta w_3^{*2} (-\zeta)^{\frac{5}{3}}.$$

Here,  $p$ ,  $w$  and  $\zeta$  are all negative and decreasing, and we are led to believe that they become  $\mathcal{O}(1)$ ; the surface is beginning to become compressed, its rate of compression is increasing, and the rod's configuration is becoming further away from configurations where vertical equilibrium are possible ( $p > 0$ ).

In the following section we study orbits that begin when  $p < 0$  and  $p = \mathcal{O}(1)$  and show that they undergo impact without collision (IWC).

### 3.3 Impact without collision

It has previously shown that for the regularised classical Painlevé problem, that when  $p < 0$  and  $p = \mathcal{O}(1)$ , the rod undergoes IWC [81, 82]. This IWC was shown to take the form of three successive modes of dynamics: slipping compression, sticking compression and lift-off [42]. In this section we show that this series of modes also occurs in the 3D problem, when  $p < 0$  and  $p = \mathcal{O}(1)$ , but with additional complications at the transition from slipping to sticking. As a result, the following sections will be organised as in the phases of IWC:

1. subsection 3.3.1 — Slipping compression
2. subsection 3.3.2 — Slipping-to-sticking and sticking compression
3. subsection 3.3.3 — Lift-off.

The dynamics of these modes occur at different scales; we will use the blowup method to match the dynamics across these scales (and not to desingularise a nonhyperbolic point). As we are extending the results of in [42] to 3D, the analysis is very similar.

Firstly, we use the blowup transformation

$$(3.56) \quad (r, (\bar{\zeta}, \bar{w}, \bar{\varepsilon})) \mapsto (\zeta, w, \varepsilon)$$

given by

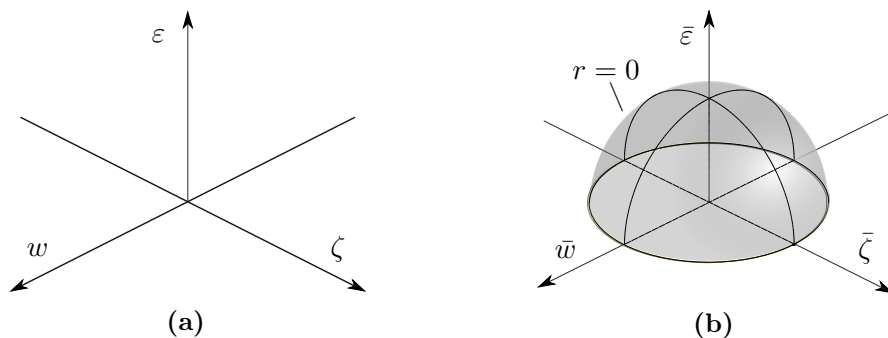
$$(3.57) \quad (\zeta, w, \varepsilon) = r(\bar{\zeta}, \bar{w}, \bar{\varepsilon}), \quad (r, (\bar{\zeta}, \bar{w}, \bar{\varepsilon})) \in [0, \infty) \times S_+^2,$$

where  $S_+^2$  is the unit hemisphere

$$(3.58) \quad S_+^2 := \{(\bar{\zeta}, \bar{w}, \bar{\varepsilon}) \mid \bar{\zeta}^2 + \bar{w}^2 + \bar{\varepsilon}^2 = 1, \bar{\varepsilon} \geq 0\}.$$

We will overload the notation used in our previous blowup transformation.





**Figure 3.10:** Sketch of the blowup of the point  $\zeta = w = \varepsilon = 0$ , in (a), to the (hemi)sphere  $\bar{\zeta}^2 + \bar{w}^2 + \bar{\varepsilon}^2 = 1$ ,  $\bar{\varepsilon} \geq 0$ , in (b).

### 3.3.1 Slipping compression

In the scaling chart of the blowup (3.57), setting  $\bar{\varepsilon} = 1$  we find the chart

$$(3.59) \quad \kappa_1 : \quad \zeta = r_1 \zeta_1, \quad w = r_1 w_1, \quad \varepsilon = r_1.$$

This transformation zooms in on  $\zeta = 0$  and  $w = 0$ . Using this substitution the equations in (3.14) become

$$(3.60) \quad \begin{aligned} x' &= \varepsilon \eta \cos(\psi + \varphi), & \eta' &= \varepsilon \left( A_1(\Psi, \Theta, \theta, \varphi) + Q_1(\theta, \varphi) \hat{F}_z(\zeta_1, w) \right), \\ y' &= \varepsilon \eta \sin(\psi + \varphi), & \eta \varphi' &= \varepsilon \left( (A_2(\Psi, \Theta, \theta, \varphi) - \eta \Psi) + Q_2(\theta, \varphi) \hat{F}_z(\zeta_1, w) \right), \\ \zeta_1' &= w_1, & w_1' &= b(\Psi, \Theta, \theta) + p(\theta, \varphi) \hat{F}_z(\zeta_1, w), \\ \psi' &= \varepsilon \Psi, & \Psi' &= \varepsilon \left( c_1(\Psi, \Theta, \theta) + d_1(\theta, \varphi) \hat{F}_z(\zeta_1, w) \right), \\ \theta' &= \varepsilon \Theta, & \Theta' &= \varepsilon \left( c_2(\Psi, \theta) + d_2(\theta, \varphi) \hat{F}_z(\zeta_1, w) \right). \end{aligned}$$

Now (3.60) is a slow-fast system in slow time where only  $\zeta_1$  and  $w_1$  are fast and the rest of the variables are slow.

In the layer problem of (3.60) (taking the limit  $\varepsilon \rightarrow 0$ ), and within the inconsistent region (where  $p < 0$ ,  $b < 0$ ) it is clear that there are no critical points because  $w_1' < 0$  since  $\hat{F}_z \geq 0$ . However, if we take the smooth extension of  $\hat{F}_z$  to  $\hat{f}_z$ , there is a critical set

$$(3.61) \quad C_1 = \{(x, y, \zeta_1, \psi, \theta, \eta, \varphi, w_1, \Psi, \Theta) | \zeta_1 = b/p, w_1 = 0\}.$$

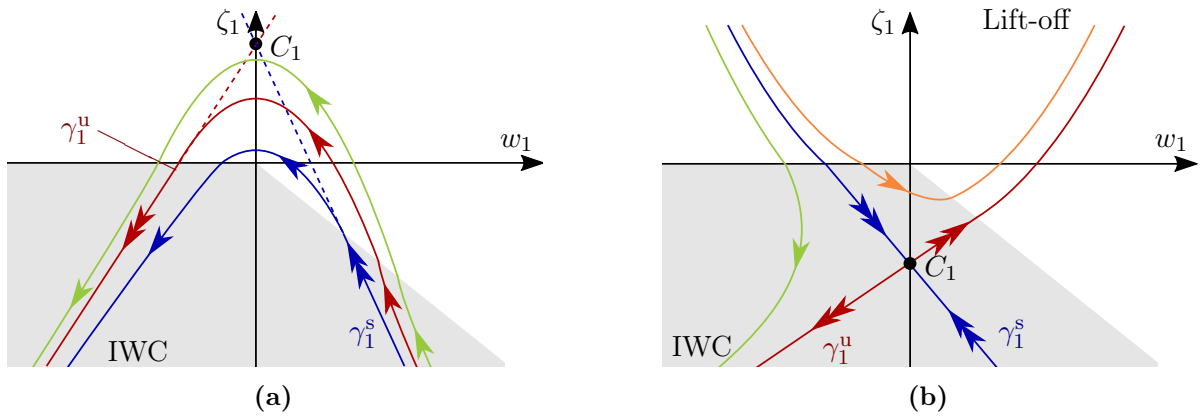
This set lies within  $\zeta_1 > 0$  and so is an artefact of the PWS system. In the indeterminate region (where  $p < 0$  and  $b > 0$ ) this critical set is within  $\zeta_1 < 0$  and exists within the PWS system.

The only nonzero eigenvalues of the Jacobian of (3.60) about  $C_1$  in the limit  $\varepsilon \rightarrow 0$  are  $\lambda_{\pm}$ , as in (3.19). The unstable and stable manifolds of  $C_1$  corresponding to  $\lambda_{\pm}$  respectively, are

tangent to

$$(3.62) \quad \gamma_1^{u,s}(x_0, y_0, \psi_0, \theta_0, \eta_0, \varphi_0, \Psi_0, \Theta_0) = \left\{ \begin{array}{l} (x, y, \zeta_1, \psi, \theta, \eta, \varphi, w_1, \Psi, \Theta) | \\ (x, y, \psi, \theta, \eta, \varphi, \Psi, \Theta) = (x_0, y_0, \psi_0, \theta_0, \eta_0, \varphi_0, \Psi_0, \Theta_0), \\ w_1 = \lambda_{\pm}(\varphi_0, \theta_0) \left( \zeta_1 - \frac{b(\Psi_0, \theta_0, \Theta_0)}{p(\varphi_0, \theta_0)} \right), \hat{F}_z(\zeta_1, w_1) > 0 \end{array} \right\}.$$

Within the inconsistent region, trajectories near to  $\zeta = w = 0$  tend to follow the unstable manifold of  $C_1$ , with both  $\zeta_1$  and  $w_1$  decreasing. In the indeterminate region, the stable manifold of  $C_1$ ,  $\gamma_1^s$ , acts as a separatrix of trajectories that undergo IWC and those that lift-off; either  $\zeta_1$  and  $w_1$  both decrease or increase. Phase portraits of the layer problem of (3.60) are shown in Figure 3.11.



**Figure 3.11:** Phase portraits of the layer problem of (3.60), for both the inconsistent (a) and indeterminate (b) regions. The region where  $\hat{F}(\zeta_1, w_1 > 0)$  is shown in gray. In (a), the critical set of the smooth extension of the layer problem of (3.60)  $C_1$  exists with in  $\zeta_1 > 0$  and is an artefact of the PWS system. Its stable and unstable manifolds ( $\gamma_1^s$  and  $\gamma_1^u$ ), however, do extend into the PWS system. In (b), this set  $C_1$  is within  $\hat{F}(\zeta_1, w_1 > 0)$  and exists in the PWS system. Its stable manifold  $\gamma_1^s$  acts a a separatrix of solutions that undergo IWC and those that lift off. These figures are effectively identical to [42, Figures 4 & 5].

To study the dynamics as the surface is compressed further, we use the chart

$$(3.63) \quad \kappa_2 : \quad \zeta = -r_2, \quad w = r_2 w_2, \quad \varepsilon = r_2 \varepsilon_2,$$

found by setting  $\bar{\zeta} = -1$  in the blowup (3.57). The coordinate transformation between  $\kappa_2$  and  $\kappa_1$  is given by

$$(3.64) \quad \kappa_{1,2} : \quad \zeta_1 = -\varepsilon_2^{-1}, \quad w_1 = \varepsilon_2^{-1} w_2, \quad r_1 = \varepsilon_2 r_2.$$

Writing  $\gamma_1^u$  (from (3.62)) in the chart  $\kappa_2$  using (3.64), we find

$$(3.65) \quad \gamma_1^u(x_0, y_0, \psi_0, \theta_0, \eta_0, \varphi_0, \Psi_0, \Theta_0) = \left\{ (x_0, y_0, r_2, \psi_0, \theta_0, \eta_0, \varphi_0, w_2, \Psi_0, \Theta_0, \varepsilon_2) \mid \right. \\ \left. w_2 = -\lambda_+ - \frac{\lambda_+ b}{p} \varepsilon_2, r_2 = 0, \varepsilon_2 > 0 \right\}.$$

Furthermore, in this chart, (3.14) becomes

$$(3.66) \quad \begin{aligned} x' &= \varepsilon \eta \cos(\psi + \varphi), & \eta' &= r_2 (\varepsilon_2 A_1(\Psi, \Theta, \theta, \varphi) + Q_1(\theta, \varphi) (1 - \delta w_2)), \\ y' &= \varepsilon \eta \sin(\psi + \varphi), & \eta \varphi' &= r_2 (\varepsilon_2 (A_2(\Psi, \Theta, \theta, \varphi) - \eta \Psi) + Q_2(\theta, \varphi)) (1 - \delta w_2), \\ r_2' &= -r_2 w_2, & w_2' &= \varepsilon_2 b(\Psi, \Theta, \theta) + p(\theta, \varphi)(1 - \delta w_2) + w_2^2, \\ \psi' &= \varepsilon \Psi, & \Psi' &= r_2 (\varepsilon_2 c_1(\Psi, \Theta, \theta) + d_1(\theta, \varphi) (1 - \delta w_2)), \\ \theta' &= \varepsilon \Theta, & \Theta' &= r_2 (\varepsilon_2 c_2(\Psi, \theta) + d_2(\theta, \varphi) (1 - \delta w_2)), \\ \varepsilon_2' &= \varepsilon_2 w_2. \end{aligned}$$

Along the equator ( $r_2 = 0, \varepsilon_2 = 0$ ), there are two sets of equilibria of (3.66),

$$(3.67) \quad M_{\pm} = \{(x, y, r_2, \psi, \theta, \eta, \varphi, w_2, \Psi, \Theta, \varepsilon_2) \mid r_2 = 0, \varepsilon_2 = 0, w_2 = -\lambda_{\mp}\}.$$

The linearisation of the system around each set equilibria  $M_{\pm}$  gives a Jacobian with three non zero eigenvalues:  $\Lambda_1^{\pm} = -\lambda_{\mp}$ ,  $\Lambda_2^{\pm} = \lambda_{\mp}$ , and  $\Lambda_3^{\pm} = \delta p - 2\lambda_{\mp} = \pm \sqrt{p(p\delta^2 - 4)}$ . Constrained to the sphere  $r_2 = 0$ ,  $M_+$  is a saddle whilst  $M_-$  is a stable node.

When  $p < 0$ ,  $\Lambda_1^- = -\lambda_+ < 0$ . The stable eigenspace of  $M_-$  corresponding to the eigenvalue  $\Lambda_1^-$  is given by

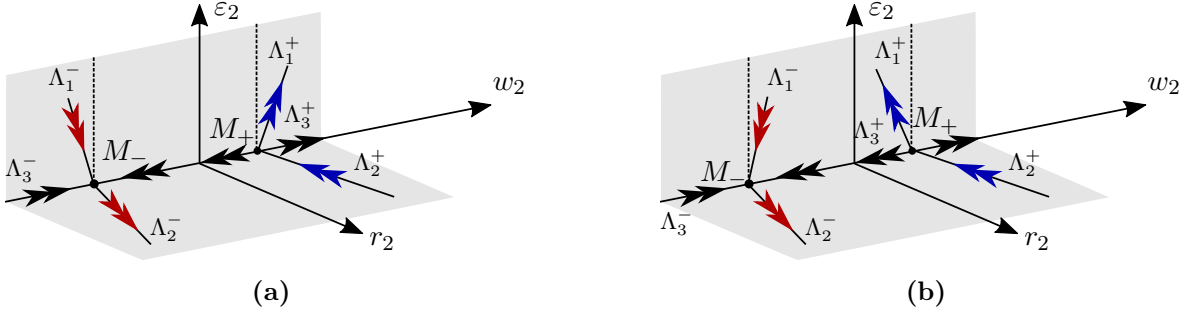
$$(3.68) \quad \gamma_2^1(x_0, y_0, \psi_0, \theta_0, \eta_0, \varphi_0, \Psi_0, \Theta_0) = \left\{ (x_0, y_0, r_2, \psi_0, \theta_0, \eta_0, \varphi_0, w_2, \Psi_0, \Theta_0, \varepsilon_2) \mid \right. \\ \left. w_2 = -\lambda_+ - \frac{\lambda_+ b}{p} \varepsilon_2 + \mathcal{O}(\varepsilon_2), r_2 = 0, \varepsilon_2 > 0 \right\}.$$

This coincides with the unstable manifold of  $C_1$  written in the chart  $\kappa_2$  (3.65).

When  $p < 0$ , exactly one of the eigenvalues of the Jacobian around  $M_-$  is positive ( $\Lambda_2^- = \lambda_+$ ). The corresponding unstable manifold of this critical set is given by

$$(3.69) \quad \gamma_2^u(x_0, y_0, \psi_0, \theta_0, \eta_0, \varphi_0, \Psi_0, \Theta_0) = \left\{ (x, y, r_2, \psi, \theta, \eta, \varphi, w_2, \Psi, \Theta, \varepsilon_2) \mid \right. \\ (x, y, \psi, \theta, \varepsilon_2) = (x_0, y_0, \psi_0, \theta_0, 0), \\ \left. (w_2, \eta, \varphi, \Psi, \Theta, \theta) = (-\lambda_+, \eta_0, \varphi_0, \Psi_0, \Theta_0, \theta_0, 0) - \frac{\lambda_+}{p} \left( \frac{\partial p}{\partial \varphi} \frac{Q_2}{\eta} \frac{\lambda_+^4}{2\lambda_-^2 - p}, Q_1, \frac{Q_2}{\eta}, d_1, d_2 \right) r_2, r_2 > 0 \right\}.$$

From (3.69), we can deduce that  $\eta$  decreases from the sign of  $Q_1$ . Since  $\eta$  is in the denominator of the  $w$  and  $\varphi$  terms, we will need to study (3.7) as  $\eta$  approaches 0.



**Figure 3.12:** Phase portraits of the layer problem of (3.66), for both the inconsistent (a) and indeterminate (b) regions. The region where  $\hat{F}(\zeta_1, w_1 > 0)$  is shown in gray.

### 3.3.2 Slipping-to-sticking and sticking compression

To obtain (3.7), we had made assumptions that the tip was slipping. However, we have now found that, following (3.69), the rod tip may stick. Here, through the regularisation of Coulomb friction and blowup, we analyse the transition from slipping to sticking and the resulting sticking dynamics<sup>20</sup>.

Starting from the equations after the initial scaling (3.7), we desingularise  $\eta = 0$ , rescaling time such that we “multiply” the right-hand side by  $\eta$

$$\begin{aligned}
 (3.70) \quad x' &= \varepsilon \eta^2 \cos(\varphi + \psi), & \eta' &= \eta \left( \varepsilon A_1(\Psi, \Theta, \theta, \varphi) + Q_1^\xi(\theta, \varphi, R(\eta, \xi)) \hat{F}_z(\zeta, w) \right), \\
 y' &= \varepsilon \eta^2 \sin(\varphi + \psi), & \varphi' &= \varepsilon \left( A_2(\Psi, \Theta, \theta, \varphi) - \eta \Psi \right) + Q_2^\xi(\theta, \varphi, R(\eta, \xi)) \hat{F}_z(\zeta, w), \\
 \zeta' &= \eta w, & w' &= \eta \left( \varepsilon b(\Psi, \Theta, \theta) + p^\xi(\theta, \varphi, R(\eta, \xi)) \hat{F}_z(\zeta, w) \right), \\
 \psi' &= \varepsilon \eta \Psi, & \Psi' &= \eta \left( \varepsilon c_1(\Psi, \Theta, \theta) + d_1^\xi(\theta, \varphi, R(\eta, \xi)) \hat{F}_z(\zeta, w) \right), \\
 \theta' &= \varepsilon \eta \Theta, & \Theta' &= \eta \left( \varepsilon c_2(\Psi, \theta) + d_2^\xi(\theta, \varphi, R(\eta, \xi)) \hat{F}_z(\zeta, w) \right).
 \end{aligned}$$

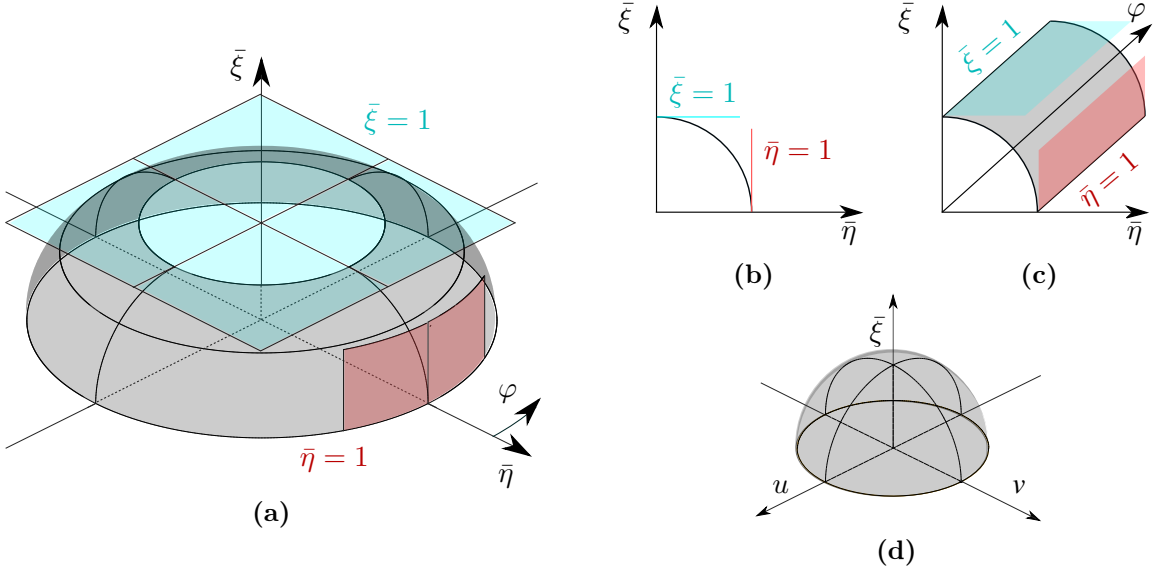
The set where  $\eta = \xi = 0$  is singular due to the nonsmoothness of  $R(\eta, \xi)$  there. However we can gain smoothness through the use of blowup. In particular we blow up  $\eta = \xi = 0$  to a section of a torus using the blowup transformation<sup>21</sup>

$$(3.71a) \quad \eta = r \bar{\eta}, \quad \xi = r \bar{\xi}, \quad \bar{\eta}, \bar{\xi}, r \geq 0,$$

$$(3.71b) \quad (\bar{\eta}, \bar{\xi}, \varphi) \in \mathbb{T}_+^2 = \{\varphi \mid \varphi \in S^1\} \times \{(\bar{\eta}, \bar{\xi}) \mid (\bar{\eta}, \bar{\xi}) \in S^1, \bar{\eta} \geq 0, \bar{\xi} \geq 0\}.$$

<sup>20</sup>The theory behind this method is given in Chapter 4.

<sup>21</sup>Whilst we would like to use a spherical blowup, the equations in the scaling chart will be much simpler using polar coordinates. Hence a toroidal blowup is convenient. Details of this blowup are given in Figure 3.13.



**Figure 3.13:** Sketch of the geometry of the blowup of  $\eta, \xi = 0$ . In (a), we show (3.71) as a toroidal blowup, with scaling chart found by setting  $\bar{\xi} = 1$  and entry chart found by setting  $\bar{\eta} = 1$  in the blowup. In (b) and (c), we show an alternative representation of the blowup: as a polar blowup of the set  $\eta = \xi = 0$ , made cylindrical by extending with  $\varphi$  in (c). (c) can be considered as the “unwrapping” of (a). (d) shows the alternative to the blowup used in (3.71): a spherical blowup of  $u = v = \xi = 0$ . Due to the convenience of the trigonometric terms and a single entry chart, this spherical blowup is not used.

To investigate how trajectories reach  $\eta = 0$  we study the entry chart of the blowup (3.71) found by setting  $\bar{\eta} = 1$  ( $\eta = r_2$ ,  $\xi = r_2\xi_2$ ). Here the equations become

$$\begin{aligned}
 (3.72) \quad x' &= \varepsilon r_2^2 \cos(\varphi + \psi), & r_2' &= r_2 \left( \varepsilon A_1(\Psi, \Theta, \theta, \varphi) + Q_1^\xi(\theta, \varphi, \tilde{R}(\xi_2)) \hat{F}_z(\zeta, w) \right), \\
 y' &= \varepsilon r_2^2 \sin(\varphi + \psi), & \varphi' &= \varepsilon (A_2(\Psi, \Theta, \theta, \varphi) - r_2 \Psi) + Q_2^\xi(\theta, \varphi, \tilde{R}(\xi_2)) \hat{F}_z(\zeta, w), \\
 \zeta' &= r_2 w, & w' &= r_2 \left( \varepsilon b(\Psi, \Theta, \theta) + p^\xi(\theta, \varphi, \tilde{R}(\xi_2)) \hat{F}_z(\zeta, w) \right), \\
 \psi' &= r_2 \varepsilon \Psi, & \Psi' &= r_2 \left( \varepsilon c_1(\Psi, \Theta, \theta) + d_1^\xi(\theta, \varphi, \tilde{R}(\xi_2)) \hat{F}_z(\zeta, w) \right), \\
 \theta' &= r_2 \varepsilon \Theta, & \Theta' &= r_2 \left( \varepsilon c_2(\Psi, \theta) + d_2^\xi(\theta, \varphi, \tilde{R}(\xi_2)) \hat{F}_z(\zeta, w) \right), \\
 & & \xi_2' &= -\xi_2 \left( \varepsilon A_1(\Psi, \Theta, \theta, \varphi) + Q_1^\xi(\theta, \varphi, \tilde{R}(\xi_2)) \hat{F}_z(\zeta, w) \right).
 \end{aligned}$$

where

$$(3.73) \quad \tilde{R}(\xi_2) \equiv R(r_2, r_2 \xi_2) = \frac{1}{\sqrt{1 + \xi_2^2}}.$$

Along the equator of the torus  $r_2 = \xi_2 = 0$ , there are two classes of sets of equilibria of (3.72),

(3.74)

$$v_1^\pm = \left\{ (x, y, \zeta, \psi, \theta, r_2, \varphi, w, \Psi, \Theta, \xi_2) \mid \varphi = \pm \frac{\pi}{2}, r_2 = 0, \xi_2 = 0 \right\}$$

and

(3.75)

$$v_2^\pm = \left\{ (x, y, \zeta, \psi, \theta, r_2, \varphi, w, \Psi, \Theta, \xi_2) \mid \varphi = \frac{\pi}{2} \pm \arccos \left( \frac{\alpha \sin \theta \hat{F}_z - \varepsilon (\Psi^2 \cos^2 \theta + \Theta^2)}{\alpha \mu \cos \theta \hat{F}_z} \right), r_2 = 0, \xi_2 = 0 \right\}$$

To study the dynamics along  $\eta = 0$  we use the  $\bar{\xi} = 1$  chart ( $\eta = \xi \eta_1$ ). Here we are left with a slow fast system in fast time with respect to  $\xi$

$$(3.76) \quad \begin{aligned} x' &= \varepsilon \xi^2 \eta_1^2 \cos(\varphi + \psi), & \eta_1' &= \eta_1 \left( \varepsilon A_1(\Psi, \Theta, \theta, \varphi) + Q_1^\xi(\theta, \varphi, \hat{R}(\eta_1)) \hat{F}_z(\zeta, w) \right), \\ y' &= \varepsilon \xi^2 \eta_1^2 \sin(\varphi + \psi), & \varphi' &= \varepsilon (A_2(\Psi, \Theta, \theta, \varphi) - \xi \eta_1 \Psi) + Q_2^\xi(\theta, \varphi, \hat{R}(\eta_1)) \hat{F}_z(\zeta, w), \\ \zeta' &= \xi \eta_1 w, & w' &= \xi \eta_1 \left( \varepsilon b(\Psi, \Theta, \theta) + p^\xi(\theta, \varphi, \hat{R}(\eta_1)) \hat{F}_z(\zeta, w) \right), \\ \psi' &= \xi \eta_1 \varepsilon \Psi, & \Psi' &= \xi \eta_1 \left( \varepsilon c_1(\Psi, \Theta, \theta) + d_1^\xi(\theta, \varphi, \hat{R}(\eta_1)) \hat{F}_z(\zeta, w) \right), \\ \theta' &= \xi \eta_1 \varepsilon \Theta, & \Theta' &= \xi \eta_1 \left( \varepsilon c_2(\Psi, \theta) + d_2^\xi(\theta, \varphi, \hat{R}(\eta_1)) \hat{F}_z(\zeta, w) \right), \end{aligned}$$

where  $\eta_1$  and  $\varphi$  are fast w.r.t.  $\xi$  and

$$(3.77) \quad \hat{R}(\eta_1) \equiv R(\xi \eta_1, \xi) = \frac{\eta_1}{\sqrt{1 + \eta_1^2}}.$$

In the layer problem ( $\lim_{\xi \rightarrow 0}$  (3.76)),  $x' = \dots = \Theta' = 0$  and

$$(3.78) \quad \begin{aligned} \eta_1' &= \eta_1 \left( \varepsilon A_1(\Psi, \Theta, \theta, \varphi) + Q_1^\xi(\theta, \varphi, \hat{R}(\eta_1)) \hat{F}_z(\zeta, w) \right), \\ \varphi' &= \varepsilon A_2(\Psi, \Theta, \theta, \varphi) + Q_2^\xi(\theta, \varphi, \hat{R}(\eta_1)) \hat{F}_z(\zeta, w). \end{aligned}$$

There are two generic classes of critical sets of this layer problem (3.78)

$$(3.79) \quad \Sigma_1^\pm = \left\{ (\eta_1, \varphi) \mid \eta_1 = 0, \varphi = \pm \frac{\pi}{2} \right\}$$

and

$$(3.80) \quad \Sigma_2^\pm = \left\{ (\eta_1, \varphi) \mid \hat{R}(\eta_1) = \hat{R}_*^\pm := \mp \frac{\cos \theta \left( \alpha \hat{F}_z \sin \theta - \varepsilon (\Psi^2 \cos^2 \theta + \Theta^2) \right)}{(1 + \alpha \cos^2 \theta) \mu \hat{F}_z}, \varphi = \pm \frac{\pi}{2} \right\}.$$

Firstly, we find that the Jacobians of (3.78) around  $\Sigma_1^\pm$  are

$$(3.81) \quad \pm \begin{pmatrix} -\alpha \hat{F}_z \sin \theta \cos \theta + \varepsilon (\Psi^2 \cos^2 \theta + \Theta^2) \cos \theta & 0 \\ 0 & \alpha \hat{F}_z \sin \theta \cos \theta - \varepsilon (\Psi^2 \cos^2 \theta + \Theta^2) \cos \theta \end{pmatrix}$$

respectively. Hence  $\Sigma_1^\pm$  are saddles of (3.78).<sup>22</sup>

Secondly, for  $\Sigma_2^\pm$ , because we are only considering  $\eta \geq 0$  (and hence  $0 \leq \hat{R} \leq 1$ ), at most one of these solutions can exist:  $\Sigma_2^+$  if  $0 < \hat{R}_*^+ < 1$ ,  $\Sigma_2^-$  if  $0 < \hat{R}_*^- < 1$ . For  $p < 0$  and  $\varepsilon$  small,  $\Sigma_2^-$  exists. It is possible to show that the Jacobian of (3.78) around  $\Sigma_2^-$  is

$$(3.82) \quad \begin{pmatrix} -\mu \hat{F}_z \eta_1^* (1 + \alpha \sin^2 \theta) \hat{R}'(\eta_1^*) & 0 \\ 0 & -(1 + \alpha) \mu \hat{R}(\eta_1^*) \end{pmatrix},$$

which corresponds to a stable node under our assumptions.

We can construct the full phase portrait of the limit  $\varepsilon \rightarrow 0$  of (3.70) in the blowup (3.71) by piecing together the dynamics in  $\bar{\eta} = 1$  and  $\bar{\xi} = 1$  (Figure 3.14). Where  $p < 0$  we are only concerned with Figure 3.14d.

We can then find the slow flow of (3.76) along  $\Sigma_2$  is given by  $x' = \dots = \varphi' = 0$

$$(3.83) \quad \begin{aligned} \zeta' &= w, & w' &= \frac{(1 + \alpha)}{1 + \alpha \sin^2 \theta} \hat{F}_z + \varepsilon \frac{(1 + \alpha)b + \alpha \cos^2 \theta}{1 + \alpha \sin^2 \theta}, \\ \psi' &= \varepsilon \Psi, & \Psi' &= \varepsilon c_1(\Psi, \Theta, \theta), \\ \theta' &= \varepsilon \Theta, & \Theta' &= \left( \varepsilon \left( \frac{\alpha \sin \theta \cos \theta (\Psi^2 \cos^2 \theta + \Theta^2)}{1 + \alpha \sin^2 \theta} + c_2 \right) + \frac{-\alpha \cos \theta}{1 + \alpha \sin^2 \theta} \hat{F}_z(\zeta, w) \right). \end{aligned}$$

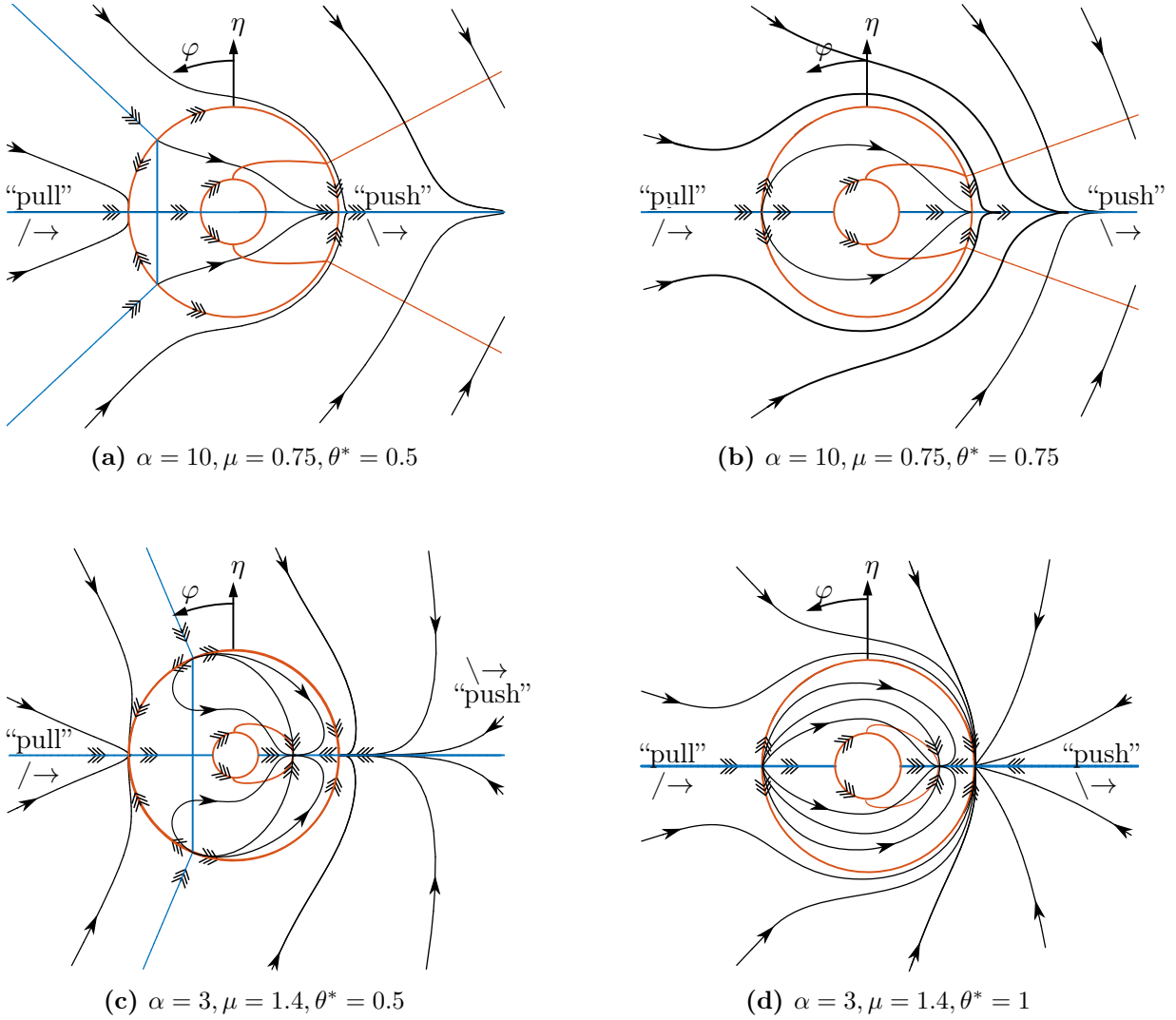
Finding the layer problem of (3.83) w.r.t  $\varepsilon$  ( $\varepsilon \rightarrow 0$ ),  $x' = \dots = \theta' = 0$  and

$$(3.84) \quad \begin{aligned} \zeta' &= w, \\ w' &= \frac{(1 + \alpha)}{1 + \alpha \sin^2 \theta} \hat{F}_z(\zeta, w) := p_S(\theta) \hat{F}_z(\zeta, w), \\ \Theta' &= \frac{-\alpha \cos \theta}{1 + \alpha \sin^2 \theta} \hat{F}_z(\zeta, w) := d_S(\theta) \hat{F}_z(\zeta, w). \end{aligned}$$

Since  $\psi' = \Psi' = 0$  and  $\varphi = -\pi/2$ , the dynamics now follow slipping compression as in the 2D problem [42, (2.9) and (4.28)] and the rod undergoes sticking compression until it lifts off.

---

<sup>22</sup>These artificial sets of equilibria are a result of the toroidal blowup in (3.71).



**Figure 3.14:** Phase portraits of the limit  $\varepsilon \rightarrow 0$  of (3.70) in the blowup (3.71) projected down onto the plane  $\xi = 0$ .

### 3.3.3 Lift-off

Qualitatively, we can see from (3.84), that  $w' > 0$  and so  $w$  increases. Therefore,  $w$  will change sign from negative to positive. Accordingly  $\zeta'$  will become positive and  $\zeta$  will increase. At some point  $\hat{F}_z(\zeta, w) = 0$  and the rod lifts off.

Solving (3.84), we find

$$\begin{aligned}
 \zeta(\tau) &= \Upsilon_+ e^{v_+ \tau} + \Upsilon_- e^{v_- \tau}, \\
 w(\tau) &= v_+ \Upsilon_+ e^{v_+ \tau} + v_- \Upsilon_- e^{v_- \tau}, \\
 \Theta(\tau) &= \Theta_0 + d_S(\theta) \left( \frac{\Upsilon_+}{v_+} (1 + \delta v_+) (1 - e^{v_+ \tau}) + \frac{\Upsilon_-}{v_-} (1 + \delta v_-) (1 - e^{v_- \tau}) \right),
 \end{aligned}
 \tag{3.85}$$



where

$$(3.86) \quad \Upsilon_{\pm} := \frac{w_0 - \zeta_0 v_{\mp}}{v_{\mp} - v_{\pm}} \equiv \mp \frac{w_0 - \zeta_0 v_{\mp}}{\sqrt{\delta^2 p_S(\theta)^2 - 4p_S(\theta)}},$$

$$(3.87) \quad v_{\pm} := \frac{-\delta p_S(\theta) \pm \sqrt{\delta^2 p_S(\theta)^2 - 4p_S(\theta)}}{2}.$$

We can determine the time at which lift-off occurs  $\tau_{\text{LO}}$ , by solving  $\hat{F}_z(\zeta(\tau_{\text{LO}}), w(\tau_{\text{LO}}))$  for  $\tau_{\text{LO}}$ :

$$(3.88) \quad \hat{F}_z(\zeta(\tau_{\text{LO}}), w(\tau_{\text{LO}})) = -\Upsilon_- (1 + \delta v_-) e^{v_- \tau_{\text{LO}}} - \Upsilon_+ (1 + \delta v_+) e^{v_+ \tau_{\text{LO}}}$$

$$(3.89) \quad \tau_{\text{LO}} = \frac{1}{v_+ - v_-} \ln \left( -\frac{\Upsilon_- (1 + \delta v_-)}{\Upsilon_+ (1 + \delta v_+)} \right)$$

$$(3.90) \quad = \frac{1}{\sqrt{\delta^2 p_S^2 - 4p_S}} \ln \left( \frac{(\zeta_0 v_- - w_0)^2 v_-^2}{w_0^2 + p \zeta_0^2 + \delta p \zeta_0 w_0 v_+^2} \right).$$

Lift-off therefore occurs when

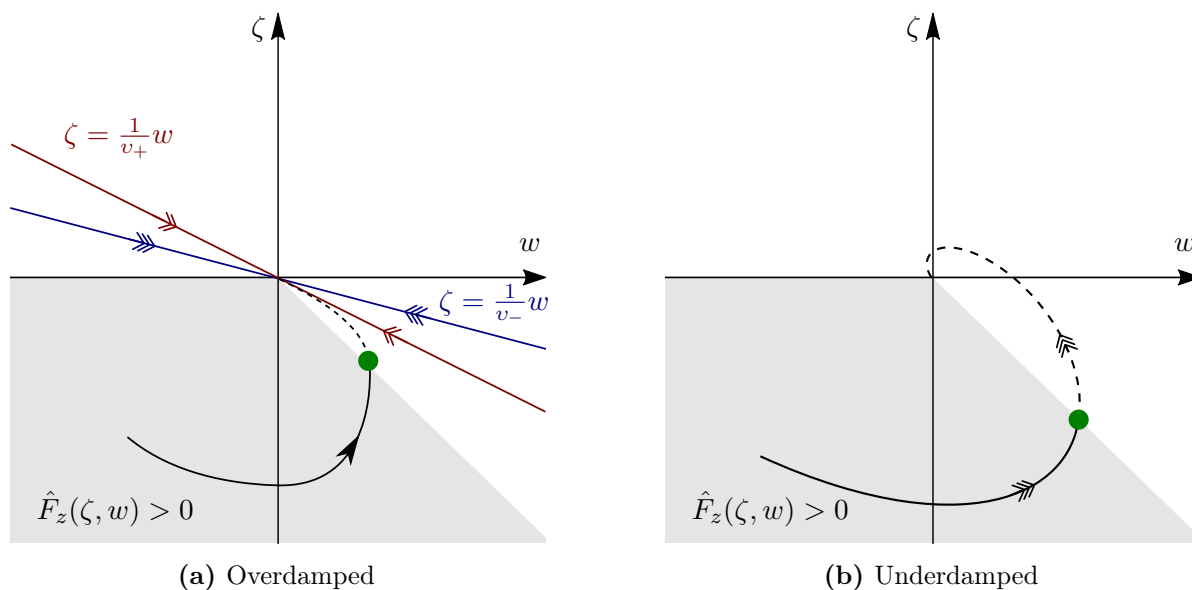
$$(3.91) \quad \zeta = \zeta(\tau_{\text{LO}}) = -\delta w(\tau_{\text{LO}}),$$

$$(3.92) \quad w = w(\tau_{\text{LO}}),$$

$$(3.93) \quad \Theta = \Theta(\tau_{\text{LO}}).$$

Since the smooth extension of (3.84) is a linear ODE, we can study the qualitative behaviour, through the eigenvectors and eigenvalues around the equilibrium  $\zeta = w = 0$ . We find that there are two eigenvalues with negative real parts  $v_{\pm}$ . If  $\delta^2 < 4/p_S$ ,  $v_{\pm}$  are a complex conjugate pair and there is anticlockwise rotation Figure 3.15b; we say that the system is underdamped. If  $\delta^2 > 4/p_S$ ,  $v_{\pm}$  are real with corresponding eigenspaces  $\zeta = \frac{1}{v_{\pm}} w$  Figure 3.15a; we say that the system is overdamped. It is straightforward to show that  $F_z \left( \frac{1}{v_{\pm}} w, w \right) = 0$ , and so these eigenspaces are artefacts of the PWS system in (3.84). The two possible phase portraits of (3.84) are shown in Figure 3.15.

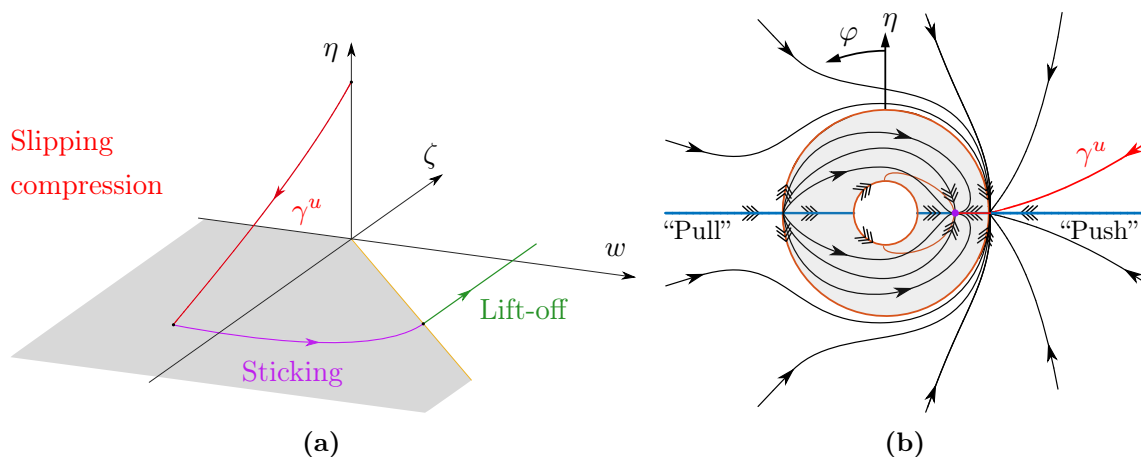
Once the rod has lifted off we should consider (3.83) where  $\hat{F}_z = 0$ , which give the equations for the rod in free-fall. Here, the rod will eventually fall back down onto the surface.



**Figure 3.15:** Phase portraits of the sticking system before lift off in both the overdamped (a) and underdamped (b) systems. The point of lift-off  $(w(\tau_{LO}), \zeta(\tau_{LO}))$  is shown in green  $\bullet$ .

### 3.3.4 Piecing together full IWC orbit

Piecing together the dynamics from subsections 3.3.1 and 3.3.2, we can find the full IWC solution (Figure 3.16a).



**Figure 3.16:** IWC. (a) Dynamics of the scaled vertical position  $\zeta$ , vertical velocity  $w$  and horizontal speed  $\eta$  of the rod tip; with the phases of IWC. (b) Dynamics of the speed  $\eta$  and relative slip angle  $\varphi$ . Top-down view of the blowup of  $\eta = \xi = 0$  to a torus.

### 3.4 Conclusions

In section 3.2, we have shown that the significant orbits discussed in Theorems 4.4 and 4.5 and [16], enter  $p < 0$  in the compliant problem. Once within  $p < 0$ , these orbits begin to undergo the first phase of IWC: slipping compression.

In section 3.3, we have demonstrated that like in the planar problem IWC is possible in both the indeterminate and inconsistent regions from the rigid-body problem. We have also found that the saddle structure around the vertical equilibrium of the rod tip found in the compliant problem also exists in the 3D problem. We find that IWC still follows 3 phases: slipping compression, sticking compression, and lift-off. However, in the 3D problem, due to the nonlinearities associated with spatial Coulomb friction, the study of the transition from slipping to sticking is more complicated. Here, we have dealt with this approach of regularising and blowing-up the discontinuity in Coulomb friction rather informally. In the following chapter, we shall discuss the theory of this approach more rigorously.

## Chapter 4

# Regularisation of isolated codimension-2 discontinuity sets

In this chapter<sup>23</sup>, we study regularisation of isolated codimension-2 discontinuity sets, studying the theory of the method used in subsection 3.3.2. For example, in the previous chapter we studied a regularised form of Coulomb friction without ensuring that our choice of regularisation function would not affect the resulting dynamics. In this chapter, we shall show that for Coulomb friction, this choice does not affect the dynamics.

### 4.1 Introduction

Piecewise-smooth (PWS) dynamical systems with discontinuity sets (along which the dynamics switches) are widely used to model systems with impact, dry friction, juddering, and buckling and in the study of relay control systems, mechanical systems, etc. [8, 49].

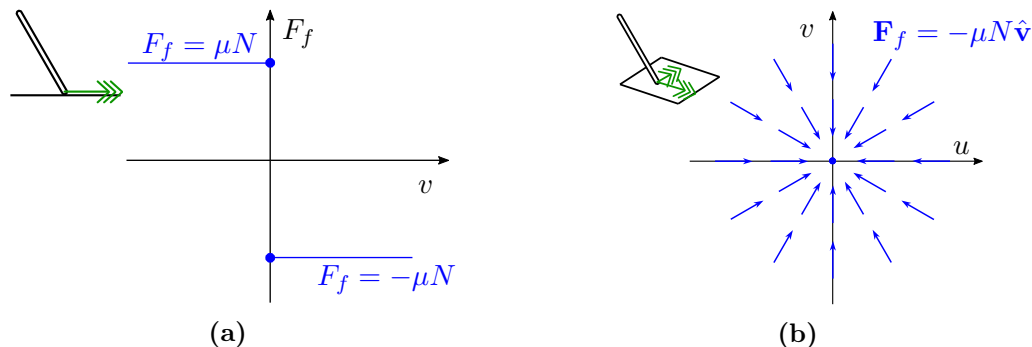
In the study of planar motion of rigid bodies with point contact, Coulomb friction results in a codimension-1 discontinuity set, where the relative velocity between two bodies is zero (see Figure 4.1a). But the existing framework for the study of these systems does not generalise to spatial motion of rigid bodies with point contact. In this case, Coulomb friction results in a codimension-2 discontinuity set [2, 3], where both components of the relative velocity between two bodies are simultaneously zero (see Figure 4.1b). Whilst friction is the primary motivation for this work, isolated codimension-2 discontinuity sets also occur in unit vector control design. For a brief introduction to unit control see [103, §3.5], and for an example of a resulting codimension-2 problem see [75].

We define our codimension-2 discontinuity problem as consisting of ODEs

$$(4.1) \quad \dot{\mathbf{x}} = \mathbf{F}(\mathbf{x}), \quad \mathbf{x} \in \mathbb{R}^n \setminus \Sigma,$$

---

<sup>23</sup>This chapter is adapted from [19]. See Acknowledgements for contributions.



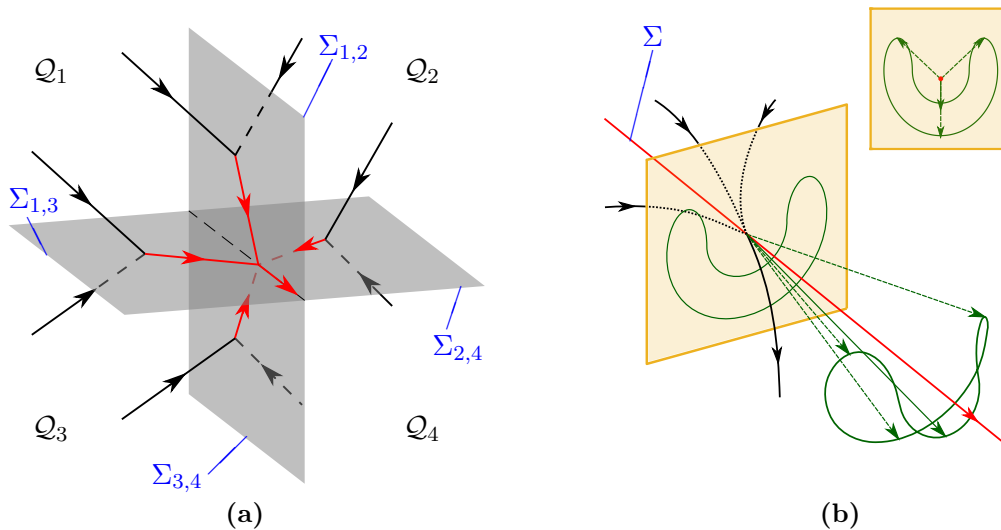
**Figure 4.1:** The discontinuity sets for Coulomb friction with (a) one and (b) two degrees of freedom in the relative velocities (shown in green) between objects, where  $\mu$  is the coefficient of friction and  $N$  is the normal reaction force. In (a), we have a planar rigid body with point contact, where Coulomb friction is given by  $F_f = -\mu N \text{sign}(v) = -\mu N \frac{v}{|v|}$  and there is a codimension-1 discontinuity at  $v = 0$ . In (b), we have a spatial rigid body system with point contact where Coulomb friction is given by  $\mathbf{F}_f = -\mu N \hat{\mathbf{v}} = -\mu N \frac{\mathbf{v}}{|\mathbf{v}|}$  where  $\mathbf{v} = (u, v)$  and there is a codimension-2 discontinuity at  $u = v = 0$ .

where  $\mathbf{F}$  is a vector field that is sufficiently smooth and well defined everywhere except on a connected *codimension-2* set  $\Sigma$  and  $(\dot{\cdot}) = \frac{d}{dt}(\cdot)$  denotes differentiation with respect to time  $t$ . Furthermore, the vector field  $\mathbf{F}$  has a well-defined directional limit onto  $\Sigma$  for each angle of approach (as with spatial Coulomb friction in Figure 4.1b).

This type of *nonsmooth* system is related to standard PWS dynamical systems [36], which consist of finitely many ODEs

$$(4.2) \quad \dot{\mathbf{x}} = \mathbf{F}_i(\mathbf{x}), \quad \mathbf{x} \in \mathcal{Q}_i \in \mathbb{R}^n,$$

where each  $\mathbf{F}_i$  is a sufficiently smooth vector field. Regions  $\mathcal{Q}_i$  are open sets separated by a codimension-1 discontinuity set  $\Sigma_{i,j}$  at the boundary between  $\mathcal{Q}_i$  and  $\mathcal{Q}_j$ . When two of these codimension-1 discontinuity sets intersect transversally, a codimension-2 discontinuity results [26–28, 36, 48, 49, 55]. As noted in [2], we must distinguish between these sorts of codimension-2 problems and isolated codimension-2 problems described by (4.1), as demonstrated in Figure 4.2.



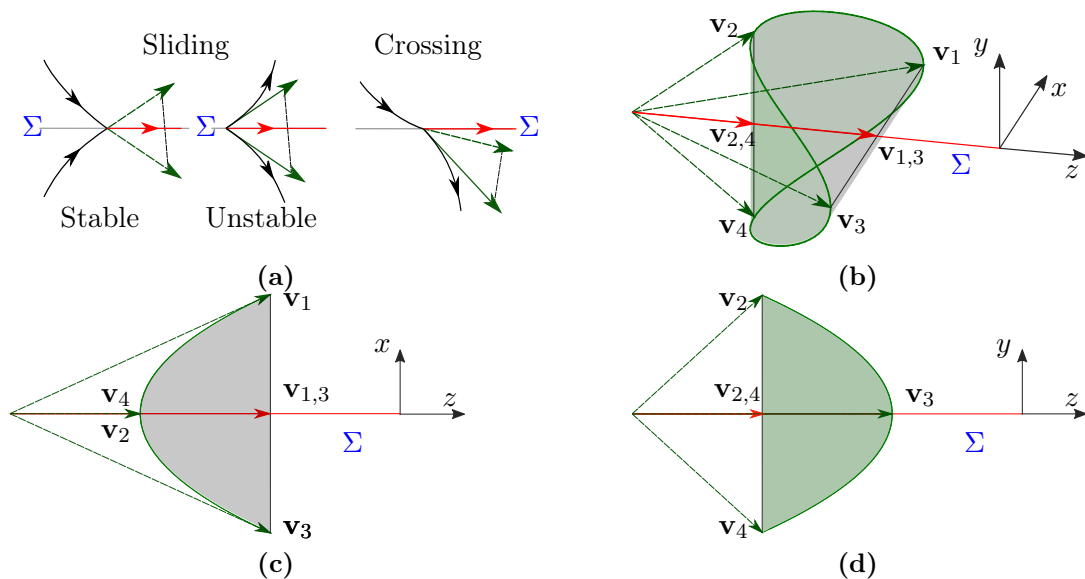
**Figure 4.2:** The difference between (a) the intersection of two codimension-1 discontinuity sets and (b) an isolated codimension-2 discontinuity set. In (a) trajectories reach the intersection of the two discontinuities along the codimension-1 discontinuities  $\Sigma_{i,j}$ . In (b) trajectories reach the codimension-2 discontinuity set  $\Sigma$  from a variety of different directions that do not correspond to codimension-1 discontinuity sets. The directional limit of  $F$  onto  $\Sigma$  is also shown (inset).

#### 4.1.1 Deficiencies of the existing framework

Standard PWS systems with codimension-1 discontinuity sets display two generic types of behaviour: crossing and sliding [36]. Crossing happens when trajectories pass through the discontinuity set without remaining on it for any period of time. Sliding occurs when trajectories reach the discontinuity set and continue along it. In many applications, it is then necessary to define a *sliding vector field* (the flow along this discontinuity set), often using the *Filippov convention*. These behaviours are shown in Figure 4.3a. If both vector fields are pointing into (or out from) the switching surface, we have sliding. If one vector field points in whilst the other points out, we have crossing.

With codimension-2 discontinuity sets, however, these definitions do not generalise intuitively. In Figure 4.2b it is not clear whether trajectories that reach  $\Sigma$  should “slide” along it or “cross” and leave it. Even if we can determine that there is sliding, how do we prescribe the sliding flow?

Motivated by Coulomb friction, Antali and Stépán gave a generalisation of the framework for standard (codimension-1) PWS systems to (codimension-2) *extended Filippov systems* [2]. They used the Filippov convention to construct the sliding vector field: a convex combination of the vectors incident to the discontinuity set, that is tangent to the discontinuity set. They noted that this convention does not generically give a unique sliding vector in the case of a codimension-2 problem.



**Figure 4.3:** Demonstration of the generic nonuniqueness of the Filippov sliding vector field for codimension-2 discontinuity sets. In (a) the convex combination of the incident vectors is one-dimensional and its intersection with the codimension-1 discontinuity set  $\Sigma$  (where it exists) is generically unique. In (b) we see that, the convex hull of the incident vectors is typically  $n$ -dimensional and its intersection with the codimension-2 discontinuity set  $\Sigma$  is  $(n - 2)$ -dimensional. Hence, there are uncountably many possible vectors that are both a convex combination of the incident vectors  $\mathbf{v}_i$  and tangential to  $\Sigma$ . By way of illustration, we show two candidate sliding vectors:  $\mathbf{v}_{1,3}$  and  $\mathbf{v}_{2,4}$ . In (c) we see the projection of (b) onto the  $(x, z)$  plane. The convex combination of  $\mathbf{v}_1$  and  $\mathbf{v}_3$  that is tangential to  $\Sigma$  (the  $z$ -axis), is the candidate sliding vector  $\mathbf{v}_{1,3}$ . In (d) we see the projection of (b) onto the  $(y, z)$  plane. Applying the Filippov convention to  $\mathbf{v}_2$  and  $\mathbf{v}_4$  gives the candidate sliding vector  $\mathbf{v}_{2,4} \neq \mathbf{v}_{1,3}$ .

Let us first consider a standard PWS system (Figure 4.3a). The Filippov convention provides a unique sliding vector; the convex combination of two incident vectors spans a one-dimensional line section and its intersection with the plane tangent to the discontinuity set  $\Sigma$  is therefore a point (or the empty set in the case of crossing). Let us now consider the same definition when applied to a codimension-2 problem (Figure 4.3b). Here the codimension-2 discontinuity set  $\Sigma$  coincides with the  $z$ -axis and we show incident vectors:  $\mathbf{v}_i$   $i \in \{1 \dots 4\}$ . The convex combination of  $\mathbf{v}_1$  and  $\mathbf{v}_3$  gives one candidate  $\mathbf{v}_{1,3}$  for the sliding vector (Figure 4.3c). But, the convex combination of  $\mathbf{v}_2$  and  $\mathbf{v}_4$  gives another candidate sliding vector  $\mathbf{v}_{2,4} \neq \mathbf{v}_{1,3}$  (Figure 4.3d). In fact, there are uncountably many candidates for the sliding vector field that satisfy the Filippov convention, given here by  $\{\lambda \mathbf{v}_{1,3} + (1 - \lambda) \mathbf{v}_{2,4} | \lambda \in [0, 1]\}$ . This nonuniqueness should be expected unless all the incident vectors are coplanar. The set defined by the convex combination of incident vectors will generically be the same dimension as the space; the intersection of that set with the discontinuity set will therefore be codimension-2.

In this work, we use slow-fast theory, geometric singular perturbation theory (GSPT) and blowup to study extended Filippov systems. This approach not only addresses the generic nonuniqueness (Figure 4.3b) and the ambiguity about the definitions of sliding and crossing (Figure 4.2b), but also allows the use of the powerful and well-understood methods from smooth dynamical systems. We will study smooth but sharp systems as perturbations away from the nonsmooth limit. An understanding of the relationship between a PWS system and a (stiff) smooth system that approximates it is important, since it can reveal the robustness (or otherwise) of the PWS system to smoothing perturbations, see [63].

We regularise the nonsmooth system (4.1), viewing it as the (suitably defined) limit of a smooth system [102]. The resulting singularly perturbed smooth system has a hidden slow fast structure in the smoothing parameter  $\varepsilon$  and GSPT can be applied. Fenichel's theorems [35], and blowup [31, 67] can be used to study this singularly perturbed problem: connecting the dynamics approaching the discontinuity with the dynamics along it. This approach has proven useful in the study of regularisations of both codimension-1 discontinuity sets [61, 63, 65, 102], and their intersections [55] (Figure 4.2a). In fact, here we follow a very similar procedure to [55], but now for isolated codimension-2 discontinuity sets.

### 4.1.2 Outline

In section 4.2, we introduce our notation and formalise what we mean by an isolated codimension-2 discontinuity. In particular, we define a vector field  $\mathbf{V}$  which depends upon a discontinuous term  $\mathbf{e}$ .

Then in section 4.3, we apply our GSPT approach to this general form of codimension-2 problem, which serves to demonstrate the procedure. In section 4.4, we study a more restrictive class of problems where we find analytic results, allowing us to classify possible phase portraits. In this class, the vector field  $\mathbf{V}$  depends linearly upon the discontinuous term  $\mathbf{e}$ , and we show that our GSPT approach and the Filippov convention result in equivalent sliding vector fields; see Theorem 4.3.

In section 4.5, we provide examples of the method's use for physical applications, and illustrate other phenomena.

## 4.2 Preliminaries

We consider the system (4.1), with a codimension-2 discontinuity set  $\Sigma$  of a vector field  $\mathbf{F}$ . We straighten out  $\Sigma$  at least locally so that  $\Sigma = \{x = 0, y = 0, \mathbf{z} \in \mathbb{R}^{n-2}\}$  or a subset thereof. Hence we have  $\mathbf{F}(x, y, \mathbf{z})$  where  $x \in \mathbb{R}$ ,  $y \in \mathbb{R}$  and  $\mathbf{z} \in \mathbb{R}^{n-2}$ . We assume the following.

**Assumption 4.1.**  $\mathbf{F}$  takes the form

$$(4.3) \quad \mathbf{F}(x, y, \mathbf{z}) \equiv \mathbf{V}(\mathbf{e}(x, y), x, y, \mathbf{z}),$$



where  $\mathbf{V} : S^1 \times \mathbb{R}^2 \times \mathbb{R}^{n-2} \rightarrow \mathbb{R}^n$  is sufficiently smooth in all its entries, and  $\mathbf{e} : \mathbb{R}^2 \setminus \{0\} \rightarrow S^1$  given by

$$(4.4) \quad \mathbf{e}(x, y) := \left( \frac{x}{\sqrt{x^2 + y^2}}, \frac{y}{\sqrt{x^2 + y^2}} \right)^\top,$$

which corresponds to the unit vector pointing radially away from the origin at  $(x, y)^\top \neq \mathbf{0}$ .

The straightening of  $\Sigma$  and the geometrical interpretation of  $\mathbf{e}$  are given in Figure 4.4.

**Remark 4.1.** There is a jump in  $\mathbf{e}(x, y)$  at the origin. If we write  $\mathbf{e}$  along a line, which passes through the origin at a fixed angle  $\theta$ , given by

$$(4.5) \quad (x, y)^\top = l(\cos \theta, \sin \theta)^\top, \quad l \in \mathbb{R},$$

then

$$(4.6) \quad \mathbf{e}(l \cos \theta, l \sin \theta) = \text{sign}(l)(\cos \theta, \sin \theta)^\top.$$

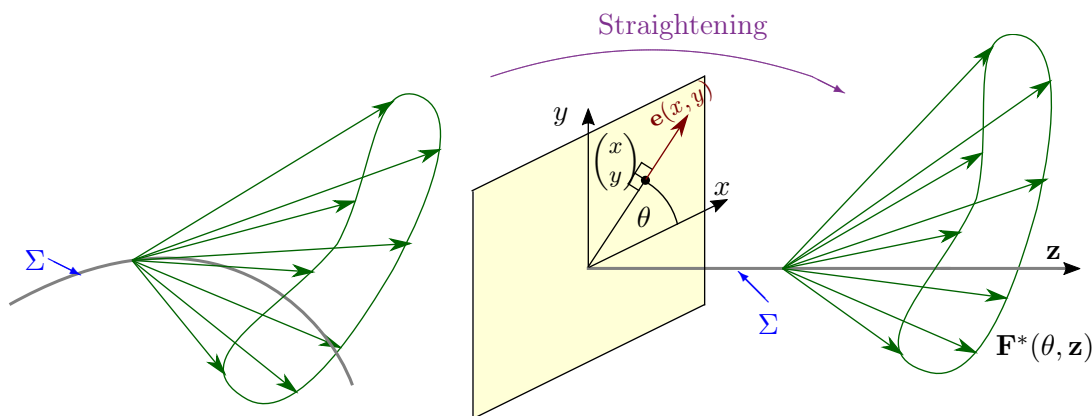
Along this line  $\mathbf{e}$  results in a standard piecewise switch. From (4.6), we note that for both  $l > 0$  and  $l \rightarrow 0^+$ , we have

$$(4.7) \quad \mathbf{e}(l \cos \theta, l \sin \theta) \equiv (\cos \theta, \sin \theta)^\top.$$

From Assumption 4.1 it follows that there is a well-defined directional *limit vector field*  $\mathbf{F}^*(\theta, \mathbf{z})$  given by

$$(4.8) \quad \mathbf{F}^*(\theta, \mathbf{z}) := \lim_{\varepsilon \rightarrow 0} \mathbf{F}(\varepsilon \cos \theta, \varepsilon \sin \theta, \mathbf{z}) = \mathbf{V}((\cos \theta, \sin \theta)^\top, 0, 0, \mathbf{z}),$$

that is sufficiently smooth in both  $\theta$  and  $\mathbf{z}$ .



**Figure 4.4:** Straightening of  $\Sigma$  so that  $\Sigma = \{x = 0, y = 0, \mathbf{z} \in \mathbb{R}^{n-2}\}$  and the geometric interpretation of  $\mathbf{e}$ .

Hence, from now on, we consider the system

$$(4.9) \quad (\dot{x}, \dot{y}, \dot{\mathbf{z}})^\top = \mathbf{V}(\mathbf{e}(x, y), x, y, \mathbf{z}),$$

where  $\mathbf{z} \in \mathbb{R}^m$ ,  $m = n - 2 > 0$ . It will often be useful to split (4.9) into two coupled ODEs

$$(4.10a) \quad (\dot{x}, \dot{y})^\top = \mathbf{U}(\mathbf{e}(x, y), x, y, \mathbf{z}),$$

$$(4.10b) \quad \dot{\mathbf{z}} = \mathbf{W}(\mathbf{e}(x, y), x, y, \mathbf{z}).$$

Equation (4.10a) corresponds to dynamics normal to  $\Sigma$ , and (4.10b) corresponds to dynamics tangent to  $\Sigma$ .

### 4.2.1 Dynamics near the discontinuity set

Following [2], we will now study (4.10) using polar coordinates  $(\rho, \theta)$ , where

$$(4.11) \quad x = \rho \cos \theta \quad \text{and} \quad y = \rho \sin \theta,$$

with the aim of describing how solutions reach  $\Sigma$ . Hence, by substituting (4.11) into (4.10), using the property in (4.7), and re-arranging, we find (4.10) becomes

$$(4.12) \quad \begin{aligned} \begin{pmatrix} \dot{\rho} \\ \dot{\theta} \end{pmatrix} &= \begin{pmatrix} 1 & 0 \\ 0 & \frac{1}{\rho} \end{pmatrix} \underline{\mathbf{R}}(\theta)^\top \mathbf{U}((\cos \theta, \sin \theta)^\top, \rho \cos \theta, \rho \sin \theta, \mathbf{z}), \\ \dot{\mathbf{z}} &= \mathbf{W}((\cos \theta, \sin \theta)^\top, \rho \cos \theta, \rho \sin \theta, \mathbf{z}), \end{aligned}$$

where  $\underline{\mathbf{R}}(\theta)$  is the rotation matrix

$$(4.13) \quad \underline{\mathbf{R}}(\theta) := \begin{pmatrix} \cos \theta & -\sin \theta \\ \sin \theta & \cos \theta \end{pmatrix}.$$

Notice that along  $\Sigma$ , which corresponds to  $\rho = 0$ , the dynamics is not defined. We therefore transform to a new time  $\mathcal{T}$ , given by  $d\mathcal{T} = \frac{1}{\rho} dt$ , so that (4.12) becomes

$$(4.14) \quad \begin{aligned} \frac{d}{d\mathcal{T}} \begin{pmatrix} \rho \\ \theta \end{pmatrix} &= \begin{pmatrix} \rho & 0 \\ 0 & 1 \end{pmatrix} \underline{\mathbf{R}}(\theta)^\top \mathbf{U}((\cos \theta, \sin \theta)^\top, \rho \cos \theta, \rho \sin \theta, \mathbf{z}), \\ \frac{d}{d\mathcal{T}} \mathbf{z} &= \rho \mathbf{W}((\cos \theta, \sin \theta)^\top, \rho \cos \theta, \rho \sin \theta, \mathbf{z}). \end{aligned}$$

With this transformation, (4.14) is well-defined along  $\Sigma$  and orbits are preserved. Note that trajectories can approach  $\rho = 0$  in finite time in (4.12), whereas trajectories can only reach  $\rho = 0$  in infinite time in (4.14).

Since  $\rho = 0$  is an invariant manifold of (4.14), equilibria of (4.14) exist when the  $\theta$  component,

$$(4.15) \quad \Theta(\rho, \theta, \mathbf{z}) := (-\sin \theta, \cos \theta) \mathbf{U}((\cos \theta, \sin \theta)^\top, \rho \cos \theta, \rho \sin \theta, \mathbf{z}),$$

is simultaneously zero. The function  $\Theta(\rho, \theta, \mathbf{z})$  is sufficiently smooth at  $\rho = 0$ , and

$$(4.16) \quad \Theta(0, \theta, \mathbf{z}) = (-\sin \theta, \cos \theta) \mathbf{U}((\cos \theta, \sin \theta)^\top, 0, 0, \mathbf{z}).$$

Let there exist  $\theta_0, \mathbf{z}_0$  such that  $\Theta(0, \theta_0, \mathbf{z}_0) = 0$ ; then

$$(4.17) \quad P_0 = (0, \theta_0, \mathbf{z}_0)$$

is an equilibrium of (4.14).

The importance of these equilibria along  $\rho = 0$  has previously been identified in [2] where they were called *limit directions*. These are the directions along which trajectories reach (or leave) the discontinuity set  $\Sigma$ . It is useful to study the stability of these equilibria. Linearising around  $P_0$ , we find that the Jacobian is given by

$$(4.18) \quad \mathbf{J}_0(\theta_0, \mathbf{z}_0) := \begin{pmatrix} \lambda_\rho(\theta_0, \mathbf{z}_0) & 0 & \mathbf{0}_{1 \times m} \\ \frac{\partial \Theta(0, \theta_0, \mathbf{z}_0)}{\partial \rho} & \frac{\partial \Theta(0, \theta_0, \mathbf{z}_0)}{\partial \theta} & \frac{\partial \Theta(0, \theta_0, \mathbf{z}_0)}{\partial \mathbf{z}} \\ \mathbf{W}((\cos \theta_0, \sin \theta_0)^\top, 0, 0, \mathbf{z}_0) & \mathbf{0}_{m \times 1} & \mathbf{0}_{m \times m} \end{pmatrix},$$

which has only two nonzero eigenvalues,

$$(4.19) \quad \lambda_\rho(\theta_0, \mathbf{z}_0) := (\cos \theta_0, \sin \theta_0) \mathbf{U}((\cos \theta_0, \sin \theta_0)^\top, 0, 0, \mathbf{z}_0)$$

and

$$(4.20) \quad \lambda_\theta(\theta_0, \mathbf{z}_0) := \frac{\partial \Theta(0, \theta_0, \mathbf{z}_0)}{\partial \theta}.$$

By the centre manifold theorem [89], if  $\lambda_\rho(\theta_0, \mathbf{z}_0) < 0$ , then there is an orbit approaching  $\Sigma$  along the direction  $\theta = \theta_0$ , and we say that the equilibrium  $P_0$  is *radially attracting*. Conversely, if  $\lambda_\rho(\theta_0, \mathbf{z}_0) > 0$ , then there is an orbit leaving  $\Sigma$  along  $\theta = \theta_0$ , and  $P_0$  is *radially repelling*. Similarly, if  $\lambda_\theta(\theta_0, \mathbf{z}_0) < 0$  then we call  $P_0$  *angularly attracting* and if  $\lambda_\theta(\theta_0, \mathbf{z}_0) > 0$  then we call  $P_0$  *angularly repelling*. If an equilibrium  $P_0$  is both angularly and radially attracting, then there is a neighbourhood of  $P_0$  that reaches  $\Sigma$  at  $P_0$  in finite time under the forward flow of (4.12).

In [2], the authors define the sliding region to be the subset  $\Sigma_{\text{sl}} \subset \Sigma$  such that for each  $\mathbf{z}_0 \in \Sigma_{\text{sl}}$ , if there exist solutions  $\theta_0$  such that  $\Theta(0, \theta_0, \mathbf{z}_0) = 0$ , then  $\lambda_\rho(\theta_0, \mathbf{z}_0) < 0$  (they have an alternative definition when no solutions exist to  $\Theta(\theta, \mathbf{z}_0) = 0$ ). We will discuss the suitability of this definition later. If there is sliding, a sliding vector field should be prescribed. Whilst [2] used the Filippov convention, we will proceed with a different approach.

### 4.2.2 Regularisation

Our strategy is to regularise the nonsmooth vector field  $\mathbf{V}$  in (4.9), viewing it as the limit of a smooth one. To proceed, let us first define a regularisation function  $\Psi(s)$ .

**Definition 4.1.** *We define a regularisation function  $\Psi(s)$  that satisfies the following conditions<sup>24</sup>.*

(R1)  $\Psi(s)$  is sufficiently smooth  $\forall s \in [0, \infty)$ .

(R2)  $\Psi(0) = 1$ .

(R3)  $\Psi(s) > 0 \forall s \in [0, \infty)$ .

(R4)  $\Psi'(s) \leq 0 \forall s \in [0, \infty)$ .

(R5)  $\Psi_1(s)$  is sufficiently smooth  $\forall s \in [0, \infty)$ , where

$$\Psi_1(s) := \begin{cases} \lim_{\sigma \rightarrow \infty} \Psi(\sigma), & s = 0 \\ \Psi(1/s), & s > 0 \end{cases}.$$

For example,  $\Psi(s) = (1+s)^{-1}$ ,  $\Psi(s) = e^{-s}$  and  $\Psi(s) = 1$  all satisfy Definition 4.1. To be able to apply center manifold theory and Fenichel's theory in the following, we will by "sufficiently smooth" require that  $\mathbf{V}$  and  $\Psi$  are at least  $C^2$  [70, 89]. We use  $\Psi$  in the regularisation of  $\mathbf{e}$  given in (4.4) as follows.

**Definition 4.2.** *Let  $D_1 \subset \mathbb{R}^2$  be the unit disc centred at the origin and let  $\Psi$  be a regularisation function as in Definition 4.1. Then we define  $\mathbf{e}_\Psi : \mathbb{R}^2 \rightarrow D_1$ , a regularisation of  $\mathbf{e}$ , as  $\mathbf{e}_\Psi(x, y; \varepsilon)$  given by*

$$(4.21) \quad \mathbf{e}_\Psi(x, y; \varepsilon) := \left( \frac{x}{\sqrt{x^2 + y^2 + \varepsilon^2 \Psi\left(\frac{x^2 + y^2}{\varepsilon^2}\right)}}, \frac{y}{\sqrt{x^2 + y^2 + \varepsilon^2 \Psi\left(\frac{x^2 + y^2}{\varepsilon^2}\right)}} \right)^\top$$

for  $0 < \varepsilon \ll 1$ .

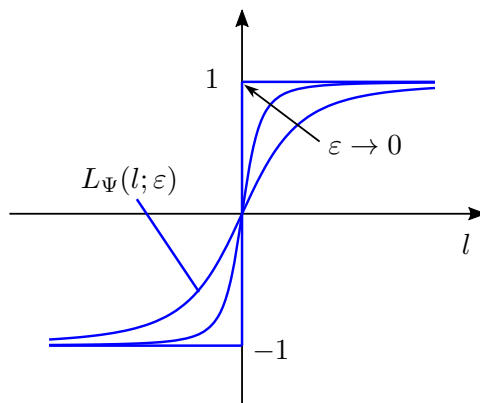
**Remark 4.2.**  $\mathbf{e}_\Psi$  does not jump discontinuously at the origin. When written along a line through the origin (4.5), we have

$$(4.22) \quad \mathbf{e}_\Psi(l \cos \theta, l \sin \theta) = L_\Psi(l; \varepsilon) (\cos \theta, \sin \theta)^\top,$$

where

$$(4.23) \quad L_\Psi(l; \varepsilon) := \frac{l}{\sqrt{l^2 + \varepsilon^2 \Psi(l^2/\varepsilon^2)}}$$

is a smooth function whose limit is a sign function as  $\varepsilon \rightarrow 0$  (see Figure 4.5).



**Figure 4.5:** The component of the map  $\mathbf{e}_\Psi$  along any line through the origin  $L_\Psi(l; \varepsilon)$  is a smooth function of  $l$ , whose limit is a sign function as  $\varepsilon \rightarrow 0$ . For example, if we set  $\Psi(s) = s/\sinh^2(\sqrt{s})$ , then  $L_\Psi(l; \varepsilon) = \tanh(l/\varepsilon)$ .

We note the following properties of  $\mathbf{e}_\Psi$ .

**Lemma 4.1.** Consider  $\mathbf{e}_\Psi : \mathbb{R}^2 \rightarrow D_1$  given by (4.21); then we have the following

(a)  $\mathbf{e}_\Psi(x, y; \varepsilon)$  is equivariant under rotations

$$(4.24) \quad \mathbf{e}_\Psi(\mathbf{R}(\phi)(x, y)^\top; \varepsilon) \equiv \mathbf{R}(\phi)\mathbf{e}_\Psi(x, y; \varepsilon)$$

for all  $\phi \in [0, 2\pi)$ , where  $\mathbf{R}(\phi)$  is a rotation matrix as in (4.13),<sup>25</sup>

(b)  $\mathbf{e}_\Psi(x, y; \varepsilon)$  satisfies the scaling property

$$(4.25) \quad \mathbf{e}_\Psi(kx, ky; k\varepsilon) \equiv \mathbf{e}_\Psi(x, y; \varepsilon),$$

for some  $k > 0$ , that is,  $\mathbf{e}_\Psi$  is a homogeneous function of degree 0 on  $(x, y, \varepsilon)$ ,

(c)  $\mathbf{e}_\Psi(x, y; 1)$  is one-to-one,

(d)  $\mathbf{e}_\Psi(x, y; \varepsilon)$  satisfies

$$(4.26) \quad \mathbf{e}_\Psi^\top \mathbf{e}_\Psi < 1.$$

The proof of Lemma 4.1 can be found in Appendix D.

We now study the system

$$(4.27) \quad (\dot{x}, \dot{y}, \dot{\mathbf{z}})^\top = \mathbf{V}(\mathbf{e}_\Psi(x, y; \varepsilon), x, y, \mathbf{z})$$

<sup>24</sup>Conditions (R1)-(R4) do not necessarily imply (R5).

<sup>25</sup>This equivariance, or rotational symmetry, seems a natural assumption in many cases. However, in certain systems (such as mechanical systems where an interaction between two bodies is rougher in one direction than another), this may not be suitable, and an alternative regularisation may be necessary.

as a regularisation of (4.9). In order to bring the singularly perturbed system (4.27) into standard slow-fast form, we adopt the scalings

$$(4.28) \quad x = \varepsilon x_2 \quad \text{and} \quad y = \varepsilon y_2.$$

As a result we find

$$(4.29) \quad \begin{aligned} \varepsilon(\dot{x}_2, \dot{y}_2)^\top &= \mathbf{U}(\mathbf{e}_\Psi(x_2, y_2; 1), \varepsilon x_2, \varepsilon y_2, \mathbf{z}), \\ \dot{\mathbf{z}} &= \mathbf{W}(\mathbf{e}_\Psi(x_2, y_2; 1), \varepsilon x_2, \varepsilon y_2, \mathbf{z}), \end{aligned}$$

using the scaling property in Lemma 4.1(b). The system (4.29) is a standard slow-fast system written in slow time. Setting  $\varepsilon = 0$  in (4.29) gives the reduced problem

$$(4.30a) \quad \mathbf{0} = \mathbf{U}(\mathbf{e}_\Psi(x_2, y_2; 1), 0, 0, \mathbf{z}),$$

$$(4.30b) \quad \dot{\mathbf{z}} = \mathbf{W}(\mathbf{e}_\Psi(x_2, y_2; 1), 0, 0, \mathbf{z}).$$

If we can solve (4.30a), finding

$$(4.31) \quad \mathbf{e}_\Psi(x_2, y_2; 1) = (c(\mathbf{z}), s(\mathbf{z}))^\top$$

such that  $\mathbf{U}((c(\mathbf{z}), s(\mathbf{z}))^\top, 0, 0, \mathbf{z}) = \mathbf{0}$ ,  $\forall \mathbf{z}$  in neighbourhood  $\mathcal{U}$ , then there exists a critical manifold given by (4.31). The slow flow, found by substituting (4.31) into (4.30b),

$$(4.32) \quad \dot{\mathbf{z}} = \mathbf{W}((c(\mathbf{z}), s(\mathbf{z}))^\top, 0, 0, \mathbf{z})$$

is independent of the regularisation  $\Psi$ .

It is evident from the limit  $\varepsilon \rightarrow 0$  of (4.28) that this slow flow corresponds to a notion of a sliding vector field along  $\Sigma$ . This definition differs from that in [2], where the Filippov convention was used. We show in section 4.4 that these definitions are equivalent, provided  $\mathbf{V}$  depends linearly on  $\mathbf{e}$ . Nevertheless, for a general  $\mathbf{V}$ , there is nothing to suggest that there is a unique solution (4.31) for any given  $\mathbf{z}$ , and thus there is no guarantee of a unique sliding flow (see Example 4.5.3 below).

We can also find the layer problem of (4.29),

$$(4.33) \quad \begin{aligned} (x'_2, y'_2)^\top &= \mathbf{U}(\mathbf{e}_\Psi(x_2, y_2; 1), 0, 0, \mathbf{z}), \\ \mathbf{z}' &= 0, \end{aligned}$$

where  $(\cdot)' = \frac{d}{d\tau}$  and the fast time  $\tau$  is given by  $d\tau = \frac{1}{\varepsilon} dt$ . From Fenichel's theorem [35], the flow of (4.29) can be approximated by combining the flow of (4.30) with the flow of (4.33) for  $0 < \varepsilon \ll 1$  where the critical manifold (4.31) is normally hyperbolic with respect to (4.33). We discuss the layer problem and its implications in subsection 4.3.2.

### 4.2.3 Summary

In subsection 4.2.1, using polar coordinates, we have shown how trajectories of the nonsmooth system (4.9) approach or leave  $\Sigma$ . In subsection 4.2.2, we have shown that the slow flows of (4.27) limit onto  $\Sigma$  as  $\varepsilon \rightarrow 0$ . However, we have not yet been able to connect the solutions of the nonsmooth system (4.9) in subsection 4.2.1 with those of the general regularised system (4.27) in subsection 4.2.2. In the next section, using blowup, we will describe these dynamical systems in two charts, which can be connected by changes of coordinates in the regions where the charts overlap.

## 4.3 Blowup for the general regularised system

In this section we study a general regularised system of the form (4.27) using blowup. This analysis acts as a demonstration of our approach in section 4.4 where  $\mathbf{V}$  depends linearly on  $\mathbf{e}$ . First, we consider the system

$$(4.34) \quad \begin{aligned} (x', y', \mathbf{z}')^\top &= \varepsilon \mathbf{V}(\mathbf{e}_\Psi(x, y; \varepsilon), x, y, \mathbf{z}), \\ \varepsilon' &= 0, \end{aligned}$$

found by rescaling time in (4.27) and treating the parameter  $\varepsilon$  as a variable. In (4.34), the set  $\varepsilon = 0$  is a hyperplane of equilibria and the intersection of  $\varepsilon = 0$  with  $\Sigma$  is singular due to the nonsmoothness of  $\mathbf{e}_\Psi$  there. But we can gain smoothness through the use of the blowup transformation

$$(4.35) \quad (\rho, (\bar{x}, \bar{y}, \bar{\varepsilon}), \mathbf{z}) \rightarrow (x, y, \varepsilon, \mathbf{z})$$

defined by

$$(4.36) \quad (x, y, \varepsilon) = \rho(\bar{x}, \bar{y}, \bar{\varepsilon}), \quad (\rho, (\bar{x}, \bar{y}, \bar{\varepsilon})) \in [0, \infty) \times S_+^2,$$

where

$$(4.37) \quad S_+^2 := \{(\bar{x}, \bar{y}, \bar{\varepsilon}) \mid \bar{x}^2 + \bar{y}^2 + \bar{\varepsilon}^2 = 1, \bar{\varepsilon} \geq 0\}$$

is the unit hemisphere. Informally, we are inserting a hemisphere at each point on  $x = y = \varepsilon = 0$  in order to make the vector field well behaved along the discontinuity set  $\Sigma$  in the limit  $\varepsilon \rightarrow 0$  (see Figure 4.6). With (4.35),  $\bar{\varepsilon}$  is then a common factor of the transformed vector field and so can be divided out. We study the resulting desingularised system in what follows.

Although blowup allows us to gain smoothness in the vector field, we cannot easily study the dynamics everywhere simultaneously. Instead we use *charts* to study multiple separate systems that are simpler but valid only in certain regions. Here, we adopt an atypical approach to charts. Whilst we study the *scaling* chart (the directional chart found by setting  $\bar{\varepsilon} = 1$ ) in the usual way,

the trigonometric terms associated with  $\mathbf{e}$  suggest that it is natural to use a single *entry/exit* chart<sup>26</sup> (found by setting  $\bar{\varepsilon} = 0$ ). In particular, near the equator  $\{S_+^2 | \bar{\varepsilon} = 0\}$  we reparameterise the blowup using polar-like coordinates  $(\rho, \bar{\varepsilon}, \theta)$  to write

$$(4.38) \quad \bar{x} = \sqrt{1 - \bar{\varepsilon}^2} \cos \theta, \quad \bar{y} = \sqrt{1 - \bar{\varepsilon}^2} \sin \theta,$$

and so obtain the local version of (4.35), the *entry/exit chart*

$$(4.39) \quad \kappa_1 : \quad x = \rho \sqrt{1 - \varepsilon_1^2} \cos \theta, \quad y = \rho \sqrt{1 - \varepsilon_1^2} \sin \theta, \quad \varepsilon = \rho \varepsilon_1,$$

with the chart-specific coordinates  $(\rho, \varepsilon_1, \theta)$ . Note that setting  $\varepsilon_1 = 0$  in (4.39) gives (4.11).

The *scaling chart* is found by setting  $\bar{\varepsilon} = 1$  in (4.36)

$$(4.40) \quad \kappa_2 : \quad x = \rho_2 x_2, \quad y = \rho_2 y_2, \quad \varepsilon = \rho_2,$$

with the chart-specific coordinates  $(x_2, y_2, \rho_2)$ . Note that (4.40) is equivalent to (4.28).

The change of coordinates between  $\kappa_2$  and  $\kappa_1$  is given by

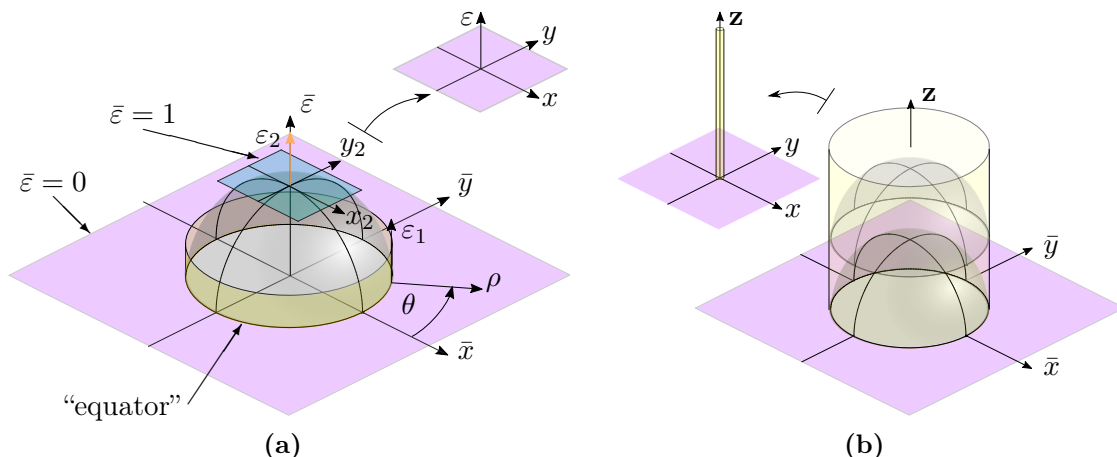
$$(4.41) \quad \kappa_{12} : (x_2, y_2, \rho_2) \mapsto \begin{cases} \rho = \frac{\rho_2}{\sqrt{1 + x_2^2 + y_2^2}} \\ \varepsilon_1 = \frac{1}{\sqrt{1 + x_2^2 + y_2^2}} \\ \theta = \arctan\left(\frac{y_2}{x_2}\right) \end{cases}.$$

These charts and coordinates are shown in Figure 4.6.

Now we shall demonstrate that the dynamics in the plane  $\varepsilon_1 = 0$  of the chart  $\kappa_1$  corresponds precisely to the dynamics studied in subsection 4.2.1, and that the dynamics in the scaling chart  $\kappa_2$  corresponds precisely to the dynamics of the scaled regularised system in subsection 4.2.2.

<sup>26</sup>We do not consider *multiple directional* entry/exit charts (found by setting  $\bar{x} = \pm 1$  and  $\bar{y} = \pm 1$  here) as is typical. Whilst Krupa and Szmolyan [67] correctly note that it is often “almost mandatory” to use multiple directional charts in order to aid analysis, the trigonometric terms here suit a single entry chart.





**Figure 4.6:** Sketches of the blowup geometry given by (4.35): **(a)** Blowup of a point  $\mathbf{z}$  on  $x = y = \varepsilon = 0$  to the unit hemisphere (note the geometric interpretations of the scaling chart  $\bar{\varepsilon} = 1$ , the plane  $\bar{\varepsilon} = 0$  and the coordinates in the charts  $\kappa_1, \kappa_2$ ). **(b)** How blowup extends the dimension of *each* point  $\mathbf{z}$  in the implicit set  $x = y = \varepsilon = 0$  (here we collapse the  $m$ -dimensional  $\mathbf{z}$  onto a single axis).

### 4.3.1 Entry chart $\kappa_1$ : dynamics near the discontinuity set

Let us study the dynamics in the chart  $\kappa_1$ . Rewriting (4.34) using (4.39) and transforming time, we divide the right-hand side by the common factor  $\varepsilon_1$ , to find

$$(4.42) \quad \begin{aligned} \frac{d}{d\mathcal{T}} \begin{pmatrix} \rho \\ \theta \end{pmatrix} &= \begin{pmatrix} \rho\xi & 0 \\ 0 & \xi^{-1} \end{pmatrix} \mathbf{R}^\top(\theta) \mathbf{U}(\tilde{\mathbf{e}}_\Psi(\theta, \varepsilon_1), \rho\xi \cos \theta, \rho\xi \sin \theta, \mathbf{z}), \\ \frac{d}{d\mathcal{T}} \mathbf{z} &= \rho \mathbf{W}(\tilde{\mathbf{e}}_\Psi(\theta, \varepsilon_1), \rho\xi \cos \theta, \rho\xi \sin \theta, \mathbf{z}), \\ \frac{d}{d\mathcal{T}} \varepsilon_1 &= -\varepsilon_1 \xi (\cos \theta, \sin \theta) \mathbf{U}(\tilde{\mathbf{e}}_\Psi(\theta, \varepsilon_1), \rho\xi \cos \theta, \rho\xi \sin \theta, \mathbf{z}), \end{aligned}$$

where  $d\mathcal{T} = \frac{\varepsilon_1}{\rho} dt = \frac{1}{\rho} dt$ ,

$$(4.43) \quad \xi = (1 - \varepsilon_1)^{\frac{1}{2}},$$

$\mathbf{U}$  is given in (4.10a),  $\mathbf{W}$  in (4.10b),

$$(4.44) \quad \begin{aligned} \tilde{\mathbf{e}}_\Psi(\theta, \varepsilon_1) &:= \mathbf{e}_\Psi(\rho\xi \cos \theta, \rho\xi \sin \theta; \rho\varepsilon_1) \\ &:= \left( \frac{1 - \varepsilon_1^2}{1 - \varepsilon_1^2 \left( 1 - \Psi_1 \left( \frac{\varepsilon_1^2}{1 - \varepsilon_1^2} \right) \right)} \right)^{\frac{1}{2}} (\cos \theta, \sin \theta)^\top \end{aligned}$$

and  $\Psi_1$  is defined as in (R5) of Definition 4.1 in subsection 4.2.2.

The singularity at  $\varepsilon_1 = 1$  does not concern us since we will only work with (4.42) near  $\varepsilon_1 = 0$ . Note that the plane  $\varepsilon_1 = 0$  is an invariant manifold and that the dynamics within the plane is identical to (4.14). Accordingly, we shall follow the analysis in subsection 4.2.1 closely.

**Theorem 4.1.** *Consider (4.42); then we have the following*

(a) *If  $\theta = \theta_0$  is a solution to*

$$(4.45) \quad \Theta(0, \theta, \mathbf{z}) := (-\sin \theta, \cos \theta) \mathbf{U}((\cos \theta, \sin \theta)^\top, 0, 0, \mathbf{z}) = 0$$

*for a given  $\mathbf{z} = \mathbf{z}_0$ , then there exists an equilibrium of (4.34) along the equator of the blown-up hemisphere at*

$$(4.46) \quad Q_0 = (0, \theta_0, \mathbf{z}_0, 0).$$

(b) *Consider such an equilibrium point  $Q_0$ : if there exists an eigenvalue  $\lambda_\rho(\theta_0, \mathbf{z}_0)$  of the linearisation of (4.42), corresponding to radial attractiveness as in subsection 4.2.1, then there exists a corresponding eigenvalue  $-\lambda_\rho(\theta_0, \mathbf{z}_0)$  with an eigenvector solely in the  $\varepsilon_1$  direction. Hence, if there is a stable manifold of  $Q_0$  within  $\varepsilon_1 = 0$  extending into  $\rho > 0$ , then there is a corresponding unstable manifold of  $Q_0$  within  $\rho = 0$  extending into  $\varepsilon_1 > 0$ , and vice versa.*

(c) *If no solutions for  $\theta$  exist to (4.45) for a given  $\mathbf{z} = \mathbf{z}_0$ , then there are no equilibria along the equator of the blown-up hemisphere inserted at that particular  $\mathbf{z}$  (the case of no limit directions in [2]). There is therefore a limit cycle on the equator which has a stable manifold in  $\varepsilon_1 = 0$  and an unstable manifold in  $\rho = 0$  if  $\int_0^{2\pi} \lambda_\rho(\theta, \mathbf{z}) / |\Theta(0, \theta, \mathbf{z})| d\theta < 0$ , and vice versa if  $\int_0^{2\pi} \lambda_\rho(\theta, \mathbf{z}) / |\Theta(0, \theta, \mathbf{z})| d\theta > 0$ .*

(d) *On the sphere, where  $\rho = 0$ ,  $\mathbf{z}$  remains constant for the flow of (4.42).*

**Proof.** Following subsection 4.2.1 closely,

(a) We have already noted that  $\varepsilon_1 = 0$  is an invariant manifold of (4.42) and that dynamics within it is given by (4.14). Therefore, if there exists an equilibrium  $P_0$  of (4.14) then  $Q_0$  is an equilibrium of (4.42).

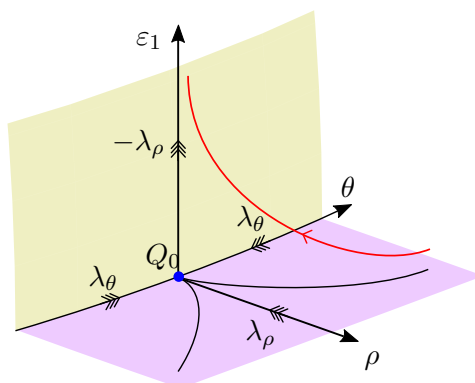
(b) The Jacobian of (4.42) at  $Q_0$ , is given by

$$(4.47) \quad \mathbf{K}_0(\theta_0, \mathbf{z}_0) := \begin{pmatrix} \mathbf{J}_0(\theta_0, \mathbf{z}_0) & \mathbf{0}_{m \times 1} \\ \mathbf{0}_{1 \times m} & -\lambda_\rho(\theta_0, \mathbf{z}_0) \end{pmatrix}.$$

It is then straightforward to show that there are now three nonzero eigenvalues:  $\lambda_\rho$ ,  $\lambda_\theta$  and  $-\lambda_\rho$ . The eigenvectors corresponding to  $\lambda_\rho$  and  $\lambda_\theta$  are as before, with 0 in the  $\varepsilon_1$  component. The eigenvector corresponding to  $-\lambda_\rho$  points solely in the  $\varepsilon_1$  direction and hence represents travelling up or down the sphere (Figure 4.7). Then by the centre manifold theorem [89], there are corresponding stable and unstable manifolds of  $Q_0$  tangent to the eigenvectors associated with  $\lambda_\rho$  and  $-\lambda_\rho$  or vice versa.

- (c) If no solutions exist to (4.45) for a fixed  $\mathbf{z} = \mathbf{z}_0$ , then along the invariant manifold of the equator ( $\rho = \varepsilon_1 = 0$ ), the  $\theta$  component of (4.42) does not change sign and there exists a limit cycle along the equator. In the plane  $\varepsilon_1 = 0$ , if we take a Poincaré section at some constant  $\theta$ , we can find that the local stability of this limit cycle is given by  $\int_0^{2\pi} \lambda_\rho(\theta, \mathbf{z}) / |\Theta(0, \theta, \mathbf{z})| d\theta$ . As with the stability of equilibria along the equator, the stability of the closed orbit is opposite within  $\rho = 0$ .
- (d) On the sphere  $\rho = 0$ , we find  $\dot{\mathbf{z}} = \mathbf{0}$  from (4.42). Hence the dynamics on the sphere of trajectories that reach the equator at  $Q_0$  is effectively parameterised by  $\mathbf{z} = \mathbf{z}_0$  in (4.42). ■

From Theorem 4.1, we note that if  $\lambda_\rho(\theta_0, \mathbf{z}_0) < 0$ , then there exists an orbit of (4.42) that approaches the equator along  $\theta = \theta_0$  (tangent to a stable manifold of the equilibrium  $Q_0$ ) and then travels along the corresponding unstable manifold of  $Q_0$  up the sphere. If both  $\lambda_\rho(\theta_0, \mathbf{z}_0) < 0$  and  $\lambda_\theta(\theta_0, \mathbf{z}_0) < 0$  then there exists an open set of orbits of the nonsmooth system that reach  $Q_0$  and travel up the sphere (see Figure 4.7). Manifolds that appear in the dynamics in the chart  $\kappa_1$  that extend into  $\varepsilon_1 > 0$  can be recovered in the scaling chart  $\kappa_2$  using (4.41), where the system is standard slow-fast.



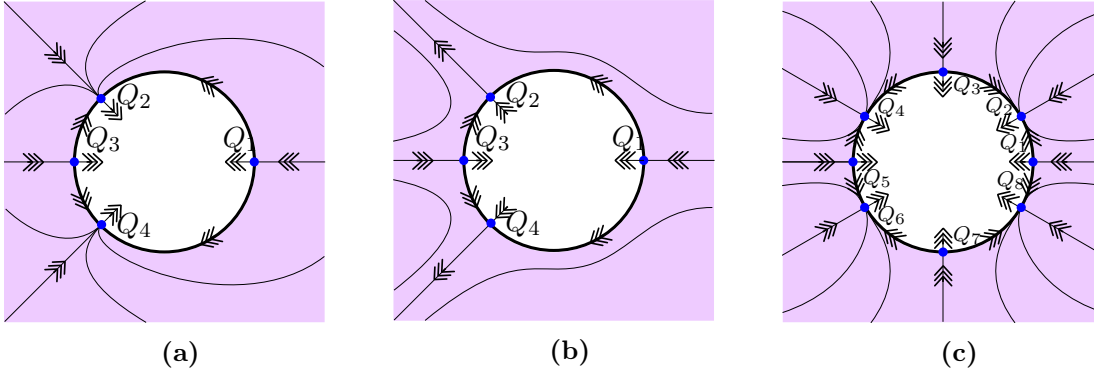
**Figure 4.7:** Sketch demonstrating how orbits travel up the side of the sphere. The yellow surface corresponds to the hemisphere of the blowup. The red orbit is for  $0 < \varepsilon \ll 1$ .

In Figure 4.8, we see sketches of dynamics in the chart  $\kappa_1$  for  $\varepsilon_1 = 0$ , projected into the  $(\bar{x}, \bar{y})$  plane. The sphere and manifolds extending from equilibria along its equator are also projected down into the same plane, ignoring the  $\mathbf{z}$  dynamics.

Odd numbers of equilibria along the equator occur at bifurcations, when

$$(4.48) \quad \Theta(0, \theta^*, \mathbf{z}) = \frac{\partial}{\partial \theta} \Theta(0, \theta^*, \mathbf{z}) = 0.$$

Where there are no solutions to (4.45), and hence no equilibria along the equator (no limit-directions), the equator is a closed orbit of the system. Therefore, from index theory [89], there



**Figure 4.8:** Sketches of the dynamics in the chart  $\kappa_1$  for  $\varepsilon_1 = 0$ , projected into the  $(\bar{x}, \bar{y})$  plane. **(a)** All equilibria on the equator are radially attracting ( $\lambda_r|_{Q_i} < 0 \forall i$ ), whilst  $Q_1$  and  $Q_3$  are angularly repelling and  $Q_2$  and  $Q_4$  are angularly attracting ( $\lambda_\theta|_{Q_i} > 0, i \in \{1, 3\}$  and  $\lambda_\theta|_{Q_i} < 0, i \in \{2, 4\}$  respectively). **(b)**  $Q_1$  and  $Q_3$  are radially attracting and angularly repelling ( $\lambda_\theta|_{Q_i} > 0, \lambda_r|_{Q_i} < 0, i \in \{1, 3\}$ ) and  $Q_2$  and  $Q_4$  are radially repelling and angularly attracting ( $\lambda_\theta|_{Q_i} < 0, \lambda_r|_{Q_i} > 0, i \in \{2, 4\}$ ). **(c)** Each  $Q_i$  is radially attracting ( $\lambda_r|_{Q_i} < 0 \forall i$ ), and  $Q_i$  are angularly attracting for  $i$  even ( $\lambda_\theta|_{Q_i} < 0, i \in \{2, 4, 6, 8\}$ ) and angularly repelling for  $i$  odd ( $\lambda_\theta|_{Q_i} > 0, i \in \{1, 3, 5, 7\}$ ). The case in **(c)** is analysed in Example 4.5.3.

must exist at least one critical set in the region enclosed by the equator. This region is described by the scaling chart  $\kappa_2$ , which we will now discuss.

### 4.3.2 Scaling chart $\kappa_2$ : dynamics on the discontinuity set

In the previous section, using the entry chart  $\kappa_1$ , we studied how orbits can reach or leave  $\Sigma$ . To study the dynamics *along*  $\Sigma$ , we use the scaling chart  $\kappa_2$ . Substituting (4.40) into (4.34), we find

$$(4.49a) \quad (x'_2, y'_2)^\top = \mathbf{U}(\mathbf{e}_\Psi(x_2, y_2; 1), \varepsilon x_2, \varepsilon y_2, \mathbf{z}),$$

$$(4.49b) \quad \mathbf{z}' = \varepsilon \mathbf{W}(\mathbf{e}_\Psi(x_2, y_2; 1), \varepsilon x_2, \varepsilon y_2, \mathbf{z}),$$

$$(4.49c) \quad \varepsilon' = 0.$$

Equations (4.49a) and (4.49b) are equivalent to (4.29) but written with respect to a fast time.

In subsection 4.2.2, we identified that if there is a solution  $\mathbf{e}_\Psi(x_2, y_2; 1) = (c(\mathbf{z}), s(\mathbf{z}))^\top$  such that  $\mathbf{U}((c(\mathbf{z}), s(\mathbf{z}))^\top, 0, 0, \mathbf{z}) = 0$ , then there exists a critical manifold in the scaling chart  $\kappa_2$  given by (4.31), and a corresponding slow flow (4.32). However, we have yet to study the layer problem (4.33) and its implications.

First, it will be useful to calculate the derivative  $D_{(x_2, y_2)} \mathbf{e}_\Psi(x_2, y_2; 1)$  to find

$$(4.50) \quad D_{(x_2, y_2)} \mathbf{e}_\Psi(x_2, y_2; 1) = \frac{1}{\sqrt{\zeta^2 + \Psi(\zeta^2)}} \mathbf{I} - \frac{1 + \Psi'(\zeta^2)}{\sqrt{\zeta^2 + \Psi(\zeta^2)}^3} \begin{pmatrix} x_2 \\ y_2 \end{pmatrix} \begin{pmatrix} x_2 & y_2 \end{pmatrix},$$

where  $\zeta^2 := x_2^2 + y_2^2$ .

**Remark 4.3.** *We note certain properties of the matrix  $D_{(x_2, y_2)} \mathbf{e}_\Psi(x_2, y_2; 1)$ . Firstly, by Definition 4.1, both the trace and determinant are positive:*

$$(4.51) \quad \text{tr}(D_{(x_2, y_2)} \mathbf{e}_\Psi(x_2, y_2; 1)) = \frac{\zeta^2 (1 - \Psi'(\zeta^2)) + 2\Psi(\zeta^2)}{(\zeta^2 + \Psi(\zeta^2))^{3/2}} > 0$$

and

$$(4.52) \quad \det(D_{(x_2, y_2)} \mathbf{e}_\Psi(x_2, y_2; 1)) = \frac{\Psi(\zeta^2) - \Psi'(\zeta^2)\zeta^2}{(\zeta^2 + \Psi(\zeta^2))^2} > 0$$

respectively. Secondly,  $D_{(x_2, y_2)} \mathbf{e}_\Psi(x_2, y_2; 1)$  is positive definite, since

$$(4.53) \quad \eta^\top D_{(x_2, y_2)} \mathbf{e}_\Psi(x_2, y_2; 1) \eta = \frac{(\eta_1 y_2 - \eta_2 x_2)^2 + \eta^\top \eta \Psi(\zeta^2) - (\eta_1 x_2 + \eta_2 y_2)^2 \Psi'(\zeta^2)}{(\zeta^2 + \Psi(\zeta^2))^{\frac{3}{2}}} > 0$$

for any  $\eta = (\eta_1, \eta_2)^\top$ .

**Theorem 4.2.** *Given a system of the form (4.34), the following hold:*

- (a) *Suppose there exist sufficiently smooth functions  $c(\mathbf{z}), s(\mathbf{z}) : c(\mathbf{z})^2 + s(\mathbf{z})^2 < 1$  for  $\mathbf{z} \in \mathcal{U}$  where*

$$(4.54) \quad \mathbf{U}((c(\mathbf{z}), s(\mathbf{z}))^\top, 0, 0, \mathbf{z}) = \mathbf{0},$$

then

$$(4.55) \quad C = \{(x_2, y_2, \mathbf{z}) \mid \mathbf{e}_\Psi(x_2, y_2; 1) = (c(\mathbf{z}), s(\mathbf{z}))^\top, \mathbf{z} \in \mathcal{U}\}$$

is a critical set of the equations in the scaling chart  $\kappa_2$ , that is, a set of equilibria of the layer problem.

- (b) The attractiveness and normal hyperbolicity of the critical set (4.55) are given by the eigenvalues of the Jacobian of the fast subsystem (4.49a) about  $C$

$$(4.56) \quad \underline{\mathbf{J}} := D_{(c,s)} \mathbf{U}((c, s)^\top, 0, 0, \mathbf{z}) D_{(x_2, y_2)} \mathbf{e}_\Psi(x_2, y_2; 1) \Big|_C.$$

Then it follows that if  $\det(D_{(c,s)} \mathbf{U}((c, s)^\top, 0, 0, \mathbf{z})) < 0$  then the critical set  $C$  is a saddle with respect to the fast flow, irrespective of the regularisation function  $\Psi$ . On the other hand, if

$$(4.57) \quad \det(D_{(c,s)} \mathbf{U}((c, s)^\top, 0, 0, \mathbf{z})) > 0$$

then the critical set  $C$  can be a stable or unstable node or focus, possibly depending on the regularisation.

- (c) When a critical set  $C$  exists, the slow flow along it is given by

$$(4.58) \quad \dot{\mathbf{z}} = \mathbf{W}((c(\mathbf{z}), s(\mathbf{z}))^\top, 0, 0, \mathbf{z}),$$

which is independent of the regularisation function  $\Psi$ .

- (d) Where a critical manifold  $C$  is compact and normally hyperbolic, it perturbs to a corresponding slow manifold  $C_\varepsilon$  in the smoothed system for  $0 < \varepsilon \ll 1$ . This slow manifold  $C_\varepsilon$  lies  $\varepsilon$ -close to  $C$  and the slow flow (4.58) gives the first order approximation to the flow along  $C_\varepsilon$ .

**Proof.** The proof is as follows.

- (a) Treating  $\varepsilon$  as a parameter, let us study the layer problem of (4.49), found by setting  $\varepsilon = 0$ ,

$$(4.59a) \quad (x'_2, y'_2)^\top = \mathbf{U}(\mathbf{e}_\Psi(x_2, y_2; 1), 0, 0, \mathbf{z})$$

$$(4.59b) \quad \mathbf{z}' = 0.$$

Evidently sets of the form (4.55) are sets of equilibria of (4.59), also described by (4.31).

- (b) In order to describe the local stability of these critical set we study the layer problem. Linearising (4.59a) around a critical set  $C$ , we find the Jacobian (4.56). Since the determinant of  $D_{(x_2, y_2)} \mathbf{e}_\Psi(x_2, y_2; 1)$  is strictly positive (Remark 4.3), we can determine that

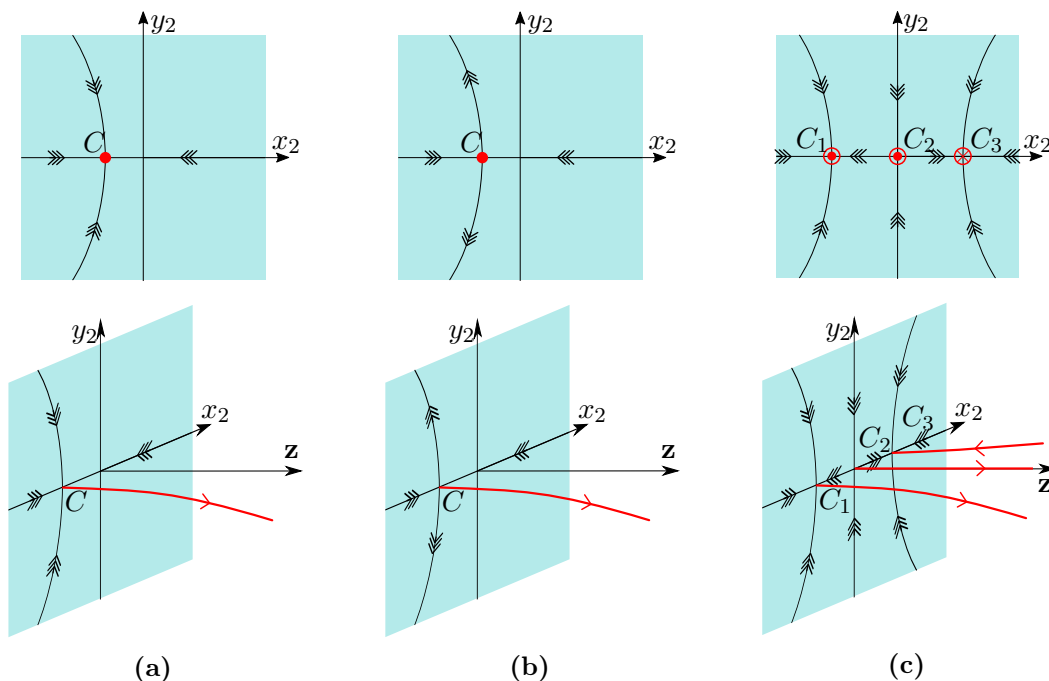
$$\begin{aligned} \text{sign}(\det \mathbf{J}) &\equiv \text{sign} \left( \det \left( D_{(c, s)} \mathbf{U}((c, s)^\top, 0, 0, \mathbf{z}) D_{(x_2, y_2)} \mathbf{e}_\Psi(x_2, y_2; 1) \right) \right) \\ &\equiv \text{sign} \left( \det \left( D_{(c, s)} \mathbf{U}((c, s)^\top, 0, 0, \mathbf{z}) \right) \right). \end{aligned}$$

Therefore, if  $\det \left( D_{(c, s)} \mathbf{U}((c, s)^\top, 0, 0, \mathbf{z}) \right) < 0$  then the critical set  $C$  is a saddle, irrespective of the regularisation function. It is not so straightforward to comment on the stability of the critical set when  $\text{sign} \left( \det \left( D_{(c, s)} \mathbf{U}((c, s)^\top, 0, 0, \mathbf{z}) \right) \right) > 0$ . In fact, in Case III of subsection 4.4.3, we prove by example that the stability of  $C$  can depend upon the regularisation function  $\Psi$ .

- (c) As in subsection 4.2.2, we find the slow flow along a critical set  $C$  is given by (4.58), subject to the algebraic constraint that  $(x_2, y_2) \in C$ , which is trivially independent of  $\Psi$ .
- (d) By Fenichel's theorem [35], where a critical manifold  $C$  is compact and normally hyperbolic, it perturbs to a slow manifold  $C_\varepsilon$  which lies Hausdorff distance  $\mathcal{O}(\varepsilon)$  from  $C$ . In addition the slow flow along  $C_\varepsilon$  is smoothly  $\mathcal{O}(\varepsilon)$  close to (4.58) from the same theorem.

■

We recall from subsection 4.2.2 that the slow flow (4.58) corresponds to sliding dynamics. Examples of dynamics in the scaling chart  $\kappa_2$  are shown in Figure 4.9. Figure 4.9a corresponds to stable sliding, Figure 4.9b to a type of unstable sliding, and Figure 4.9c to nonunique sliding.



**Figure 4.9:** Sketches of possible limiting dynamics in the scaling chart  $\kappa_2$ , corresponding to  $\bar{\varepsilon} = 1$  in (4.36). **(a)** There exists one critical set  $C$  which is a stable in the layer problem. **(b)** There exists one critical set — a saddle node in the layer problem. **(c)** There are three critical sets — two stable nodes and one saddle with respect to the fast flow, each with a different slow flow. The case in **(c)** is analysed in Example 4.5.3.

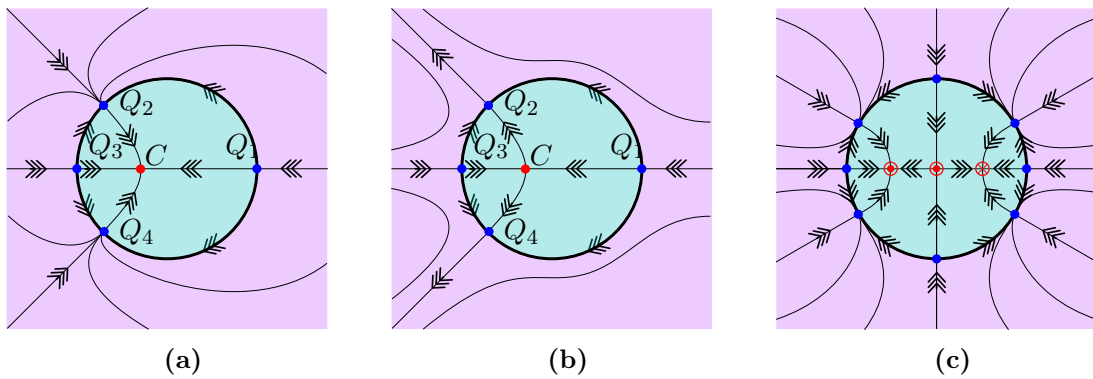
### 4.3.3 Summary

We can piece together solutions to the full system (4.34) from the dynamics in charts  $\kappa_1$  and  $\kappa_2$ . In the regions where charts  $\kappa_1$  and  $\kappa_2$  overlap, we can track how orbits in the entry/exit chart appear in the scaling chart and vice versa, using the change of coordinates  $\kappa_{12}$  (4.41).

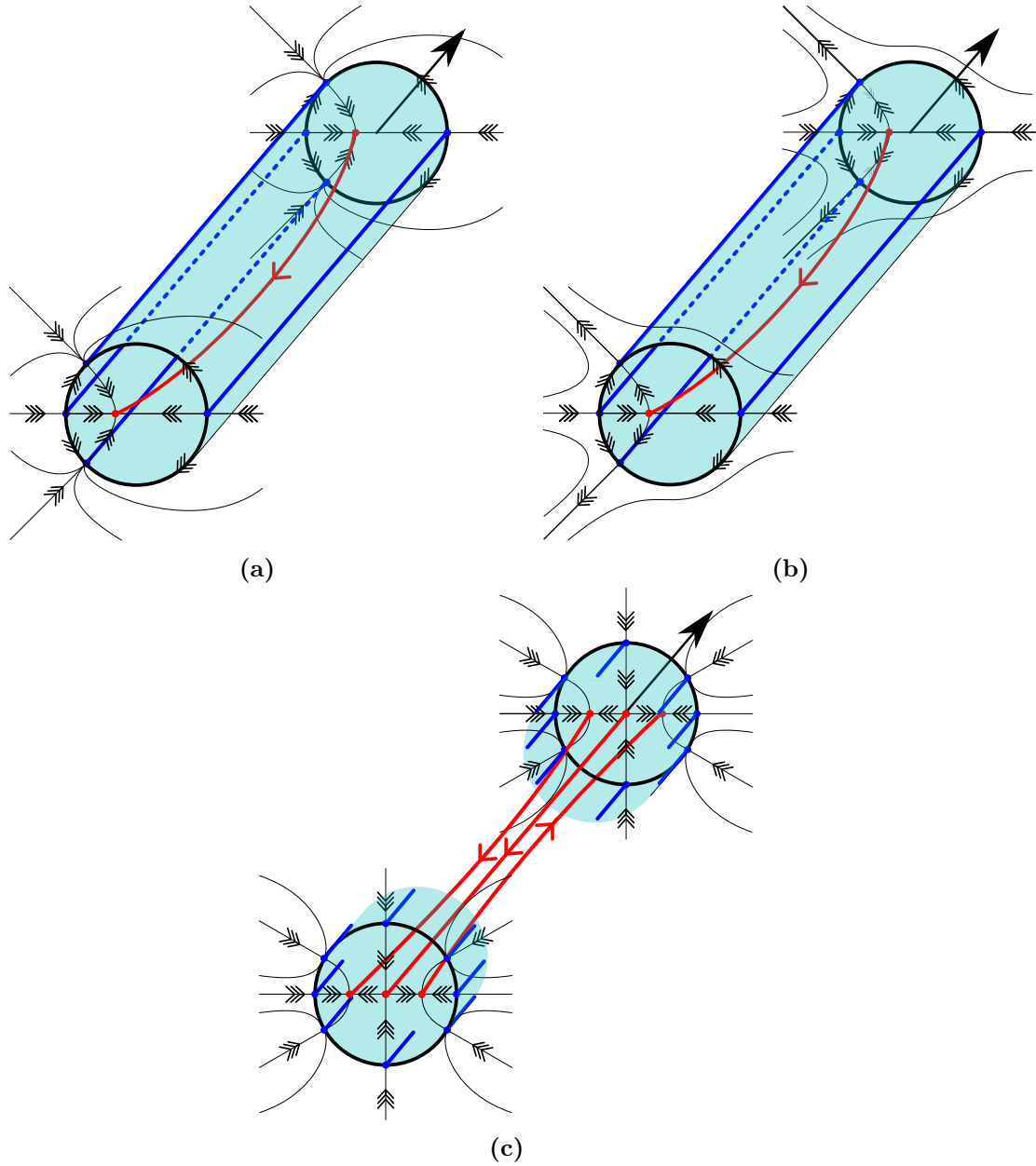
In Figures 4.10 and 4.11, we give sketches of the phase portraits of the dynamics of the full system (4.34) after the blowup in the nonsmooth limit  $\varepsilon \rightarrow 0$  for each of the three examples in Figures 4.8 and 4.9, corresponding to stable sliding, unstable sliding and nonunique sliding respectively.

For a general  $\mathbf{V}$ , it is difficult to comment any further. Depending on the nonlinearity of the vector field, finding solutions to (4.45) will typically be difficult, even impossible, and the dynamics in the scaling chart can become complex, including nonunique sliding (as in Figures 4.9c, 4.10c and 4.11c) and limit cycles. We have already noted that these dynamics may depend upon the regularisation function  $\Psi$ . For that reason we shall analyse a simpler setting, where the vector field  $\mathbf{V}$  is linear in  $\mathbf{e}$ , the so-called “ $\mathbf{e}$ -linear” system.





**Figure 4.10:** Sketches of examples of the dynamics of (4.34) after the blowup in (4.35) projected into the  $(\bar{x}, \bar{y})$  plane. Each subfigure pieces together the respective dynamics in the plane  $\varepsilon_1 = 0$  of the chart  $\kappa_1$  (Figure 4.8) and in the limit  $\varepsilon \rightarrow 0$  of the scaling chart  $\kappa_2$  (Figure 4.9). Labels are omitted in (c), where  $\odot$  signifies that the slow flow along the critical manifold is moving out of the plane whilst  $\otimes$  signifies that it is moving into the plane. We see that the sliding vector field is dependent upon the direction in which trajectories approach the discontinuity set. Any trajectory that starts in the right-hand plane tends to the rightmost critical manifold  $C_3$ , and hence travels ‘into the page’, yet any trajectory that starts in the left-hand plane tends to the leftmost critical manifold  $C_1$ , and hence travels ‘out of the page’. The case in (c) is analysed in Example 4.5.3.



**Figure 4.11:** Sketches of the dynamics projected onto  $(\bar{x}, \bar{y}, \mathbf{z})$  space. Each subfigure pieces together the respective dynamics in the plane  $\varepsilon_1 = 0$  of the chart  $\kappa_1$  (Figure 4.8) and in the limit  $\varepsilon \rightarrow 0$  of the scaling chart  $\kappa_2$  (Figure 4.9). In (c), the projection of the equator is cut away, so that the slow flow is visible.

## 4.4 Classification of the “e-linear” system

Let us consider a normal form of (4.9) that is linear in  $\mathbf{e}$

$$(4.60) \quad \begin{pmatrix} \dot{x} \\ \dot{y} \\ \dot{\mathbf{z}} \end{pmatrix} = \begin{pmatrix} \underline{\mathbf{A}}(\mathbf{z}) \\ \underline{\mathbf{B}}(\mathbf{z}) \end{pmatrix} \mathbf{e}(x, y) + \begin{pmatrix} \mathbf{f}(x, y, \mathbf{z}) \\ \mathbf{g}(x, y, \mathbf{z}) \end{pmatrix},$$

where  $\underline{\mathbf{A}}(\mathbf{z}) \in \mathbb{R}^{2 \times 2}$ ,  $\underline{\mathbf{B}}(\mathbf{z}) \in \mathbb{R}^{m \times 2}$ ,  $\mathbf{f}(x, y, \mathbf{z}) \in \mathbb{R}^2$  and  $\mathbf{g}(x, y, \mathbf{z}) \in \mathbb{R}^m$ . Here  $\underline{\mathbf{A}}$ ,  $\underline{\mathbf{B}}$ ,  $\mathbf{f}$  and  $\mathbf{g}$  are assumed to be well defined at  $\Sigma$ . Without loss of generality (see Appendix E), we can consider  $\underline{\mathbf{A}}(\mathbf{z})$  to be of the form

$$(4.61) \quad \underline{\mathbf{A}}(\mathbf{z}) = \begin{pmatrix} a(\mathbf{z}) & -b(\mathbf{z}) \\ b(\mathbf{z}) & d(\mathbf{z}) \end{pmatrix}.$$

**Remark 4.4.** *A lemma on the suitability of the particular form of the e-linear normal form is given in Lemma G.1 in Appendix G. An additional lemma that extends the form of (4.60) to include models such as Stribeck friction[88] is given in Lemma F.1 in Appendix F.*

We study this particular class of systems for a number of reasons. Most importantly, the physical systems that have motivated this paper fit into this form. Rigid body mechanical systems in 3D with Coulomb friction [3] can be written as (4.60), with  $b = 0$  [3]. In addition, the Filippov convention is well-posed here and the resulting unique sliding vector field can be compared to the slow flow from the regularisation approach. With (4.61), combinations of pairs of incident vectors are coplanar, so there is a unique *affine* combination of incident vectors that is tangent to the discontinuity (see Figure 4.12). Where this affine combination is also a convex combination, there is sliding (Figure 4.12a), and where the combination is not convex, there is crossing (Figure 4.12b). Moreover, (4.60) is analogous to standard Filippov systems: the linear dependence on  $\mathbf{e}$  relates to the linear dependence of standard Filippov problems on sign functions (unlike the nonlinear dependence of problems on sign functions in [49]).

Using the Filippov approach, the limit vector field (4.8) is given by

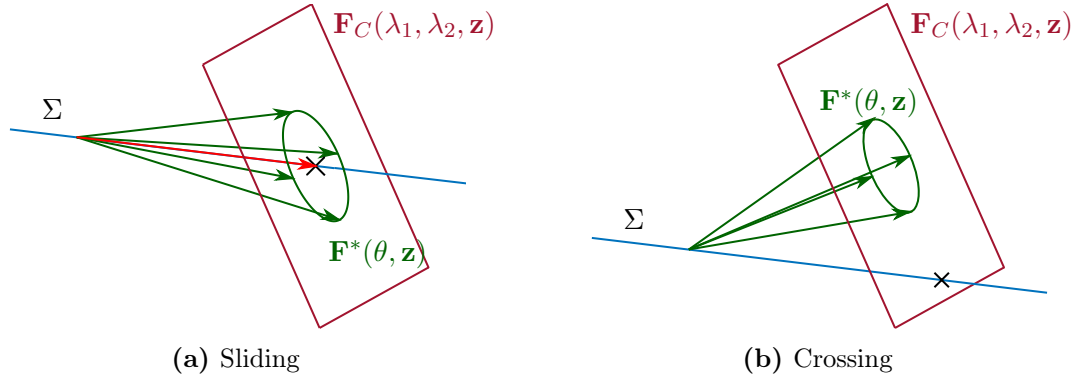
$$(4.62) \quad \mathbf{F}^*(\theta, \mathbf{z}) = \begin{pmatrix} \underline{\mathbf{A}}(\mathbf{z}) \\ \underline{\mathbf{B}}(\mathbf{z}) \end{pmatrix} \begin{pmatrix} \cos \theta \\ \sin \theta \end{pmatrix} + \begin{pmatrix} \mathbf{f}(0, 0, \mathbf{z}) \\ \mathbf{g}(0, 0, \mathbf{z}) \end{pmatrix}.$$

The plane of affine combinations of pairs of these limit vectors  $\mathbf{F}_C(\lambda_1, \lambda_2, \mathbf{z})$  is given by

$$(4.63) \quad \begin{aligned} \mathbf{F}_C(\lambda_1, \lambda_2, \mathbf{z}) &= \alpha_1 \mathbf{F}^*(\theta_1, \mathbf{z}) + \alpha_2 \mathbf{F}^*(\theta_2, \mathbf{z}), \quad \theta_1 \neq \theta_2, \quad \theta_1, \theta_2 \in [0, 2\pi), \quad \alpha_1 + \alpha_2 = 1, \\ \mathbf{F}_C(\lambda_1, \lambda_2, \mathbf{z}) &= \begin{pmatrix} \underline{\mathbf{A}}(\mathbf{z}) \\ \underline{\mathbf{B}}(\mathbf{z}) \end{pmatrix} \begin{pmatrix} \lambda_1 \\ \lambda_2 \end{pmatrix} + \begin{pmatrix} \mathbf{f}(0, 0, \mathbf{z}) \\ \mathbf{g}(0, 0, \mathbf{z}) \end{pmatrix} \end{aligned}$$

where  $(\lambda_1, \lambda_2) \in \mathbb{R}^2$ . The intersection of this plane with  $\Sigma$  is unique and given by

$$(4.64) \quad \mathbf{F}_\Sigma(\mathbf{z}) = \begin{pmatrix} 0 \\ 0 \\ -\underline{\mathbf{B}}(\mathbf{z})\underline{\mathbf{A}}^{-1}(\mathbf{z})\mathbf{f}(0, 0, \mathbf{z}) + \mathbf{g}(0, 0, \mathbf{z}) \end{pmatrix}.$$



**Figure 4.12:** Sliding and crossing in the e-linear system (4.60) and (4.61). In (a), there is sliding, when a convex combination of a pair of limit vectors is tangent to  $\Sigma$ . In (b), there is crossing, when no affine combination is convex.  $\mathbf{F}^*(\theta, \mathbf{z})$  is the limit vector field, given in (4.62).  $\mathbf{F}_C(\lambda_1, \lambda_2, \mathbf{z})$  is the plane of affine combinations of pairs of these limit vectors, given in (4.63). A cross ( $\times$ ) marks the unique intersection of  $\mathbf{F}_C(\lambda_1, \lambda_2, \mathbf{z})$  with  $\Sigma$ , given by (4.64).

$\mathbf{F}_C(\lambda_1, \lambda_2, \mathbf{z})$  is *convex* when  $(\lambda_1, \lambda_2) \in D_1$ , the unit disc centred on the origin (see Definition 4.2), i.e. when

$$(4.65) \quad (\underline{\mathbf{A}}^{-1}(\mathbf{z})\mathbf{f}(0, 0, \mathbf{z}))^\top (\underline{\mathbf{A}}^{-1}(\mathbf{z})\mathbf{f}(0, 0, \mathbf{z})) \leq 1.$$

As already noted, the Filippov convention is well-posed here. Nevertheless, it is worth studying the linear case given by (4.60) and (4.61) using regularisation in order to understand the robustness of the convention to perturbations and the stability of sliding. Furthermore, in Theorem 4.3 of subsection 4.4.1, we show that the slow flow in the scaling chart from our regularisation approach is equivalent to the sliding vector field resulting from the Filippov convention (4.64).

So we regularise and augment (4.60), to give

$$(4.66) \quad \begin{pmatrix} x' \\ y' \\ \mathbf{z}' \end{pmatrix} = \varepsilon \left( \begin{pmatrix} \underline{\mathbf{A}}(\mathbf{z}) \\ \underline{\mathbf{B}}(\mathbf{z}) \end{pmatrix} \mathbf{e}_\Psi(x, y; \varepsilon) + \begin{pmatrix} \mathbf{f}(x, y, \mathbf{z}) \\ \mathbf{g}(x, y, \mathbf{z}) \end{pmatrix} \right), \\ \varepsilon' = 0$$

and then study the dynamics of (4.61) and (4.66) in the charts  $\kappa_1$  and  $\kappa_2$ .

#### 4.4.1 Entry chart $\kappa_1$ : dynamics near the discontinuity set

As in the general case, we consider the augmented system and blowup  $x = y = \varepsilon = 0$  to a sphere using (4.35). We first study the equations in chart  $\kappa_1$ , so that (4.42) becomes

$$(4.67) \quad \begin{aligned} \frac{d}{d\mathcal{T}} \begin{pmatrix} \rho \\ \theta \end{pmatrix} &= \begin{pmatrix} \rho\xi & 0 \\ 0 & \xi^{-1} \end{pmatrix} \mathbf{R}^\top(\theta) \left( \underline{\mathbf{A}}(\mathbf{z}) \hat{\mathbf{e}}_\Psi(\theta, \varepsilon_1) + \mathbf{f}(\rho\xi \cos \theta, \rho\xi \sin \theta, \mathbf{z}) \right), \\ \frac{d}{d\mathcal{T}} \mathbf{z} &= \rho \left( \underline{\mathbf{B}}(\mathbf{z}) \hat{\mathbf{e}}_\Psi(\theta, \varepsilon_1) + \mathbf{g}(\rho\xi \cos \theta, \rho\xi \sin \theta, \mathbf{z}) \right), \\ \frac{d}{d\mathcal{T}} \varepsilon_1 &= -\frac{\varepsilon_1}{\rho} \dot{\rho}. \end{aligned}$$

The equator  $\rho = \varepsilon_1 = 0$  is once again an invariant manifold, with equilibria when

$$(4.68) \quad \begin{aligned} \Theta(0, \theta, \mathbf{z}) &= (0, 1) \mathbf{R}^\top(\theta) \left( \underline{\mathbf{A}}(\mathbf{z}) \begin{pmatrix} \cos \theta \\ \sin \theta \end{pmatrix} + \mathbf{f}(0, 0, \mathbf{z}) \right) \\ &= (d(\mathbf{z}) - a(\mathbf{z})) \sin \theta \cos \theta + f_2(0, 0, \mathbf{z}) \cos \theta - f_1(0, 0, \mathbf{z}) \sin \theta + b(\mathbf{z}) = 0. \end{aligned}$$

Solutions of (4.68) can be viewed as the intersection of the hyperbola

$$(4.69) \quad \begin{pmatrix} \bar{x} & \bar{y} \end{pmatrix} \begin{pmatrix} 0 & \frac{d(\mathbf{z})-a(\mathbf{z})}{2} \\ \frac{d(\mathbf{z})-a(\mathbf{z})}{2} & 0 \end{pmatrix} \begin{pmatrix} \bar{x} \\ \bar{y} \end{pmatrix} + \begin{pmatrix} f_2(0, 0, \mathbf{z}) & -f_1(0, 0, \mathbf{z}) \end{pmatrix} \begin{pmatrix} \bar{x} \\ \bar{y} \end{pmatrix} + b(\mathbf{z}) = 0$$

with the unit circle (the equator)

$$(4.70) \quad \begin{pmatrix} \bar{x} & \bar{y} \end{pmatrix} \begin{pmatrix} 1 & 0 \\ 0 & 1 \end{pmatrix} \begin{pmatrix} \bar{x} \\ \bar{y} \end{pmatrix} - 1 = 0.$$

Hence there can be at most four unique equilibria. This is clear either algebraically when writing (4.69) and (4.70) as a single quartic in either  $\bar{x}$  or  $\bar{y}$ , or geometrically in Figure 4.13. Generically, equilibria on the equator are created in saddle node bifurcations (subsection 4.4.4). These occur where (4.48) is satisfied, resulting in

$$(4.71) \quad \begin{aligned} f_1 &= b \sin \theta - (a - d) \cos^3 \theta \\ f_2 &= (a - d) \sin^3 \theta - b \cos \theta. \end{aligned}$$

However, closed form solutions to (4.71) are too lengthy to be of much use. In our geometric interpretation, this bifurcation occurs when the hyperbola (4.69) is tangent to the unit circle (4.70).

There are also degenerate cases of (4.68) to consider as follows:

(D1)  $a(\mathbf{z}) = d(\mathbf{z})$ :

In this case, unique equilibria are given by

$$\theta = \theta^*(\mathbf{z}) = \arcsin \left( \frac{b(\mathbf{z})}{|\mathbf{f}(0, 0, \mathbf{z})|} \right) + \arctan \left( \frac{f_2(0, 0, \mathbf{z})}{f_1(0, 0, \mathbf{z})} \right).$$

Here we have no equilibria when  $|b(\mathbf{z})| > |\mathbf{f}(0, 0, \mathbf{z})|$  and 2 equilibria when  $|b(\mathbf{z})| < |\mathbf{f}(0, 0, \mathbf{z})|$  (with a saddle node bifurcation when  $|b(\mathbf{z})| = |\mathbf{f}(0, 0, \mathbf{z})|$ ).

(D2) At least one of  $f_1(0, 0, \mathbf{z})$  or  $f_2(0, 0, \mathbf{z})$  is zero and  $b(\mathbf{z}) = 0$ :

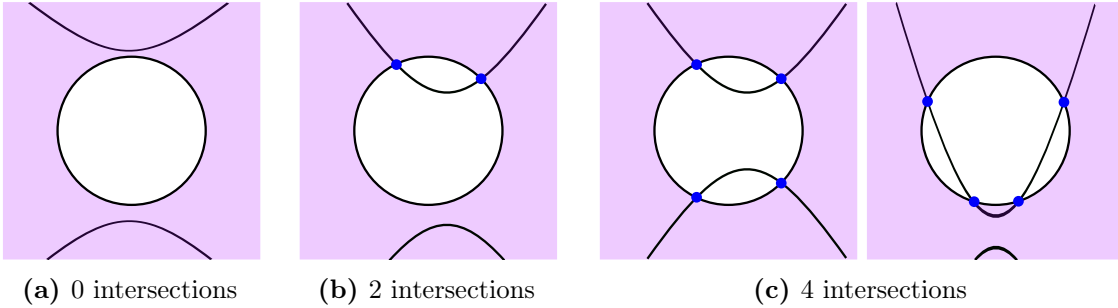
Without loss of generality we shall suppose that  $f_2(0, 0, \mathbf{z}) = 0$ , then (4.68) becomes

$$\sin \theta ((a(\mathbf{z}) - d(\mathbf{z})) \cos \theta - f_1(0, 0, \mathbf{z})) = 0.$$

In this case we always have two equilibria  $\theta = \theta^*(\mathbf{z}) = 0, \pi$  on the equator. Other equilibria are born in pitchfork bifurcations at  $|f_1(0, 0, \mathbf{z})| = |d(\mathbf{z}) - a(\mathbf{z})|$ , given by

$$\theta = \theta^*(\mathbf{z}) = \pm \arccos \left( \frac{f_1(0, 0, \mathbf{z})}{d(\mathbf{z}) - a(\mathbf{z})} \right)$$

when  $|f_1(0, 0, \mathbf{z})| < |d(\mathbf{z}) - a(\mathbf{z})|$ . The analysis when  $f_2(0, 0, \mathbf{z}) = 0$  and  $b(\mathbf{z}) = 0$  is similar.



**Figure 4.13:** Intersections of conics: the ways that the hyperbola (4.69) and the unit circle (4.70) can intersect generically. There can be only 0, 2 or 4 intersections of these conics and hence only 0, 2 or 4 equilibria on the equator (or “limit directions”) for our linear system (4.60). Each subfigure depicts the  $(\bar{x}, \bar{y})$  plane and the unit circle corresponds to the equator of the blowup.

#### 4.4.2 Scaling chart $\kappa_2$ : dynamics on the discontinuity set

Following the same procedure as for the general system we study the dynamics in the scaling chart  $\kappa_2$ , setting  $\bar{\varepsilon} = 1$ , to obtain

$$(4.72) \quad \begin{aligned} \varepsilon(\dot{x}_2, \dot{y}_2)^\top &= \underline{\mathbf{A}}(\mathbf{z})\mathbf{e}_\Psi(x_2, y_2; 1) + \mathbf{f}(\varepsilon x_2, \varepsilon y_2, \mathbf{z}), \\ \dot{\mathbf{z}} &= \underline{\mathbf{B}}(\mathbf{z})\mathbf{e}_\Psi(x_2, y_2; 1) + \mathbf{g}(\varepsilon x_2, \varepsilon y_2, \mathbf{z}). \end{aligned}$$

As expected we obtain a slow-fast system where  $x_2$  and  $y_2$  are fast.

**Theorem 4.3.** *Considering the dynamics in the scaling chart  $\kappa_2$  given by (4.72), then we have the following:*

(a) Where  $\underline{\mathbf{A}}(\mathbf{z})$  and  $\mathbf{f}(0, 0, \mathbf{z})$  satisfy

$$(4.73) \quad (\underline{\mathbf{A}}(\mathbf{z})^{-1}\mathbf{f}(0, 0, \mathbf{z}))^\top \underline{\mathbf{A}}(\mathbf{z})^{-1}\mathbf{f}(0, 0, \mathbf{z}) < 1,$$

there exists exactly one unique equilibrium of the layer problem in the scaling chart  $\kappa_2$  given by

$$(4.74) \quad C = \{(x_2, y_2, \mathbf{z}) | \underline{\mathbf{A}}(\mathbf{z})\mathbf{e}_\Psi(x_2, y_2; 1) + \mathbf{f}(0, 0, \mathbf{z}) = 0\}$$

for a fixed  $\mathbf{z}$ . On the other hand, if

$$(4.75) \quad (\underline{\mathbf{A}}(\mathbf{z})^{-1}\mathbf{f}(0, 0, \mathbf{z}))^\top \underline{\mathbf{A}}(\mathbf{z})^{-1}\mathbf{f}(0, 0, \mathbf{z}) > 1,$$

then there is no such critical set.

(b) Where a unique critical set  $C$  exists, the slow flow in the reduced problem is given by

$$(4.76) \quad \dot{\mathbf{z}} = -\underline{\mathbf{B}}(\mathbf{z})\underline{\mathbf{A}}^{-1}(\mathbf{z})\mathbf{f}(0, 0, \mathbf{z}) + \mathbf{g}(0, 0, \mathbf{z}),$$

which coincides with the Filippov convention [2, (5.20)].

**Proof.** Rescaling time in (4.72), we obtain the system in fast time

$$(4.77) \quad \begin{aligned} (x'_2, y'_2)^\top &= \underline{\mathbf{A}}(\mathbf{z})\mathbf{e}_\Psi(x_2, y_2; 1) + \mathbf{f}(\varepsilon x_2, \varepsilon y_2, \mathbf{z}), \\ \mathbf{z}' &= \varepsilon (\underline{\mathbf{B}}(\mathbf{z})\mathbf{e}_\Psi(x_2, y_2; 1) + \mathbf{g}(\varepsilon x_2, \varepsilon y_2, \mathbf{z})). \end{aligned}$$

The layer problem is given by the limit  $\varepsilon \rightarrow 0$

$$(4.78) \quad \begin{aligned} (x'_2, y'_2)^\top &= \underline{\mathbf{A}}(\mathbf{z})\mathbf{e}_\Psi(x_2, y_2; 1) + \mathbf{f}(0, 0, \mathbf{z}) \\ \mathbf{z}' &= 0. \end{aligned}$$

(a) A unique critical set (4.74) exists for a given  $\mathbf{z}$  in the scaling chart  $\kappa_2$  if there is a solution to

$$(4.79) \quad \mathbf{e}_\Psi(x_2, y_2; 1) = -\underline{\mathbf{A}}^{-1}(\mathbf{z})\mathbf{f}(0, 0, \mathbf{z}).$$

When (4.73) holds, solutions to (4.79) exist, since  $\mathbf{e}_\Psi^\top \mathbf{e}_\Psi < 1$ , from (4.26). If the critical set exists, it is unique, from Lemma 4.1(c). When (4.75) holds, no solutions exist to (4.79), and therefore there can be no critical set  $C$ . Condition (4.79), together with (4.26), can be thought of as  $\mathbf{f}(0, 0, \mathbf{z})$  lying within the ellipse

$$(4.80) \quad (\underline{\mathbf{A}}(\mathbf{z})^{-1}\mathbf{h})^\top \underline{\mathbf{A}}(\mathbf{z})^{-1}\mathbf{h} = 1$$

since  $\det((\underline{\mathbf{A}}(\mathbf{z})^{-1})^\top \underline{\mathbf{A}}(\mathbf{z})^{-1}) = \det(\underline{\mathbf{A}}(\mathbf{z}))^{-2}$  (see Figure 4.14).

(b) If the critical set (4.74) exists, the slow flow along it is given by (4.76), found by substituting (4.79) into the reduced problem (4.72).

■

As with the general system, the slow flow (4.76) corresponds to the sliding vector field in Filippov terminology.

Limit cycles may also occur in the scaling chart  $\kappa_2$ . Hyperbolic limit cycles persist and therefore form a cylinder. The reduced flow along such a cylinder is defined by an average of the slow component of the vector field.

**Proposition 4.1.** *If there exists a limit cycle in the layer problem of the scaling chart, then the reduced flow along the limit cycle is given by (4.76).*

**Proof.** If we suppose that there exists a limit cycle where  $(x_2(\tau+T), y_2(\tau+T)) = (x_2(\tau), y_2(\tau))$ , then averaging the layer problem (4.78) over the period  $T$ , we find

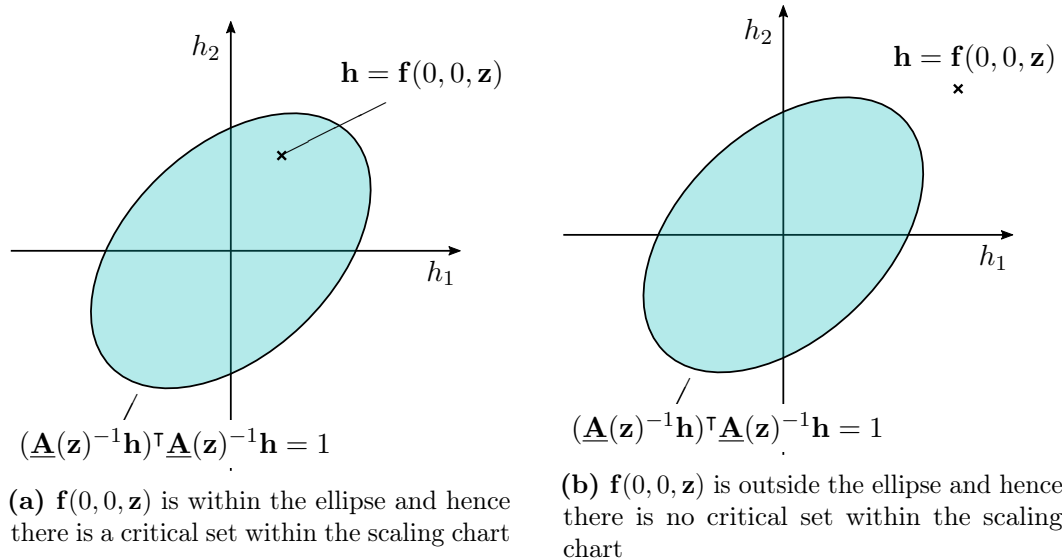
$$(4.81) \quad \frac{1}{T} \int_0^T \begin{pmatrix} x_2(\tau)' \\ y_2(\tau)' \end{pmatrix} d\tau = \frac{1}{T} \int_0^T \left( \underline{\mathbf{A}}(\mathbf{z}) \mathbf{e}_\Psi(x_2(\tau), y_2(\tau); 1) + \mathbf{f}(0, 0, \mathbf{z}) \right) d\tau$$

$$(4.82) \quad \implies \mathbf{0} = \underline{\mathbf{A}}(\mathbf{z}) \left( \frac{1}{T} \int_0^T \left( \mathbf{e}_\Psi(x_2(\tau), y_2(\tau); 1) \right) d\tau \right) + \mathbf{f}(0, 0, \mathbf{z})$$

Accordingly, the reduced problem along the limit cycle will be given by

$$(4.83) \quad \dot{\mathbf{z}} = \underline{\mathbf{B}}(\mathbf{z}) \left( \frac{1}{T} \int_0^T \left( \mathbf{e}_\Psi(x_2(\tau), y_2(\tau); 1) \right) d\tau \right) + \mathbf{g}(0, 0, \mathbf{z}),$$

which, using (4.82), results in (4.76). ■



**Figure 4.14:** Sketch of a geometric interpretation of the condition on  $\mathbf{f}(0, 0, \mathbf{z})$  for the existence of a critical set in the scaling chart.

It is also possible to infer some of the dynamics in the scaling chart  $\kappa_2$  purely from an examination of the entry chart  $\kappa_1$  using arguments from index theory (as was done in subsection 4.3.1 when there were no equilibria on the equator).



### 4.4.3 Cases

In order to classify the possible global dynamics of (4.66) we shall now consider three cases of our  $\mathbf{e}$ -linear system (4.60), determined by the elements of  $\underline{\mathbf{A}}(\mathbf{z})$  given by (4.61), and described in Table 4.1.

Case I	$\text{sign}(a) = \text{sign}(d)$	$\det(\underline{\mathbf{A}}) > 0$
Case II	$\text{sign}(a) \neq \text{sign}(d)$	$\det(\underline{\mathbf{A}}) < 0$
Case III		$\det(\underline{\mathbf{A}}) > 0$

Table 4.1: The 3 cases of the linear normal form (4.60) with (4.61).

#### 4.4.3.1 Case I

We consider  $a, d < 0$  for fixed  $\mathbf{z}$  and hence  $\det(\underline{\mathbf{A}})$  is necessarily positive (the analysis of  $a, d > 0$  is equivalent after a reversal of time).

#### Theorem 4.4.

- (a) *If  $(\underline{\mathbf{A}}(\mathbf{z})^{-1}\mathbf{f}(0, 0, \mathbf{z}))^\top \underline{\mathbf{A}}(\mathbf{z})^{-1}\mathbf{f}(0, 0, \mathbf{z}) < 1$ , there exists a unique critical set in the scaling chart. Furthermore, all orbits in the layer problem of the scaling chart limit onto the critical set. Generically, there can be 0, 2 or 4 equilibria along the equator for a fixed  $\mathbf{z}$ .*
- (b) *If  $(\underline{\mathbf{A}}(\mathbf{z})^{-1}\mathbf{f}(0, 0, \mathbf{z}))^\top \underline{\mathbf{A}}(\mathbf{z})^{-1}\mathbf{f}(0, 0, \mathbf{z}) > 1$ , no critical set exists in the scaling chart and there can be either 2 or 4 equilibria along the equator generically.*
- (c) *There are 5 qualitatively different types of generic phase portraits for systems of the form (4.60) with (4.61) for Case I.*

**Proof.** Let us consider (4.60) with (4.61). From Theorem 4.3, if (4.73) holds, then there exists a critical set in the layer problem in the scaling chart and that if

$$(\underline{\mathbf{A}}^{-1}\mathbf{f}(0, 0, \mathbf{z}))^\top \underline{\mathbf{A}}(\mathbf{z})^{-1}\mathbf{f}(0, 0, \mathbf{z}) > 1$$

there is no critical set.

- (a) Let us assume that such a critical set exists. The divergence of the vector field of the layer problem

$$(4.84) \quad \text{div}(\dot{x}_2, \dot{y}_2) = \left( \frac{\partial}{\partial x_2}, \frac{\partial}{\partial y_2} \right) (\underline{\mathbf{A}}(\mathbf{z})\mathbf{e}_\Psi(x_2, y_2; 1) + \mathbf{f}(0, 0, \mathbf{z}))$$

$$(4.85) \quad = \frac{(a(\mathbf{z}) + d(\mathbf{z}))\Psi(\zeta^2) - (a(\mathbf{z})x_2^2 + d(\mathbf{z})y_2^2)\Psi'(\zeta^2) + (a(\mathbf{z})y_2^2 + d(\mathbf{z})x_2^2)}{(\zeta^2 + \Psi(\zeta^2))}$$

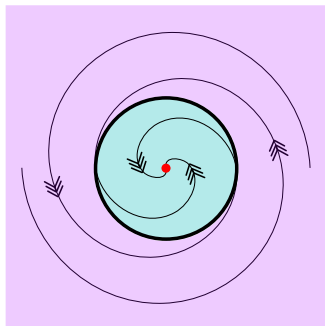
is negative everywhere for our class of regularisation functions (Definition 4.1), so all orbits in the layer problem tend to it and there can be no limit cycles. Furthermore, it is straightforward to show that there can be 0, 2 or 4 equilibria along the equator generically for a fixed  $\mathbf{z}$  (see Figures 4.15a to 4.15c and 4.16a to 4.16c). Each equilibria along the equator is radially attracting and the angular attractiveness can be determined using arguments from index theory.

- (b) If  $(\underline{\mathbf{A}}(\mathbf{z})^{-1}\mathbf{f}(0, 0, \mathbf{z}))^\top \underline{\mathbf{A}}(\mathbf{z})^{-1}\mathbf{f}(0, 0, \mathbf{z}) > 1$ , we have no critical set and from Theorem 4.1(c) there must be at least two equilibria along the equator. Again it is straightforward to show that, generically, it is possible to have either 2 or 4 equilibria on the equator for a fixed  $\mathbf{z}$ , whose radial and angular attractiveness can be determined using arguments from index theory (see Figures 4.15d, 4.15e, 4.16d and 4.16e).
- (c) Thus, given the three possible types of dynamics when there exists a critical manifold, and the two possible types of dynamics when there is not critical set, there are 5 different possible types of dynamics for Case I.

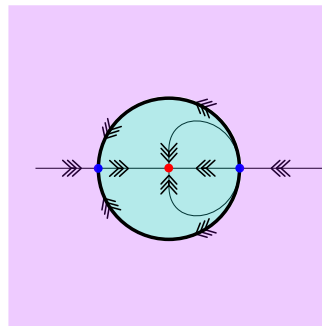
■

Sketches of the five possible phase portraits for Case I when  $a, d < 0$  are given in Figure 4.15. Numerical examples are given in Figure 4.16 .

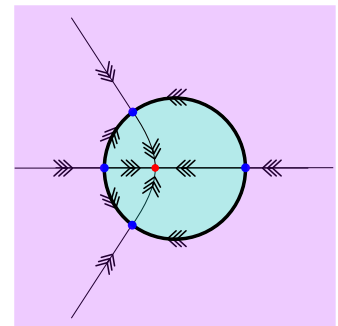
Coulomb friction falls into our Case I and results in  $b(\mathbf{z}) \equiv 0$ . In that case, the hyperbola (4.69) passes through the origin and so there are at least two intersections with the unit circle: at least two equilibria along the equator. Hence Figure 4.15a is not possible for Coulomb friction and Figures 4.15b to 4.15e correspond to the “four generic cases” in [3, section 4.2.4].



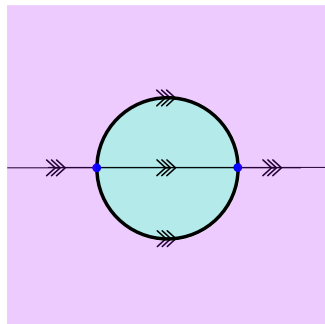
(a) Critical set, no equilibria on the equator



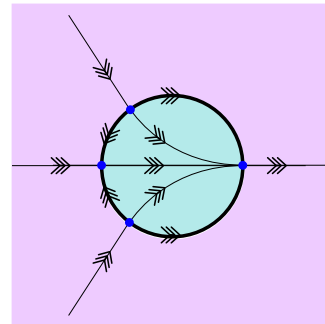
(b) Critical set, 2 equilibria on the equator



(c) Critical set, 4 equilibria on the equator

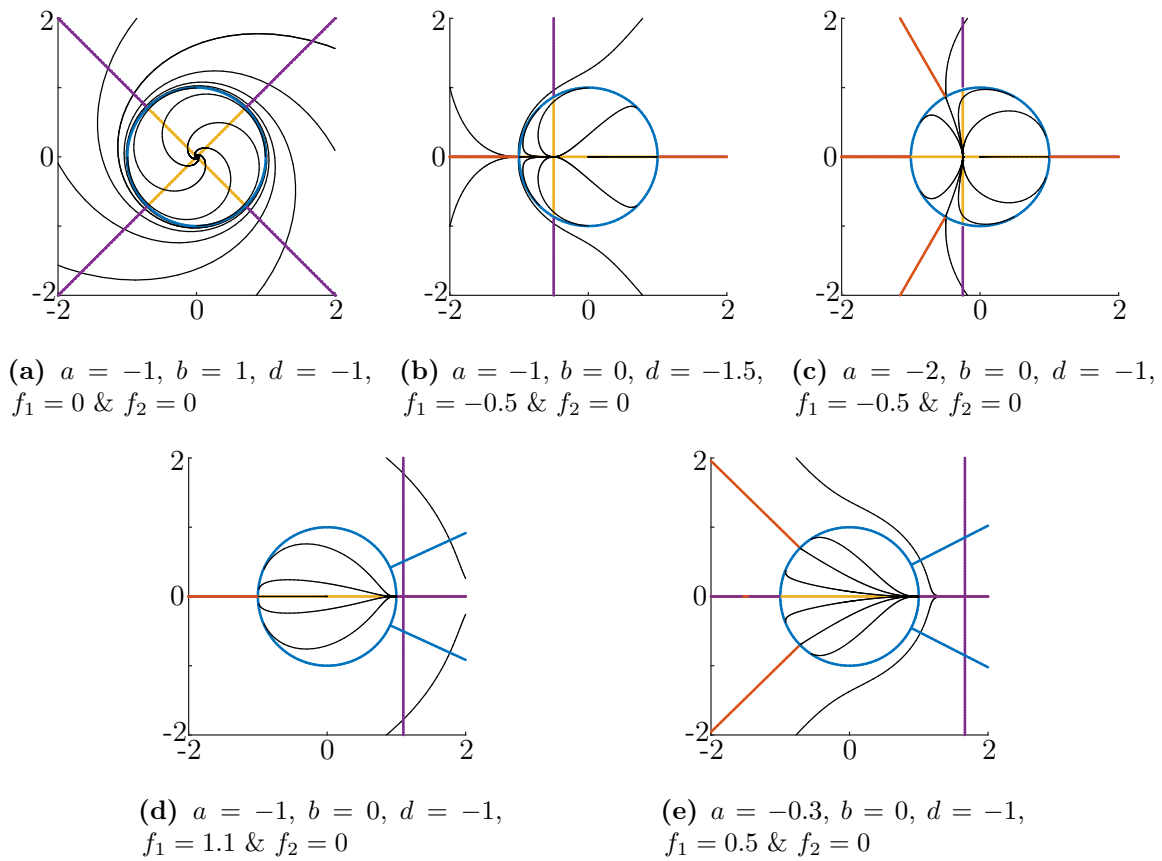


(d) No critical set, 2 equilibria on the equator



(e) No critical set, 4 equilibria on the equator

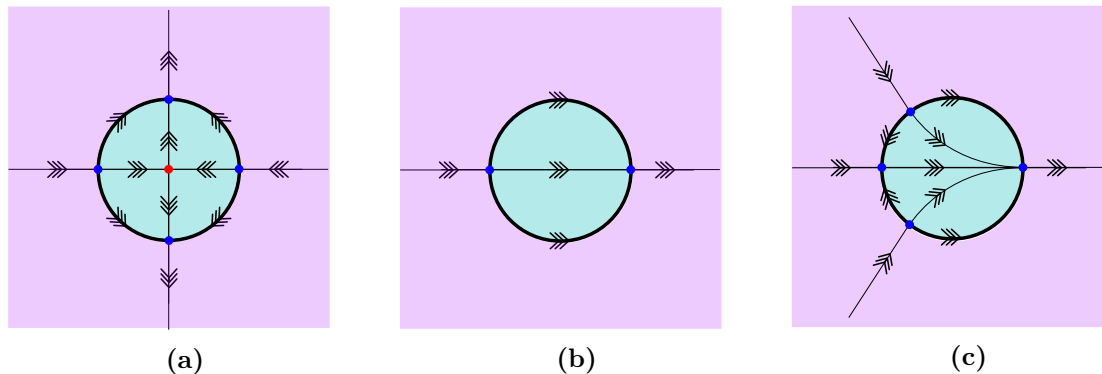
**Figure 4.15:** Sketches of the five possible cases of dynamics for Case I when  $a, d < 0$ . The blown-up sphere from Figure 4.6 is projected down onto a plane. Blue dots are equilibria of the system along the equator, whilst red dots are critical sets of the layer problem in the scaling chart  $\kappa_2$ . Sketches for  $a, d > 0$  can be obtained after a reversal of time.



**Figure 4.16:** Numerical examples of the five possible cases of dynamics of Case I when  $a, d < 0$ . The blown-up sphere from Figure 4.6 is projected down onto the  $(\bar{x}, \bar{y})$  plane, and the equator is the unit circle. Trajectories are plotted in black  $\blacksquare$ . In  $\bar{\varepsilon} = 0$ , nullclines of  $\dot{\rho}$  are shown in  $\blacksquare$  and nullclines of  $\dot{\theta}$  are shown in  $\blacksquare$ . The lines  $a\bar{x} - b\bar{y} = f_1$  and  $b\bar{x} + d\bar{y} = f_2$  are also shown ( $\blacksquare$  when inside the unit circle and  $\blacksquare$  outside).

### 4.4.3.2 Case II

Here  $a, d$  have opposite signs and  $\det(\underline{\mathbf{A}}) < 0$ . In this case there are three qualitatively different generic phase portraits for fixed  $\mathbf{z}$ , as shown in Figure 4.17.



**Figure 4.17:** Sketches of the three possible qualitative phase portraits of Case II for the blown up system of (4.60) when  $\text{sign}(a) \neq \text{sign}(d)$  and  $\det(\underline{\mathbf{A}}) = ad + b^2 < 0$ . Figure 4.17a shows the only possible phase portrait when there is a critical set in the scaling chart. Figures 4.17b and 4.17c (equivalent to Figures 4.15d and 4.15e) show the two possible phase portraits when there is no critical set in the scaling chart.

#### Theorem 4.5.

- (a) If  $(\underline{\mathbf{A}}(\mathbf{z})^{-1}\mathbf{f}(0, 0, \mathbf{z}))^\top \underline{\mathbf{A}}(\mathbf{z})^{-1}\mathbf{f}(0, 0, \mathbf{z}) < 1$ , then there exists exactly one unique critical set in the layer problem of the scaling chart, which is a saddle regardless of the regularisation function  $\Psi$ . Hence there are exactly four equilibria along the equator, each of which is a saddle with respect to the radial and angular flows.
- (b) If  $(\underline{\mathbf{A}}(\mathbf{z})^{-1}\mathbf{f}(0, 0, \mathbf{z}))^\top \underline{\mathbf{A}}(\mathbf{z})^{-1}\mathbf{f}(0, 0, \mathbf{z}) > 1$ , then there is no critical set in the layer problem of the scaling chart and there are generically either 2 or 4 equilibria along the equator as in Case I.

**Proof.** Here it is straightforward to show that when  $a$  and  $d$  are of opposite signs there can be either one unique critical set in the scaling chart or none.

- (a) If  $(\underline{\mathbf{A}}(\mathbf{z})^{-1}\mathbf{f}(0, 0, \mathbf{z}))^\top \underline{\mathbf{A}}(\mathbf{z})^{-1}\mathbf{f}(0, 0, \mathbf{z}) < 1$  there is exactly one unique critical set in the scaling chart. Furthermore, if  $\det \underline{\mathbf{A}} = ad + b^2 < 0$  then, due to the positive definiteness of  $D\mathbf{e}_\Psi$ , the critical set is a saddle with respect the fast flow. Then from the uniqueness of the critical set we can infer that there will be exactly 4 equilibria along the equator: one for each of the intersections of the stable and unstable manifolds of the critical set with the equator. The radially attractiveness of these equilibria correspond to the stable/unstable manifolds of the equilibria in the scaling chart. This is the only possible type of dynamics when there is an equilibrium in the scaling chart.

- (b) Conversely, if  $(\underline{\mathbf{A}}(\mathbf{z})^{-1}\mathbf{f}(0, 0, \mathbf{z}))^\top \underline{\mathbf{A}}(\mathbf{z})^{-1}\mathbf{f}(0, 0, \mathbf{z}) > 1$  then there is no critical set in the scaling chart. It follows from index theory that, generically, there must be at least 2 equilibria along the equator. It is straightforward to verify that there can be either 2 or 4 equilibria in this case.

■

**Remark 4.5.** *The result that if there is a critical set in the scaling chart there must be at least two equilibria on the equator, or conversely, and perhaps more intuitively, that if there are no equilibria on the equator then there must be at least one critical set in the scaling chart is a consequence of index theory [89, 101] and strongly connected to the Hairy Ball Theorem [90, 100].*

#### 4.4.3.3 Case III

For a system of the form (4.60) where  $\text{sign}(a) \neq \text{sign}(d)$  and  $\det \underline{\mathbf{A}} = ad + b^2 > 0$ , the dynamics is sensitive to the regularisation function  $\Psi$  in the scaling chart  $\kappa_2$ . We demonstrate this in the following example. Consider a system of the form (4.60) where

$$(4.86) \quad a(\mathbf{z}) = 172, \quad b(\mathbf{z}) = 186, \quad d(\mathbf{z}) = -200, \quad f_1(x, y, \mathbf{z}) = -86, \quad f_2(x, y, \mathbf{z}) = -93.$$

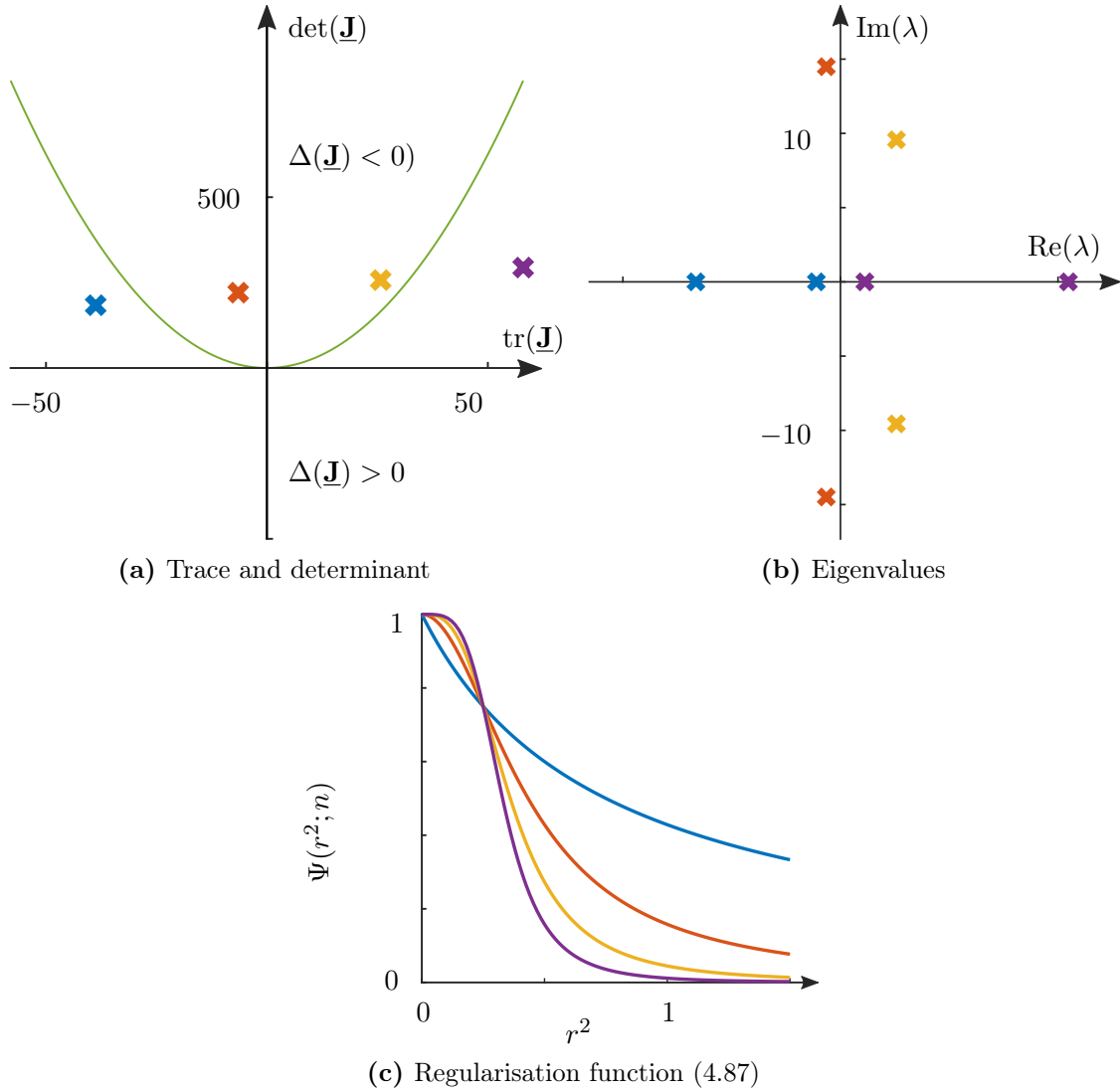
Let us also consider a particular class of regularisation functions

$$(4.87) \quad \Psi(r^2; n) = \frac{3}{3 + (4r^2)^n},$$

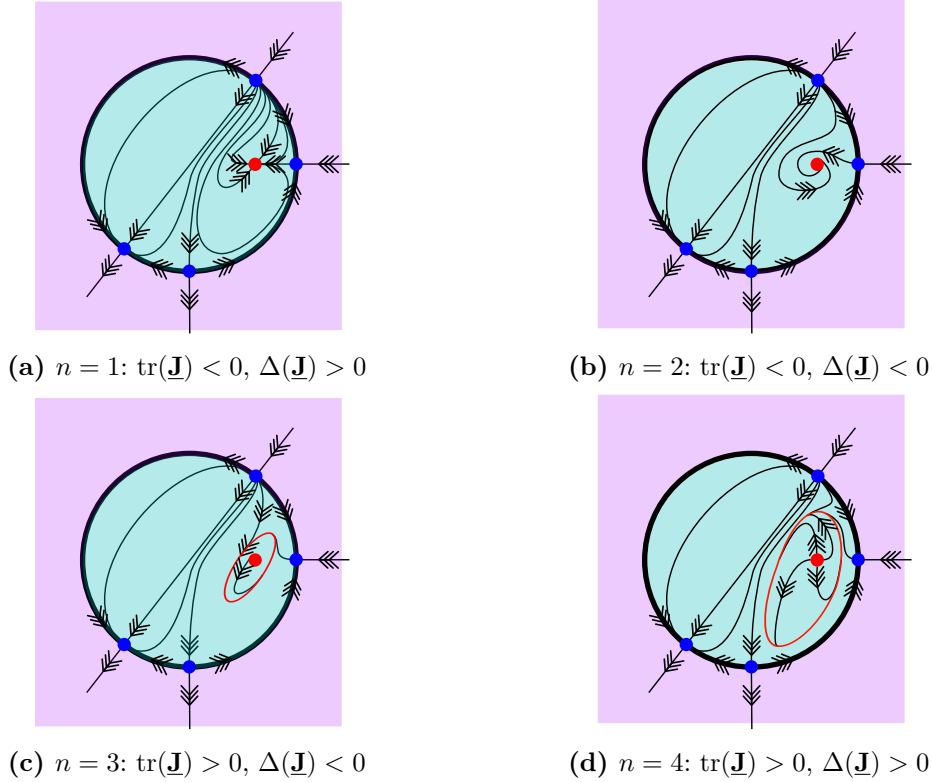
chosen such that  $\Psi((\frac{1}{2})^2; n) = \frac{3}{4}$  is independent of  $n$ . It is easy to show that the critical manifold in the scaling chart is a stable node for  $n = 1$ , a stable focus for  $n = 2$ , an unstable focus for  $n = 3$  and an unstable spiral for  $n = 4$  (see Figures 4.18 and 4.19). In order to understand the stability of the critical manifold, we study the trace  $\text{tr}(\underline{\mathbf{J}})$ , determinant  $\det(\underline{\mathbf{J}})$ , and discriminant  $\Delta(\underline{\mathbf{J}}) := \text{tr}(\underline{\mathbf{J}})^2 - 4\det(\underline{\mathbf{J}})$  of the Jacobian of the fast flow  $\underline{\mathbf{J}}$ , given in (4.56), around the critical manifold, as shown in Figure 4.18.

As evident from Figure 4.19, limit cycles can exist in the scaling chart for Case III. The slow flow along these limit cycles is given by (4.76) (Proposition 4.1). We should also note here that whether trajectories slide or cross depends upon their initial conditions.

We have demonstrated the sensitivity of the dynamics in the scaling chart  $\kappa_2$  to the regularisation. Classification of all possible phase portraits for Case III with one up to one limit cycle in the scaling chart is possible using arguments from index theory.



**Figure 4.18:** Demonstration of the effect the choice of regularisation function can have on the dynamics for Case III. For  $a(\mathbf{z}) = 172$ ,  $b(\mathbf{z}) = 186$ ,  $d(\mathbf{z}) = -200$ ,  $f_1(x, y, \mathbf{z}) = -86$ ,  $f_2(x, y, \mathbf{z}) = -93$ , choosing a different regularisation function (4.87) can cause the unique equilibrium to be a stable node, a stable focus, an unstable focus or an unstable node (for  $n = 1$  ■,  $n = 2$  ■,  $n = 3$  ■, and  $n = 4$  ■ respectively). (a) the trace  $\text{tr}(\mathbf{J})$  and determinant  $\det(\mathbf{J})$  of the Jacobian of the linearisation around the unique equilibrium for each  $n$ , (b) the eigenvalues of the same matrix and (c) the regularisation function  $\Psi(r^2; n)$  (4.87) for  $n = 1 \dots 4$ . Note the different gradients at  $r^2 = \frac{1}{4}$  for each  $n$ . Also note that the sign of the discriminant of  $\mathbf{J}$ ,  $\Delta(\mathbf{J}) := \text{tr}(\mathbf{J})^2 - 4 \det(\mathbf{J})$ , is also shown in (a).



**Figure 4.19:** Phase portraits for Case III of the “e-linear” system (4.60) and (4.61), for parameters given in (4.86), with regularisation function (4.87), for  $n = 1 \dots 4$  (see also Figure 4.18a). In (a) the critical manifold is a stable node, whereas in (b) it is a stable focus. In (c),  $\text{tr}(\mathbf{J})$  has changed sign and the critical manifold undergoes a supercritical Hopf bifurcation; it is now an unstable focus enclosed by a limit cycle (shown in red) in the layer problem. In (d), the limit cycle persists, but the critical manifold has become an unstable node.

#### 4.4.4 Bifurcations

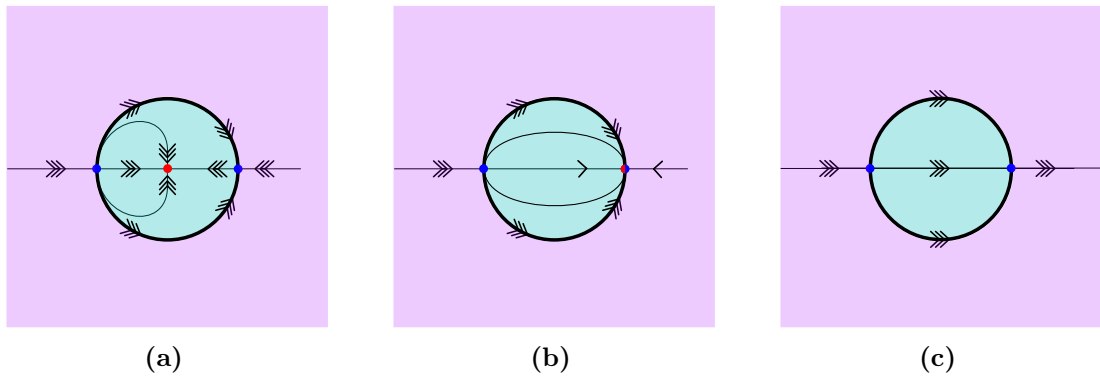
So far, we have studied the generic cases of (4.66) for fixed  $\mathbf{z}$ . Here we detail some possible bifurcations that are codimension-1 in parameter space, or which can be unfolded by the slow variable  $\mathbf{z}$ .

In Figure 4.20 a critical set is created at infinity in the scaling chart  $\kappa_2$ , for the case when there are two equilibria on the equator (there could also be four equilibria on the equator). The radial attractiveness of one equilibrium switches at the bifurcation. This bifurcation occurs when

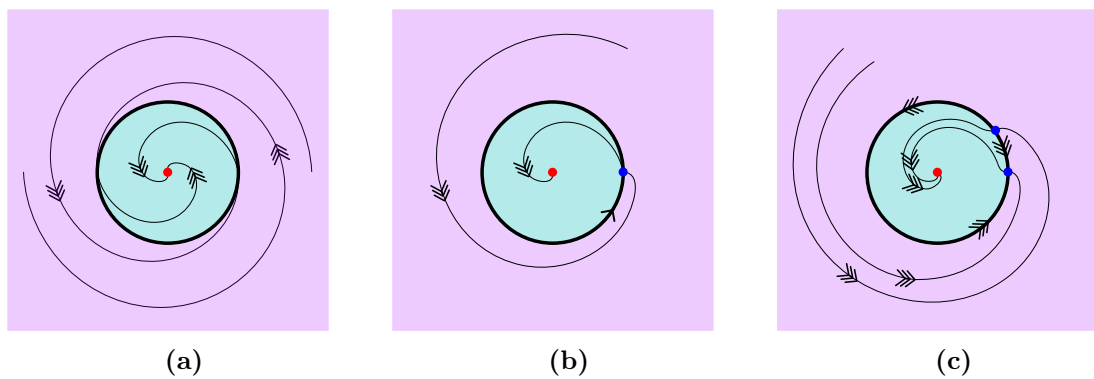
$$(4.88) \quad (\underline{\mathbf{A}}(\mathbf{z})^{-1} \mathbf{f}(0, 0, \mathbf{z}))^\top \underline{\mathbf{A}}(\mathbf{z})^{-1} \mathbf{f}(0, 0, \mathbf{z}) = 1.$$

In Figure 4.21, we consider the saddle-node bifurcation between zero and two equilibria on the equator where there is critical set in the scaling chart (we could also pass between two and four equilibria). Each pair of equilibria created on the equator has opposite angular attractiveness.





**Figure 4.20:** (a) there are two equilibria on the equator (blue dots), both radially attracting and of opposite angular attractiveness, and a critical set (in red) in the scaling chart  $\kappa_2$ . (b) there are two equilibria on the equator, one of which is radially nonhyperbolic, with a critical set at infinity. (c) there are two equilibria along the equator, one of which is now radially repelling and no critical set in the scaling chart.



**Figure 4.21:** Saddle-node bifurcation of equilibria on the equator. (a) No equilibria along the equator and a critical set in the scaling chart  $\kappa_2$ ; (b) The saddle-node bifurcation: one angularly nonhyperbolic equilibrium appears on the equator with a heteroclinic connection to the critical set and a homoclinic connection; (c) Two equilibria on the equator: one angularly attracting, the other repelling and both with heteroclinic connections to the critical set.

This bifurcation occurs when  $\theta \mapsto \Theta(0, \theta, \mathbf{z})$  has a double root:  $\Theta(0, \theta, \mathbf{z}) = \frac{\partial}{\partial \theta} \Theta(0, \theta, \mathbf{z}) = 0$ . Geometrically, this occurs when the hyperbola (4.69) is tangent to unit circle (4.70).

### 4.4.5 Tables of classification

Here we present tables of more complete classification. In Table 4.2, we show the possible generic combinations of radially attracting and repelling equilibria along the equator.

		Attracting				
		0	1	2	3	4
Repelling	0	✓	×	✓	×	✓
	1	×	✓	×	✓	⊗
	2	✓	×	✓	⊗	⊗
	3	×	✓	⊗	⊗	⊗
	4	✓	⊗	⊗	⊗	⊗

Table 4.2: Generic multiplicity of radially attracting and repelling equilibria along the equator for the linear case. We discount cases with more than 4 equilibria along the equator (denoted by  $\otimes$ ) due to the conic sections argument. We also discount cases with an odd number of equilibria along the equator (denoted by  $\times$ ) since these cannot occur generically (from topology). Possible cases are denoted by  $\checkmark$ . However, we need not consider all of these, as cases in the upper triangle ( $\checkmark$ ) are equivalent to cases in the lower triangle after a reversal of time.

In this section we introduce new notation for the classification of phase portraits.

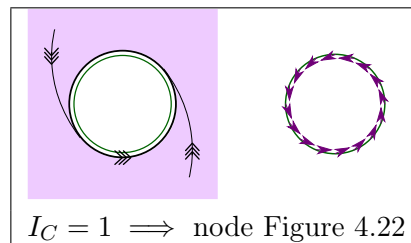


Table 4.3: Index for 0 equilibria along the equator.

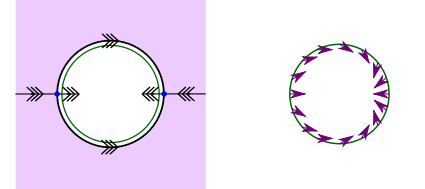
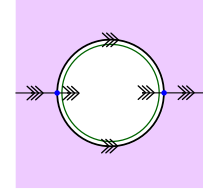
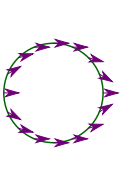
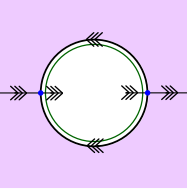
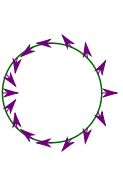
		$I_C = 1 \implies$ node Figure 4.23
		$I_C = 0 \implies$ no eq. Figure 4.24
		$I_C = 0 \implies$ inconsistent

Table 4.4: Indices for 2 equilibria along the equator. We need not consider 2 radially repelling as equivalent to reversal of time of 2 radially attracting. In the linear case there can be at most 1 equilibria in the scaling chart, therefore we can discount indices  $\notin \{-1, 0, 1\}$ .

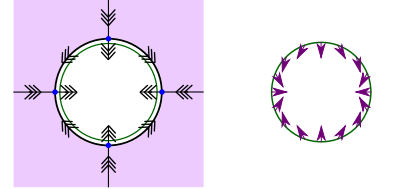
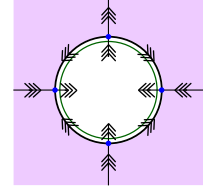
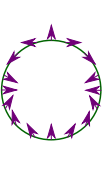
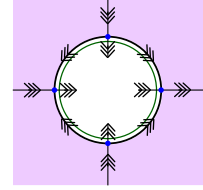
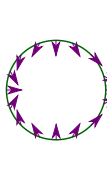
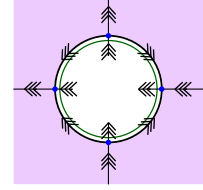

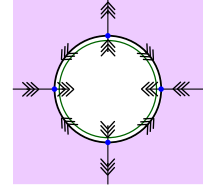

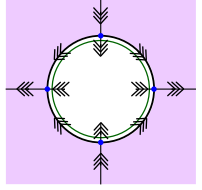

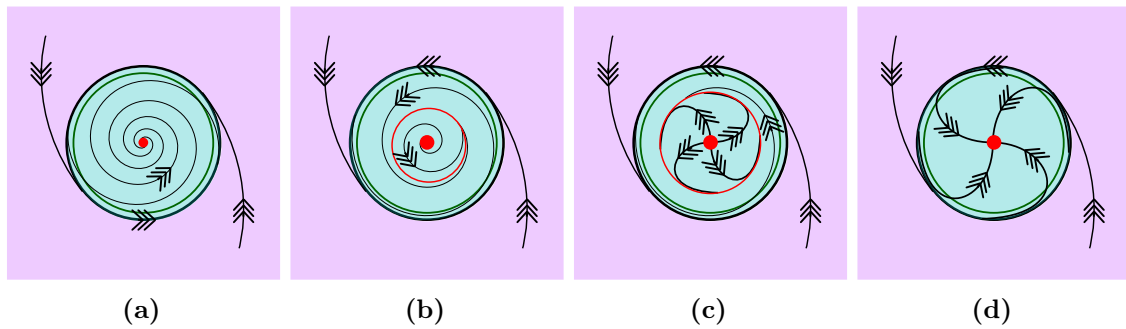
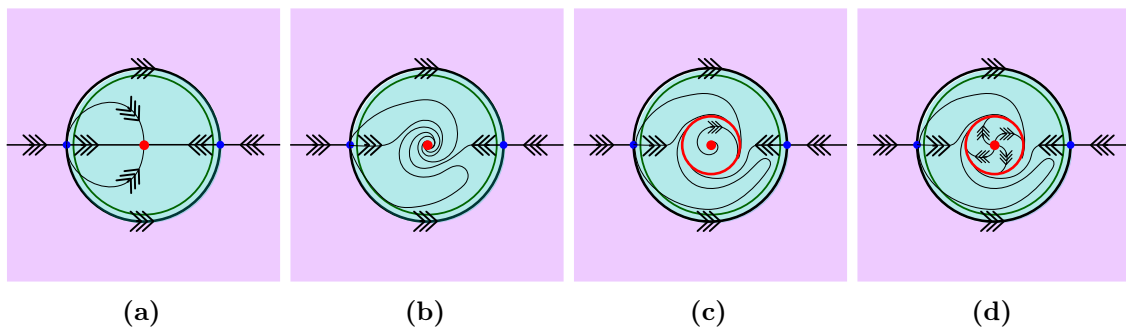
		$I_C = 1 \implies$ node Figure 4.25
		$I_C = 2 \implies$ inconsistent
		$I_C = 0 \implies$ no eq. Figure 4.26
		$I_C = 1 \implies$ node Figure 4.27
		$I_C = 3 \implies$ inconsistent
		$I_C = -1 \implies$ saddle Figure 4.28

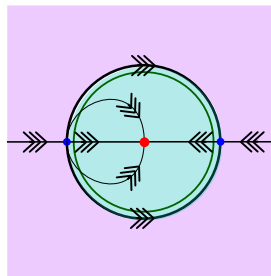
Table 4.5: Indices for four equilibria along the equator. We need not consider three or four radially repelling as equivalent to reversal of time of three and four radially attracting. In the linear case there can be at most one equilibria in the scaling chart, therefore we can discount indices  $\notin \{-1, 0, 1\}$ .



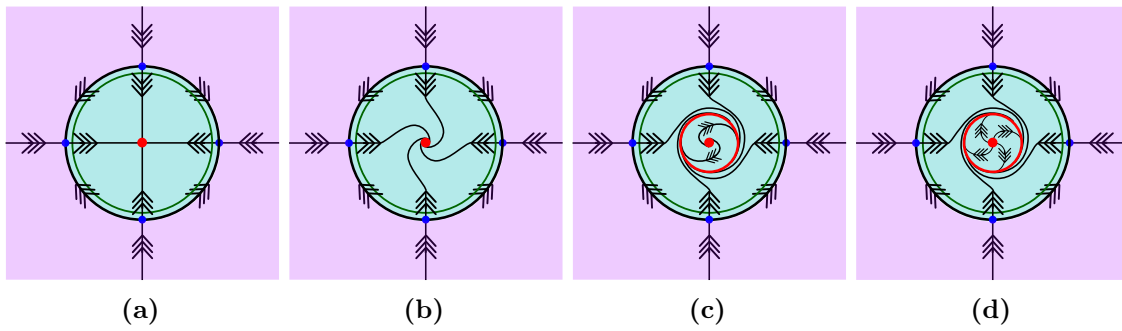
**Figure 4.22:** Possible phase portraits for 0 equilibria along the equator.



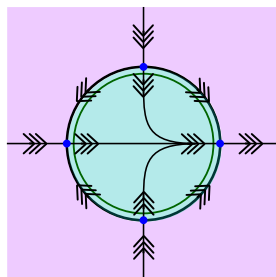
**Figure 4.23:** Possible phase portraits for 2 equilibria along the equator, both radially attracting.



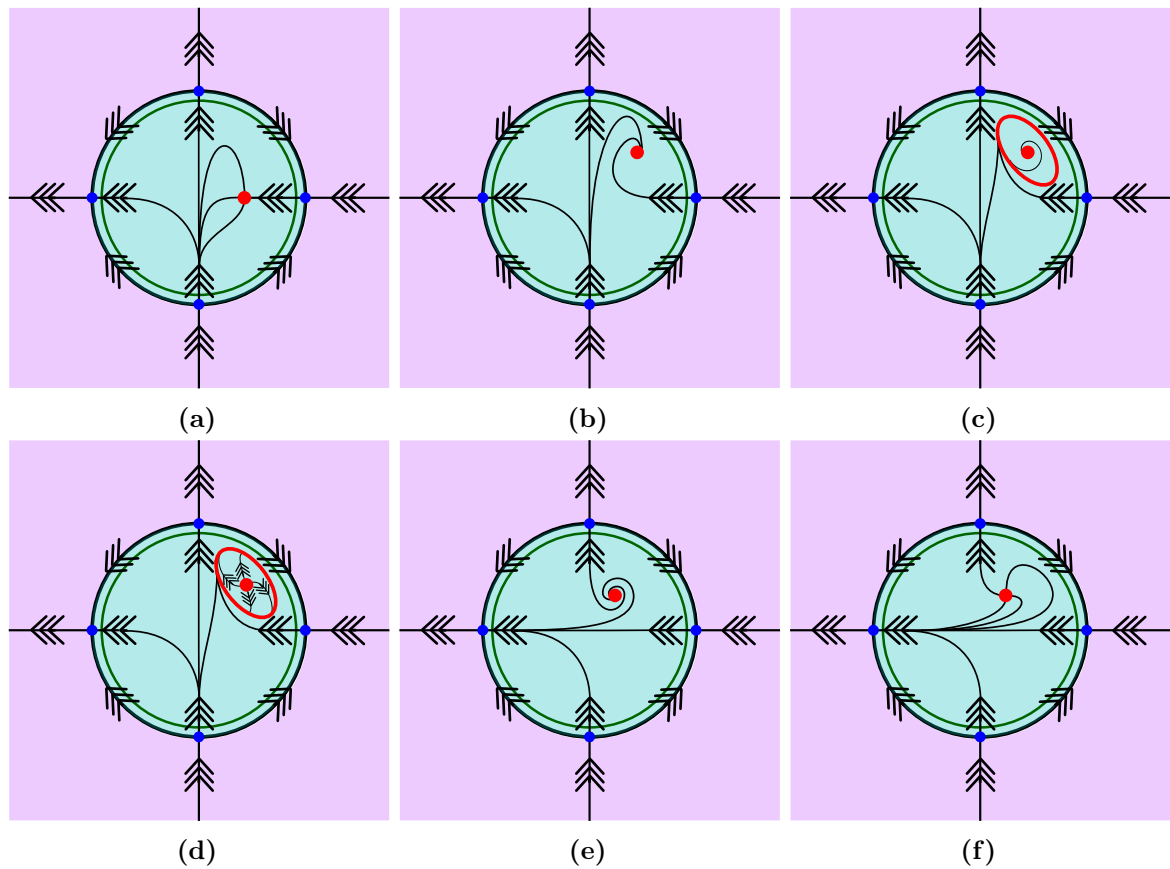
**Figure 4.24:** Possible phase portraits for 2 equilibria along the equator, one radially attracting, one radially repelling.



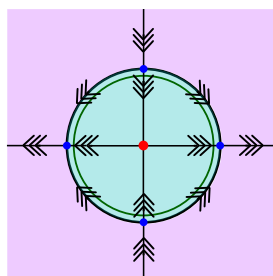
**Figure 4.25:** Possible phase portraits for 4 equilibria along the equator, all radially attracting.



**Figure 4.26:** Possible phase portraits for 4 equilibria along the equator, all but one radially attracting.



**Figure 4.27:** Possible phase portraits for 4 equilibria along the equator, two adjacent equilibria radially attracting, whilst the other two are radially repelling. (a) and (b) are equivalent to (f) and (e) respectively, but included as to demonstrate the system undergoing a heteroclinic bifurcation in the scaling chart.



**Figure 4.28:** Possible phase portraits for 4 equilibria along the equator, two opposite equilibria radially attracting.

#### 4.4.6 Beyond the e-linear normal form

Let us briefly consider a normal form of (4.9) that includes order- $N$  powers of the components of  $\mathbf{e}$ ,

$$(4.89) \quad \begin{pmatrix} \dot{x} \\ \dot{y} \\ \dot{\mathbf{z}} \end{pmatrix} = \left( \sum_{k=1}^N \left( \sum_{i+j=k} \begin{pmatrix} a_{i,j}(\mathbf{z}) \\ b_{i,j}(\mathbf{z}) \\ c_{i,j}(\mathbf{z}) \end{pmatrix} \frac{x^i y^j}{(x^2 + y^2)^{\frac{i+j}{2}}} \right) \right) + \begin{pmatrix} \mathbf{f}(x, y, \mathbf{z}) \\ \mathbf{g}(x, y, \mathbf{z}) \end{pmatrix}.$$

In the entry chart, the equilibria along the equator are given by the solutions to

$$(4.90) \quad \Theta(0, \theta, \mathbf{z}) = (-\sin \theta, \cos \theta) \left( \left( \sum_{k=1}^N \left( \sum_{i+j=k} \begin{pmatrix} a_{i,j}(\mathbf{z}) \\ b_{i,j}(\mathbf{z}) \end{pmatrix} \cos^i \theta \sin^j \theta \right) \right) + \mathbf{f}(0, 0, \mathbf{z}) \right),$$

which can be written as a trigonometric polynomial of order  $(N + 1)$ . Therefore, generically, there can be any nonnegative even number of equilibria  $l$  along the equator, up to and including  $2(N + 1)$  [92].

Let us now consider the number of possible cases of the dynamics in the entry chart for a particular number of equilibria along the equator  $l$ . From the structure of the number of possible cases of the dynamics in the chart  $\kappa_1$  for  $l = 0, 2$  and  $4$  equilibria along the equator (see Tables 4.3 to 4.5), we might expect that the number of qualitatively different phase portraits to follow  $2, 4, 9, 16\dots$  with  $(1 + l/2)^2$  (or  $1, 3, 6, 10\dots$  with  $\frac{1}{4}l(\frac{n}{2} + 1)$  if we include time reversal). However, for a positive even number of equilibria along the equator  $l$ , the number of possible cases ignoring time reversal follows

$$(4.91) \quad M(l) = \frac{1}{2} \left( 2^{\frac{l}{2}+1} + \frac{2}{l} \sum_{d|\frac{l}{2}} 2^{2d} \phi_{\Gamma} \left( \frac{l}{2d} \right) \right)$$

[91], where  $\phi_{\Gamma}$  is the Euler totient function, and

$$(4.92) \quad M(2) = 4, \quad M(4) = 9, \quad M(6) = 20, \quad M(12) = 51\dots$$

Therefore, for an order- $N$  equation of the form (4.89), the number of possible qualitatively different phases portraits in the entry chart follows

$$(4.93) \quad P(N) = 2 + \sum_r^{N+1} M(2r).$$

Within the scaling chart there can be up to  $N$  critical sets for a normal form of order  $N$ . Hence only indices over the equator  $\in [-N, N]$  are possible. We leave detailed investigation of the possible scaling charts to further work.



### 4.4.7 Codimension- $n$

The task of extending this method to higher codimension problems is not trivial. Consider the linear normal form of a codimension- $n$  system

$$(4.94) \quad \begin{pmatrix} \dot{\mathbf{x}} \\ \dot{\mathbf{z}} \end{pmatrix} = \begin{pmatrix} \underline{\mathbf{A}}(\mathbf{z}) \\ \underline{\mathbf{B}}(\mathbf{z}) \end{pmatrix} \frac{\mathbf{x}}{|\mathbf{x}|} + \begin{pmatrix} \mathbf{f}(\mathbf{x}, \mathbf{z}) \\ \mathbf{g}(\mathbf{x}, \mathbf{z}) \end{pmatrix},$$

where  $\mathbf{x} \in \mathbb{R}^n$ ,  $\mathbf{z} \in \mathbb{R}^m$ ,  $\underline{\mathbf{A}} \in \mathbb{R}^{n \times n}$ ,  $\underline{\mathbf{B}} \in \mathbb{R}^{m \times m}$ ,  $\mathbf{f} \in \mathbb{R}^n$ , and  $\mathbf{g} \in \mathbb{R}^m$ .

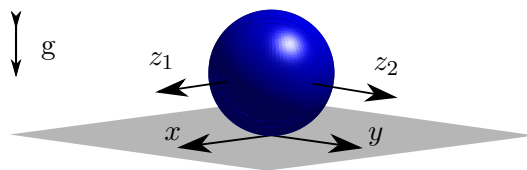
For codimension-2 problems, we have benefitted from the use of polar coordinates. This would no-longer be practical with higher-codimension problems as hyper-spherical coordinate systems [10] would be necessary. Instead of being able to write a single entry chart as in subsection 4.3.1, one might have to study multiple directional entry charts. This may result in a potential  $2n$  entry charts, unless symmetries are present and can be exploited.

## 4.5 Examples

We now discuss some examples, including some from [2].

### 4.5.1 Ball at bottom of a pool [2]

We consider a rigid ball of mass  $m$  slipping at the bottom of a pool of viscous fluid, as in Figure 4.29. Coulomb friction acts on the ball at the point of contact with the pool floor and viscous friction acts through the centre of mass of the ball due to the viscous fluid. The coefficient of Coulomb friction is  $\mu$ , and coefficient of viscous friction is  $K > 0$ .



**Figure 4.29:** Ball at the bottom of a pool:  $(x, y)$  is the relative velocity at the contact point, whilst  $\mathbf{z} = (z_1, z_2)^\top$  is the velocity of the centre of mass. Both Coulomb and viscous friction act upon the ball.

The dynamics is governed by ODEs

$$(4.95) \quad \begin{pmatrix} \dot{x} \\ \dot{y} \\ \dot{z}_1 \\ \dot{z}_2 \end{pmatrix} = \mathbf{F}(x, y, z_1, z_2) = \begin{bmatrix} -\frac{7}{2}\mu g \frac{x}{\sqrt{x^2+y^2}} - \frac{K}{m} z_1 \\ -\frac{7}{2}\mu g \frac{y}{\sqrt{x^2+y^2}} - \frac{K}{m} z_2 \\ -\mu g \frac{x}{\sqrt{x^2+y^2}} - \frac{K}{m} z_1 \\ -\mu g \frac{y}{\sqrt{x^2+y^2}} - \frac{K}{m} z_2 \end{bmatrix}$$

where  $(x, y)$  is the relative velocity at the point of contact of the ball with the pool, and  $\mathbf{z} = (z_1, z_2)$  is the velocity of the centre of mass of the ball in the same axes (for details of the derivation, see [2, section 6.2]). These equations can be written in our  $\mathbf{e}$ -linear normal form given by (4.60) and (4.61), where

$$(4.96) \quad \underline{\mathbf{A}} = -\frac{7}{2}\mu g \begin{pmatrix} 1 & 0 \\ 0 & 1 \end{pmatrix}, \quad \mathbf{f}(\mathbf{z}) = -\frac{K}{m} \begin{pmatrix} z_1 \\ z_2 \end{pmatrix}, \quad \underline{\mathbf{B}} = -\mu g \begin{pmatrix} 1 & 0 \\ 0 & 1 \end{pmatrix}, \quad \mathbf{g}(\mathbf{z}) = -\frac{K}{m} \begin{pmatrix} z_1 \\ z_2 \end{pmatrix}.$$

In the entry chart  $\kappa_1$ , this is degenerate case (D1), since the diagonal elements of  $\underline{\mathbf{A}}$  are equal. Since the off-diagonal elements of  $\underline{\mathbf{A}}$  are zero, there are two unique equilibria on the equator, given by

$$(4.97) \quad \theta_1^* = \arctan\left(\frac{f_2}{f_1}\right) = \arctan\left(\frac{z_2}{z_1}\right), \quad \theta_2^* = \theta_1^* + \pi.$$

These equilibria have eigenvalues given by

$$(4.98) \quad \lambda_\rho(\theta_1^*) = -\frac{7}{2}\mu g - \frac{K}{m}|\mathbf{z}|, \quad \lambda_\theta(\theta_1^*) = +\frac{K}{m}|\mathbf{z}|,$$

$$(4.99) \quad \lambda_\rho(\theta_2^*) = -\frac{7}{2}\mu g + \frac{K}{m}|\mathbf{z}|, \quad \lambda_\theta(\theta_2^*) = -\frac{K}{m}|\mathbf{z}|,$$

where  $|\mathbf{z}| = \sqrt{z_1^2 + z_2^2}$ . Hence, as noted by [2],

- the equilibrium  $\theta_1^*$  is always angularly repelling and radially attracting; and
- the equilibrium  $\theta_2^*$  is always angularly attracting, but it is radially attracting when  $|\mathbf{z}| < z_{\text{crit}}$  and radially repelling when  $|\mathbf{z}| > z_{\text{crit}}$ ,

where  $z_{\text{crit}} = \frac{7\mu mg}{2K} > 0$ .

In the scaling chart  $\kappa_2$  ( $\bar{\varepsilon} = 1$ ), the critical manifold (4.55) is given by

$$(4.100) \quad C = \left\{ (x_2, y_2, \mathbf{z}) \left| c(\mathbf{z}) = -\frac{2K}{7\mu mg} z_1, s(\mathbf{z}) = -\frac{2K}{7\mu mg} z_2 \right. \right\}.$$

To exist,  $C$  must lie within  $D_1$ , the unit disc centred on the origin (see Definition 4.2), and so

$$(4.101) \quad |\mathbf{z}| < z_{\text{crit}},$$

equivalent to the constraint that  $\theta_2^*$  is radially attracting.

When  $C$  exists, the reduced dynamics along it is given by

$$(4.102) \quad \begin{aligned} \dot{z}_1 &= \frac{2K}{7m} z_1 - \frac{K}{m} z_1 = -\frac{5K}{7m} z_1 \\ \dot{z}_2 &= \frac{2K}{7m} z_2 - \frac{K}{m} z_2 = -\frac{5K}{7m} z_2 \end{aligned}$$

and so the speed of the ball tends to zero in this case. From Theorem 4.2, the stability of the critical manifold  $C$  is given by the eigenvalues of

$$(4.103) \quad D_{(c,s)}\mathbf{U}((c,s)^\top, 0, 0, \mathbf{z}) D_{(x_2, y_2)}\mathbf{e}_\Psi(x_2, y_2; 1) = \begin{bmatrix} -\frac{7}{2}\mu g & 0 \\ 0 & -\frac{7}{2}\mu g \end{bmatrix} D\mathbf{e}_\Psi.$$

Since

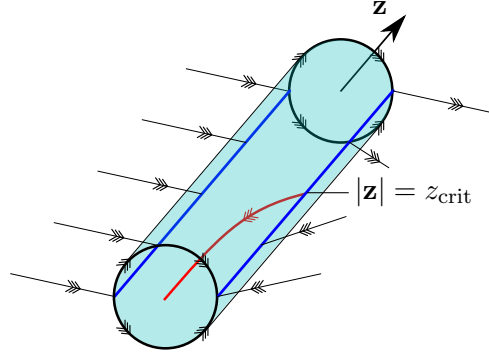
$$(4.104) \quad \text{tr}(D_{(c,s)}\mathbf{U}((c,s)^\top, 0, 0, \mathbf{z}) D_{(x_2, y_2)}\mathbf{e}_\Psi(x_2, y_2; 1)) = -\frac{7}{2}\mu g \text{tr}(D\mathbf{e}_\Psi) < 0$$

and

$$(4.105) \quad \det(D_{(c,s)}\mathbf{U} D\mathbf{e}_\Psi) = \frac{49}{4}\mu^2 g^2 \det(D\mathbf{e}_\Psi) > 0,$$

(using properties from Remark 4.3) the critical manifold  $C$ , when it exists, is stable, independent of the regularisation  $\Psi$ , as expected from Theorem 4.4.

This problem contains the bifurcation shown in Figure 4.20, when the critical manifold  $C$  appears on the equator at  $\theta_2^*$  (scaled such that  $\theta_2^* = 0$ ). Physically, we can interpret the bifurcation as follows. In Figure 4.20a, all trajectories end up on the critical manifold  $C$ ; the speed of the centre of mass  $|\mathbf{z}| < z_{\text{crit}}$ , so the ball sticks and starts rolling, slowing due to viscous friction. In Figure 4.20b, at the critical speed  $|\mathbf{z}| = z_{\text{crit}}$ , the ball is on the point of slipping, as the equilibrium  $\theta_2^*$  becomes radially nonhyperbolic at the bifurcation. Finally in Figure 4.20c, for  $|\mathbf{z}| > z_{\text{crit}}$  all trajectories are slipping except for the singular trajectory across the unit circle, where the ball instantaneously sticks, only to slip again. This bifurcation can occur dynamically as shown in Figure 4.30. This example demonstrates that the limiting case of our analysis is identical to that from other methods. The advantage is that it is now possible to analyse perturbations away from this nonsmooth limits using standard techniques, and to study the system with the framework of smooth dynamical systems.



**Figure 4.30:** Ball at the bottom of the pool. There is a tangency of the vector field to the discontinuity at  $|\mathbf{z}| = z_{\text{crit}} \equiv \frac{7\mu mg}{2K}$ . This could be considered to be the extension of a PWS invisible fold tangency to an isolated codimension-2 discontinuity [36, 65]. Taking sections at  $|\mathbf{z}| < z_{\text{crit}}$ ,  $|\mathbf{z}| = z_{\text{crit}}$  and  $|\mathbf{z}| > z_{\text{crit}}$  gives Figures 4.20a to 4.20c, respectively. The cylindrical surface corresponds to the equator of the blowup for each  $\mathbf{z}$  whilst the cylinder's volume corresponds to the scaling chart. The blue lines along the cylinder are therefore sets of equilibria in the entry chart, whilst the red curve corresponds to the critical manifold in the scaling chart.

#### 4.5.2 System with attracting and repelling directions

Consider the following system [2, Example 4.5], which is nonlinear in  $\mathbf{e}$ .

$$(4.106) \quad \begin{aligned} \dot{x} &= -\frac{x}{\sqrt{x^2 + y^2}} + \frac{2x^2}{x^2 + y^2} - \frac{1}{2} \\ \dot{y} &= -\frac{y}{\sqrt{x^2 + y^2}} \\ \dot{z} &= -z. \end{aligned}$$

Using our approach, we recover the results in [2] and quantify the effects of regularisation on the dynamics.

Regularising (4.106), we obtain

$$(4.107) \quad \begin{aligned} \dot{x} &= -\frac{x}{\sqrt{r^2 + \varepsilon^2 \Psi(r^2/\varepsilon^2)}} + \frac{2x^2}{r^2 + \varepsilon^2 \Psi(r^2/\varepsilon^2)} - \frac{1}{2} \\ \dot{y} &= -\frac{y}{\sqrt{r^2 + \varepsilon^2 \Psi(r^2/\varepsilon^2)}} \\ \dot{z} &= -z \end{aligned}$$

where  $r^2 = x^2 + y^2$ .

In the entry chart  $\kappa_1$ , written in desingularised polar coordinates, (4.107) becomes

$$(4.108) \quad \begin{aligned} \frac{d}{d\mathcal{T}}\rho &= \rho\xi \left( 2\cos^3\theta - \cos\theta - \frac{1}{2} \right), \\ \frac{d}{d\mathcal{T}}\theta &= \xi^{-1} \frac{\sin\theta}{2} (1 - 2\cos\theta)(1 + 2\cos\theta), \\ \frac{d}{d\mathcal{T}}z &= -\rho z, \\ \frac{d}{d\mathcal{T}}\varepsilon_1 &= -\frac{\varepsilon_1}{\rho} \frac{d}{d\mathcal{T}}\rho. \end{aligned}$$

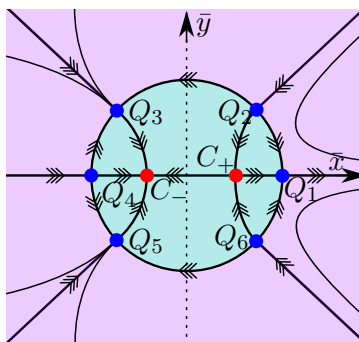
Equilibria on the equator occur at  $Q_i = \{(\rho, \theta, z, \varepsilon_1) | \rho = 0, \theta = \theta_i, \varepsilon_1 = 0\}$  where  $\theta_i = (i-1)\frac{\pi}{3}$ . Equilibria  $Q_i, i \in \{1, 3, 5\}$  are angularly attracting ( $\lambda_\theta < 0$  for  $\theta_i, i \in \{1, 3, 5\}$ ), whilst the others are angularly repelling. Furthermore,  $Q_i, i \in \{2, 3, 4, 5, 6\}$  are all radially attracting ( $\lambda_\rho < 0$  for  $\theta_i, i \in \{2, 3, 4, 5, 6\}$ ), whilst  $Q_1$  is radially repelling.

In the scaling chart  $\kappa_2$  ( $\bar{\varepsilon} = 1$ ) critical sets are given implicitly by

$$(4.109) \quad C_\pm = \left\{ (x_2, y_2) \mid y_2 = 0, x_2 = x_2^*, x_2^* = \pm \sqrt{\left(1 \pm \frac{2}{\sqrt{5}}\right) \Psi(x_2^{*2})} \right\},$$

where  $C_+$  is always a saddle, whilst  $C_-$  is always a stable node.

The combined dynamics projected into the  $(\bar{x}, \bar{y})$  plane is shown in Figure 4.31. This example demonstrates the ambiguity of the terms *crossing* and *sliding* for problems with isolated codimension-2 discontinuities. For initial conditions  $(x_0, y_0)$  where  $|\arctan(y_0/x_0)| < \frac{\pi}{3}$  there is crossing; otherwise, there is sliding.



**Figure 4.31:** Figure showing the blown-up discontinuity  $x = y = \varepsilon = 0$  of (4.107). Equilibria  $Q_i, i \in \{1, 3, 5\}$ , are angularly attracting whilst  $Q_i, i \in \{2, 4, 6\}$ , are angularly repelling.  $Q_1$  is radially repelling whilst the other equilibria along the equator are radially attracting. Within the scaling chart  $\kappa_2$ , there are two critical manifolds  $C_\pm$  (4.109), a saddle and a stable node respectively with respect to the fast flow.

Note that in this example (4.106),  $\dot{z}$  is independent of  $\mathbf{e}$  and so the slow flow in the regularised problem is the same for the two critical sets  $C_\pm$  (4.109). In the next example  $\dot{z}$  depends on  $\mathbf{e}$ .

We will show that when there are multiple stable critical sets in the scaling chart with different corresponding slow flows, this can result in nonunique sliding in the nonsmooth limit. This sliding can then depend upon the direction along which trajectories approach the discontinuity set  $\Sigma$ .

### 4.5.3 System with nonunique sliding vector field

Consider the following system, which is nonlinear in  $\mathbf{e}$  and where  $\dot{z}$  depends on  $\mathbf{e}$ .

$$(4.110) \quad \begin{aligned} \dot{x} &= -\frac{x}{\sqrt{x^2+y^2}} \left( \frac{x}{\sqrt{x^2+y^2}} - \frac{1}{2}\chi(z) \right) \left( \frac{x}{\sqrt{x^2+y^2}} + \frac{1}{2}\chi(z) \right), \\ \dot{y} &= -\frac{1}{2} \frac{y}{\sqrt{x^2+y^2}}, \\ \dot{z} &= -2 \frac{x}{\sqrt{x^2+y^2}} + \frac{1}{4} \end{aligned}$$

where  $\chi(z) = (1+2z^2)/(1+z^2)$ . This system has been chosen such that there exist multiple critical manifolds in the scaling chart, each with a different slow flow.

Regularising as before, (4.110) becomes

$$(4.111) \quad \begin{aligned} \dot{x} &= -\frac{x}{\sqrt{r^2 + \varepsilon^2 \Psi\left(\frac{r^2}{\varepsilon^2}\right)}} \left( \frac{x}{\sqrt{r^2 + \varepsilon^2 \Psi\left(\frac{r^2}{\varepsilon^2}\right)}} - \frac{1}{2}\chi(z) \right) \left( \frac{x}{\sqrt{r^2 + \varepsilon^2 \Psi\left(\frac{r^2}{\varepsilon^2}\right)}} + \frac{1}{2}\chi(z) \right), \\ \dot{y} &= -\frac{1}{2} \frac{y}{\sqrt{r^2 + \varepsilon \Psi\left(\frac{r^2}{\varepsilon^2}\right)}}, \\ \dot{z} &= -2 \frac{x}{\sqrt{r^2 + \varepsilon \Psi\left(\frac{r^2}{\varepsilon^2}\right)}} + \frac{1}{4}. \end{aligned}$$

Following the procedure (4.42) of using polar coordinates in the plane  $\bar{\varepsilon} = 0$  (the entry chart  $\kappa_1$ ), we find that (4.111) becomes

$$(4.112) \quad \begin{aligned} \frac{d}{d\mathcal{T}}\rho &= -\rho \left( \cos^4 \theta - \frac{\chi(z)^2 + 2}{4} \cos^2 \theta + \frac{1}{2} \right), \\ \frac{d}{d\mathcal{T}}\theta &= \sin \theta \cos \theta \left( \cos^2 \theta - \frac{\chi(z)^2 + 2}{4} \right), \\ \frac{d}{d\mathcal{T}}z &= -2\rho \cos \theta z + \frac{1}{4}, \\ \frac{d}{d\mathcal{T}}\varepsilon_1 &= -\frac{\varepsilon_1}{\rho} \frac{d}{d\mathcal{T}}\rho. \end{aligned}$$

There are eight equilibria (limit directions)  $Q_i = \{(\rho, \theta, z) | \rho = 0, \theta = \theta_i(z), i = 1 \dots 8\}$  of (4.112) along the equator, where

$$(4.113) \quad \theta_1 = 0, \quad \theta_2 = -\theta_8 = \arccos\left(\frac{\sqrt{\chi^2 + 2}}{2}\right), \quad \theta_3 = -\theta_7 = \frac{\pi}{2}, \quad \theta_4 = -\theta_6 = \pi - \theta_2, \quad \theta_5 = \pi.$$

They are all radially attracting ( $\lambda_\rho(\theta_i(z), z) < 0, \forall i$ ). The equilibria  $\theta = \theta_i, i \in \{1, 3, 5, 7\}$  are angularly repelling ( $\lambda_\theta(\theta_i(z), z) > 0, i \in \{1, 3, 5, 7\}$ ) whilst the equilibria  $\theta = \theta_i, i \in \{2, 4, 6, 8\}$  are angularly attracting ( $\lambda_\theta(\theta_i(z), z) < 0, i \in \{2, 4, 6, 8\}$ ).

We now proceed to study the dynamics in the scaling chart  $\kappa_2$  of (4.111) after the blowup. We find the slow-fast system

$$(4.114) \quad \begin{aligned} \varepsilon \dot{x}_2 &= -\frac{x_2}{\sqrt{\zeta^2 + \Psi(\zeta^2)}} \left( \frac{x_2}{\sqrt{\zeta^2 + \Psi(\zeta^2)}} - \frac{1}{2}\chi(z) \right) \left( \frac{x_2}{\sqrt{\zeta^2 + \Psi(\zeta^2)}} + \frac{1}{2}\chi(z) \right), \\ \varepsilon \dot{y}_2 &= -\frac{1}{2} \frac{y_2}{\sqrt{\zeta^2 + \Psi(\zeta^2)}}, \\ \dot{z} &= -2 \frac{x_2}{\sqrt{\zeta^2 + \Psi(\zeta^2)}} + \frac{1}{4}, \end{aligned}$$

where  $\zeta = x_2^2 + y_2^2$  as before. There are three critical sets (4.55) given by

$$(4.115a) \quad C_1 = \left\{ (x_2, y_2, z) | y_2 = 0, x_2 / \sqrt{x_2^2 + \Psi(x_2^2)} = -\frac{1}{2}\chi(z) \right\},$$

$$(4.115b) \quad C_2 = \left\{ (x_2, y_2, z) | y_2 = 0, x_2 / \sqrt{x_2^2 + \Psi(x_2^2)} = 0 \right\},$$

$$(4.115c) \quad C_3 = \left\{ (x_2, y_2, z) | y_2 = 0, x_2 / \sqrt{x_2^2 + \Psi(x_2^2)} = +\frac{1}{2}\chi(z) \right\}.$$

For a fixed  $z$ ,  $C_1$  and  $C_3$  are stable nodes in the layer problem for all regularisation functions  $\Psi$  in our class (Definition 4.1), whilst  $C_2$  is a saddle.

The slow flow along  $C_1$  is  $\dot{z} = \chi(z) + \frac{1}{4}$ , and  $\dot{z} = -\chi(z) + \frac{1}{4}$  along  $C_3$ . We can see the dynamics of this example in Figures 4.8c, 4.9c, 4.10c and 4.11c.

These critical sets correspond to different sliding vector fields in the nonsmooth limit. Hence we have constructed an example where the sliding vector field is dependent upon the direction of approach to the codimension-2 discontinuity set  $\Sigma$ .

## 4.6 Discussion and conclusions

In this work, we have proposed an approach for the study of general dynamical systems with isolated codimension-2 discontinuity sets (4.1), by using GSPT and blowup to study a regularised version of the system, which also helps with the understanding of the robustness of these discontinuous problems to smoothing perturbations.

For our general system (4.9), with a directional limit of the vector field onto  $\Sigma$ ,  $\mathbf{F}^*(\theta, \mathbf{z})$  (4.8), we have demonstrated that the methods and terminology of Filippov [36] can be ambiguous. In particular, sliding and crossing are dependent upon the approach to the discontinuity set (as in Example 4.5.2), and it is possible to have more than one sliding vector field (see Example 4.5.3).

We have also proposed a natural extension of standard Filippov systems to codimension-2 problems in section 4.4: the  $\mathbf{e}$ -linear system. For such systems, we have classified the dynamics into three cases and found analogues to sliding, crossing and the sliding vector field.

Within our framework there is potential for sliding if there is a critical set (4.31) in the scaling chart  $\kappa_2$ . In particular, the sliding vector field corresponds to the slow flow along the critical set. In the  $\mathbf{e}$ -linear system, this flow will be unique, even if there are limit cycles Proposition 4.1. Whether or not there is sliding can depend upon the direction of approach to the discontinuity set (see Figure 4.19), and we have the possibility of multiple sliding vector fields in Example 4.5.3.

In this paper, we consider the class of regularisation functions  $\Psi$  that lead to monotonic smoothed step functions (see Figure 4.5). Hence within our current framework, we study Coulomb friction. Other types of regularisation would be needed to study other friction laws, such as “stiction” [12, 62]. Using our regularisation approach, certain physical phenomena that are not covered here may be facilitated. For example, we can expect stick-slip oscillations to be given by heteroclinic connections between equilibria along the equator, where one of the connections occurs in the chart  $\kappa_1$  and the other in the chart  $\kappa_2$  (slip and stick respectively).

A piece of further work could be to link this analysis to the concept of friction cones. For an application of friction cones, see [16]).





## Chapter 5

# Discussion and Conclusions

We have demonstrated the nonexistence and nonuniqueness of forward-time solutions due to the conflict between the rigid-body assumptions and the the resulting dynamics seen in the 2D problem also occur in the 3D problem (see also [16, 109, 110]). Crucial to the paradox are the nondimensional terms  $p(\theta, \varphi; \alpha, \mu)$  and  $b(\theta, \Psi, \Theta)$  (given in (1.25) and (1.26)).

We have extended the understanding of geometry of the planar Painlevé problem to the full 3D problem. We show that the planar problem is a singular subset of the full 3D problem. We have given generalisations of certain key results from [38] where possible, and demonstrated where these results do not generalise to the full 3D problem.

Notably, we have demonstrated that the critical value of the coefficient of friction  $\mu_C$  is not as significant in the extended problem. Furthermore, we have demonstrated the importance of the relative slip angle  $\varphi$  and the azimuthal angular velocity  $\Psi$ . This angular velocity (not present in the planar problem) is particularly key to the dynamics, both in avoiding the paradox and causing lift-off. Nonetheless, we have shown only part of the richness of the dynamics of the Painlevé paradox in 3D.

We prove that unlike in the planar problem, it is typical for the rod to reach inconsistency. These orbits, identified in [16], may be particularly important in applications, as they could provide a new mechanism for mechanical systems to undergo juddering behaviours. This may be an unwanted phenomenon which could cause damage to machinery, or a useful response if bouncing is desired.

We then proceed to resolve the “paradox” through the incorporation of compliance, generalising results obtained by Hogan and Kristiansen from the 2D problem [42] to the 3D problem. This compliance includes both stiffness and damping terms and leads to the introduction of a small parameter  $\varepsilon$ . We use GSPT to study the problem, singularly perturbed by this  $\varepsilon$ , using the framework of blowup to “zoom-in on”, and match across, regimes.

We recover IWC in the compliant system in both inconsistent and indeterminate regions. We find that the saddle structure in the indeterminate region shown in [42], also occurs in the 3D problem. This saddle is significant as it acts as a separatrix between initial conditions that

lead to IWC and those that lift off. Whilst we find that IWC is still comprised of 3 phases in the 3D problem (slipping compression, sticking compression, and lift-off), we also find that the transition between slipping and sticking is important.

We follow the significant orbits present in the rigid-body problem that reach the inconsistent region from slipping and find that they also undergo IWC with the inclusion of compliance. We use blowup to “zoom-in on” the boundary between the slipping and inconsistent regions. Within the scaling chart of this blowup, we find that the dynamics are governed by the type I Painlevé equation (a satisfying mathematical coincidence) and that a special solution begins the slipping compression phase. In order to conveniently study the transition from slipping to sticking, we also view spatial Coulomb friction as the limit of a smooth system and use blowup to analyse the resulting singularly perturbed system.

Finally, we study this approach of smoothing Coulomb friction more generally. For planar rigid body problems, Coulomb friction results in a codimension-1 discontinuity. The de-facto approach to these PWS dynamical systems is to use the Filippov framework. But this framework does not generalise to systems with higher codimension discontinuities, such as 3D rigid body problems with point contact. We study a general system with an isolated codimension-2 discontinuity set, not limiting ourselves to spatial Coulomb friction. Continuing our approach of regularisation and blowup, we regularise the nonsmooth system by taking it to be the limit of a smooth one and use blowup to study the singularly perturbed dynamics.

We present a framework for studying these codimension-2 problems, drawing from existing literature on the regularisation of codimension-1 discontinuities [12, 61, 63, 65, 102] and the intersections thereof [55]. Whilst this work shares many similarities with that by Antali and Stépán [2, 3], our approach enables the use of several advantageous theories from smooth dynamical systems (including GSPT and index theory). For our codimension-2 problems, we have described the local dynamics, and generalising Filippov sliding, crossing, and sliding vector fields in terms of the nomenclature of smooth dynamical systems, slow-fast theory and blowup. Whilst motivated by Coulomb friction, the approach is sufficiently general as to apply to any nonsmooth dynamical system with finite-time approach to a codimension-2 discontinuity. We have also presented an important class of codimension-2 discontinuities, the  $\mathbf{e}$ -linear problem. This case is analogous to standard Filippov systems, which are linear in signum or Heaviside functions, and includes spatial Coulomb friction. For this class, we have given a more complete classification of the possible local dynamics, and discussed the possible bifurcations. However, our physical examples show only a small sample of the possible cases in the  $\mathbf{e}$ -linear problem. It would be interesting to find systems that result in no equilibria along the equator of the blowup or those that demonstrate sensitivity to the regularisation function. These phenomena would have particularly curious physical implications.

The central thesis of this work is to motivate and further develop the approach of using regularisation and blowup to study mechanical systems, particularly those that exhibit Painlevé

---

paradoxes, nonsmoothness, or nonexistence or nonuniqueness of solutions. Both the lack of existence or uniqueness of solutions in the Painlevé paradox and the ambiguity of solutions to mechanical systems with spatial Coulomb friction can be overcome using this methodology.

This approach can often be physically justified. In the case of the Painlevé problem, we may expect the surface not to be rigid but to have very large stiffness (very small compliance). Whilst in this work we introduce linear stiffness and damping, there are alternative resolutions of the paradox: wave propagation in the rod [6], Hertzian contact [52], or more complicated contact mechanics that include asperities [39]. In the case of friction, there exist models that include “creep forces”, where friction is indeed a smooth but sharp system [7, 46, 88, 97]. Independent of the physical justification, the approach of viewing the system as a small perturbation to a smooth system is a powerful one, as it enables the use of well understood theory from smooth dynamical systems.

The theories used in this work are also very powerful. GSPT enables the deconstruction of extremely complicated high-dimensional nonlinear ODEs into multiple simpler differential equations that are valid in different regimes. The theory then allows the matching across these regimes. In this work we have used this mathematical toolbox in a relatively novel way, not to build up rigorous proofs, but instead as a form of dimensional reduction, used to simplify equations in order to gain insight into the potential dynamics. Previously, blowup has mainly featured in the detailed analysis of relatively low-dimensional dynamical systems [43, 50, 59, 60, 66]. However, this level of detail can become intractable for higher-dimensional problems.

However, in applications where even in high dimensional systems there is a clear structure or different scales in time or space, it is possible that the use of GSPT can be extended. For example, in multi-layer or network-on-networks, where there exist many similar nodes or patches governed by similar equations, it is possible that the difficulties in the mathematical computation can be overcome [47].



# Appendices

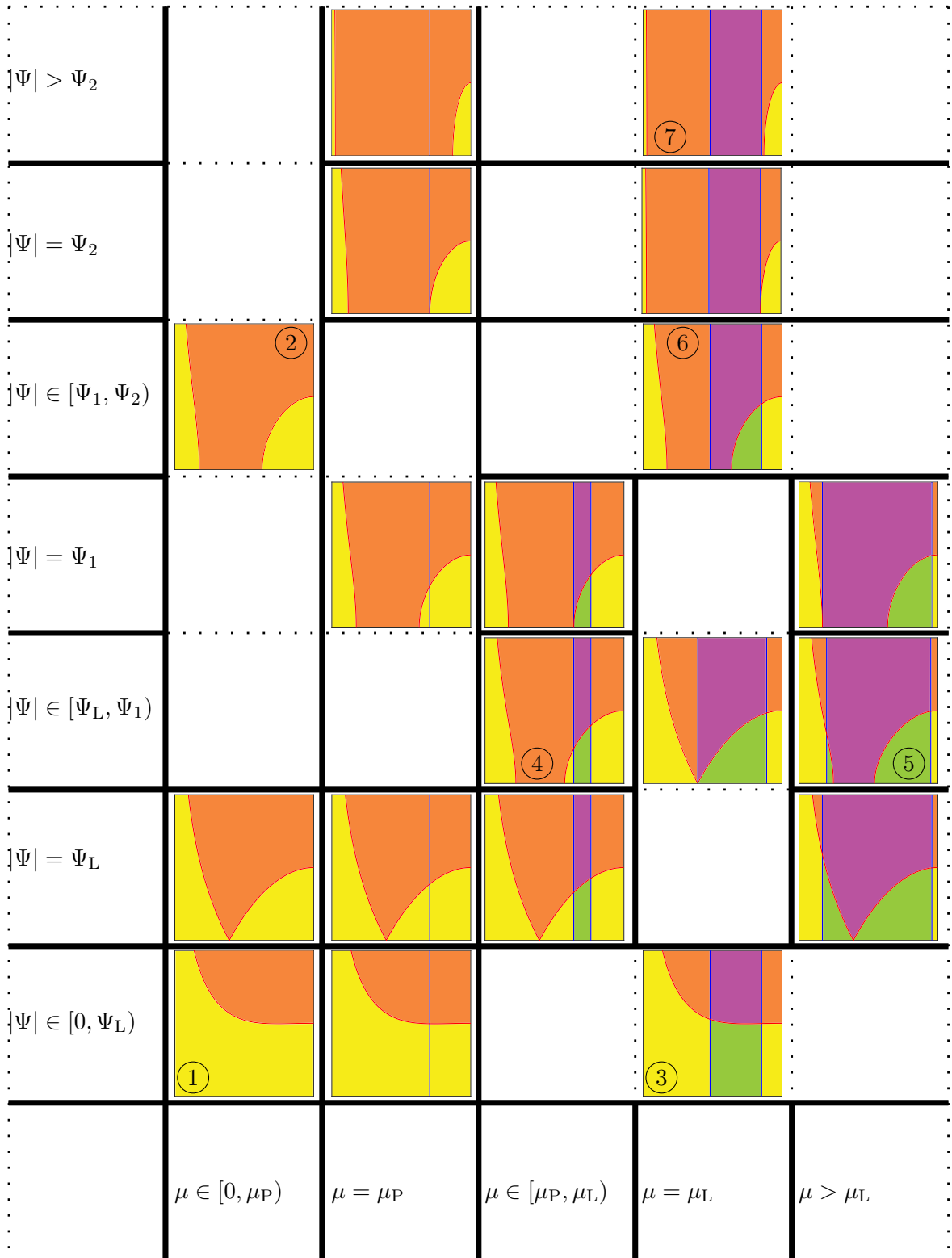


## Appendix A

# Bifurcations of the geometry of $p = 0$ and $b = 0$

In Figure A.1, we demonstrate the bifurcations in the geometry of the surfaces  $p = 0$  and  $b = 0$  for fixed  $\Psi$  with changes in the variable  $\Psi$  and the parameter  $\mu$ . All codimension-1 and codimension-2 bifurcations in  $(\mu, \Psi)$  space are shown, which occur at the curves  $\mu = \mu_P$ ,  $\mu = \mu_L$ ,  $\Psi = \Psi_L$ ,  $\Psi = \Psi_1$ ,  $\Psi = \Psi_2$ , and their pairwise intersections (where they exist). Certain regions are grouped qualitatively (e.g. for  $|\Psi| > \Psi_2$  and  $\mu > \mu_P$  all the geometries are qualitatively equivalent), whilst others are grouped due to being exactly equivalent (e.g. for  $\mu = \mu_L$   $\Psi_L \equiv \Psi_1$ ).



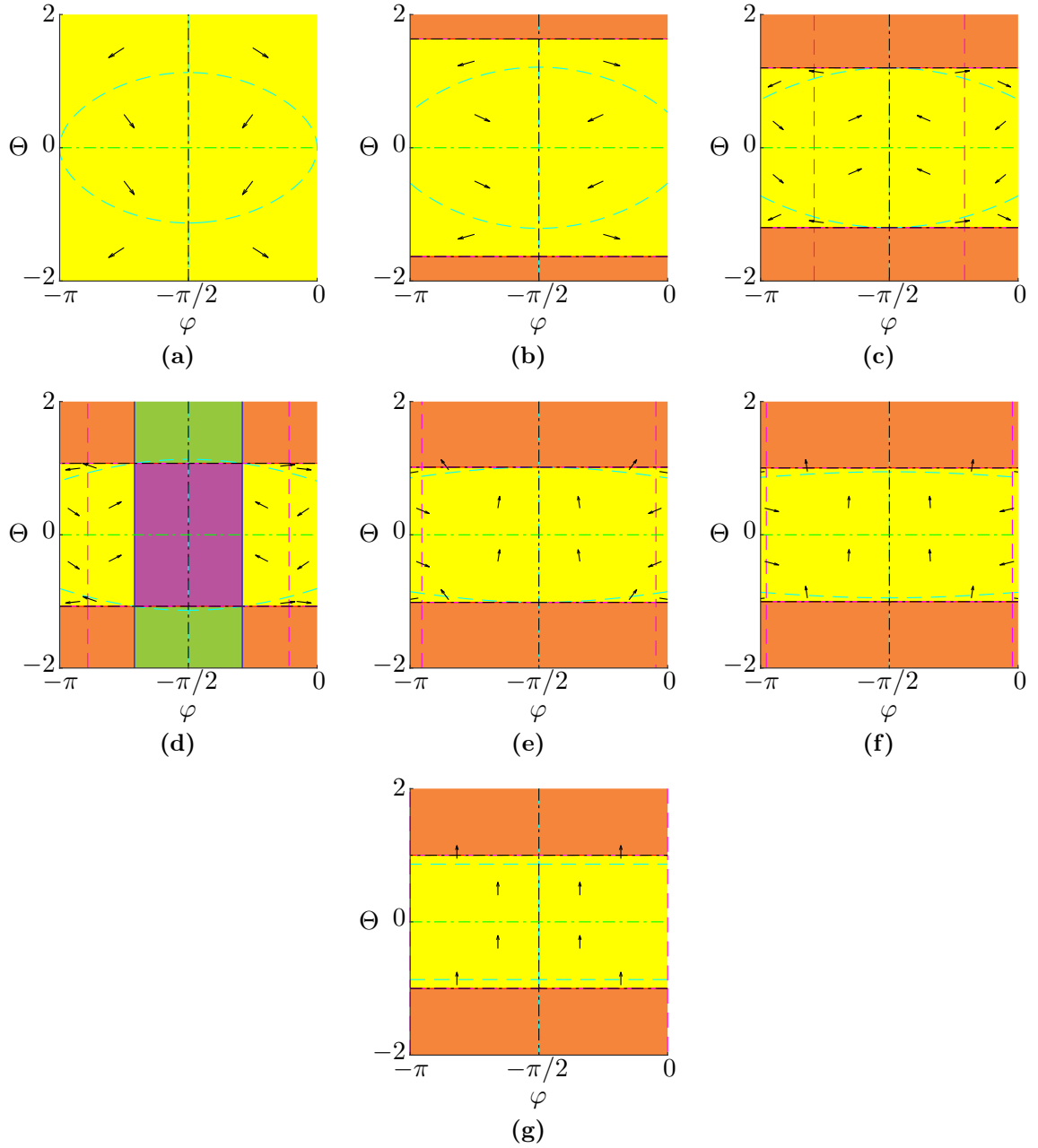


**Figure A.1:** Here we show all possible codimension-1 and codimension-2 bifurcations between geometric cases ①–⑦ in  $(\mu, \Psi)$  space. This figure accompanies Figures 2.17 and 2.18a.

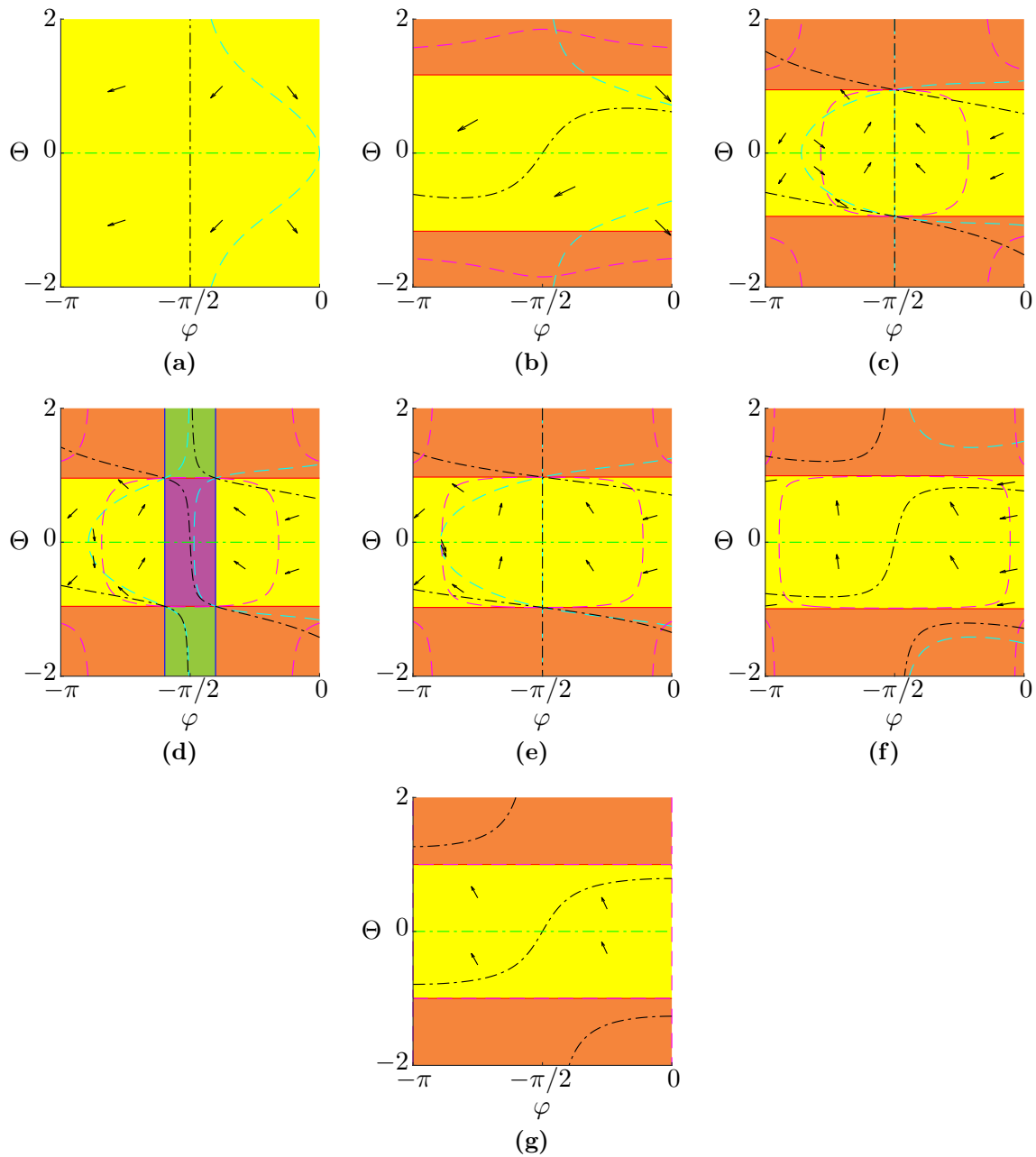
## Appendix B

# Phase portraits of the constrained 3D Painlevé problem

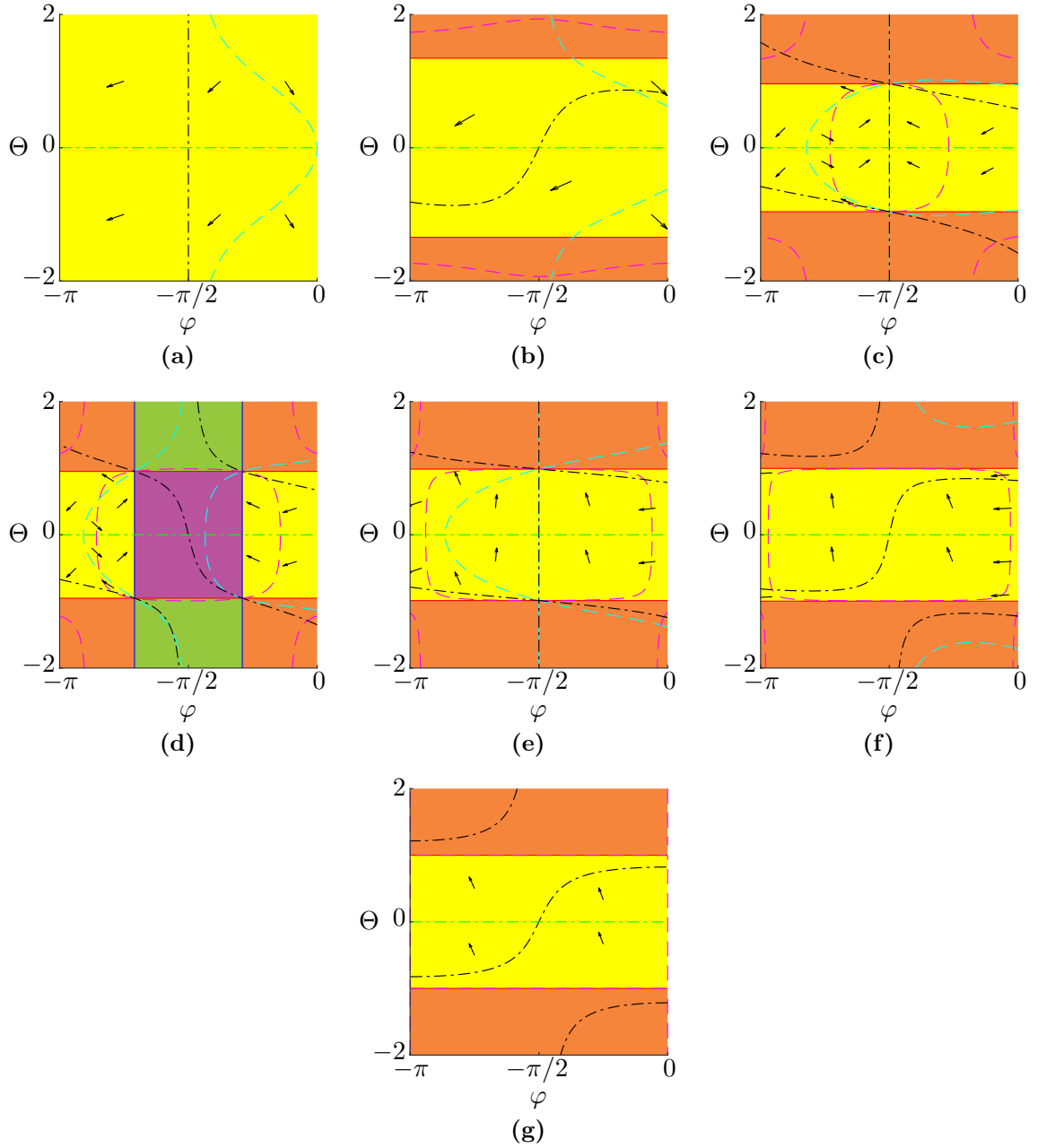
In Figures B.1 to B.3, as in section 2.9, we present phase portraits in  $(\varphi, \Theta)$  space for varying values of parameters and variables. Similarly, in Figures B.4 to B.7, we present phase portraits in  $(\theta, \Theta)$  space for varying values of parameters and at sections of fixed variables. Whilst these are included for completeness as analogues to crucial results from [38], they indicate that due to the higher number of dimensions involved in the study of the 3D Painlevé, it will be necessary to find useful projections to qualitatively describe the dynamics.



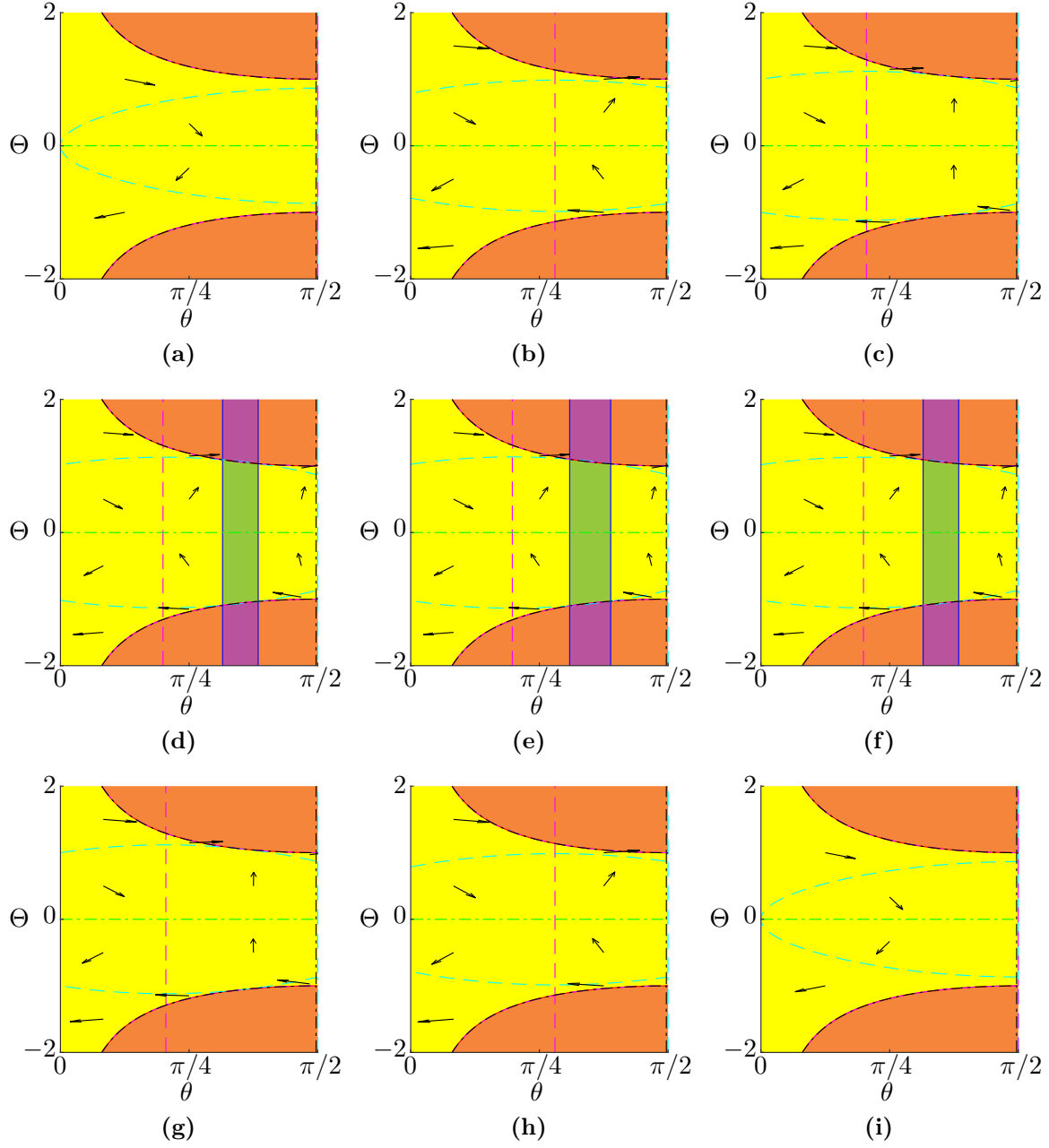
**Figure B.1:** Phase portraits in  $(\varphi, \Theta)$  for fixed  $\Psi = 0$  and sections of  $\theta$ . (a)  $\theta = 0$ , (b)  $\theta = 0.38459$ , (c)  $\theta = 0.76918$ , (d)  $\theta = 1.0513$ , (e)  $\theta = 1.3333$ , (f)  $\theta = 1.4521$ , (g)  $\theta = 1.5708$ .  $\dot{\varphi} = 0$  ■,  $\dot{\theta} = 0$  ■,  $\dot{\Psi} = 0$  ■,  $\dot{\Theta} = 0$  ■. The parameters  $\alpha = 3$  and  $\mu = 1.7$ .



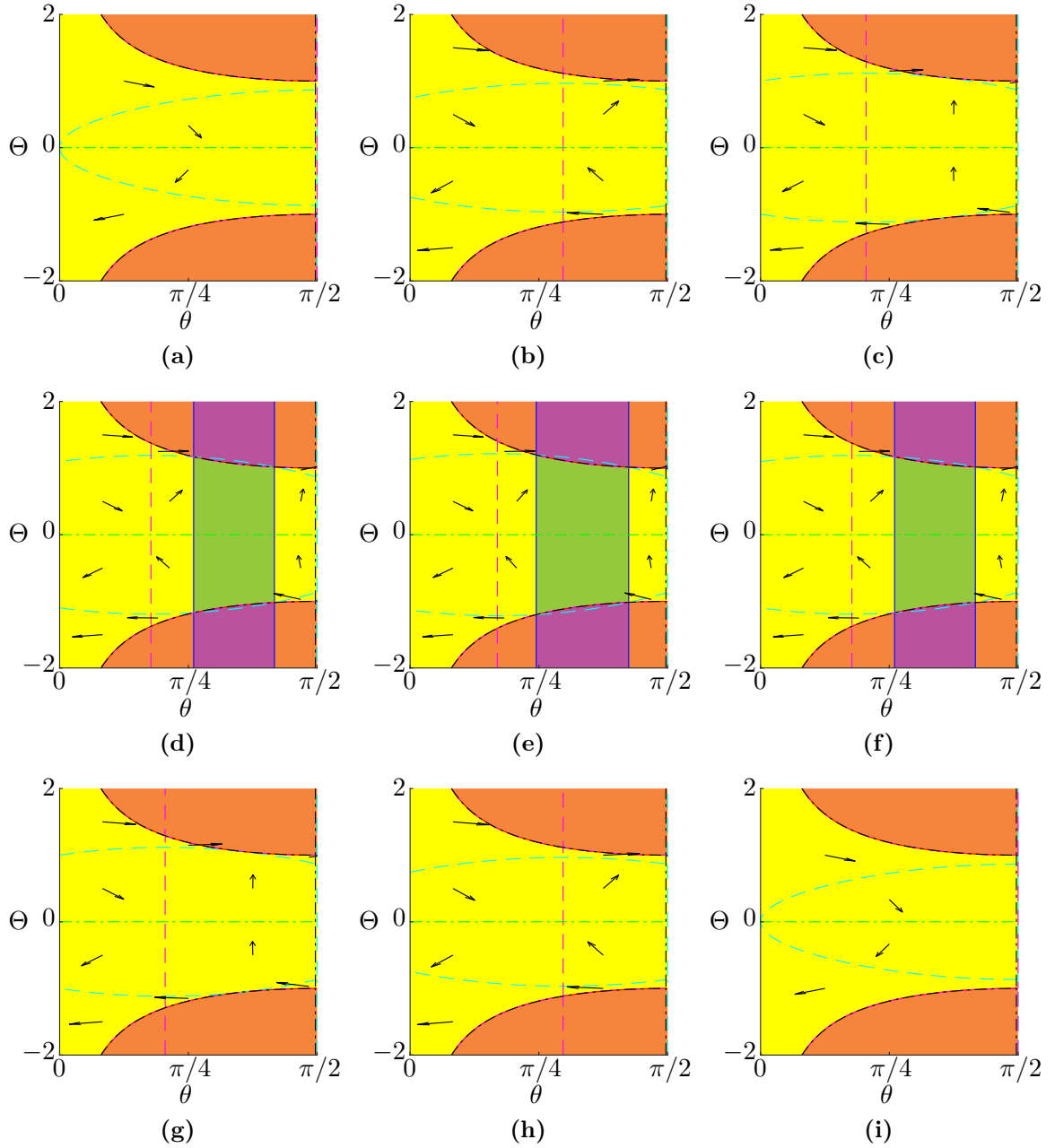
**Figure B.2:** Phase portraits in  $(\varphi, \Theta)$  for fixed  $\Psi = 1$  and sections of  $\theta$ . (a)  $\theta = 0$ , (b)  $\theta = 0.48508$ , (c)  $\theta = 0.97016$ , (d)  $\theta = 1.0955$ , (e)  $\theta = 1.2209$ , (f)  $\theta = 1.3958$ , (g)  $\theta = 1.5708$ .  $\dot{\varphi} = 0$  ■,  $\dot{\theta} = 0$  ■,  $\dot{\Psi} = 0$  ■,  $\dot{\Theta} = 0$  ■. The parameters  $\alpha = 3$  and  $\mu = 1.4$ .



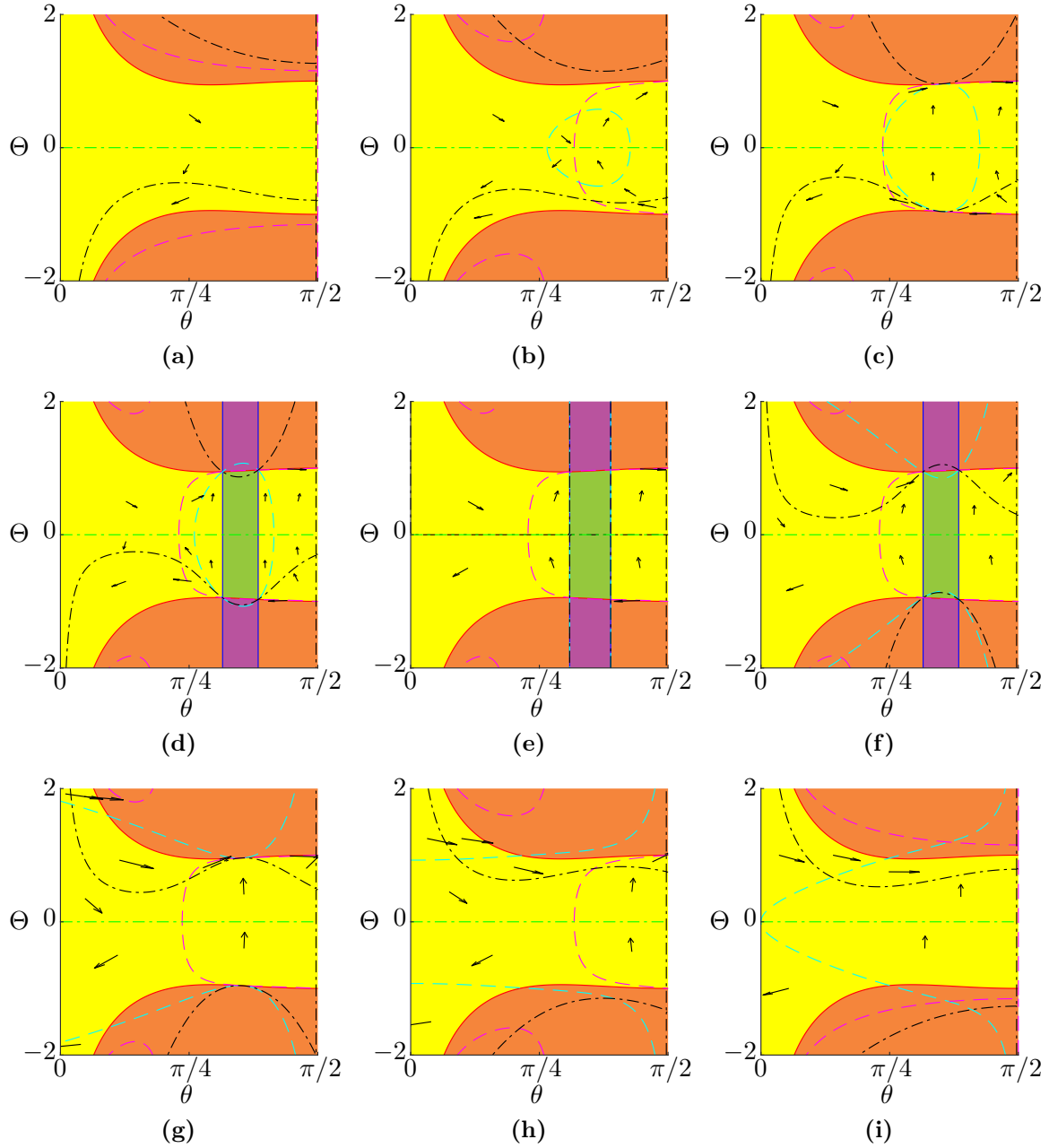
**Figure B.3:** Phase portraits in  $(\varphi, \Theta)$  for fixed  $\Psi = 0$  and sections of  $\theta$ . (a)  $\theta = 0$ , (b)  $\theta = 0.38459$ , (c)  $\theta = 0.76918$ , (d)  $\theta = 1.0513$ , (e)  $\theta = 1.3333$ , (f)  $\theta = 1.4521$ , (g)  $\theta = 1.5708$ .  $\dot{\varphi} = 0$  ■,  $\dot{\theta} = 0$  ■,  $\dot{\Psi} = 0$  ■,  $\dot{\Theta} = 0$  ■. The parameters  $\alpha = 3$  and  $\mu = 1.7$ .



**Figure B.4:** Phase portraits in  $(\theta, \Theta)$  for fixed  $\Psi = 0$  and sections of  $\varphi$ . (a)  $\varphi = -3.1416$ , (b)  $\varphi = -2.5111$ , (c)  $\varphi = -1.8806$ , (d)  $\varphi = -1.7257$ , (e)  $\varphi = -1.5708$ , (f)  $\varphi = -1.4159$ , (g)  $\varphi = -1.261$ , (g)  $\varphi = -0.63048$ , (i)  $\varphi = 0$ .  $\dot{\varphi} = 0$  ■,  $\dot{\theta} = 0$  ■,  $\Psi = 0$  ■,  $\dot{\Theta} = 0$  ■. The parameters  $\alpha = 3$  and  $\mu = 1.4$ .

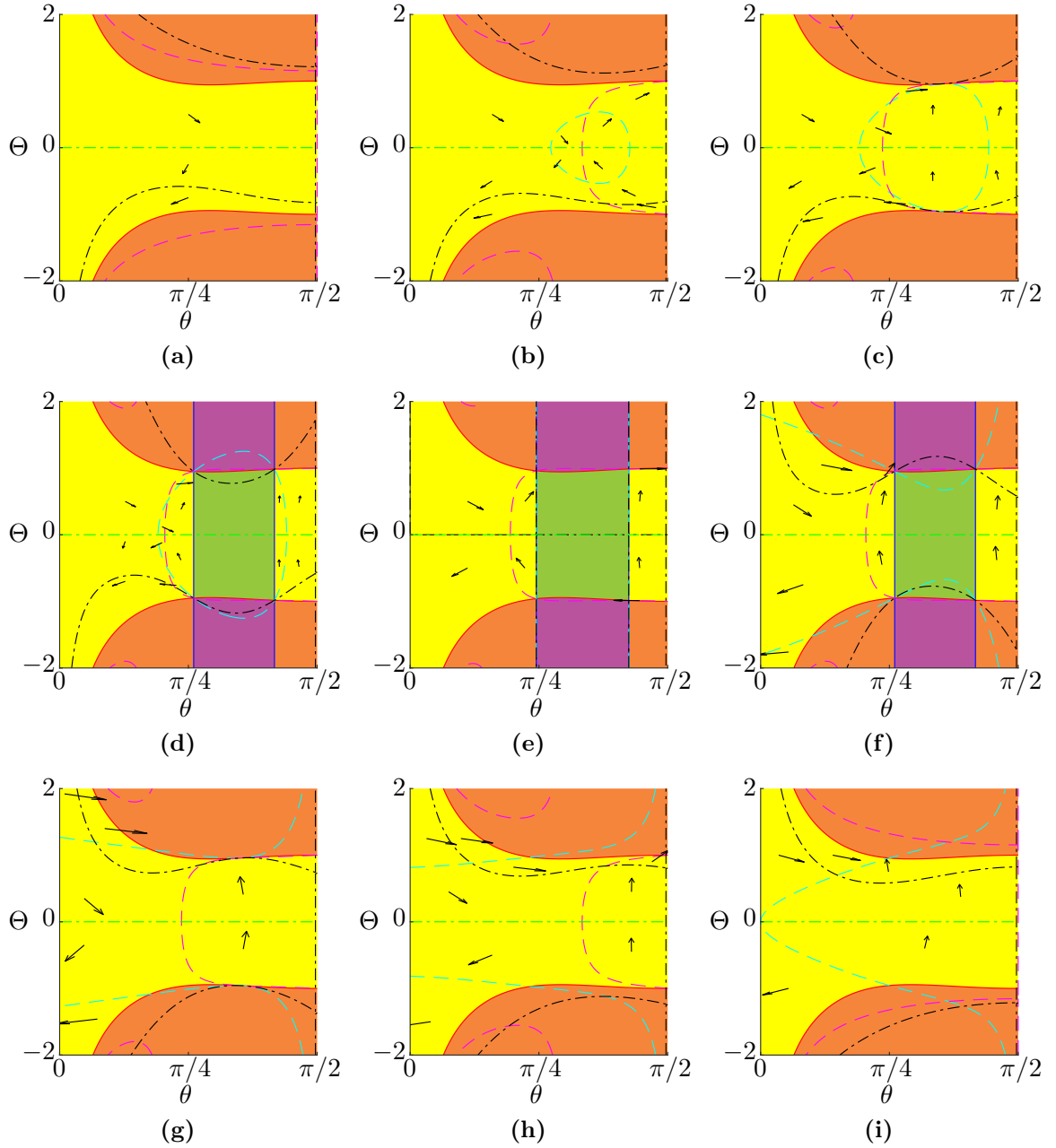


**Figure B.5:** Phase portraits in  $(\theta, \Theta)$  for fixed  $\Psi = 0$  and sections of  $\varphi$ . (a)  $\varphi = -3.1416$ , (b)  $\varphi = -2.6908$ , (c)  $\varphi = -2.24$ , (d)  $\varphi = -1.9054$ , (e)  $\varphi = -1.5708$ , (f)  $\varphi = -1.2362$ , (g)  $\varphi = -0.90159$ , (g)  $\varphi = -0.45079$ , (i)  $\varphi = 0$ .  $\dot{\varphi} = 0$  ■,  $\dot{\theta} = 0$  ■,  $\dot{\Psi} = 0$  ■,  $\dot{\Theta} = 0$  ■. The parameters  $\alpha = 3$  and  $\mu = 1.7$ .



**Figure B.6:** Phase portraits in  $(\theta, \Theta)$  for fixed  $\Psi = 1$  and sections of  $\varphi$ . (a)  $\varphi = -3.1416$ , (b)  $\varphi = -2.5111$ , (c)  $\varphi = -1.8806$ , (d)  $\varphi = -1.7257$ , (e)  $\varphi = -1.5708$ , (f)  $\varphi = -1.4159$ , (g)  $\varphi = -1.261$ , (g)  $\varphi = -0.63048$ , (i)  $\varphi = 0$ .  $\dot{\varphi} = 0$  ■,  $\dot{\theta} = 0$  ■,  $\dot{\Psi} = 0$  ■,  $\dot{\Theta} = 0$  ■. The parameters  $\alpha = 3$  and  $\mu = 1.4$ .





**Figure B.7:** Phase portraits in  $(\theta, \Theta)$  for fixed  $\Psi = 1$  and sections of  $\varphi$ . (a)  $\varphi = -3.1416$ , (b)  $\varphi = -2.6908$ , (c)  $\varphi = -2.24$ , (d)  $\varphi = -1.9054$ , (e)  $\varphi = -1.5708$ , (f)  $\varphi = -1.2362$ , (g)  $\varphi = -0.90159$ , (g)  $\varphi = -0.45079$ , (i)  $\varphi = 0$ .  $\dot{\varphi} = 0$  ■,  $\dot{\theta} = 0$  ■,  $\dot{\Psi} = 0$  ■,  $\dot{\Theta} = 0$  ■. The parameters  $\alpha = 3$  and  $\mu = 1.7$ .

# Appendix C

## Initial conditions and parameter values for the numerics in Section 3.2

For all numerics in section 3.2, MATLAB's stiff solver `ode23s` was used with default tolerances.

### C.1 Initial conditions and parameter values for the numerics in Figure 3.6

In Table C.1, we show the initial conditions and parameter values used in the numerics in Figure 3.6. These values were chosen for the following reasons.  $\alpha$  and  $\mu$  were chosen as the typical values such that  $\mu > \mu_P(\alpha)$ .  $\delta = 2$  was chosen for its overdamping.  $\varepsilon = 10^{-4}$  was chosen to give a very stiff surface.  $\eta(0) = 1$  was chosen as an  $\mathcal{O}(1)$  slipping speed.  $\theta(0)$  and  $\varphi(0)$  were chosen as follows.  $\theta(0) = \frac{1}{2}(\theta_1(\mu, \alpha) + \theta_2(\mu, \alpha))$  such that  $\theta(0) \in (\theta_1(\mu, \alpha), \theta_2(\mu, \alpha))$ , and  $\varphi(0) = \varphi_-(\theta(0); \alpha, \mu) - 0.2$ , such that  $p(\theta(0), \varphi(0); \alpha, \mu) = 0.1355$  is fairly small but positive.  $\Psi(0) = 0$  and  $\Theta(0) = 0.1060$  were chosen to give a negative  $b(\Psi(0), \Theta(0), \theta(0)) = -0.9900$ . The initial conditions  $r_1(0) = \sqrt{p(\theta(0), \varphi(0); \alpha, \mu)}$  and  $\varepsilon_1(0) = \varepsilon r_1(0)^{-5}$  are found using the chart (3.23). Finally  $\zeta(0) = \varepsilon_1(0)b(\Psi(0), \Theta(0), \theta(0))$  was chosen to demonstrate a perturbation away from the potential invariant manifold on the sphere. Initial conditions where  $\zeta = n\zeta(0)$  and  $\varepsilon = n\varepsilon(0)$  for  $n \in \{2, 4, 6, 8, 10\}$  were also used.

$\alpha$	$\mu$	$\delta$	$\varepsilon$	$\theta(0)$	$\eta(0)$	$\varphi(0)$	$\Psi(0)$	$\Theta(0)$	$r_1(0)$	$\varepsilon_1(0)$	$\zeta_1(0)$
3	1.4	2	$10^{-4}$	1.0955	1	-2.0793	0	0.1060	0.3682	0.0148	-0.0146

Table C.1: Parameter values and initial conditions used in the numerics in Figure 3.6.

## C.2 Initial conditions and parameter values for the numerics in Figures 3.7 and 3.8

$b$	$k$	$\zeta_2(0)$	$p_2(0)$	$w_2(0)$	$r_2 = 0$
-0.5	-0.3244	-0.0315	15.8489	0	0
-0.5	-0.3244	-0.0631	15.8489	0	0

Table C.2: Parameter values and initial conditions used in the numerics in Figures 3.7 and 3.8.

In Table C.2, we give the initial conditions/parameters used in the numerical integration of equation (3.33).  $b$  was chosen as a negative (between its minimum of  $-1$  and  $0$ ).  $k = k(\theta(0), \varphi_-(\theta(0); \alpha, \mu), \eta(0), 0)$ , where  $\alpha = 3$ ,  $\mu = 1.4$ , and  $\theta(0) = \frac{1}{2}(\theta_1(\alpha, \mu) + \theta_2(\alpha, \mu))$  (such that  $p = 0$ ).  $\zeta_2(0)$ ,  $p_2(0)$ , and  $w_2(0)$  were found by rewriting the linear terms of (3.29) for some small  $\varepsilon_1^* = 0.001$ ,

$$\begin{aligned}
 \zeta_1 &= b\varepsilon_1^* \\
 w_1 &= 0 \\
 \varepsilon_1 &= \varepsilon_1^*
 \end{aligned}
 \tag{C.1}$$

in the chart  $k_2$

$$\begin{aligned}
 \zeta_2 &= b\varepsilon_1^{*\frac{2}{5}} \approx -0.0315 \\
 w_2 &= 0 \\
 p_2 &= \varepsilon_1^{*-\frac{2}{5}} \approx 15.8489.
 \end{aligned}
 \tag{C.2}$$

In Figure 3.8, where we study an orbit close to the special solution, the initial condition  $\zeta_2(0) = 2b\varepsilon_1^{*\frac{2}{5}}$  is used.

## Appendix D

# Proof of the regularisation function lemma

Proof of Lemma 4.1

**Proof.** a From the definition of  $\underline{\mathbf{R}}(\phi)$  (4.13), we have that

$$\begin{aligned}
 \text{(D.1)} \quad \mathbf{e}_\Psi(\underline{\mathbf{R}}(\phi)(x, y)^\top; \varepsilon) &= \mathbf{e}_\Psi(x \cos \phi - y \sin \phi, x \sin \phi + y \cos \phi; \varepsilon). \\
 \text{(D.2)} \quad &= \frac{((x \cos \phi - y \sin \phi), (x \sin \phi + y \cos \phi))^\top}{\sqrt{x^2 + y^2 + \varepsilon^2 \Psi\left(\frac{x^2 + y^2}{\varepsilon^2}\right)}}, \\
 \text{(D.3)} \quad &= \underline{\mathbf{R}}(\phi) \frac{(x, y)^\top}{\sqrt{x^2 + y^2 + \varepsilon^2 \Psi\left(\frac{x^2 + y^2}{\varepsilon^2}\right)}}, \\
 \text{(D.4)} \quad &\equiv \underline{\mathbf{R}}(\phi) \mathbf{e}_\Psi(x, y; \varepsilon)
 \end{aligned}$$

$$\text{since } |\underline{\mathbf{R}}(\phi)(x, y)^\top|^2 = |(x, y)^\top|^2$$

b From the definition of  $\mathbf{e}_\Psi$  (4.21), we have that

$$\begin{aligned}
 \text{(D.5)} \quad \mathbf{e}_\Psi(kx, ky; k\varepsilon) &= \frac{(kx, ky)^\top}{\sqrt{k^2 x^2 + k^2 y^2 + k^2 \varepsilon^2 \Psi\left(\frac{k^2 x^2 + k^2 y^2}{k^2 \varepsilon^2}\right)}} \\
 \text{(D.6)} \quad &= \frac{k(x, y)^\top}{\sqrt{k^2} \sqrt{x^2 + y^2 + \varepsilon^2 \Psi\left(\frac{x^2 + y^2}{\varepsilon^2}\right)}}.
 \end{aligned}$$

Therefore, for  $k > 0$ ,

$$\begin{aligned}
 \text{(D.7)} \quad \mathbf{e}_\Psi(kx, ky; k\varepsilon) &= \frac{(x, y)^\top}{\sqrt{x^2 + y^2 + \varepsilon^2 \Psi\left(\frac{x^2 + y^2}{\varepsilon^2}\right)}}, \\
 \text{(D.8)} \quad &\equiv \mathbf{e}_\Psi(x, y; \varepsilon).
 \end{aligned}$$

c Writing

$$(D.9) \quad \mathbf{e}_\Psi(\tilde{\rho} \cos \tilde{\theta}, \tilde{\rho} \cos \tilde{\theta}; \varepsilon) = \mathbf{e}_\Psi(\rho \cos \theta, \rho \cos \theta; \varepsilon)$$

in terms of polar coordinates,

$$(D.10) \quad \left\langle \frac{\tilde{\rho}}{\sqrt{\tilde{\rho}^2 + \varepsilon^2 \Psi(\tilde{\rho}^2/\varepsilon^2)}}, \tilde{\theta} \right\rangle = \left\langle \frac{\rho}{\sqrt{\rho^2 + \varepsilon^2 \Psi(\rho^2/\varepsilon^2)}}, \theta \right\rangle.$$

Comparing components, we have  $\theta \equiv \tilde{\theta}$ , and from the monotonicity of  $\Psi$  (Definition 4.1), we have  $\rho \equiv \tilde{\rho}$ . ■

## Appendix E

### Lemma on the e-linear normal form

**Lemma E.1.** Consider the e-linear normal (4.60) from section 4.4 given by

$$(E.1) \quad \begin{pmatrix} \dot{x} \\ \dot{y} \\ \dot{\mathbf{z}} \end{pmatrix} = \begin{pmatrix} \underline{\mathbf{A}}(\mathbf{z}) \\ \underline{\mathbf{B}}(\mathbf{z}) \end{pmatrix} \mathbf{e}(x, y) + \begin{pmatrix} \mathbf{f}(x, y, \mathbf{z}) \\ \mathbf{g}(x, y, \mathbf{z}) \end{pmatrix}.$$

Then there is transformation such that the system can be re-written as in (E.1), with  $\underline{\mathbf{A}}$  in the form

$$(E.2) \quad \underline{\mathbf{A}}(\mathbf{z}) = \begin{pmatrix} a(\mathbf{z}) & -b(\mathbf{z}) \\ b(\mathbf{z}) & d(\mathbf{z}) \end{pmatrix}.$$

**Proof.** Let us consider the system

$$\begin{pmatrix} \dot{x} \\ \dot{y} \\ \dot{\mathbf{z}} \end{pmatrix} = \begin{pmatrix} \underline{\mathbf{A}}(\mathbf{z}) \\ \underline{\mathbf{B}}(\mathbf{z}) \end{pmatrix} \mathbf{e}(x, y) + \begin{pmatrix} \mathbf{f}(x, y, \mathbf{z}) \\ \mathbf{g}(x, y, \mathbf{z}) \end{pmatrix}$$

where  $\underline{\mathbf{A}}$  is any real matrix

$$\underline{\mathbf{A}}(\mathbf{z}) = \begin{pmatrix} a(\mathbf{z}) & b(\mathbf{z}) \\ c(\mathbf{z}) & d(\mathbf{z}) \end{pmatrix}.$$

We can write  $\underline{\mathbf{A}}(\mathbf{z})$  as

$$\underline{\mathbf{A}}(\mathbf{z}) = \mathbf{R}^\top(\phi(\mathbf{z})) \tilde{\underline{\mathbf{A}}}(\mathbf{z}) \mathbf{R}(\phi(\mathbf{z}))$$

where  $\mathbf{R}$  is a rotation matrix through the angle

$$\phi(\mathbf{z}) = \frac{1}{2} \arctan \left( \frac{\tilde{b}(\mathbf{z}) + \tilde{c}(\mathbf{z})}{\tilde{d}(\mathbf{z}) - \tilde{a}(\mathbf{z})} \right),$$

and  $\tilde{\underline{\mathbf{A}}}$  is a matrix in the same form as (E.2)

$$\tilde{\underline{\mathbf{A}}} := \begin{pmatrix} \tilde{a}(\mathbf{z}) & -\tilde{b}(\mathbf{z}) \\ \tilde{b}(\mathbf{z}) & \tilde{d}(\mathbf{z}) \end{pmatrix}.$$

Let us now change to coordinates  $(\tilde{x}, \tilde{y}, z)$  using the coordinate transformation given by

$$(E.3) \quad (\tilde{x}, \tilde{y})^\top = \mathbf{R}(\phi(\mathbf{z}))(x, y)^\top.$$

Differentiating (E.3)

$$\begin{pmatrix} \dot{\tilde{x}} \\ \dot{\tilde{y}} \end{pmatrix} = \mathbf{R}(\phi(\mathbf{z})) \begin{pmatrix} \dot{x} \\ \dot{y} \end{pmatrix} + \frac{\partial \phi}{\partial \mathbf{z}} \dot{\mathbf{z}} \frac{\partial}{\partial \phi} (\mathbf{R}(\phi(\mathbf{z}))) \begin{pmatrix} x \\ y \end{pmatrix},$$

then substituting and using the equivariance of  $\mathbf{e}$  from Lemma 4.1(a)

$$\begin{aligned} &= \mathbf{R}(\phi(\mathbf{z})) (\mathbf{A}(\mathbf{z}) \mathbf{R}^\top(\phi(\mathbf{z})) \mathbf{e}(\tilde{x}, \tilde{y}) + \mathbf{f}(\mathbf{R}^\top(\phi(\mathbf{z}))(\tilde{x}, \tilde{y})^\top, \mathbf{z}),) + \\ &\quad \frac{\partial \phi}{\partial \mathbf{z}} \dot{\mathbf{z}} \frac{\partial}{\partial \phi} \mathbf{R}(\phi(\mathbf{z})) \mathbf{R}^\top(\phi(\mathbf{z})) (\tilde{x}, \tilde{y})^\top \\ &= \tilde{\mathbf{A}}(\mathbf{z}) \mathbf{e}(\tilde{x}, \tilde{y}) + \mathbf{R}(\phi(\mathbf{z})) \mathbf{f}(\mathbf{R}^\top(\phi(\mathbf{z}))(\tilde{x}, \tilde{y})^\top, \mathbf{z}) + \frac{\partial \phi}{\partial \mathbf{z}} \dot{\mathbf{z}} \mathbf{R}(\pi/2) (\tilde{x}, \tilde{y})^\top \\ (E.4) \quad &(\dot{\tilde{x}}, \dot{\tilde{y}})^\top := \tilde{\mathbf{A}}(\mathbf{z}) \mathbf{e}(\tilde{x}, \tilde{y}) + \tilde{\mathbf{f}}(\tilde{x}, \tilde{y}, \mathbf{z}). \end{aligned}$$

Similarly

$$\begin{aligned} \dot{\mathbf{z}} &= \mathbf{B}(\mathbf{z}) \mathbf{R}^\top(\phi(\mathbf{z})) \mathbf{e}(\tilde{x}, \tilde{y}) + \mathbf{g}(\mathbf{R}^\top(\phi(\mathbf{z}))(\tilde{x}, \tilde{y})^\top, \mathbf{z}), \\ (E.5) \quad \dot{\mathbf{z}} &:= \tilde{\mathbf{B}}(\mathbf{z}) \mathbf{e}(\tilde{x}, \tilde{y}) + \tilde{\mathbf{g}}(\tilde{x}, \tilde{y}, \mathbf{z}) \end{aligned}$$

■

## Appendix F

# Lemma on an alternative e-linear normal form with radial dependence

$$(F.1) \quad \begin{pmatrix} \dot{x} \\ \dot{y} \\ \dot{\mathbf{z}} \end{pmatrix} = \begin{pmatrix} \underline{\mathbf{A}}(\mathbf{z}) \\ \underline{\mathbf{B}}(\mathbf{z}) \end{pmatrix} \gamma(x^2 + y^2) \mathbf{e}(x, y) + \begin{pmatrix} \mathbf{f}(x, y, \mathbf{z}) \\ \mathbf{g}(x, y, \mathbf{z}) \end{pmatrix}.$$

**Lemma F.1.** *Consider (F.1), which is linear in  $\mathbf{e}$  but now with some radial dependence  $\gamma(x^2 + y^2)$ . Then there is transformation such that the system can be written as in (F.1), with  $\underline{\mathbf{A}}$  in the form*

$$(F.2) \quad \underline{\mathbf{A}}(\mathbf{z}) = \begin{pmatrix} a(\mathbf{z}) & -b(\mathbf{z}) \\ b(\mathbf{z}) & d(\mathbf{z}) \end{pmatrix}.$$

**Proof.** Let us consider the system (F.1) where  $\underline{\mathbf{A}}$  is any real matrix

$$\underline{\mathbf{A}}(\mathbf{z}) = \begin{pmatrix} a(\mathbf{z}) & b(\mathbf{z}) \\ c(\mathbf{z}) & d(\mathbf{z}) \end{pmatrix}.$$

We can write  $\underline{\mathbf{A}}(\mathbf{z})$  as

$$\underline{\mathbf{A}}(\mathbf{z}) = \mathbf{R}^\top(\phi(\mathbf{z})) \tilde{\underline{\mathbf{A}}}(\mathbf{z}) \mathbf{R}(\phi(\mathbf{z}))$$

where  $\mathbf{R}$  is a rotation matrix through the angle

$$\phi(\mathbf{z}) = \frac{1}{2} \arctan \left( \frac{\tilde{b}(\mathbf{z}) + \tilde{c}(\mathbf{z})}{\tilde{d}(\mathbf{z}) - \tilde{a}(\mathbf{z})} \right),$$

and  $\tilde{\underline{\mathbf{A}}}$  is a matrix in the same form as (F.2)

$$\tilde{\underline{\mathbf{A}}}(\mathbf{z}) := \begin{pmatrix} \tilde{a}(\mathbf{z}) & -\tilde{b}(\mathbf{z}) \\ \tilde{b}(\mathbf{z}) & \tilde{d}(\mathbf{z}) \end{pmatrix}.$$



Let us now change to coordinates  $(\tilde{x}, \tilde{y}, z)$  using the coordinate transformation given by

$$(F.3) \quad (\tilde{x}, \tilde{y})^\top = \underline{\mathbf{R}}(\phi(\mathbf{z}))(x, y)^\top.$$

Differentiating (F.3)

$$\begin{pmatrix} \dot{\tilde{x}} \\ \dot{\tilde{y}} \end{pmatrix} = \underline{\mathbf{R}}(\phi(\mathbf{z})) \begin{pmatrix} \dot{x} \\ \dot{y} \end{pmatrix} + \left( \frac{\partial \phi}{\partial \mathbf{z}} \dot{\mathbf{z}} \right) \frac{\partial}{\partial \phi} (\underline{\mathbf{R}}(\phi(\mathbf{z}))) \begin{pmatrix} x \\ y \end{pmatrix},$$

then substituting and using the equivariance of  $\mathbf{e}$  from Lemma 4.1(a)

$$\begin{aligned} &= \underline{\mathbf{R}}(\phi(\mathbf{z})) (\underline{\mathbf{A}}(\mathbf{z})\gamma(\tilde{x}^2 + \tilde{y}^2) \underline{\mathbf{R}}^\top(\phi(\mathbf{z})) \mathbf{e}(\tilde{x}, \tilde{y}) + \mathbf{f}(\underline{\mathbf{R}}^\top(\phi(\mathbf{z}))(\tilde{x}, \tilde{y})^\top, \mathbf{z})) \\ &\quad + \frac{\partial \phi}{\partial \mathbf{z}} \dot{\mathbf{z}} \frac{\partial}{\partial \phi} \underline{\mathbf{R}}(\phi(\mathbf{z})) \underline{\mathbf{R}}^\top(\phi(\mathbf{z}))(\tilde{x}, \tilde{y})^\top \\ &= \tilde{\underline{\mathbf{A}}}(\mathbf{z})\gamma(\tilde{x}^2 + \tilde{y}^2) \mathbf{e}(\tilde{x}, \tilde{y}) + \underline{\mathbf{R}}(\phi(\mathbf{z})) \mathbf{f}(\underline{\mathbf{R}}^\top(\phi(\mathbf{z}))(\tilde{x}, \tilde{y})^\top, \mathbf{z}) \\ &\quad + \frac{\partial \phi}{\partial \mathbf{z}} \dot{\mathbf{z}} \underline{\mathbf{R}}(\pi/2)(\tilde{x}, \tilde{y})^\top \end{aligned}$$

$$(F.4) \quad (\dot{\tilde{x}}, \dot{\tilde{y}})^\top := \tilde{\underline{\mathbf{A}}}(\mathbf{z})\gamma(\tilde{x}^2 + \tilde{y}^2) \mathbf{e}(\tilde{x}, \tilde{y}) + \tilde{\mathbf{f}}(\tilde{x}, \tilde{y}, \mathbf{z}).$$

Similarly

$$\begin{aligned} \dot{\mathbf{z}} &= \underline{\mathbf{B}}(\mathbf{z})\gamma(\tilde{x}^2 + \tilde{y}^2) \underline{\mathbf{R}}^\top(\phi(\mathbf{z})) \mathbf{e}(\tilde{x}, \tilde{y}) + \mathbf{g}(\underline{\mathbf{R}}^\top(\phi(\mathbf{z}))(\tilde{x}, \tilde{y})^\top, \mathbf{z}), \\ (F.5) \quad \dot{\mathbf{z}} &:= \tilde{\underline{\mathbf{B}}}(\mathbf{z})\gamma(\tilde{x}^2 + \tilde{y}^2) \mathbf{e}(\tilde{x}, \tilde{y}) + \tilde{\mathbf{g}}(\tilde{x}, \tilde{y}, \mathbf{z}) \end{aligned}$$

■

## Appendix G

# Lemma on the suitability of the e-linear normal form

**Lemma G.1.** *For the following set of ODEs*

$$(G.1) \quad \begin{pmatrix} \dot{x} \\ \dot{y} \\ \dot{\mathbf{z}} \end{pmatrix} = \begin{pmatrix} \underline{\mathbf{A}}(x, y, \mathbf{z}) \\ \underline{\mathbf{B}}(x, y, \mathbf{z}) \end{pmatrix} \mathbf{e}(x, y) + \begin{pmatrix} \mathbf{f}(x, y, \mathbf{z}) \\ \mathbf{g}(x, y, \mathbf{z}) \end{pmatrix},$$

where  $\underline{\mathbf{A}}$  and  $\underline{\mathbf{B}}$  depend smoothly on  $(x, y, \mathbf{z})$ , the system can be re-written as in (E.1), with  $\underline{\mathbf{A}}$  in the form

$$(G.2) \quad \underline{\mathbf{A}}(\mathbf{z}) = \begin{pmatrix} a(\mathbf{z}) & b(\mathbf{z}) \\ c(\mathbf{z}) & d(\mathbf{z}) \end{pmatrix}.$$

**Proof.** Let us consider the system, as in (G.1)

$$\begin{pmatrix} \dot{x} \\ \dot{y} \\ \dot{\mathbf{z}} \end{pmatrix} = \begin{pmatrix} \underline{\mathbf{A}}(x, y, \mathbf{z}) \\ \underline{\mathbf{B}}(x, y, \mathbf{z}) \end{pmatrix} \mathbf{e}(x, y) + \begin{pmatrix} \mathbf{f}(x, y, \mathbf{z}) \\ \mathbf{g}(x, y, \mathbf{z}) \end{pmatrix}.$$

Writing the matrices  $\underline{\mathbf{A}}$  and  $\underline{\mathbf{B}}$  as Taylor series with respect to  $x$  and  $y$  and grouping terms that are constant w.r.t  $(x, y)$  and the terms with dependence upon  $(x, y)$ ,

$$\underline{\mathbf{A}} = \underline{\mathbf{A}}(0, 0, \mathbf{z}) + (\underline{\mathbf{A}}(x, y, \mathbf{z}) - \underline{\mathbf{A}}(0, 0, \mathbf{z}))$$

and

$$\underline{\mathbf{B}} = \underline{\mathbf{B}}(0, 0, \mathbf{z}) + (\underline{\mathbf{B}}(x, y, \mathbf{z}) - \underline{\mathbf{B}}(0, 0, \mathbf{z}))$$

we find

$$\begin{aligned} \begin{pmatrix} \dot{x} \\ \dot{y} \\ \dot{z} \end{pmatrix} &= \left( \begin{pmatrix} \underline{\mathbf{A}}(0, 0, \mathbf{z}) \\ \underline{\mathbf{B}}(0, 0, \mathbf{z}) \end{pmatrix} + \begin{pmatrix} \underline{\mathbf{A}}(x, y, \mathbf{z}) - \underline{\mathbf{A}}(0, 0, \mathbf{z}) \\ \underline{\mathbf{B}}(x, y, \mathbf{z}) - \underline{\mathbf{B}}(0, 0, \mathbf{z}) \end{pmatrix} \right) \mathbf{e}(x, y) + \begin{pmatrix} \mathbf{f}(x, y, \mathbf{z}) \\ \mathbf{g}(x, y, \mathbf{z}) \end{pmatrix} \\ \text{(G.3)} \quad \begin{pmatrix} \dot{x} \\ \dot{y} \\ \dot{z} \end{pmatrix} &= \begin{pmatrix} \underline{\mathbf{A}}(0, 0, \mathbf{z}) \\ \underline{\mathbf{B}}(0, 0, \mathbf{z}) \end{pmatrix} \mathbf{e}(x, y) + \left( \begin{pmatrix} \underline{\mathbf{A}}(x, y, \mathbf{z}) - \underline{\mathbf{A}}(0, 0, \mathbf{z}) \\ \underline{\mathbf{B}}(x, y, \mathbf{z}) - \underline{\mathbf{B}}(0, 0, \mathbf{z}) \end{pmatrix} \mathbf{e}(x, y) + \begin{pmatrix} \mathbf{f}(x, y, \mathbf{z}) \\ \mathbf{g}(x, y, \mathbf{z}) \end{pmatrix} \right). \end{aligned}$$

Finally, we can re-write (G.3) in the form

$$\begin{pmatrix} \dot{x} \\ \dot{y} \\ \dot{z} \end{pmatrix} = \begin{pmatrix} \tilde{\mathbf{A}}(\mathbf{z}) \\ \tilde{\mathbf{B}}(\mathbf{z}) \end{pmatrix} \mathbf{e}(x, y) + \begin{pmatrix} \tilde{\mathbf{f}}(x, y, \mathbf{z}) \\ \tilde{\mathbf{g}}(x, y, \mathbf{z}) \end{pmatrix},$$

where

$$\begin{aligned} \tilde{\mathbf{A}}(\mathbf{z}) &= \underline{\mathbf{A}}(0, 0, \mathbf{z}), \\ \tilde{\mathbf{B}}(\mathbf{z}) &= \underline{\mathbf{B}}(0, 0, \mathbf{z}), \\ \tilde{\mathbf{f}}(x, y, \mathbf{z}) &= (\underline{\mathbf{A}}(x, y, \mathbf{z}) - \underline{\mathbf{A}}(0, 0, \mathbf{z})) \mathbf{e}(x, y) + \mathbf{f}(x, y, \mathbf{z}), \end{aligned}$$

and

$$\tilde{\mathbf{g}}(x, y, \mathbf{z}) = (\underline{\mathbf{B}}(x, y, \mathbf{z}) - \underline{\mathbf{B}}(0, 0, \mathbf{z})) \mathbf{e}(x, y) + \mathbf{g}(x, y, \mathbf{z}).$$

This is possible because both  $(\underline{\mathbf{A}}(x, y, \mathbf{z}) - \underline{\mathbf{A}}(0, 0, \mathbf{z})) \mathbf{e}(x, y)$  and  $(\underline{\mathbf{B}}(x, y, \mathbf{z}) - \underline{\mathbf{B}}(0, 0, \mathbf{z})) \mathbf{e}(x, y)$  are both well defined as  $\mathbf{0}$  when  $x = y = 0$ . ■

# Bibliography

- [1] L. S. AN, *The Painleve paradoxes and the law of motion of mechanical systems with Coulomb friction*, Journal of Applied Mathematics and Mechanics, 54 (1990), pp. 430–438, [https://doi.org/https://doi.org/10.1016/0021-8928\(90\)90052-C](https://doi.org/https://doi.org/10.1016/0021-8928(90)90052-C).
- [2] M. ANTALI AND G. STÉPÁN, *Sliding dynamics on codimension-2 discontinuity surfaces*, Trends in Mathematics, 8 (2017), pp. 7–12, [https://doi.org/10.1007/978-3-319-55642-0\\_2](https://doi.org/10.1007/978-3-319-55642-0_2).
- [3] M. ANTALI AND G. STÉPÁN, *Nonsmooth analysis of three-dimensional slipping and rolling in the presence of dry friction*, Nonlinear Dynamics, 97 (2019), pp. 1799–1817, <https://doi.org/10.1007/s11071-019-04913-x>.
- [4] H. BEGHIN, *Sur certains problèmes de frottement*, Nouvelles Annales de Mathématiques 5<sup>e</sup> série, 2 (1923), pp. 305–312, [http://www.numdam.org/item/NAM\\_1923\\_5\\_2\\_\\_305\\_0/](http://www.numdam.org/item/NAM_1923_5_2__305_0/).
- [5] H. BEGHIN, *Sur l'indétermination des certains problèmes de frottement*, Nouvelles Annales de Mathématiques 5<sup>e</sup> série, 3 (1924), pp. 343–347, [http://www.numdam.org/item/NAM\\_1924\\_5\\_3\\_\\_343\\_1/](http://www.numdam.org/item/NAM_1924_5_3__343_1/).
- [6] Y. BERDENI, *Resolving rigid body contact problems through wave propagation*, PhD thesis, University of Bristol, 2016.
- [7] S. BEREGI, D. TAKÁCS, AND C. HŐS, *Nonlinear analysis of a shimmying wheel with contact-force characteristics featuring higher-order discontinuities*, Nonlinear Dynamics, 90 (2017), pp. 877–888, <https://doi.org/10.1007/s11071-017-3699-3>.
- [8] M. BERNARDO, C. BUDD, A. R. CHAMPNEYS, AND P. KOWALCZYK, *Piecewise-smooth dynamical systems: theory and applications*, vol. 163, Springer, 2008, <https://doi.org/10.1007/978-1-84628-708-4>.
- [9] D. S. BERNSTEIN, *Matrix Mathematics*, Princeton University Press, 2nd ed., 2009, <https://doi.org/10.1515/9781400833344>.

## BIBLIOGRAPHY

---

- [10] L. BLUMENSON, *A derivation of  $n$ -dimensional spherical coordinates*, The American Mathematical Monthly, 67 (1960), pp. 63–66, <https://doi.org/10.2307/2308932>.
- [11] A. BLUMENTHALS, B. BROGLIATO, AND F. BERTAILS-DESCOUBES, *The contact problem in Lagrangian systems subject to bilateral and unilateral constraints, with or without sliding Coulomb's friction: a tutorial*, Multibody System Dynamics, 38 (2016), pp. 43–76, <https://doi.org/10.1007/s11044-016-9527-6>.
- [12] E. BOSSOLINI, M. BRØNS, AND K. U. KRISTIANSEN, *Canards in stiction: on solutions of a friction oscillator by regularization*, SIAM Journal on Applied Dynamical Systems, 16 (2017), pp. 2233–2258, <https://doi.org/10.1137/17M1120774>.
- [13] F. P. BOWDEN AND D. TABOR, *The friction and lubrication of solids*, vol. 1, Oxford University Press, 1950.
- [14] B. BROGLIATO, *Nonsmooth Mechanics: Models, Dynamics and Control*, Springer, 3rd ed., 2016, <https://doi.org/10.1007/978-3-319-28664-8>.
- [15] S. J. BURNS AND P. T. PIIRONEN, *Numerical location of Painlevé paradox-associated jam and lift-off in a double-pendulum mechanism*, Journal of Computational and Nonlinear Dynamics, 12 (2017), p. 061007, <https://doi.org/10.1115/1.4037033>.
- [16] A. R. CHAMPNEYS AND P. L. VÁRKONYI, *The Painlevé paradox in contact mechanics*, IMA Journal of Applied Mathematics, 81 (2016), pp. 538–588, <https://doi.org/10.1093/imamat/hxw027>.
- [17] N. CHEESMAN, S. J. HOGAN, AND K. U. KRISTIANSEN, *The geometry of the Painlevé paradox*, Submitted for publication, (2021), <https://arxiv.org/abs/2110.14324>.
- [18] N. CHEESMAN, K. U. KRISTIANSEN, AND S. J. HOGAN, *The Painlevé paradox in three dimensions: resolving with regularisation of rigidity and friction*. (Manuscript in preparation), 2021.
- [19] N. CHEESMAN, K. U. KRISTIANSEN, AND S. J. HOGAN, *Regularization of isolated codimension-2 discontinuity sets*, SIAM Journal on Applied Dynamical Systems, 20 (2021), pp. 2630–2670, <https://doi.org/https://doi.org/10.1137/21M142157X>.
- [20] C. CHICONE, *Ordinary Differential Equations with Applications*, vol. 34, Springer, 2006.
- [21] G. DARBOUX, *Étude géométrique sur les percussions et le choc des corps*, Bulletin des Sciences Mathématiques et Astronomiques, 4 (1880), pp. 126–160, <http://eudml.org/doc/85056>.

- 
- [22] M. DE SPARRE, *Sur le frottement de glissement*, Comptes Rendu des Séances de l'Académie des Sciences, 141 (1905), pp. 310–312, <https://gallica.bnf.fr/ark:/12148/bpt6k3095m/f310.item>.
- [23] E. DELASSUS, *Considérations sur le frottement de glissement*, Nouvelles Annales de Mathématiques 4<sup>e</sup> série, 20 (1920), pp. 485–496, [http://www.numdam.org/item/NAM\\_1920\\_4\\_20\\_\\_485\\_0/](http://www.numdam.org/item/NAM_1920_4_20__485_0/).
- [24] E. DELASSUS, *Sur les lois du frottement de glissement*, Bulletin de la Société Mathématique de France, 51 (1923), pp. 22–33, <https://doi.org/10.24033/bsmf.1029>.
- [25] E. A. DEULIN, V. MIKHAILOV, Y. V. PANFILOV, AND R. NEVSHUPA, *Mechanics and physics of precise vacuum mechanisms*, vol. 91, Springer, 2010, <https://doi.org/10.1007/978-90-481-2520-3>.
- [26] L. DIECI AND F. DIFONZO, *The moments sliding vector field on the intersection of two manifolds*, Journal of Dynamics and Differential Equations, 29 (2017), pp. 169–201, <https://doi.org/10.1007/s10884-015-9439-9>.
- [27] L. DIECI, C. ELIA, AND L. LOPEZ, *A Filippov sliding vector field on an attracting co-dimension 2 discontinuity surface, and a limited loss-of-attractivity analysis*, Journal of Differential Equations, 254 (2013), pp. 1800–1832, <https://doi.org/10.1016/j.jde.2012.11.007>.
- [28] L. DIECI AND L. LOPEZ, *Sliding motion on discontinuity surfaces of high co-dimension. A construction for selecting a Filippov vector field*, Numerische Mathematik, 117 (2011), pp. 779–811, <https://doi.org/10.1007/s00211-011-0365-4>.
- [29] *NIST Digital Library of Mathematical Functions*.  
<http://dlmf.nist.gov/>, Release 1.1.1 of 2021-03-15, 2021, <http://dlmf.nist.gov/>.  
F. W. J. Olver, A. B. Olde Daalhuis, D. W. Lozier, B. I. Schneider, R. F. Boisvert, C. W. Clark, B. R. Miller, B. V. Saunders, H. S. Cohl, and M. A. McClain, eds.
- [30] F. DUMORTIER AND R. ROUSSARIE, *Geometric singular perturbation theory beyond normal hyperbolicity*, in Multiple-time-scale dynamical systems, Springer, 2001, pp. 29–63, [https://doi.org/10.1007/978-1-4613-0117-2\\_2](https://doi.org/10.1007/978-1-4613-0117-2_2).
- [31] F. DUMORTIER, R. ROUSSARIE, AND R. H. ROUSSARIE, *Canard cycles and center manifolds*, vol. 577, American Mathematical Society, 1996, <http://doi.org/10.1090/memo/0577>.
- [32] P. E. DUPONT AND S. P. YAMAJAKO, *Stability of frictional contact in constrained rigid-body dynamics*, IEEE Transactions on Robotics and Automation, 13 (1997), pp. 230–236, <https://doi.org/10.1109/70.563645>.

- [33] B. C. EAVES, *On the basic theorem of complementarity*, Mathematical Programming, 1 (1971), pp. 68–75, <https://doi.org/10.1007/BF01584073>.
- [34] H. A. ELKARANSHAWY, K. T. MOHAMED, A. S. ASHOUR, AND H. M. ALKOMY, *Solving Painlevé paradox: P-R sliding robot case*, Nonlinear Dynamics, 88 (2017), pp. 1691–1705, <https://doi.org/10.1007/s11071-017-3339-y>.
- [35] N. FENICHEL, *Geometric singular perturbation theory for ordinary differential equations*, Journal of Differential Equations, 31 (1979), pp. 53–98, [https://doi.org/10.1016/0022-0396\(79\)90152-9](https://doi.org/10.1016/0022-0396(79)90152-9).
- [36] A. F. FILIPPOV, *Differential equations with discontinuous righthand sides*, vol. 18, Springer, 1988, <https://doi.org/10.1007/978-94-015-7793-9>.
- [37] A. GARCIA, E. PÉREZ-CHAVELA, AND A. SUSIN, *A generalization of the Poincaré compactification*, Archive for rational mechanics and analysis, 179 (2006), pp. 285–302, <https://doi.org/10.1007/s00205-005-0389-y>.
- [38] F. GÉNOT AND B. BROGLIATO, *New results on Painlevé paradoxes*, European Journal of Mechanics - A/Solids, 18 (1999), pp. 653–677, [https://doi.org/10.1016/S0997-7538\(99\)00144-8](https://doi.org/10.1016/S0997-7538(99)00144-8).
- [39] J. A. GREENWOOD AND J. P. WILLIAMSON, *Contact of nominally flat surfaces*, Proceedings of the Royal Society A, 295 (1966), pp. 300–319, <https://doi.org/10.1098/rspa.1966.0242>.
- [40] B. HALL, *Why Does Chalk Squeek? Master*, Master’s Thesis, Department of Engineering Mathematics, University of Bristol, 140 (2011).
- [41] G. HAMEL, *Bemerkungen zu den vorstehenden Aufsätzen der Herren F. Klein und R. v. Mises*, Zeitschrift für angewandte Mathematik und Physik, 58 (1909), pp. 195–196.
- [42] S. J. HOGAN AND K. U. KRISTIANSEN, *On the regularization of impact without collision: the Painlevé paradox and compliance*, Proceedings of the Royal Society A, 473 (2017), p. 20160073, <https://doi.org/10.1098/rspa.2016.0773>.
- [43] A. IUORIO, N. POPOVIC, AND P. SZMOLYAN, *Singular perturbation analysis of a regularized mems model*, SIAM Journal on Applied Dynamical Systems, 18 (2019), pp. 661–708, <https://doi.org/10.1137/18M1197552>.
- [44] A. IVANOV, *On the correctness of the basic problem of dynamics in systems with friction*, Journal of Applied Mathematics and Mechanics, 50 (1986), pp. 547–550, [https://doi.org/10.1016/0021-8928\(86\)90026-2](https://doi.org/10.1016/0021-8928(86)90026-2).

- 
- [45] A. IVANOV, *Singularities in the dynamics of systems with non-ideal constraints*, Journal of Applied Mathematics and Mechanics, 67 (2003), pp. 185–192, [https://doi.org/10.1016/S0021-8928\(03\)90004-9](https://doi.org/10.1016/S0021-8928(03)90004-9).
- [46] S. IWNICKI, *Simulation of wheel–rail contact forces*, Fatigue & fracture of engineering materials & structures, 26 (2003), pp. 887–900, <https://doi.org/10.1046/j.1460-2695.2003.00699.x>.
- [47] H. JARDÓN-KOJAKHMETOV AND C. KUEHN, *On fast–slow consensus networks with a dynamic weight*, Journal of Nonlinear Science, 30 (2020), pp. 2737–2786, <https://doi.org/10.1007/s00332-020-09634-9>.
- [48] M. R. JEFFREY, *Dynamics at a switching intersection: Hierarchy, isonomy, and multiple sliding*, SIAM Journal on Applied Dynamical Systems, 13 (2014), pp. 1082–1105, <https://doi.org/10.1137/13093368X>.
- [49] M. R. JEFFREY, *Hidden dynamics: the mathematics of switches, decisions and other discontinuous behaviour*, Springer, 2018, <https://doi.org/10.1007/978-3-030-02107-8>.
- [50] S. JELBART, K. U. KRISTIANSEN, AND M. WECHSELBERGER, *Singularly perturbed boundary-focus bifurcations*, Journal of Differential Equations, 296 (2021), pp. 412–492, <https://doi.org/10.1016/j.jde.2021.06.008>.
- [51] J. H. JELLET, *Treatise on the Theory of Friction*, Hodges, Foster and Co., Dublin, 1872, <https://archive.org/details/cu31924001082555>.
- [52] K. L. JOHNSON, *Contact mechanics*, Cambridge University Press, 1987, <https://doi.org/10.1017/CBO9781139171731>.
- [53] C. JONES AND N. KOPELL, *Tracking invariant manifolds with differential forms in singularly perturbed systems*, Journal of Differential Equations, 108 (1994), pp. 64–88.
- [54] C. K. JONES, *Geometric singular perturbation theory*, Dynamical systems, (1995), pp. 44–118, <https://doi.org/10.1007/BFb0095239>.
- [55] P. KAKLAMANOS AND K. U. KRISTIANSEN, *Regularization and geometry of piecewise smooth systems with intersecting discontinuity sets*, SIAM Journal on Applied Dynamical Systems, 18 (2019), pp. 1225–1264, <https://doi.org/10.1137/18M1214470>.
- [56] A. A. KAPAEV, *Asymptotic behavior of the solutions of the painlevé equation of the first kind*, Differentsial'nye Uravneniya, 24 (1988), pp. 1684–1695, <http://mi.mathnet.ru/eng/de6681>.
- [57] J. B. KELLER, *Impact with friction*, Transactions of the ASME, Journal of Applied Mechanics, 53 (1986), pp. 1–4, <https://doi.org/10.1115/1.3171712>.



## BIBLIOGRAPHY

---

- [58] F. KLEIN, *Zu Painlevés Kritik der Coulombschen Reibgesetze*, Zeitschrift für angewandte Mathematik und Physik, 58 (1909), pp. 186–191.
- [59] I. KOSIUK AND P. SZMOLYAN, *Scaling in singular perturbation problems: blowing up a relaxation oscillator*, SIAM Journal on Applied Dynamical Systems, 10 (2011), pp. 1307–1343, <https://doi.org/10.1137/100814470>.
- [60] K. U. KRISTIANSEN, *Geometric singular perturbation analysis of a dynamical target mediated drug disposition model*, Journal of Mathematical Biology, 79 (2019), pp. 187–222, <https://doi.org/10.1007/s00285-019-01354-3>.
- [61] K. U. KRISTIANSEN, *The regularized visible fold revisited*, Journal of Nonlinear Science, 30 (2020), pp. 2463–2511, <https://doi.org/10.1007/s00332-020-09627-8>.
- [62] K. U. KRISTIANSEN, *A stiction oscillator under slowly varying forcing: Uncovering small scale phenomena using blowup*, SIAM Journal on Applied Dynamical Systems, 20 (2021), p. 2359–2390, <https://doi.org/10.1137/21M140050X>.
- [63] K. U. KRISTIANSEN AND S. J. HOGAN, *On the use of blowup to study regularizations of singularities of piecewise smooth dynamical systems in  $\mathbb{R}^3$* , SIAM Journal on Applied Dynamical Systems, 14 (2015), pp. 382–422, <https://doi.org/10.1137/140980995>.
- [64] K. U. KRISTIANSEN AND S. J. HOGAN, *Le canard de Painlevé*, SIAM Journal on Applied Dynamical Systems, 17 (2018), pp. 859–908, <https://doi.org/10.1137/17M1122256>.
- [65] K. U. KRISTIANSEN AND S. J. HOGAN, *Resolution of the piecewise smooth visible–invisible two-fold singularity in  $\mathbb{R}^3$  using regularization and blowup*, Journal of Nonlinear Science, 29 (2019), pp. 723–787, <https://doi.org/10.1007/s00332-018-9502-x>.
- [66] K. U. KRISTIANSEN AND P. SZMOLYAN, *Relaxation oscillations in substrate-depletion oscillators close to the nonsmooth limit*, Nonlinearity, 34 (2021), p. 1030, <https://doi.org/10.1137/100814470>.
- [67] M. KRUPA AND P. SZMOLYAN, *Extending geometric singular perturbation theory to non-hyperbolic points - fold and canard points in two dimensions*, SIAM Journal on Mathematical Analysis, 33 (2001), pp. 286–314, <https://doi.org/10.1137/S0036141099360919>.
- [68] M. KRUPA AND P. SZMOLYAN, *Extending slow manifolds near transcritical and pitchfork singularities*, Nonlinearity, 14 (2001), pp. 1473–1491, <https://doi.org/10.1088/0951-7715/14/6/304>.
- [69] M. KRUPA AND P. SZMOLYAN, *Relaxation oscillation and canard explosion*, Journal of Differential Equations, 174 (2001), pp. 312–368, <https://doi.org/10.1006/jdeq.2000.3929>.

- 
- [70] C. KUEHN, *Multiple time scale dynamics*, vol. 191, Springer, 2015, <https://doi.org/10.1007/978-3-319-12316-5>.
- [71] L. LECORNU, *Sur la loi de Coulomb*, Comptes Rendu des Séances de l'Academie des Sciences, 140 (1905), pp. 847–848, <https://gallica.bnf.fr/ark:/12148/bpt6k30949/f899.item>.
- [72] L. LECORNU, *Sur le frottement de glissement*, Comptes Rendu des Séances de l'Academie des Sciences, 140 (1905), pp. 635–637, <https://doi.org/https://gallica.bnf.fr/ark:/12148/bpt6k30949/f675.item>.
- [73] R. LEINE, B. BROGLIATO, AND H. NIJMEIJER, *Periodic motion and bifurcations induced by the Painlevé paradox*, European Journal of Mechanics A/Solids, 21 (2002), pp. 869–896, [https://doi.org/10.1016/S0997-7538\(02\)01231-7](https://doi.org/10.1016/S0997-7538(02)01231-7).
- [74] C. E. LEMKE, *On complementary pivot theory*, Mathematics of the Decision Science, 1 (1968), pp. 95–114.
- [75] A. LEVANT AND B. SHUSTIN, *Quasi-continuous mimo sliding-mode control*, IEEE Transactions on Automatic Control, 63 (2017), pp. 3068–3074, <https://doi.org/10.1109/TAC.2017.2778251>.
- [76] C. LIU, Z. ZHAO, AND B. CHEN, *The bouncing motion appearing in a robotic system with unilateral constraint*, Nonlinear Dynamics, 49 (2007), pp. 217–232, <https://doi.org/10.1007/s11071-006-9123-z>.
- [77] P. LÖTSTEDT, *Coulomb friction in two-dimensional rigid body systems*, Zeitschrift für Angewandte Mathematik und Mechanik, 64 (1981), pp. 605–615, <https://doi.org/10.1002/zamm.19810611202>.
- [78] N. H. MCCLAMROCH, *A singular perturbation approach to modeling and control of manipulators constrained by a stiff environment*, in Proceedings of the 28th IEEE Conference on Decision and Control, December 1989, pp. 2407–2411, <https://doi.org/10.1109/CDC.1989.70609>.
- [79] R. MISES, *Zur Kritik der Reibungsgesetze*, Zeitschrift für angewandte Mathematik und Physik, 58 (1909), pp. 191–194.
- [80] Y. I. NEIMARK AND N. A. FUFAYEV, *The Painlevé paradoxes and the dynamics of a brake shoe*, Journal of Applied Mathematics and Mechanics, 59 (1995), pp. 343–352, [https://dx.doi.org/10.1016/0021-8928\(95\)00041-M](https://dx.doi.org/10.1016/0021-8928(95)00041-M).
- [81] A. NORDMARK, H. DANKOWICZ, AND A. CHAMPNEYS, *Friction-induced reverse chatter in rigid-body mechanisms with impacts*, IMA Journal of Applied Mathematics, 76 (2011), pp. 85–119, <https://doi.org/10.1093/imamat/hxq068>.

## BIBLIOGRAPHY

---

- [82] A. NORDMARK, P. L. VÁRKONYI, AND A. CHAMPNEYS, *Dynamics beyond dynamic jam; unfolding the Painlevé paradox singularity*, SIAM Journal on Applied Dynamical Systems, 17 (2018), pp. 1267–1309, <https://doi.org/10.1137/17M1141242>.
- [83] Y. OR, *Painlevé’s paradox and dynamic jamming in simple models of passive dynamic walking*, Regular and Chaotic Dynamics, 19 (2014), pp. 64–80, <https://dx.doi.org/10.1134/S1560354714010055>.
- [84] Y. OR AND E. RIMON, *Investigation of Painlevé’s paradox and dynamic jamming during mechanism sliding motion*, Nonlinear Dynamics, 67 (2012), pp. 1647–1668, <https://doi.org/10.1007/s11071-011-0094-3>.
- [85] P. PAINLEVÉ, *Sur les lois du frottement de glissement*, Comptes Rendu des Séances de l’Academie des Sciences, 121 (1895), pp. 112–115, <https://gallica.bnf.fr/ark:/12148/bpt6k3077p/f112.item>.
- [86] P. PAINLEVÉ, *Sur les lois du frottement de glissement*, Comptes Rendu des Séances de l’Academie des Sciences, 141 (1905), pp. 401–405, <https://gallica.bnf.fr/ark:/12148/bpt6k3095m/f401.item>.
- [87] P. PAINLEVÉ, *Sur les lois du frottement de glissement*, Comptes Rendu des Séances de l’Academie des Sciences, 141 (1905), pp. 546–552, <https://gallica.bnf.fr/ark:/12148/bpt6k3095m/f546.item>.
- [88] E. PENNISTRÌ, V. ROSSI, P. SALVINI, AND P. P. VALENTINI, *Review and comparison of dry friction force models*, Nonlinear dynamics, 83 (2016), pp. 1785–1801, <https://doi.org/10.1007/s11071-015-2485-3>.
- [89] L. PERKO, *Differential equations and dynamical systems*, vol. 7, Springer, 2013, <https://doi.org/10.1007/978-1-4613-0003-8>.
- [90] H. POINCARÉ, *Sur les courbes définies par les équations différentielles*, Journal de Mathématiques Pures et Appliquées, (1885), p. 167–244, <https://eudml.org/doc/235596>.
- [91] H. O. POLLAK AND N. J. A. SLOANE, *The on-line encyclopedia of integer sequences*. Published electronically <https://oeis.org>, sequence A161221, 2021.
- [92] M. J. D. POWELL ET AL., *Approximation theory and methods*, Cambridge University Press, 1981, <https://doi.org/10.1017/CBO9781139171502>.
- [93] L. PRANDTL, *Bemerkungen zu den Aufsätzen der Herren F. Klein, R. v. Mises und G. Hamel*, Zeitschrift für angewandte Mathematik und Physik, 58 (1909), pp. 196–197.

- [94] Y. SHEN, *Painlevé paradox and dynamic jam of a three-dimensional elastic rod*, Archive of Applied Mechanics, 85 (2015), pp. 805–816, <https://doi.org/10.1007/s00419-015-0992-9>.
- [95] Y. SHEN AND W. J. STRONGE, *Painlevé's paradox during oblique impact with friction*, European Journal of Mechanics A/Solids, 30 (2011), pp. 457–467, <https://doi.org/10.1016/j.euromechsol.2011.03.001>.
- [96] M. SLEMROD, *Monotone increasing solutions of the Painlevé 1 equation  $y'' = y^2 + x$  and their role in the stability of the plasma-sheath transition*, European Journal of Applied Mathematics, 13 (2002), p. 663–680, <https://doi.org/10.1017/S0956792502004977>.
- [97] G. STÉPÁN, *Delay, nonlinear oscillations and shimmying wheels*, in IUTAM Symposium on New Applications of Nonlinear and Chaotic Dynamics in Mechanics, Springer, 1999, pp. 373–386, [https://doi.org/10.1007/978-94-011-5320-1\\_38](https://doi.org/10.1007/978-94-011-5320-1_38).
- [98] D. E. STEWART, *Existence of solutions to rigid body dynamics and the paradoxes of Painlevé*, Comptes Rendu des Séances de l'Academie des Sciences Sér. I Math, 325 (1997), pp. 689–693, [https://doi.org/10.1016/S0764-4442\(97\)84784-2](https://doi.org/10.1016/S0764-4442(97)84784-2).
- [99] D. E. STEWART, *Rigid-body dynamics with friction and impact*, SIAM Review, 42 (2000), pp. 3–39, <https://doi.org/10.1137/S0036144599360110>.
- [100] S. H. STROGATZ, *Nonlinear dynamics and chaos lecture series*, 2014, [https://youtube.com/playlist?list=PLbN57C5Zdl6j\\_qJA-pARJnKsmROzPnO9V](https://youtube.com/playlist?list=PLbN57C5Zdl6j_qJA-pARJnKsmROzPnO9V).  
Accessed: 2022–01-12.
- [101] S. H. STROGATZ, *Nonlinear dynamics and chaos with student solutions manual: With applications to physics, biology, chemistry, and engineering*, CRC press, 2018, <https://doi.org/10.1201/9780429492563>.
- [102] M. A. TEIXEIRA AND P. R. DA SILVA, *Regularization and singular perturbation techniques for non-smooth systems*, Physica D, 241 (2012), pp. 1948–1955, <https://doi.org/10.1016/j.physd.2011.06.022>.
- [103] V. UTKIN, J. GULDNER, AND M. SHIJUN, *Sliding mode control in electro-mechanical systems*, vol. 34, CRC press, 1999, <https://doi.org/10.1201/9781420065619>.
- [104] P. L. VÁRKONYI, *On the stability of rigid multibody systems with applications to robotic grasping and locomotion*, ASME Journal of Mechanisms and Robotics, 7 (2015), p. 041012, <https://doi.org/10.1115/1.4029402>.
- [105] P. L. VÁRKONYI, *Dynamics of mechanical systems with two sliding contacts: new facets of Painlevé's paradox*, Archive of Applied Mechanics, 87 (2017), pp. 785–799, <https://doi.org/10.1007/s00419-016-1165-1>.

- [106] P. L. VÁRKONYI, *Transitions and singularities during slip motion of rigid bodies*, European Journal of Applied Mathematics, 29 (2018), pp. 778–804, <https://doi.org/10.1017/S0956792518000062>.
- [107] E. V. WILMS AND H. COHEN, *Planar motion of a rigid body with a friction rotor*, ASME Journal of Applied Mechanics, 48 (1981), pp. 205–206, <https://doi.org/10.1115/1.3157576>.
- [108] E. V. WILMS AND H. COHEN, *The occurrence of Painlevé’s paradox in the motion of a rotating shaft*, ASME Journal of Applied Mechanics, 64 (1997), pp. 1008–1010, <https://doi.org/10.1115/1.2788965>.
- [109] Z. ZHAO, C. LIU, AND B. CHEN, *Numerical method for three-dimensional impact with friction of multi-rigid-body system*, Science in China, Series G: Physics Astronomy, 49 (2006), pp. 102–118, <https://doi.org/10.1007/s11433-005-0065-0>.
- [110] Z. ZHAO, C. LIU, AND B. CHEN, *The Painlevé paradox studied at a 3D slender rod*, Multibody System Dynamics, 19 (2008), pp. 323–343, <https://doi.org/10.1007/s11044-007-9098-7>.
- [111] Z. ZHAO, C. LIU, B. CHEN, AND B. BROGLIATO, *Asymptotic analysis of Painlevé’s paradox*, Multibody System Dynamics, 35 (2015), pp. 299–319, <https://doi.org/10.1007/s11044-014-9448-1>.
- [112] Z. ZHAO, C. LIU, W. MA, AND B. CHEN, *Experimental investigation of the Painlevé paradox in a robotic system*, ASME Journal of Applied Mechanics, 75 (2008), p. 041006, <http://dx.doi.org/10.1115/1.2910825>.